Mixing Behaviour of Side Injection of Air Jets and Gaseous Fuel Jets into The Axial Flow of Tunnel Kilns

Dissertation

For the award of the degree

Doktoringenieur

(Dr.-Ing.)

by

M. Sc. Adnan Ghareeb Tuaamah Al-Hasnawi

Date of birth: 1. July 1980

in Baghdad, Iraq

Accepted by

The Faculty of Process and Systems Engineering
of the Otto-von-Guericke-University of Magdeburg

Reviewers:

Prof. Dr.-Ing. Echehard Specht (Reviewer and supervisor)
Institute of Fluid Dynamics and Thermodynamics,
Universität Magdeburg, Germany.

Prof. Dr.-Ing. Mohamed Attalla (Reviewer)
Faculty of Engineering - Mechanical Power and Energy Dept.
South valley University, Egypt.

Dr.-Ing Anne Tretau (Reviewer)
Brick and Tile Research Institute, Germany.

Jprof. Dr.-Ing Fabian Herz (Chairman)
Institute of Fluid Dynamics and Thermodynamics,
Universität Magdeburg, Germany.

Submitted on :   29.06.2016
Graduation Colloquium on: 22.09.2016

Preface

This dissertation is submitted to Otto von Guericke University, Magdeburg for the degree of Doctor of Engineering. The research described herein was conducted under the supervision of **Prof. Dr.-Ing. Eckehard Specht** from April 2013 to September 2016. To the best of my knowledge, this work is original except where suitable references are made to previous works. Neither this, nor any substantially similar dissertation has been submitted for any degree, diploma, or qualification at any other university or institution.

Magdeburg, June 28, 2016

Adnan Ghareeb Tuaamah Al-Hasnawi

Acknowledgement

Firstly, deepest gratitude goes to God for his uncountable blessings (Alhamdulillaah).

Abstract

This work reports on the investigation of the gas temperature distribution of the kiln atmosphere, especially between the kiln cars. Therefore, the mixing of the axial flow with injection of cold air into the preheating zone as well as the flame behavior while combustion of gaseous fuels in firing zone. Different geometric and operation parameters are varied. Additionally, it also discusses about the special injector nozzle in case of the roller hearth kiln and its influence on the mixing.

3D simulations (CFD ANSYS) are used to evaluate the quality of mixing for a part of preheating zone in a tunnel kiln. The influence of geometric parameters on temperature distribution in the preheating zone is studied. These parameters include the number and position of the side injection, cross-section area of ware, shape of nozzle outlet, kiln geometry and production inside the kiln. The quality of mixing is shown through three different plots, i.e. contour plot of temperature, frequency of temperature distribution and the plot of maximum temperature difference.

The better mixing quality is achieved by positioning the two side injections on the opposite walls and the maximum height and through the presence of products inside kiln. The results also showed that geometry of products inside the kiln seems to have great influence on the mixing inside the kiln while the shape of cross-section of the nozzle does not influence on mixing inside the kiln. Furthermore, effect of operation parameters on mixing quality, which include temperature and velocity of side injection, mixing ratio and velocity of ware stream to the gas stream ratio is studied. The injection velocity and the injected mass flow rate are combined in a parameter called impulse.

Better mixing is achieved with an increasing impulse of side injection. The slope of curve of temperature difference decreases strongly up to 4N impulse and after that it decreases slowly. The temperature of the side injection does not effect mixing, but merely affect the temperature of the mixture. As the ware to gas relative velocity decreases, the mixing quality is being better.

2D simulations using CFD (ANSYS) are carried out for annular ring burner with gaseous fuels in order to study the effect of geometric and operation parameters on flame behavior.

The mass fraction of gaseous fuels and the velocity of the mixture in dimensionless form are calculated analytically using equations derived from the laws of conservation of mass and momentum and then compared with numerical

results. The comparison of numerical results with analytical results in different axial positions shows that it is identical with maximum relative error ~29.5%.

The plots and contours are presented for flame length and temperature distribution under various operation and geometric parameters. The results show that the flame length is directly proportional to the air inlet diameter and temperature of the surroundings. It has a shorter flame with smaller air inlet diameter (high velocity of air inlet) and it has a longer flame with higher temperature of the surroundings. The excess air number and O_2 concentration of the combustion gas have a significant effect on the flame temperature profiles. The fuel velocity has almost no effect on flame behavior. The peak temperature when the surrounding is air, is relatively higher than that when the surrounding is combustion gas. Also the flame is longer in case when the surrounding is air.

In roller hearth kiln, hot air from the cooling zone is available at the end of the firing zone, allowing to use it again using injectors. 3D simulations in a domain containing injector nozzles are carried out to evaluate maximum velocity, quantity of air suction, streamlines and temperature distribution in the roller kiln. It is shown that the maximum velocity of air at the outlet of the core is about 90m/s. The temperature distribution with upstream model is found better than with downstream. Also, it could be proposed that the burner with longer outlet duct protects the product from direct exposure to the flame.

Zusammenfassung

In dieser Arbeit wird die Temperaturverteilung innerhalb der Ofenatmosphäre in Tunnelöfen, speziell zwischen den Ofenwagen, untersucht. Dabei wird die Vermischung des axialen Gasstroms durch Eindüsung von Kaltluft in die Vorwärmzone und das Abbrandverhalten von gasförmigem Brennstoff in der Brennzone betrachtet. Verschiedene Geometrie- und Betriebsparameter werden variiert. Darüber hinaus wird auch die Vermischung betrachtet, wenn Injektordüsen im Falle der Rollenherdofen genutzt werden.

Zur Untersuchung der Eindüsung von Kaltluft in die Vorwärmzone des Brennkanals werden 3D-Simulationen (CFD ANSYS) durchgeführt. Dabei wird der Einfluss geometrischer Parameter auf die Temperaturverteilung und somit auf die Qualität der Vermischung analysiert. Diese Parameter umfassen die Anzahl und Position der Seiteneindüsungen, die Querschnittsfläche der Ware, die Form des Düsenquerschnitts, die Ofengeometrie und der Besatzaufbau innerhalb des Ofens. Die Qualität der Vermischung wird mit Hilfe von Temperaturfeldern, Häufigkeitsverteilungen und der maximalen axialen Temperaturdifferenz quantifiziert.
Eine gute Mischgüte wird erreicht, indem je eine Eindüsung an den gegenüberliegenden Wänden mit einem möglichst großen vertikalen Abstand zueinander eingesetzt wird. Die Ergebnisse zeigen auch, dass die Geometrie der Ware einen großen Einfluss auf die Durchmischung im Inneren des Ofens hat, während die Form des Düsenquerschnitts die Mischgüte nicht beeinflusst. Weitere Betriebsparameter wie die Gastemperatur der Eindüsung, die Einblasgeschwindigkeit, das Verhältnis der Volumenströme aus Eindüsung und axialer Hauptströmung werden variiert. Die Einblasgeschwindigkeit sowie der Massenstrom der Eindüsung werden im Impulsstrom als Parameter zusammengefasst.
Es wird gezeigt, dass die Mischgüte mit zunehmendem Impulsstrom bis 4 N stark ansteigt und sich der Effekt danach langsam abschwächt. Die Gastemperatur der Eindüsung wirkt sich nicht auf die Vermischung aus, jedoch wird die Mischtemperatur beeinflusst.

Des Weiteren wurden zweidimensionale CFD-Simulationen durchgeführt, um das Abbrandverhalten von gasförmigen Brennstoffen unter Nutzung von Parallelstrombrennern mit einer Diffusionsflamme zu untersuchen.

Der Massenanteil des gasförmigen Brennstoffs und das Geschwindigkeitsfeld des Gemisches werden unter Verwendung von Gleichungen aus den Gesetzen der Masse- und Impulserhaltung abgeleitet. Der Vergleich der numerischen Ergebnisse mit analytischen Ergebnissen für verschiedene axiale Positionen zeigt eine gute Übereinstimmung mit einem maximalen relativen Fehler von ca. 29.5%.

Es wird die Flammenlänge und die Temperaturverteilung für verschiedene Geometrie- und Betriebsparameter dargestellt. Die Ergebnisse zeigen, dass die Flammenlänge zu dem Lufteinlassdurchmesser und der Temperatur der Umgebung direkt proportional ist. Es ergibt sich eine kürzere Flamme bei kleinem Lufteinlassdurchmesser (hohe Geschwindigkeit der Eindüsung) sowie eine längere Flamme bei höherer Umgebungstemperatur. Die Luftzahl und die O_2-Konzentration des umgebenden Verbrennungsgases haben einen signifikanten Einfluss auf das Temperaturprofil innerhalb der Flamme. Die Eintrittsgeschwindigkeit des Brennstoffs zeigt nur einen geringen Effekt auf das Flammenverhalten. Die Maximaltemperatur innerhalb der Flamme sowie die Flammenlänge sind am größten, wenn die Flamme von Frischluft umgeben ist anstatt von Verbrennungsgas.

Im Rollenherdofen steht am Ende der Brennzone Heißluft aus der Kühlzone zur Verfügung, die durch Injektorbrenner genutzt wird. 3D-Simulationen wurden durchgeführt, um die Maximalgeschwindigkeit der Eindüsung, die abgesaugte Luftmenge, die Temperaturverteilung innerhalb des Brennkanals bzw. die Vermischung zu untersuchen. Es wird gezeigt, dass die maximale Austrittsgeschwindigkeit der Luft etwa 90 m/s beträgt. Die Vermischung ist intensiver für den Fall, dass axial und entgegengesetzt zum Hauptstrom eindedüst wird, gegenüber dem Fall der Eindüsung stromabwärts. Außerdem wird eine größere Eintauschtiefe der Brennerlanze vorgeschlagen, um den Kontakt von Flamme und Ware zu vermeiden.

List of Contents

Nomenclature

Only commonly used symbols are defined here and some specific used symbols are defined explicitly within the text.

Latin letter symbols

Symbol	Meaning	Unit
A	Area	$[m^2]$
B	Kiln width	$[m]$
b	Ware width	$[m]$
B.Z.	Boundary Zone	$[-]$
c_p	Specific heat	$[KJ/kg.K]$
D	Diameter	$[m]$
d_p	Air inlet diameter	$[m]$
d_o	Fuel inlet diameter	$[m]$
d_j	Jet diameter	$[m]$
f	Mixture fraction	$[-]$
f_o	Initial mixture fraction	$[-]$
f_a	Axial mixture fraction	$[-]$
G	Geometry	$[-]$
H	Height	$[m]$
H_K	Kiln height	$[m]$
h_W	Ware height	$[m]$
h	Nozzle height	$[m]$
IFR	Impulse flow rate	$[N]$
I_o	Initial Momentum	$[N]$
I_z	Momentum after z distance	$[N]$
L	Air demand	$[-]$
L_f	Flame length	$[m]$
M	Mixing	$[-]$
$\dot{M}$	Mass flow rate	$[Kg/s]$
p	Pressure	$[N/m^2]$
t	Temperature	$[°C]$
Δt_o	Initial temperature difference	$[^oC]$
V^o	Volume flow rate	$[m^3/s]$
V	volume	$[m^3]$
w	Velocity	$[m. s^{-1}]$
w_o	Fuel velocity	$[m. s^{-1}]$
w_a	Axial velocity	$[m. s^{-1}]$
$\overline{w}$	Mean velocity	$[m. s^{-1}]$
x_o	Initial fuel mass fraction	$[-]$

| x_a | Axial fuel mass fraction | [-] |
| z | Longitudinal dimension | [m] |

Greek symbols

α	Jet angle	[degee]
Δ	Difference	[-]
ε	Turbulent dissipation rate	[m^2/s^3]
θ	Dimensionless temperature difference	[-]
k	Turbulent kinetic energy	[m^2/s^2]
μ	Dynamic viscosity	[$N.s/m^3$]
λ	Excess air number	[-]
ρ	Density	[Kg/m^3]
φ	Porosity	[-]

Subscripts

a	Axial direction
G	Gas
i	Incoming flow
inj	Side injection
j	Jet
k	Kiln
main	Main axial flow
max	Maximum
min	Minimum
p	Primary air
R	Ratio
st	Stoichiometric
r	Relative
f	Fuel
W	Ware
z	Mixing length

Abbreviations

2D	Two dimensions
3D	Three dimensions
CFD	Computational fluid dynamics
CAD	Computer aided design
tan	tangent
Eq	equation
surr.	surroundings
comb. gas	Combustion gas
SST	Shear Stress Transport
Par.	Particle

No.   Number

1 Introduction
1.1 Ceramic
Ceramic products are commonly utilized in daily life and industries. The term ceramic [1] is derived from the Greek 'keramos' which means pottery. Rrecent research shows that the processing of clay started around 19000 BC. The manufacturing process of ceramics involves the thermal treatment, adjustment of the grain size and moisture of the inorganic substances. Some of them are completely molten to be formed into ceramics as glass. While others are heat-treated and made in the ceramic products in the sintered state immediately before being melted [2].

1.2 Classification of ceramics
Ceramics can be classified in many way. They can be classied as **traditional and industrial ceramics** group, also called **whiteware**.This group includes the wall and floor tiles, table ware, ornamental ware, sanitary ware and technical ceramics. Another group is **Coarse or construction** group, which includes the bricks and roof tiles, vitrifies clay pipes and refractory products. Figure 1.1 shows another classification of ceramics if consider some of them (ceramics) are completely molten to be formed into ceramics[2].
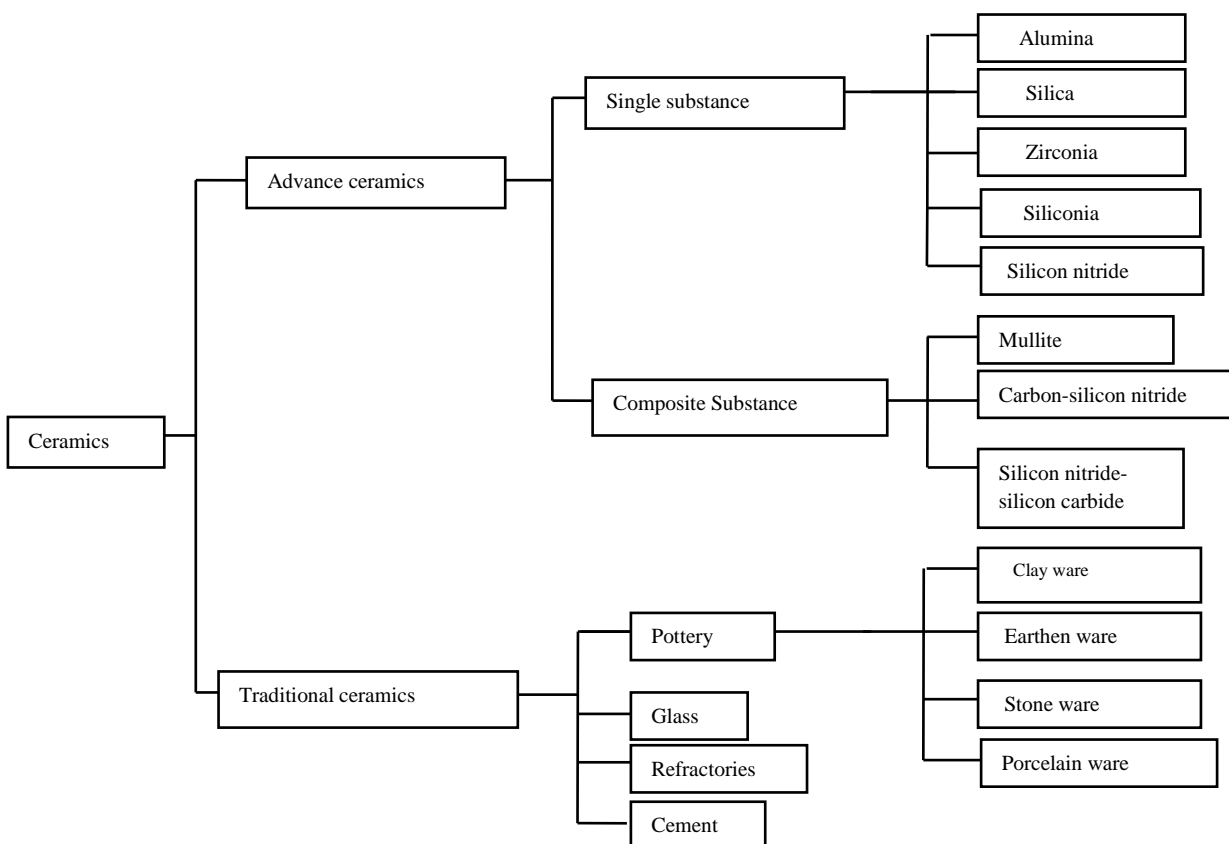
Figure 1.1: Classification of ceramic materials [2]

The third classification based on the manufacturing of ceramic products and their importance in terms of employment and economics, defined as follows [1].

- Bricks and roof tiles
- Vitrified clay pipes
- Refractory products
- Sanitary ware
- Wall and floor tiles
- Table- and ornamental ware
- Technical ceramics
- Expanded clay aggregates
- Inorganic bonded abrasives.

Following sections are dedicated to the brief description of some of these products:

1.2.1 Bricks and roof tiles

Bricks are widely used in construction and manufacturing industries and was first produced in a sun-dried from at least 6000 years ago. The basic ingredient of brick is clay. This clay is mined from open pits after that molded and then fired in a kiln to obtain strength, hardness and heat resistance to form bricks.

Brick usually has a standard size and shape, however, this standard varies according to different countries. There are different types of bricks manufactured [4] in order to suit a particular requirement, for example acid resistant bricks, common building solid bricks, facing bricks, heavy duty bricks, perforated bricks sewer bricks and soling bricks. Figure 1.2 shows some of these bricks.

Figure 1.2: Demonstrate types of bricks and roof tiles [4]

1.2.2 Vitrified clay pipes

Vitrified clay pipes in some classification are classified as **Stoneware**. Primarily they are produced for stoneware from non- refractory fire clay or some combination of clay, fluxes, and silica. These components when fired has properties similar to stoneware made from fire clay. There are various applications for vitrified clay, including: pipes for drains and acids, and flue in fireplace as shown in figure 1.3.

(a)   (b)
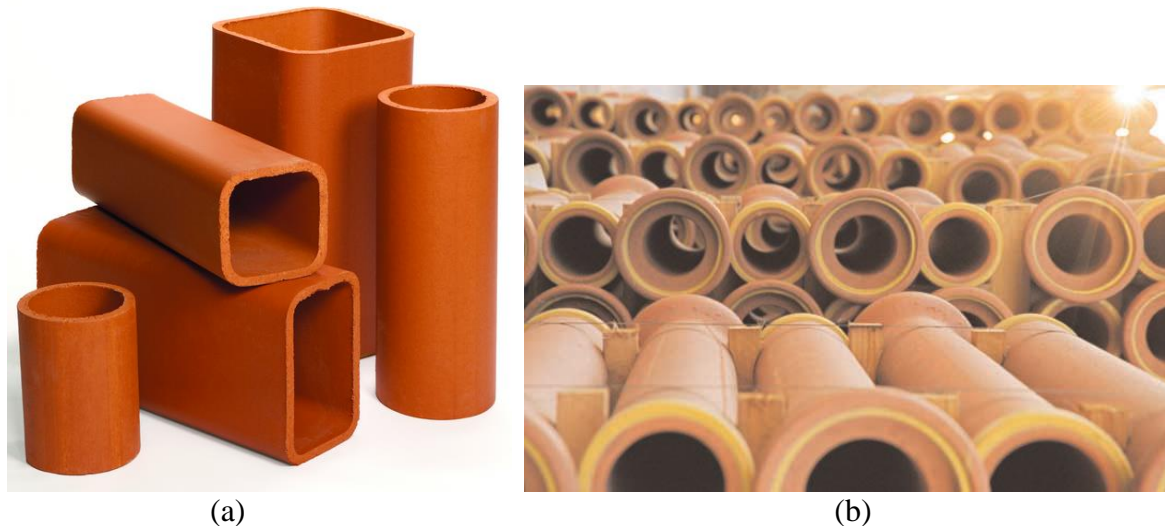
Figure 1.3: (a) Flue used in fireplaces [5] and (b) vitrified clay pipes [6]

1.2.3 Refractory products

Refractory products are classified according to their principal constituent [1].They are also classified according to high, low alumina, silica and special products, based on carbon, graphite. Thes ceramics are capable of withstanding temperatures above 1500°C. Refractory products in a wide variety of shapes and forms are used in many industrial applications of steel, iron, cement, lime, glass, ceramic, aluminium, copper and petrochemical industries, in incinerators and power plants.

1.2.4 Table- and ornamental ware

Table- and ornamental ware can be defined as porcelain, glazed or unglazed. It is used primarily for artistic purposes as dishes, cups, bowls, jugs and vases as shown in figure 1.4.

Figure 1.4: Porcelain [8]

1.2.5 Sanitary ware

It is one of the chinaware applications according to some classification [7] used for sanitary purposes. Typical sanitary ceramic products are lavatory bowls, bidets, wash basins. Figure 1.5 shows some applications of sanitary ware.

Figure 1.5: Sanitary ware [9]

1.2.6 Technical ceramics

Technical ceramics are applied in many industries, which include vitreous ceramic whiteware. They cover both established products like insulators and new applications like supply equipment for the aerospace and automotive industries (engine part and ceramic brake system), electronics (capacitors), environment protection (filters) and many others. The following figures show some types of technical ceramics

Figure 1.6: Technical Ceramics [10][3]

1.3   Manufacturing process of traditional ceramics (Bricks)

In general the manufacturing process of ceramics is largely dependent on the materials used and type of final product. The typical process [1] has been show in the schematic Figure 1.7. Also it is display possible or necessary supply and disposal facilities. In this dissertation give a description of some of the manufacturing process of traditional ceramics:

1.3.1 Raw material

Soils are made up of a complex mixture of solids, liquids and gases. The solid fraction of soils are consists of organic and inorganic components[11]. The inorganic component of the soil makes up more than 90% of the soil solids.

The inorganic solids in a crystalline structure are called minerals. The inorganic component includes both primary and secondary minerals.

Clay is an essential raw material for the production of ceramics (bricks). The common clay minerals are hydrated aluminium silicates that usually founded from the weathering of rocks[12]. Different types of clay minerals can form various types of pottery items based on their characteristics. Characteristics of clay can also affect the quality of the ceramics. Forthermore, clay minerals have many uses in the chemical and oil industries and could be used in wastewater treatment and spill control situations.
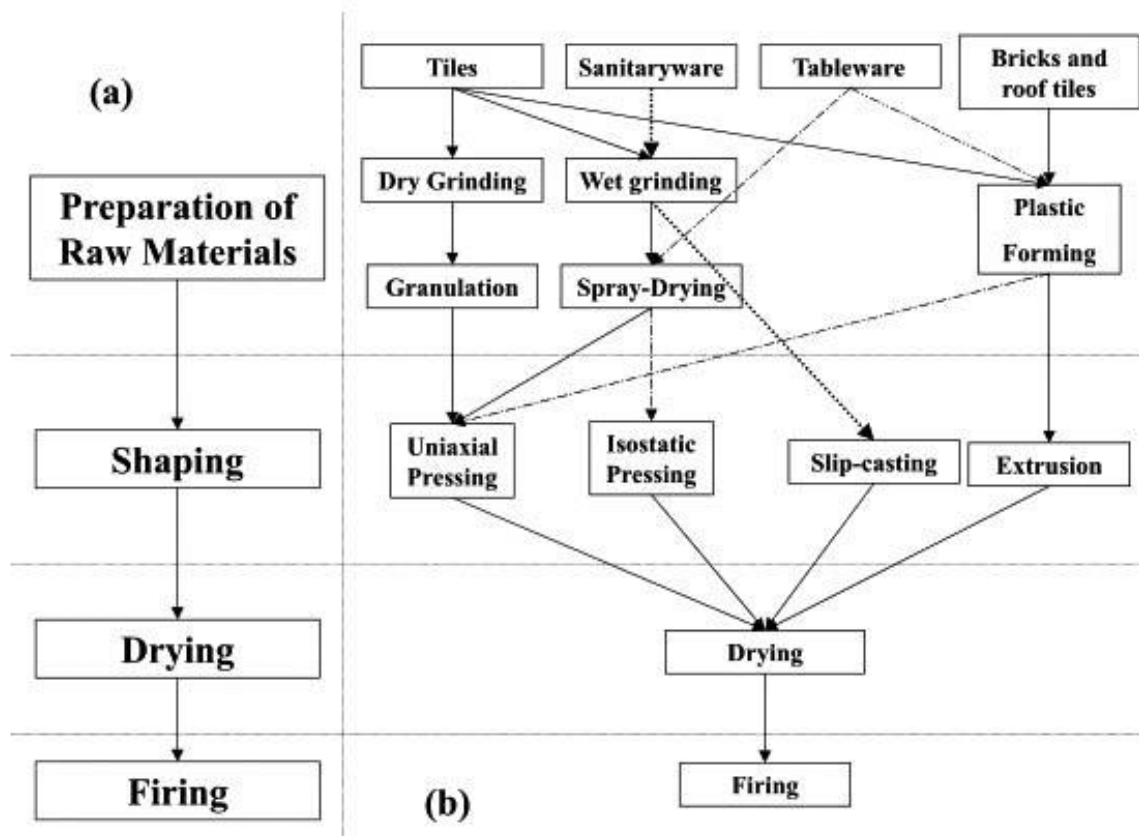
Figure 1.7: Stages in the manufacture of ceramic products [1]

1.3.2 Drying process

Drying means loss of moisture from the surface of the substance by evaporation. The drying process is an important process affecting the product yield. It is considered the greatest energy consumer second to the firing process. Although, the drying speed depends on the temperature and humidity. It requires a longer time than many of the other processes in a kiln. The waste heat of the kiln is generally used as the heat source for drying. The relationship between the drying time and speed [2] is shown in Figure 1.8. The period of constant rate drying occurs when there is balance kept between moisture shifting from inside the substance to the surface and moisture evaporation from the surface.

First falling drying rate occurs when moisture shifts from inside the substance to the surface with reduced moisture evaporating from the surface. The second falling drying rate period is the period when evaporation takes place inside and vapor diffuses to the surface without moisture shifting from inside the substance. Sometimes during drying cracks occur due to shrinking of the green body. This occurs when temperature gradient is steep under drying conditions between the constant rate drying period and first falling drying rate period, or when the temperature is excessively low.
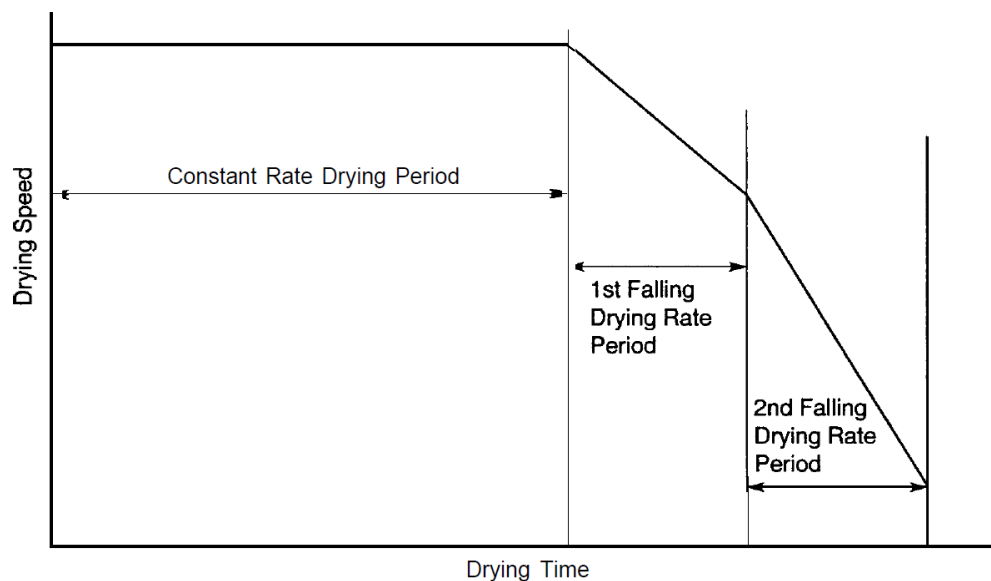
Figure 1.8: Drying time and speed [2]

1.3.3 Firing process

The firing process is a one of the most important stages in ceramic production. It could be defined as sintering process. This process is responsible to control many properties of the final ceramic products such as fire resistance, dimensional stability, resistance to water and chemicals, abrasion resistance and mechanical strength. Firing process can be divided in two steps [2]:

- **Room temperature to 900 ^{o}C**

After drying the green ware may contain 1 to 2 percent moisture before entering the kiln. This moisture is driven off before the temperature reaches 200°C. The organic substances contained in the material are carbonized or combusted when the temperature is between about 300°C and 500°C. During this period the strength of the material is reduced. The water of crystallization contained in the material is subjected to hydration and decomposition take place at 500 to 700°C. Because this reaction is an endothermic reaction, heat is absorbed into the gray body and temperature does not rise. This requires a supply of necessary heat in sufficient amount. The organic substance carbonized at 300 to 500°C and exposed to oxidation at about 800°C and so-called soot removal is carried out. It is necessary to take the time to supply a sufficient amount of air during this period to remove soot completely. Firing-starts partly at the end of the oxidation period. The strength of the green body is increased slightly.

- **From 900°C to the maximum temperature**

Active sintering begins to take place during this period, and the gray body continues to shrink. Therefore, temperature should be raised uniformly while sufficient attention is paid to avoid uneven shrinkage and deformation. At this stage, reduction and sintering may take place depending on the type of the firing goods. The temperature of the sintered pottery is raised to the specified value. Then heating is terminated. Table 1.1 shows the firing temperature of different types of ceramics.

Earth ware	1000-1150°C
Facing bricks and clinkers	1000-1200 °C
Silica bricks	1450-1550 °C
Vitreous china	1200-1300 °C
High alumina bricks	1500-1800 °C
Basic bricks	1400-1800 °C
Clay blocks	880-1020 °C
Wall and floor tiles	1080-1300 °C
Pottery ware	750-950 °C
Stoneware	1130-1280 °C
Porcelain	1300-1450 °C
Roof tiles	1000-1150 °C
Fireclay bricks	1250-1500 °C

Table 1.1: Firing temperature of different types of ceramics [1]

1.4   Kilns classification

1.4.1 Introduction

Kilns are facilities used to house heating for eventual conversion of green clay ware into hard stone-like ware. The range of kiln used for ceramic production from ancient times to now is very large. Some classifications depend on method of firing, direction of flow of gases while transferring their heat to the ware, accessibility for machine setting and whether the furnace gases come into contact with the ware or not. If it is investgated in depth, it is found that there exist not only different typs of the kiln but also many variants with each typ of kiln. There are two basic types of kilns to produce ceramics if classified on method of firing:

1.4.2 Intermittent (Periodic) kilns

In periodic kilns, product is loaded, sealed, heated, cooled and unloaded for every firing. Modern periodic kiln have a few common variants. Fixed-hearth kiln, which is still one of the most common form for a periodic kiln [1]. It has a door on the side or top for loading the kiln. The box kiln is a classic example of a fixed-hearth kiln.

The shuttle kiln has one or more doors and one or more cars that support the ware to be fired and act as the floor for the kiln. By shuttling two sets of cars to and from one kiln, the downtime for loading the kiln can be reduced.

This kind of kilns are mainly used for smaller scale manufactureing of specialized products, such as special shaped bricks, pipe fittings, roof tile fittings and refractory products, etc. They offer flexibility when the ceramics composition is altered frequently. These advantages outweigh their somewhat lower energy efficiency.

The following Figures show the front view and cross-section of a shuttle kiln.

(a)   (b)
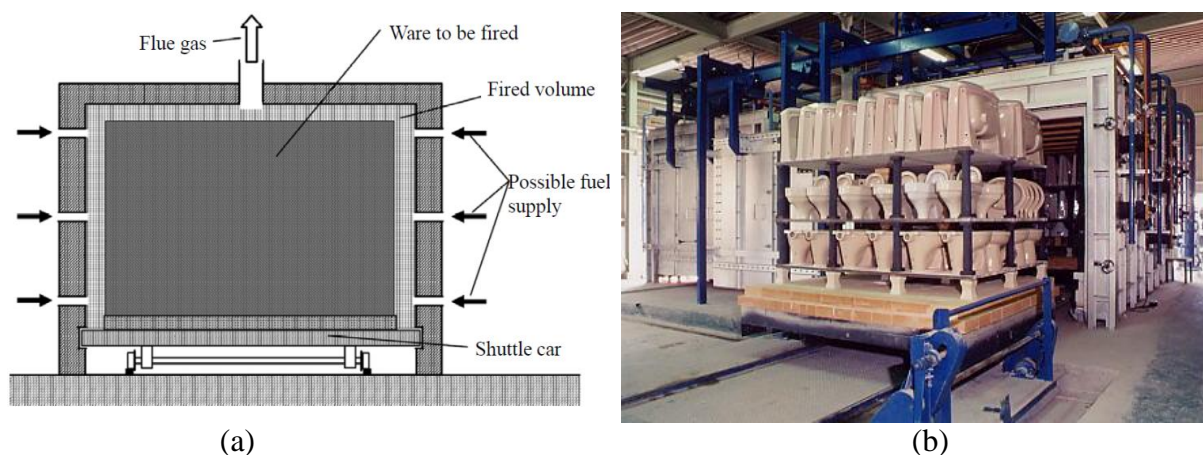
Figure 1.9: Shuttle kiln (a) cross-section [1] (b) front view [13]

1.4.3   Continuous kilns

In continuous kilns, once the fire is lit. They keep on operating until deliberately stopped. Here, either load moves through the firing zone or the fire travels through the kiln as the fuel inlet position changes. Within these classifications, there exist many subclasses for each type. While it is impossible to enumerate all types of kilns, some of the most important kilns are discussed to give an idea about their technical and operational principles.

- **Roller hearth kiln**

This kiln is designed as a continuous kiln. The roller conveyer is installed from the kiln inlet to the outlet and used to carry the product to be fired from the inlet to the outlet. Initially it was used to produce floor and wall tiles, but lately its use has been extended to all types of tableware (decoration, biscuit firing, gloss firing), sanitary ware and even clay materials for civil construction. Compared to tunnel kiln (which will be explained later), roller hearth kilns do not need the thermal indifferent kiln cars or the heavy lining and large rail network as the goods shall be loaded with refractory plates in case they are not suitable to be loaded on the rollers directly, Figure 1.10 shows the roller kiln with the transport goods. Furthermore, This type of kilns usually work contineausly. Depending on the type of insulation and conveyor rollers used, it can operate at temperatures up to 1250°C for pottery firing and up to 1400 ^{o}C for porcelain firing [14].

Figure 1.10: Schematic diagram of roller hearth kiln

- **Tunnel kiln**

Tunnel kilns are widely used in industry for making ceramics and brick [15]. It is an elongated kiln, which looks like a tunnel and is made of refractory and heat insulated construction material. Inside the kiln, kiln cars transport the green wares and eventually the final products. It has a typical length between 35 m and 250 m, width between 1 m and 6 m and height between 1 m and 2 m [16]. The green wares are loaded on kiln cars and sen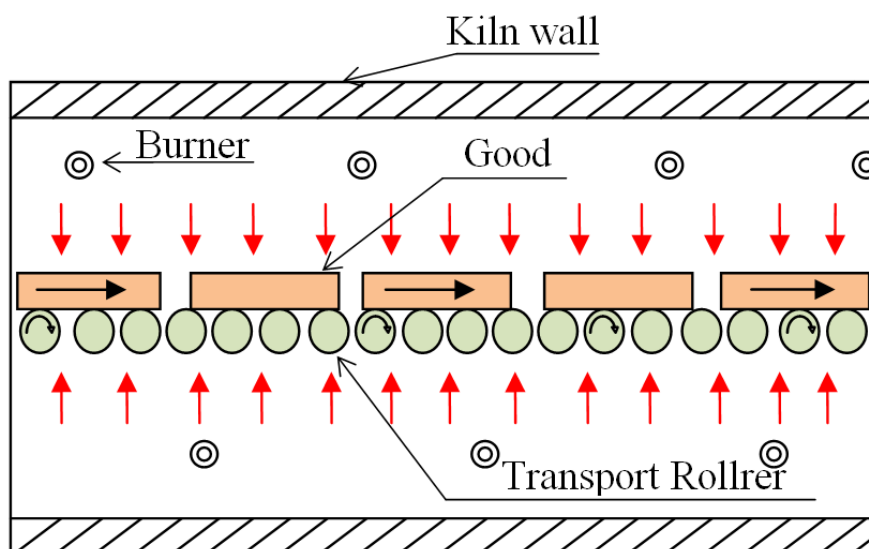t to separate champer to remove moisture. Then green ware is preheated. At enters the kiln from one end. The kiln cars enter the kiln one after another. Kiln cars move through different temperature zone along the kiln. Figure 1.11 shown schematic diagram of tunnel kiln.

Tunnel kiln operating conditions

In tunnel kiln, the green wares are exposed to a sequence of heat treatment stage. Starting with **preheating zone.** In this zone temperature of green product increases gradually until a certain temperature due to contact with flue gases which are coming from the firing zone.

The second is a **firing zone.** It is also called sintering zone. This zone is considered the main zone in the kiln. This zone is responsible to heat up the green products to the desired temperature by subjecting the green ware to heat from the combustion of fuel and to produce the products before leaving it. In the preheating and firing zones, the heat from the high temperature flue gas preheats the green ware.

The third zone is **cooling zone**. It is considered the last zone in tunnel kiln, where the heat is recovered. This zone is responsible to cool down the product by blowing air at the end side of the tunnel kiln. Therefore, the heat exchanger in cooling zone acts as a countercurrent heat exchanger.

In general there are three main stages in cooling zone [17]; **rapid cooling** to avoid the low- valency Fe to be oxidized, **static cooling** to avoid cracks in the products and **final cooling** to increase the production speed and improve the productivity. After complete cooling the products are removed and the empty kiln car is going to the other side of the kiln, to begin the next production cycle as shown in figure 1.11.

The heat exchange process in preheating, firing and cooling zones is a countercurrent. That means the solid on the kiln cars moves continuously in the opposite direction of the gas flow in the kiln as shown in figure 1.12.
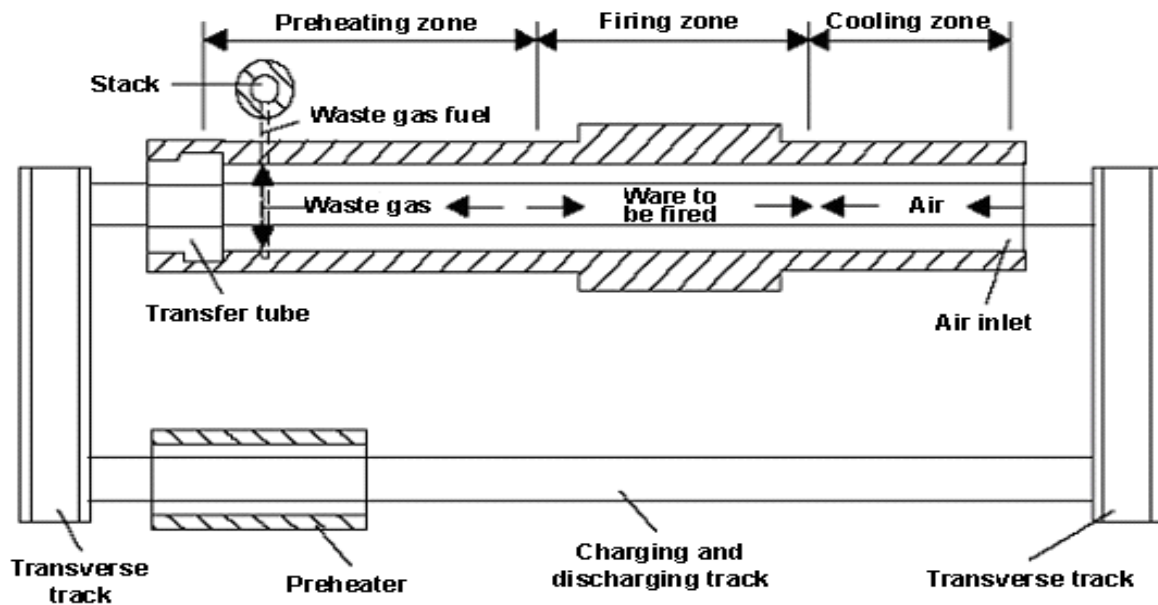
Figure 1.11: Schematic view of tunnel kiln [1]
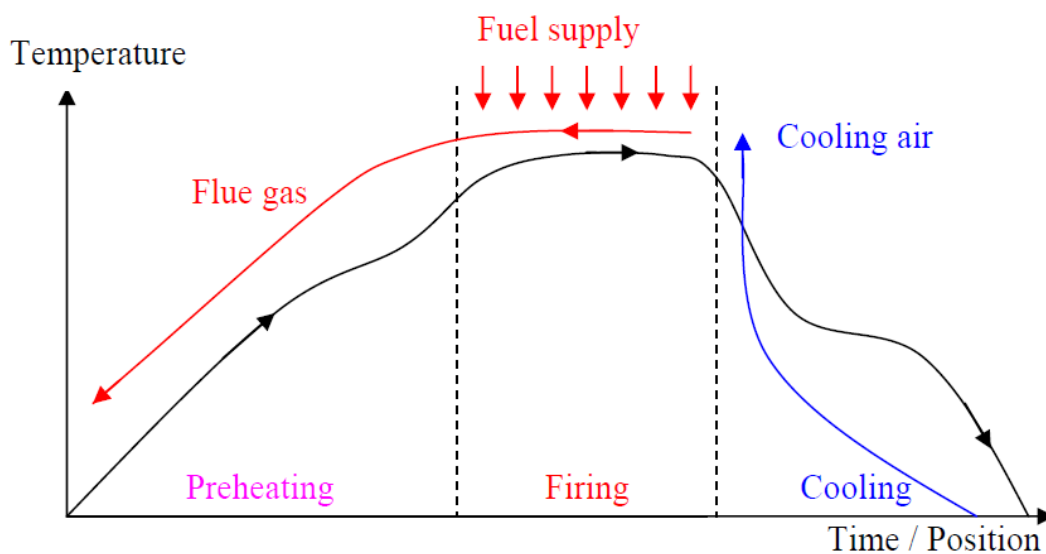
Figure 1.12: Flow direction and temperature profile of goods and gas [12]

The behavior of atmosphere and pressure of the tunnel kiln for porcelain firing [2] is shown in Figure 1.13. It shows the specific characteristic of high temperature reducing atmosphere. It is important to ensure a complete oxidizing atmosphere in the preheating zone. The flow of the combustion gas is constant, which is going from the firing zone to the preheating zone.

On the other hand, there is a zero pressure line between the cooling and firing zone. It is achieved by blowing the ambient air at the very beginning of the cooling zone. It is also useful to avoid the reversal of the air flow from the firing to the cooling zone [15].
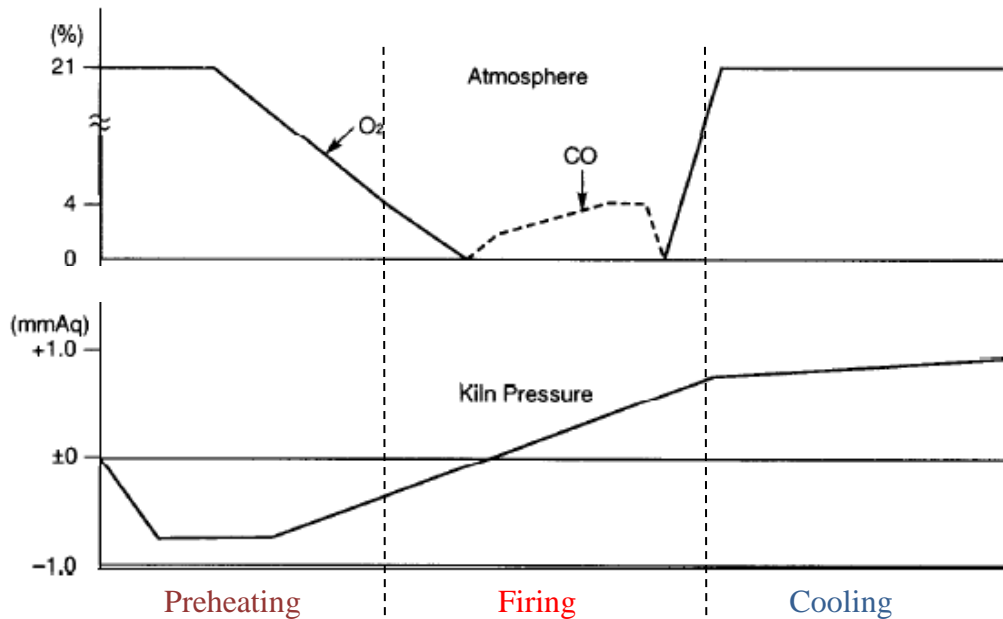
Figure 1.13: The atmosphere and pressure of the tunnel kiln [2]

the following steps must be taken to achieve constant flow of combustion gas and constant pressure in kiln [2]:

• Uniform pattern of the loading (ware) on the kiln car. It is very important to ensure a stable flow of combustion gas.

• Constant supply of air and fuel.

• Usage of sand to fill the apron of the interior of the kiln to prevent air from entering the kiln through the bottom of the car.

If sand gets short, it leads to the entrance of air to the kiln and this incoming air reduce the temperature at the bottom of the preheating zone in the tunnel kiln. As a result there is greater temperature differences between the top and bottom. Figure 1.14 shows the sand seal of the kiln.

• Speed of the kiln car should not be changed suddenly. In case of increase or decrease in the amount of product, it must be changed slowly step by step with changing fuel.
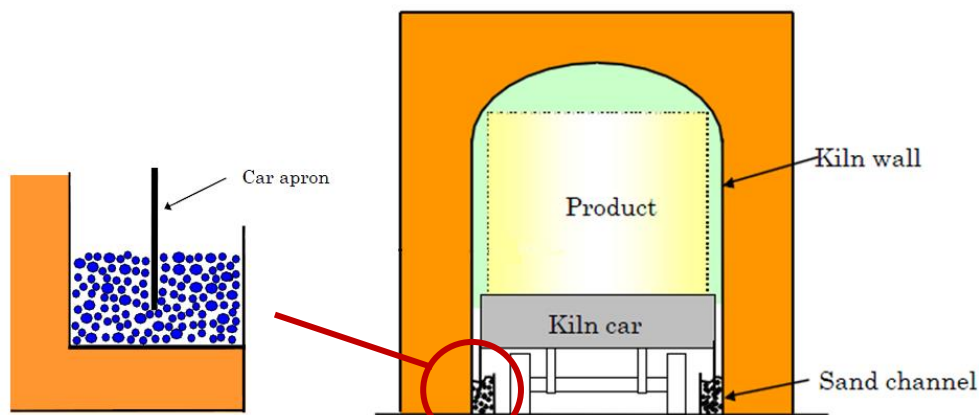
Figure 1.14: Sand seal of the kiln.

1.5 Motivation

Contineous kilns are being used extensively in industry for the productions of wide range of ceramics. Tunnel kilns and roller hearth kilns are the major variants of continuous kiln.

Loading kiln car of tunnel kiln for firing is not a simple matter of placing shelves and stacking ware. The better product quality needs more thoughtful planning. Ware and shelf placement, the size of the load, the firing characteristics of the kiln and the type of the ware being fired are all important factors. Limited amount of heat is available in prehating zone in tunnel kiln. This heat is transferred to the surface of the ware and kiln furnature through radiation and then it is conducted through the thickness of product piece.

If the piece is very thick, it can lead to the higher temperature difference within the product piece. This uneven heating can lead to the cracks in the ware. Cracks can also form if pieces are densely loaded or shaded from the heating elements by kiln furnature or the ware. Most of the gases flow along the gap between products and walls of tunnel kiln due to the low resistance to their flow than they face on their passage between the products. Low resistance in gap causes the gases to have high temperature while higher resistance to flow of gases through product leads to more heat transfer, hence low temperature of gases.

Thus there exist two temperature zones, i.e. The higher temperature zone close to the kiln walls and a lower temperature zone in the center of the kiln (between pieces). This variation of temperature is increased due to the motion of the ware in preheating zone [18] and the air enterering the kiln when car is pushed into the kiln. Thus their always exists a temperature difference between core and tangent stream in tunnel kiln. Figure 1.15 shows the gases flowing through the tunnel kiln.

Firing process occurs in specific volume in the firing zone. This process has a significant effect on the product quality and fuel consumption.

In roller kilns the injectors are supported on the roof. These injectors contain the mixture of air and fuel. They also suck air from the surroundings. The influence of geometric parameters of burners, sucked air, and direction of main flow in relation to the direction of propagate of flame inside the kiln is not well studied area. This work is also going to study this part additionally.

This work could contributed to several aspects of industrial interest such as reduction of cost on maintenance of the refractory walls, improvement in productivity, increase in the efficiency, optimization of burner position, and kiln geometry.
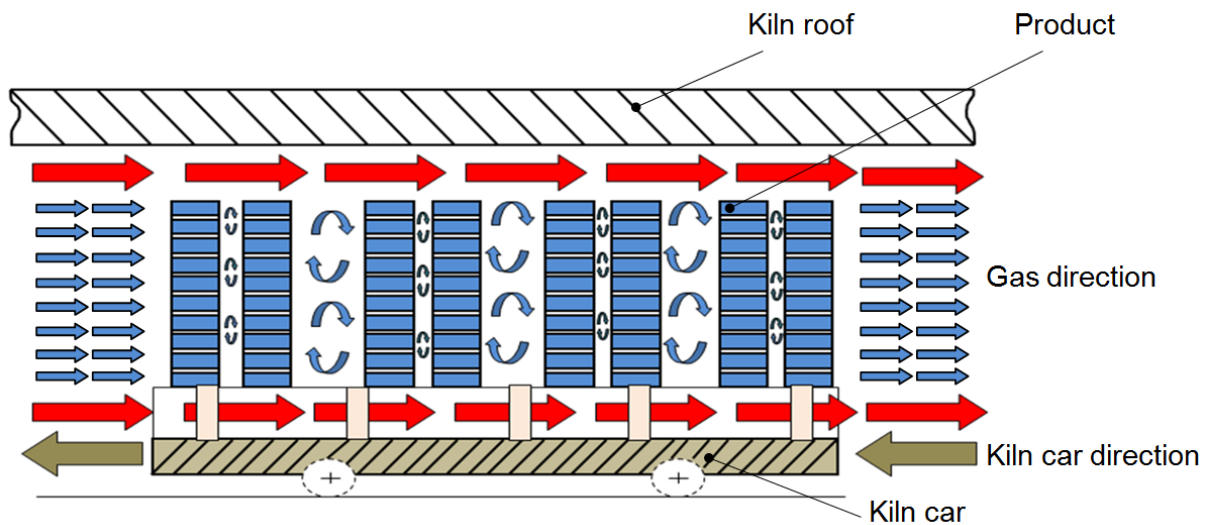
Figure 1.15: Schematic diagram of a part of tunnel kiln

The above considerations show that, there is a need of an understanding of the process inside the kiln to achieve better mixing quality and temperature distribution inside the preheating zone. So that a fundamental area independent of the product can be proposed. Furthermore, there is also a need to understand firing hence the flame behaviour. This work is going to address these needs.

A 3D- simulation with commercial (CFD) code (ANSYS) will be carried out to simulate the part of the tunnel kiln i.e. between the cars.

This simulation will be used to study the effect of flow and geometric parameters on the quality of the mixing and temperature distribution. Also, 2D-simulation using ANSYS for annular ring burner with different gaseous fuel will be conducted in order to see the effects of operating and geometric parameters on the flame behaviour. Additionally 3D-simulation for injector nozzle in the roller kiln will be carried out to evaluate the maximum velocity, quantity of air sucked, streamlines and temperature distribution.

Literature Review
2.1 Introduction

In this Chapter, a brief description of the common features to simulate tunnel kilns is presented. Tunnel kilns are not optimally operated. This is mainly due to the difficulty to collect data from the process in the plant. It makes difficult to identify the main parameters (ambient temperature, heat losses, complete oxidation, etc.) that affect the operation. Furthermore, the main factors that affect the economy of the price are the product quality, the fuel consumption, the production rate and the heat losses through the walls of the kiln [15]. Therefore, the most commonly used simulation to design and to study the operation parameters in tunnel kiln.

2.2 Modelling of tunnel kiln using CFD (Design and Simulation)

CFD modelling proved to be beneficial to understand the fluid flow, combustion and heat transfer phenomena in tunnel kiln. It can also help in the efficiency. In general, the simulation codes of computational fluid dynamics (CFD) are based on Finite Element Method (FEM) and Finite Volume Method (FVM).

2.2.1 Modelling of the tunnel by a finite volume method

In 2012, A.H. Tehzeeb et al. [20] developed a new model for the brick making process in a tunnel kiln by using ANSYS. The geometry was created by using ANSYS Design. The length of the kiln was taken as 100m while the width and height were taken as 3.2 m and 1.5 m respectively. One-sixth of the width (540 mm) was taken in the simulation as of the geometry of the kiln is symmetric as shown in Figure 2.1a.

Most of the elements were hexahedral as shown in Figure 2.1b. Turbulence (k-ε) model was chosen for turbulence modeling, Eddy Dissipation Model (EDM) for combustion and Differential Approximation (P-1) for radiation.

The assumptions taken for process simulation were state conditions, the temperature at any cross section remained temporarily constant, and there was no temperature variation along the brick height inside the kiln. They found the highest temperature generated and the lowest temperature were about 1350 K and 300 K respectively. CO2 and NO_x volumes generated inside the kiln were estimated to be 1.01 m^3/s and   0.108 m^3/s respectively. The direction of flow of air and gas and velocity inside the tunnel were identified. Furthermore, The results of simulation were validated by comparing with the values provided in previous research and with real emission data.
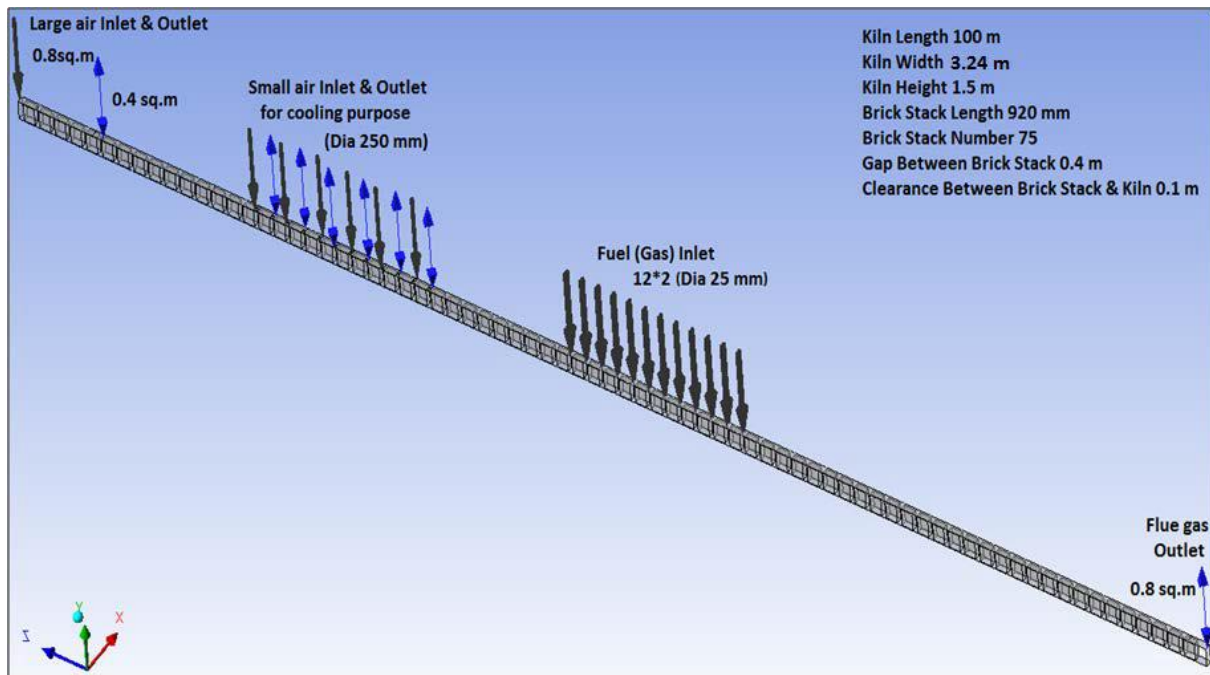
(a)
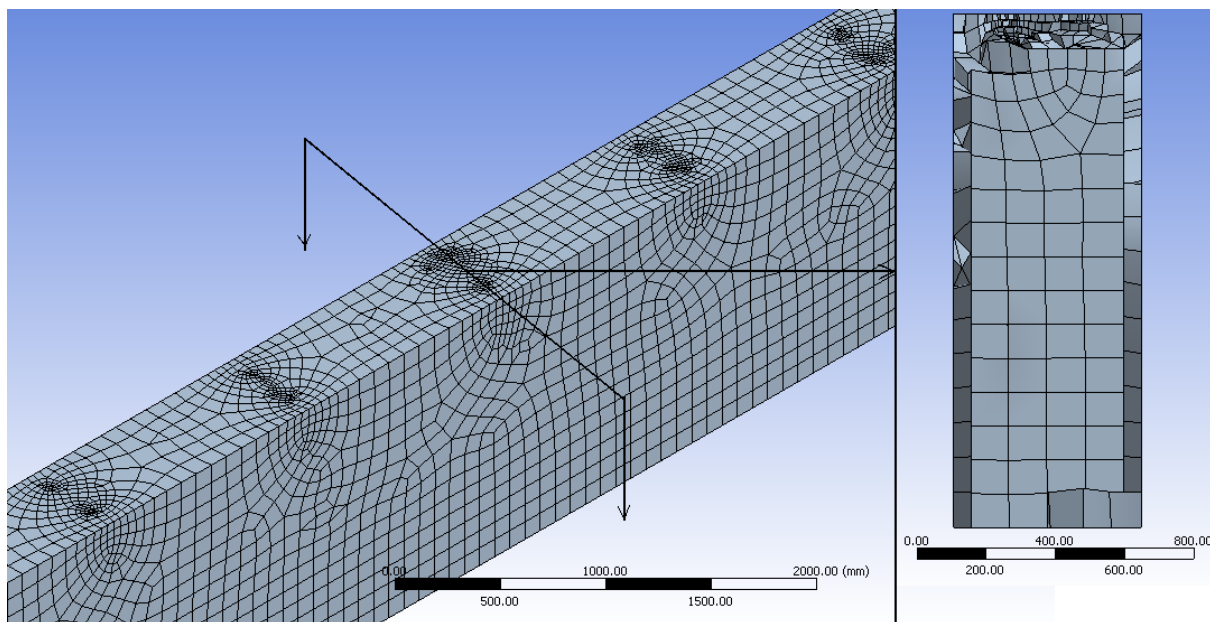
(b)

Figure 2.1: (a) Geometry of a tunnel kiln modelled by ANSYS Design Modeller
(b) Meshing done by ANSYS Mesh [20]

In 2011 Renato Oba et al. [16] presented a numerical model to simulate a tunnel kiln used in ceramic Industry. It was idealized as a rectangular structure with constant width and height of 3 m and 90 m length. The tile load represented as one block, but porous. The domain of the resolution was divided in sub-domains for several volumes as shown in Figure 2.2.

The model was solved for the energy distribution in the burning zone, the radiation between ceramic load and refractory walls, the advection of gases

inside the kiln and loss of the energy from the kiln to the surroundings. The results were presented in term of the characteristic firing curve of the kiln, the temperature distribution in the load, walls and gases.
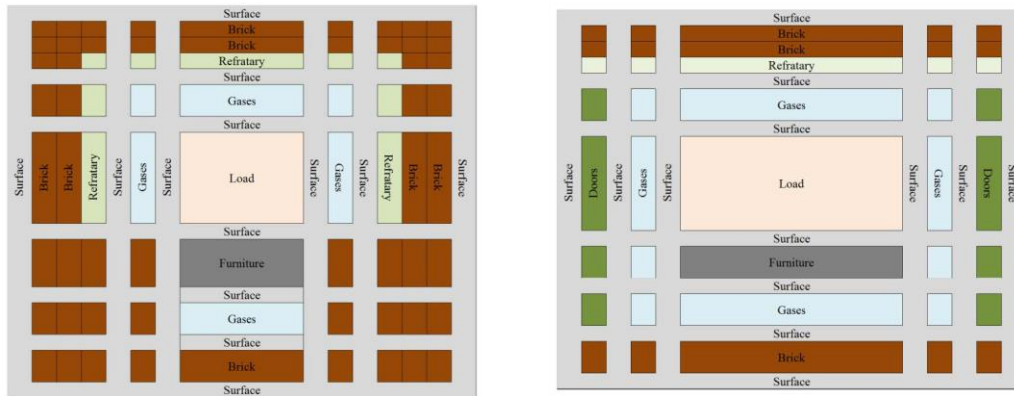
Figure 2.2: The left image is a transversal cut while the right one is a longitudinal [16]

In 2009 Talita Sauter Possamai et al. [21] presented a model of thermal energy transport in ceramic frits melting kilns with oxy-firing combustion process. They developed a numerical simulation in Fortran language coupled with simulation in a CFD software. The rectangular refractory kiln working at a mean inside temperature of 1400 ^{o}C was used as a domain in the analysis.

A non uniform hexahedral mesh was generated for the cavity as shown in Figure 2.3. k-ε model was adopted for turbulence modelling. The coupled codes were proved to be a helpful tool in two main aspects. Firstly, by providing a good estimation of values for different variables which allow easy investigation of the influence of several variables in the process such as kiln geometry, burner position, fuel, and oxidizing type. Secondary by providing a better approach towards the problem the structure of the kiln was not idealized.

CFD results were compared with experimental data and proved that the mathematical models used in the numerical simulation were consistent in practice. Furthermore, comparison with global results from the FORTRAN code were expected to have even better accuracy with experimental values.
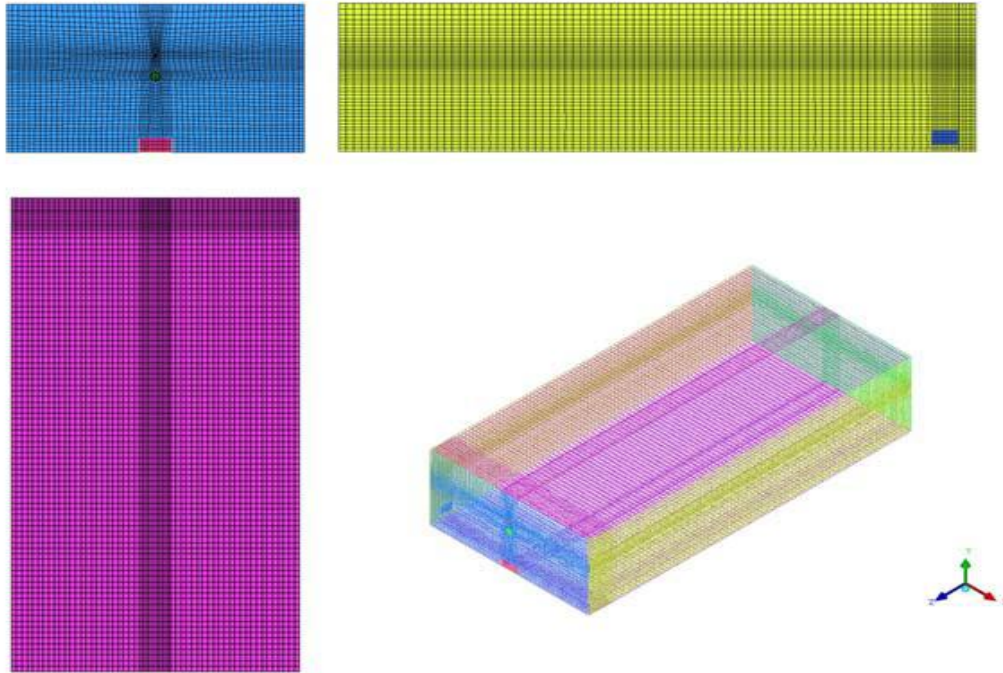
Figure 2.3: Hexahedral mesh properties   Number of nodes 304,832   Number of elements 291,238   [21]

In 2005 Monica F. Naccache et al. [19] presented a numerical simulation of a tunnel kiln by using Fluent software (Fluent Inc.). This kind of furnace is used for fabrication of red ceramic, originally with sawdust as fuel.

The analysis was performed in a two dimensional situation and a steady-state formulation. The combustion process inside the combustion chambers was not analysed, and the load was considered as a homogeneous porous medium. The simplified geometry of the tunnel kiln is shown in Figure 2.4.

From the simulation they found the colder region of the preheating zone, the temperature was almost constant, where at the other regions the temperature variations were larger, with higher temperatures near the walls and lower temperatures in the central regions and that at different axial positions in two sections in the pre-heating zone (x=20m and x=47m), and in one section in the firing zone (x=62m) as shown in Figure 2.5. They presented a comparison between numerical and experimental results by using temperature through the kiln at two positions, y=0.55m, which corresponds to a position near the wall and at the center of the kiln y=1.225m.

The comparison between the numerical and experimental results showed better agreement at y=0.55, as shown in Figure 2.6. Moreover, the results showed a large variation at the lateral section, with very low temperatures at the central region and high temperatures near the walls. Which indicats less efficient heating at the center of the kiln, due to low values of porosity and ceramic heat

conductivity as shown in Figure 2.7. They concluded that the natural gas can be used as a fuel for this type of furnace.
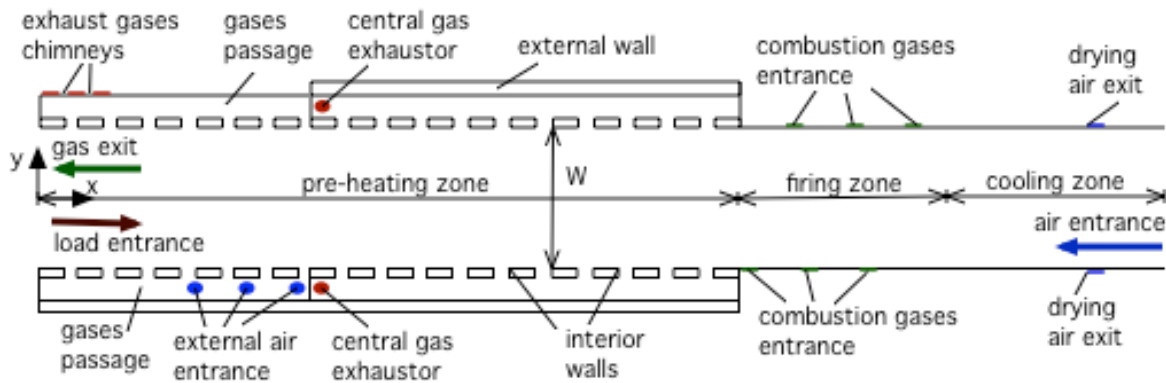

Figure 2.4: The furnace geometry [19]
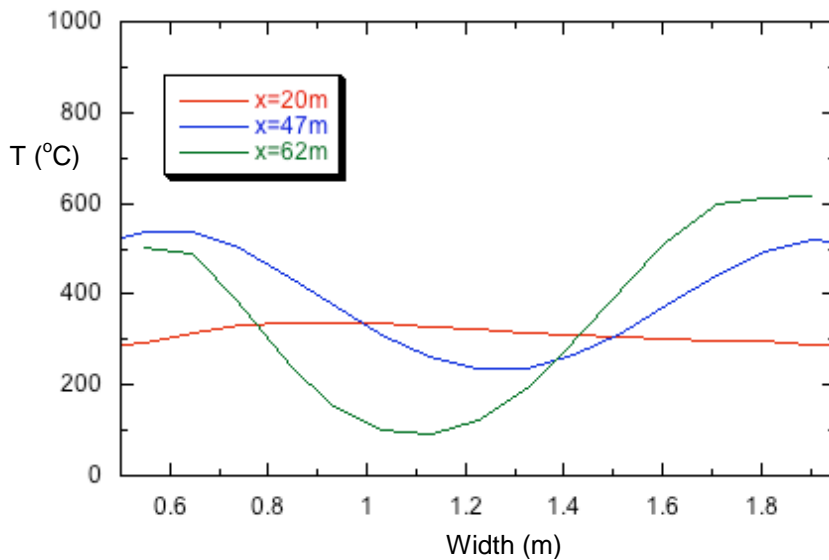
Figure 2.5: Temperature versus at three axial positions [19]
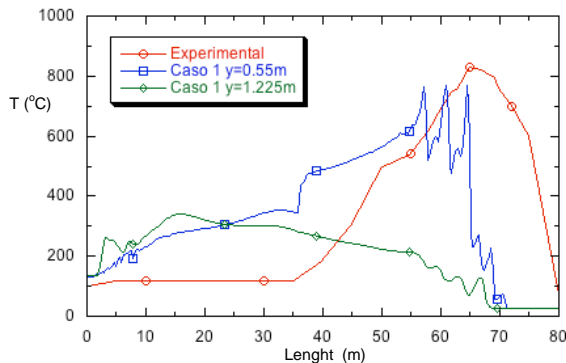
Figure 2.6: Temperature through the kiln, Comparison with experimental results
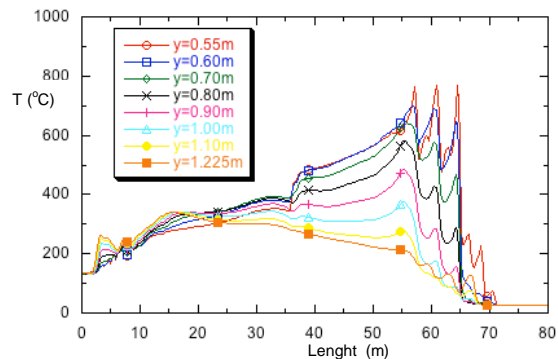
Figure 2.7: Temperature at different lateral positions

In 2006 Friedherz H. Becker et al. [22] studied convective heat transfer under superimposed longitudinal and cross flow conditions in a fast firing tunnel kiln for glost firing of porcelain. A commercial CFD-code for the simulation was used. Due to complexity of geometry, hence huge number of cells. Flow model was segregated into three (models)

By determined convective heat transfer is using 1:5 cold model of a real existing tunnel kiln for firing at tableware in which heat transfer (Nußelt-number) is function of Reynolds numbers for longitudinal flow (Re_L) and for cross flow (Re_Q) as shown in Figure 2.8. A satisfactory compliance between the CFD results and measurements of total energy demand was found on a real kiln plant.
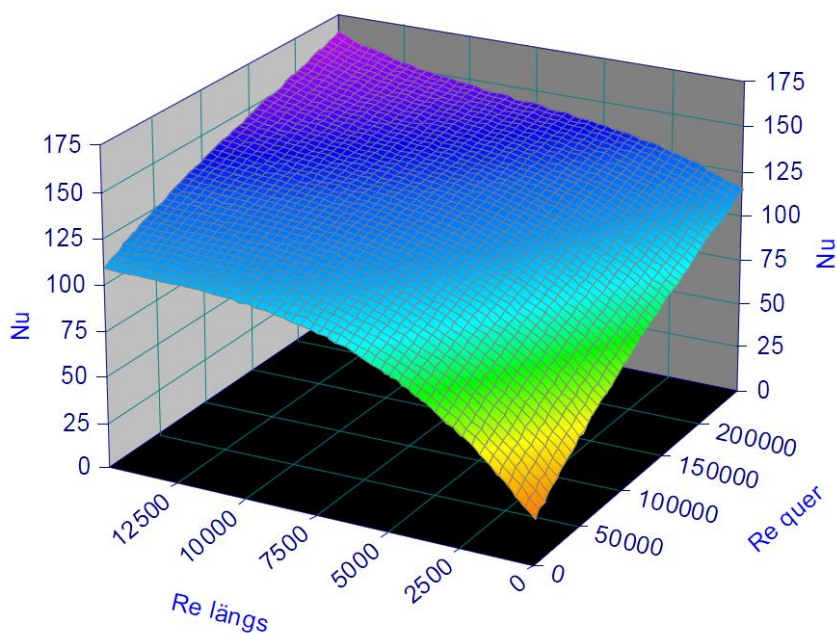
Figure 2.8: 3D-view of the function Nu=f(Re_L,Re_Q) for the middle plate in the lower level of the stack

Tie Zhanxu et al. [23] in 2009 presented a numerical simulation model of coal gangue brick tunnel kiln system in a coal mine to study the waste heat recovery. Also, they analysed the gas flow and heat transfer.

Simulation results show that the layout of bricks has a certain impact on heat transfer. Optimizing the layout of coal gangue brick in the tunnel kiln can improve the efficiency of waste heat utilization. They found that, the gas temperature was higher in the gap between the horizontal and vertical gap junctions and in the preheating zone (z=14 m) as shown in Figure 2.9. Furthermore, the gas flows toward through the upper region of the arch was larger than that through the gap between the bricks as shown in Figure 2.10.

The authors concluded that, the brick car moves in the opposite direction with gas flow in the gangue brick tunnel kiln. This movement can make full use of waste heat. And it can enhance heat transfer between gangue brick and gas by optimizing the arrangement of the location of rock to increase the gas flow disturbance. Then the gas can bring more heat to preheating bricks and drying the wet bricks.
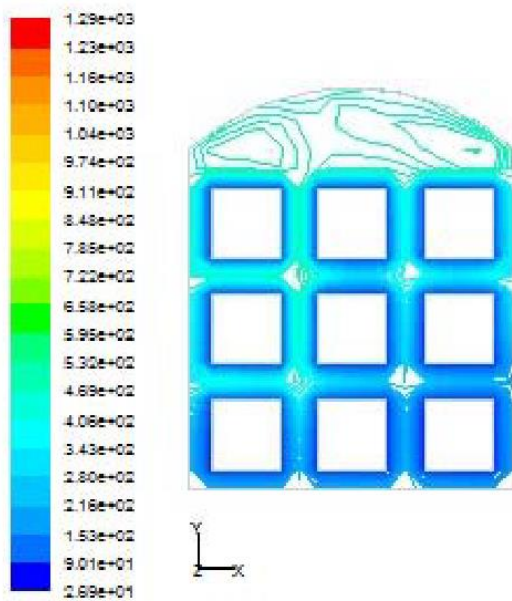
Figure 2.9: Gas temperature
in preheating zone
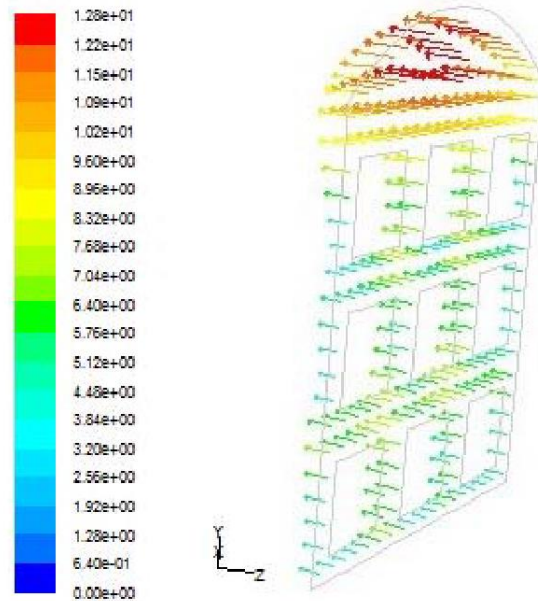
Figure 2.10: Velocity vector
distribution at plan z=5m

In 2014 R. Oba et al. [24] presented a thermal analysis of a tunnel kiln used for the production of roof tiles, fueled by firewood and shale oil.

They used a three dimensional numerical model based on the finite volume method to model the thermal behaviour of the kiln. The kiln was idealized as a hexagonal prism and the load was considered continuous over the entire kiln length and is in form of one block. The cross section of the load configuration and dimensions is shown in Figure 2.11. The fuel combustion was treated as a one step complete reaction. Surface to surface radiation between the kiln walls and load surfaces with nonparticipating media was considered. Furthermore, they used the prescribed flow of flue gas and air to overcome the obstacle of high computational cost due to the large dimensions of the numerical domain.

The numerical results (temperature distribution in many positions) were compared with experimental measurements. Figure 2.12 presents the

experimental and numerical mean temperature distributions for the gas flow inside the kiln, along the length and near the load surface. It indicated that there is a good agreement with experimental measurements. The results showed that 35% of the energy input to the kiln through fuel combustion is lost through the walls and roof to the surroundings. Also, radiation heat flux was more significant to heat transfers to and from the load accounting for more than 75% of the heat transfer.

Finally, the researchers concluded that the temperature and heat flux distributions estimated by the numerical model can be used to optimize the efficiency of the kiln and to better control the heating and cooling of the load.
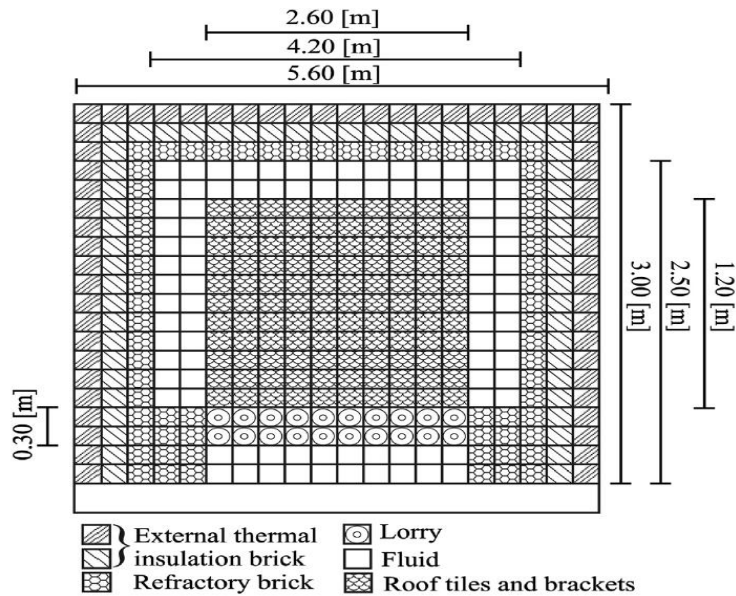
Figure 2.11: Transverse section dimensions [24]
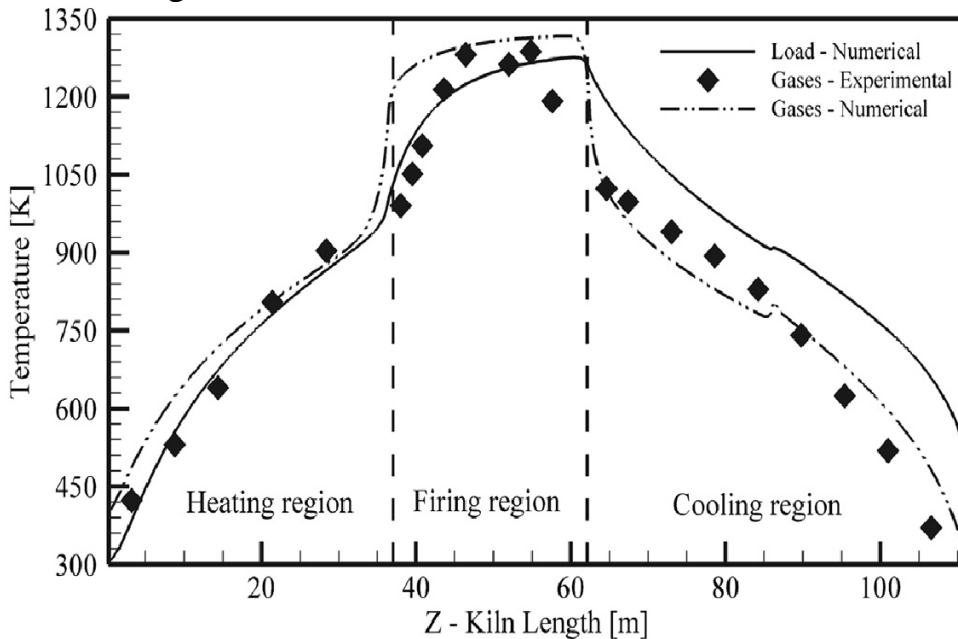
Figure 2.12: Mean gas temperature distributions along the kiln, near the load surface [24]

2.2.2 Modelling of the tunnel by finite element method

In 1994 Boming Yu [25] developed a dynamic model of a tunnel kiln, based on the transient heat conduction occurring in the products (or wares) and in the lining bricks of kiln cars, as well as on the gas continuity, heat balance, and material balance equations. He simulated two oxygen schedules under one firing schedule and three lining brick structures. The length of the tunnel kiln was 72 m that was used for firing bricks.

He found that the different lining brick structures do not seriously affect the temperature profiles at the interface between the blades and lining bricks as shown in Figure 2.13. Furthermore, heat storage in the wares was much greater than in the lining brick with different lining brick structures as shown in Figure 2.14. The heat storage rate in ware at a typical heating location was much greater than that in lining bricks as shown in Figure2.15. Boming Yu also concluded that his dynamic model can be used not only to describe the thermodynamic processes, but also can help to design a tunnel kiln and to compute heat balances.
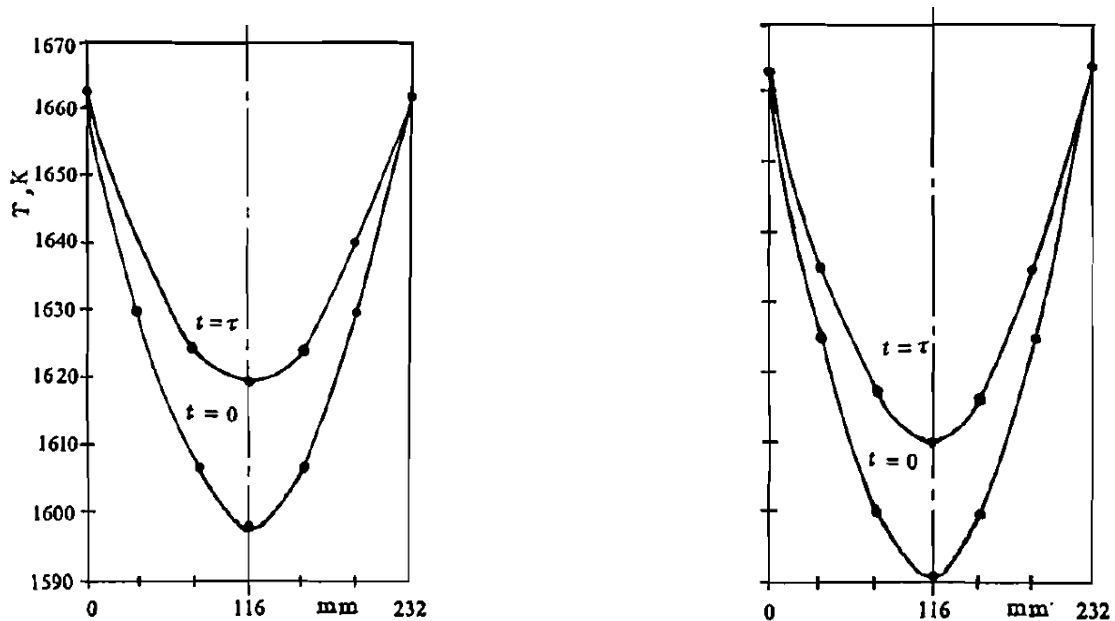
Figure 2.13: Typical temperature profiles at the interface between the blades and lining bricks at the last soaking location for different lining bricks
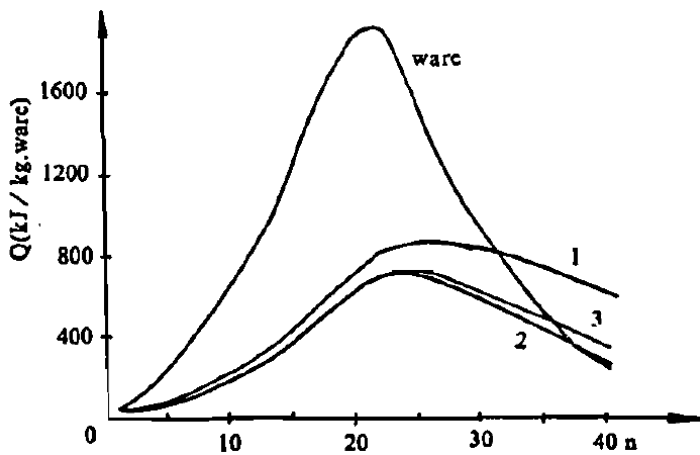
Figure 2.14:Heat storage in wares and in the lining bricks structure (1,2, 3) at different locations
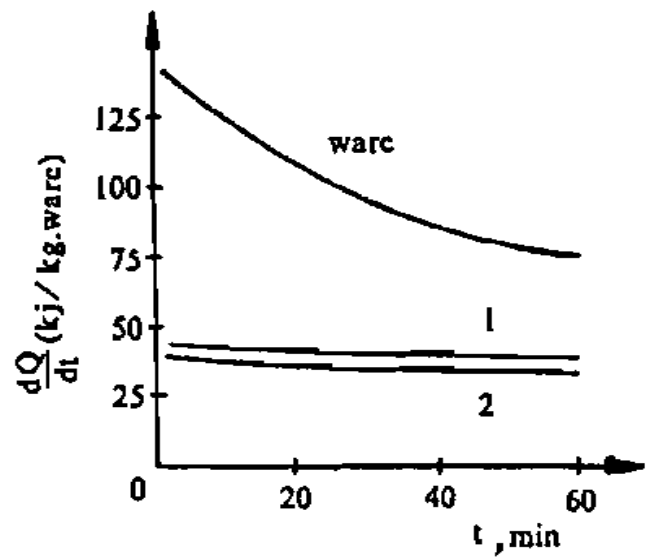
Figure 2.15:Rate of heat storage in ware and in lining brick structure

In 2009 Vicent et al. [26] presented a numerical simulation of tunnel kiln used for firing clay tiles, bricks, and similar products with natural gas and sawdust as fuels. They developed a thermal model which allows efficient and less energy consuming design. The results demonstrated the amount of reduction in fuel consumption to increase in the thermal insulation thickness used on the wall and the influence of the load internal area on the heat exchanged with combustion gases inside the kiln. The results were also shown for the effectiveness of the heat exchange inside the load stacks which occurs above a threshold value for the internal area to external area ratio. The results showed the need to use a larger number of less tortuous channels inside the load to promote efficient gas circulation. Also, the numerical simulation results were compared with measured values.

2.3   Mathematical models

Mathematical modelling of the tunnel kilns can be used as a tool to improve the operation conditions and design. The appropriate control strategy is used in order to satisfy the quality constraints and to minimize the fuel consumption. The mathematical models of tunnel kilns classified in two main parts are:

2.3.1   Mathematic model for whole tunnel kiln, preheating zone

In 2011 Mancuhan et al. [27] developed a one dimensional model to simulate the drying process of bricks in the preheating zone of a tunnel kiln. This model

was used to describe the gas flow, heat transfer between gas and bricks and evaporation of bound water. Two different profiles and vent locations in the preheating zone for the ambient air were used to achieve the desired gas temperature for high quality bricks. Furthermore, the simulation results were compared to measured plant data.

In 2008 O.B. Gol tsova et al. [28] developed mathematical model of a brick firing kiln. It could be used to maintain the process parameters in real time as a function of the amount of brick manufactured.
The kiln was divided into 48 zones as equal processing zones and assumed that the temperature in each zone was constant and it did not depend upon of time. The results of theoretical calculation were compared with experimental observation. They found that the mathematical model was satisfactory and it reflects the real operation of the kiln. Furthermore, The rhythm of operating conditions varies up to 10 times each month that which affected the quality of the bricks. So, the power consumption is a large.

G. Halasz et al. [29] in 1988 proposed a 1-D model of tunnel kiln in the form of an integral equation. The boundary conditions were characterized by kernel function. The parameters of this kernel function could be measured directly on a real kiln. They proposed a simple optimization procedure for minimization of the specific energy with respect to unit product mass in the steady-state of the kiln. Technological requirements were given in the form of inequalities for the temperature and temperature gradient of the product in the kiln. Frome results, the optimal condition for tunnel kiln could be found and 5-8% energy could be saved.

In 2006 J. Durakovic, et al. [30] proposed mathematical model to define temperature fields inside a tunnel kiln during brick production process at real conditions. It was used to analyse all significant parameters that affect fuel consumption. They concluded that kiln in ceramics industry can be optimized according to requested quality of products which ought to use minimal fuel consumption. The results showed that the heat can be expressed by temperature.

Zuobing Chena et al [31] in 1999 presented an intelligent computer-aided design system for ceramic kiln with an object-oriented database. The kiln structure was separated from up to down because of the complexity of geometry. They established the structure graph of knowledge separation according to the frame

class tree in the integrated intelligent CAD system. They provided results as a foundation for the intelligent automatic design of ceramic kilns.

In 2009 Ebru Mancuhan [32] analysed and optimized the drying of green bricks in a tunnel dryer. He used 1D-model to find the total cost of the energy required for drying. The cost of the electricity consumed by the fans for the circulation of the drying air was also included in the objective function. Drying process is required for the removal of most of the water in the green brick body to reduce the water content of the brick to about 10% before firing in the tunnel kiln. Without this preheating step, the water within the clay body turns to steam in the firing process and damages the bricks severely. Microsoft Excel solver was used to find the optimal values of the hot and outdoor air mass flow rates per kilogram of the brick to realize optimization of the drying process. The results showed that 59 to 62% of the total energy was used for drying per unit of green bricks.

2.3.2 Mathematic model for firing zone

Sinem Kaya et al in 2009 [33] improved firing zone of tunnel kiln to minimize the fuel cost as being the objective function by finding the optimal operating variables. Mathematical models were used to represent the simplest form the phenomena of heat transfer, combustion of admixed coal and pulverized coal, together with gas flow. The optimized value of pulverized coal was found to be lower than that the existing in tunnel kiln. Therefore, it makes a certain decrease in the plant operating cost when based on yearly production. They concluded that the overall energy balance predicted an energy use of 3385 KJ/kg brick, which is 2.7% higher than the optimized results.

S.H. Pulko et al [34] carried out modelling of tunnel kiln to study the behaviour of ceramics during firing and their variation with time. The TLM technique was used to model heat conduction within the ceramic, to represent the change of state and chemical reaction. It was coupled with a model of deformation, in order to predict the effect of the firing schedule on final piece geometry. Effect of radiation was considered to occur between the surface of one ceramic body and another. It was also considered between a ceramic body and the kiln walls, kiln function and any visible burner. The results demonstrated the feasibility of the deformation of the a piece of ceramic during firing.

Maria da Carvalho et al in 1997 [35] presented a 1-D mathematical steady state model and dynamic models of a tunnel kiln for ceramics firing to find optimal operating condition. The steady state model was used to compute the ware and gas temperature profiles along the kiln, for given cooling air, extracted gas, in-leakage air, fuel and combustion air flow rates. Dynamic model was accounted for the transient behaviour, as well as the injected air, extracted gas, and fuel flow rates. Furthermore, the models were validated against available from measurement data obtained on a tunnel kiln for the firing of building bricks in the heavy clay brick industry.

Sinem kaya et al [15] in 2008 optimized heat recovery in firing zone of a tunnel kiln, by finding the optimum suction and blowing air as shown in Figure 2.16. In addition to the ambient air flow rate entering from the brick exit side to minimize the pressure drop. The mathematical model presented the phenomena of heat transfer and fluid flow. Also, it was developed to compute the state variables such as the air mass flow rate, brick and air temperatures along the cooling zone of a tunnel kiln. They also found that the temperatures measured from the cooling zone were practically values between the brick and air temperatures as shown in figure 2.17. Furthermore, the minimum pressure drop was obtained by considering the tunnel kiln's cooling zone composed of two regions of suction and two regions of blowing.
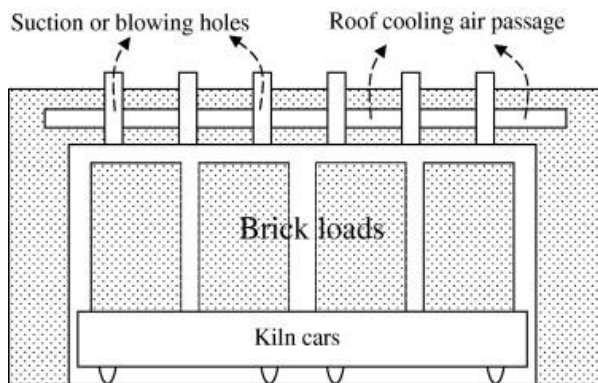
Figure 2.16: Cross section view of the tunnel kiln with brick loads and kiln car
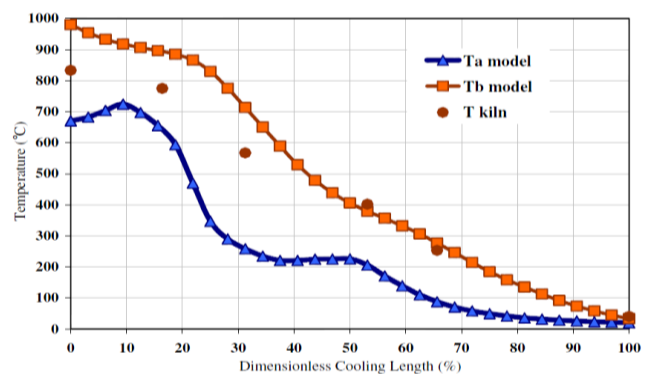
Figure 2.17: Comparison of the measured temperature to the computed air and brick temperature

Robert H. Essenhigh in 2001 [36] presented an analysis of tunnel kiln to determine the relation between input energy (H_f) and useful output energy (H_s). The firing equation in standard form was found by integral energy equation. The analytical structure was developed specifically for the tunnel kiln, and it was

represented as a firing section flanked by two upstream and downstream heat exchanger (A and B) as shown in Figure 2.18. He believed that the general design and theoretical structure have potentially wider application in heat exchangers. From the analyses he established the thermal and processing efficiency for the optimum design and configuration at the theoretical adiabatic limit. The thermal efficiency for the system converges to 100%, and the processing efficiency can converge to infinity. These are limits that are impossible to achieve in practical operations, but he proved it could serve as a basis for evaluating expected design performance.
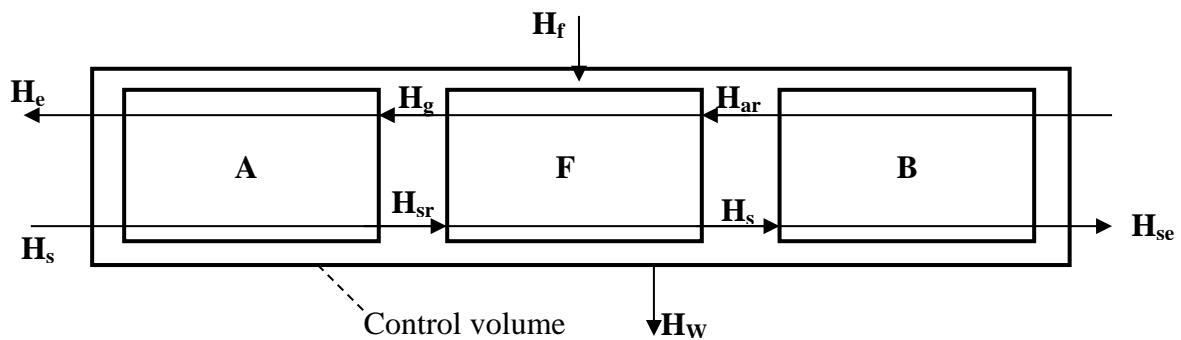
Figure 2.18: Schematric of continous tunnel kiln represented as a central firing section (F) flanked by two heat exchangers (A and B) [36]

Where:

Material flow is from left to right; air/POC flow is from right to left

Air and raw materials to be processed (cold entrance)

H_f: Input enthalpy from fuel into firing section

H_{sr}: Enthalpy of preheated raw materials entering firing section

H_{ar}: Enthalpy of preheated air entering firing section

H_g: POC exhaust enthapy leaving firing section

H_s: Enthalpy of processed material, leaving firing section

H_e: POC exhaust enthalpy leaving kiln

H_{se}: Enthalpy of cooled processed mate- rial leaving kiln

H_{so}: enthalpy of raw material entering kiln

H_w: wall loss.

In 2014 Ana Mezquita et al. [37] presented a calculation methodology, based on certain kiln operating parameters to obtain energy to save in tunnel kiln. They proposed a part of cooling gases must be recovered in the firing chamber and it should not exhaust into the atmosphere as shown in figure 1.19.   They concluded that, the profiles of static pressure and oxygen content in the studied ceramic tile kiln confirmed that gases circulate from the fast cooling zone into the combustion chamber. Furthermore, they determined the air and gas volume

flow rates in each burner ring and the oxygen content in the kiln chamber enabled the gas volume flow rate from the cooling to the firing zone. Furthermore, the results were compared with experimental data as shown in Figure 2.20. And they conclude that 17% of energy could be saved in the kiln.
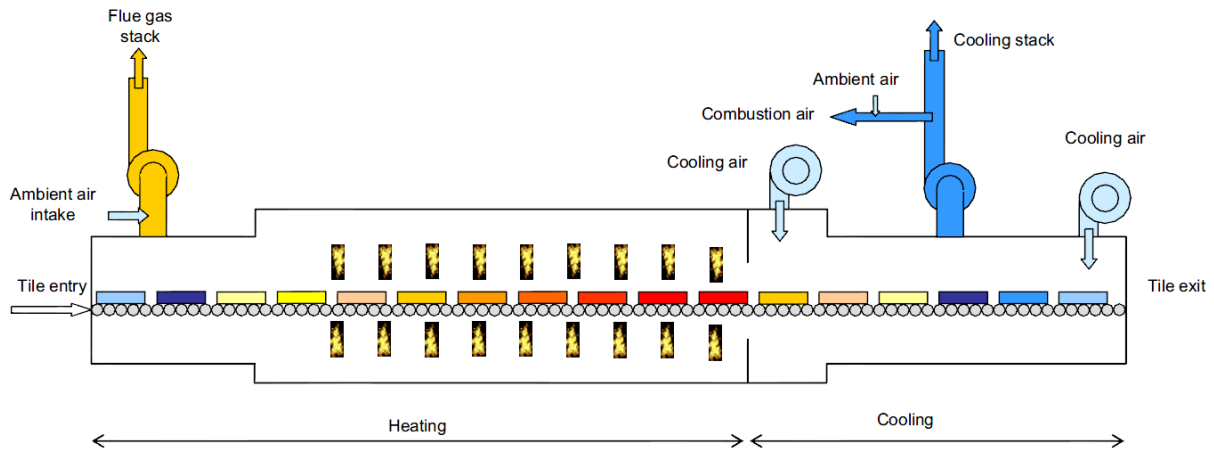
Figure 2.19:Scheme of the studied ceramic tile kiln [37]
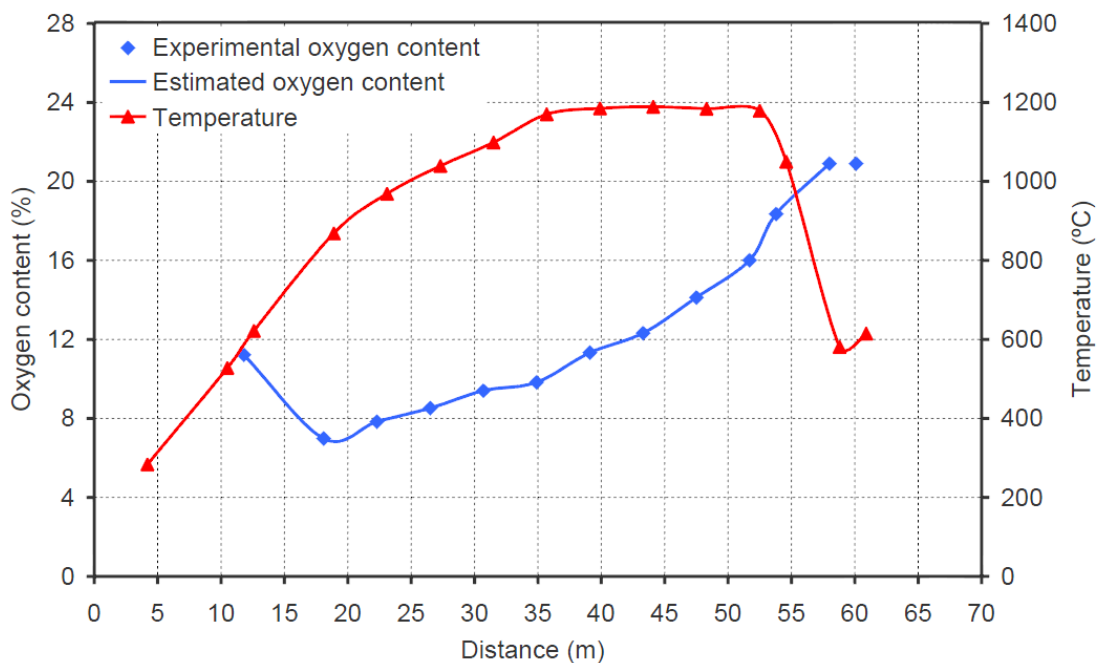
Figure 2.20:Simulation for oxygen content in the kiln [37]

Manchu Han et al. [38] in 2006 proposed an optimization process for fuel and air used around a tunnel kiln. This optimization was special for tunnel kiln producing bricks with a low calorific value using coal as an additive.

The data from plant was used to calculate energy to be supplied by fuels, using mass and energy balance. They found that an advantage to use admixed coal for both cases pulverized coal or natural gas in the firing zone.

Admixed coal improved heating value of pulverized coal, thereby causing no significant change of the fuel cost. Natural gas eases the combustion and thus satisfies a good control of the temperature profile in the firing zone, and decreases environmental degradation.

2.4   Conclusions of literature review

This brief literature review provides guidelines and an extensive background for the present study. The literature survey of the previous work shows that the FVM has been the most frequently used CFD code in tunnel kiln research, but few papers published, indicates the use of FEM. Several problems associated with thermal process were identified. Some researchers employed CFD to simulate a tunnel kiln applied in the ceramic industry to investigate the temperature profiles during firing, emissions, heat transfer, air and gas velocity, and flow direction inside the tunnel kiln.

On the other hand, the mathematical models have also been developed to simulate the thermal process and find the relation between input and useful output energy and energy saving in certain tunnel kilns. Notably, most of former searches are based on the brick tunnel kiln.

It is important to have a homogeneous condition in the kiln cross section. From the literature review, it is clear that the most of models and studies assumed a homogenous gas distribution in the cross section and there is no such research that focused on distance between cars. Furthermore, specific distance between the kiln cars (firing chamber) makes the study of the flame behaviour is important.

3. Computational fluid dynamics modelling using ANSYS

3.1 Introduction

Computational Fluid Dynamics or CFD is the analysis of systems involving fluid flow, heat transfer and associated phenomena such as chemical reactions by means of computer-based simulation. The technique is very powerful and spans a wide range of industrial and non-industrial application areas. Some examples are listed below [39]:

- Aerodynamics of aircraft and vehicles: lift and drag.
- Hydrodynamics of ships.
- Power plant: combustion in IC engines and gas turbines.
- Turbomachinery: flows inside rotating passages, diffusers etc.
- Electrical and electronic engineering: cooling of equipment including micro-circuits.
- Chemical process engineering: mixing and separation, polymer moulding.
- External and internal environment of buildings: wind loading and heating/ventilation.
- Marine engineering: loads on off-shore structures.
- Environmental engineering: distribution of pollutants and effluents.
- Hydrology and oceanography: flows in rivers, estuaries, oceans
- Meteorology: weather prediction.
- Biomedical engineering: blood flows through arteries and veins.

The commercial CFD programs have many default settings and can almost always give results from the simulations, but to obtain reliable results the model must be chosen with a logical methodology. A converged solution displays the results of the specifically chosen models with the given mesh, but it may not reveal the whole truth. So that without proper understanding of the CFD program and the modelling theories behind it, CFD can be limited to colourful fluid display. For a good understanding CFD simulation, fluid flow characteristics need to be understood along with the provided options in the CFD software.
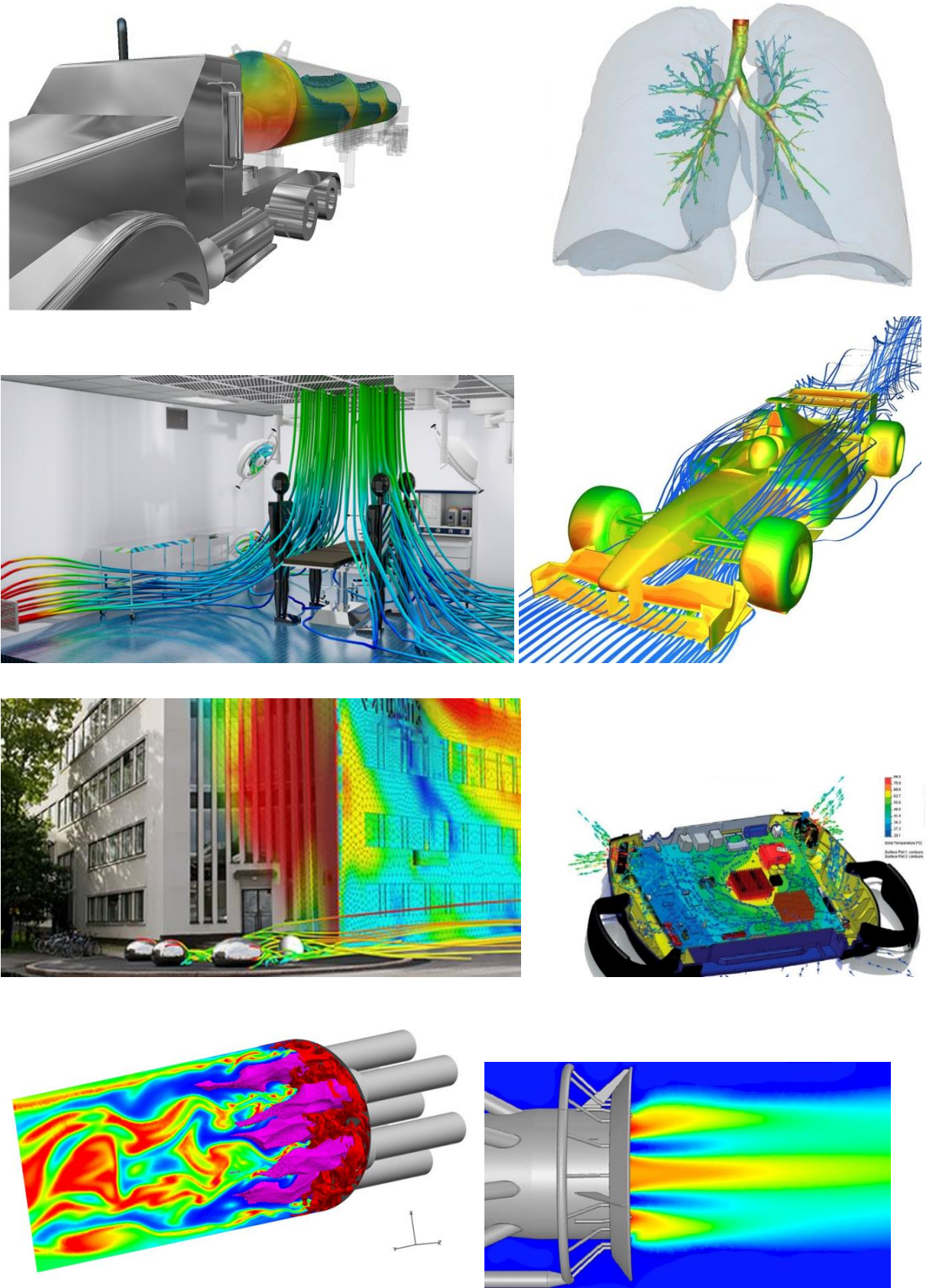
Figure 3.1: Some common CFD applications

3.2   Fluid Flow Characteristics

It is useful to classify flow simulation in CFD into the following categories: laminar-turbulent, steady-unsteady-transient and single phase-multiphase.

The laminar flow is a definition of higher order fluid motion and is characterized by smooth layer. In this flow, Navier-Stokes equations that describe the momentum transport of flow, dominated by viscous force. With CFD it is possible to obtain very accurate flow simulations for single-phase laminar flow. On the other hand the highly disordered fluid motion that typically occurs at high velocities and is characterized by velocity fluctuations is called turbulent.

Navier-Stokes equations which describe the turbulent flow can be solved by CFD simulations which seldom possible to solve analytically for real engineering applications because of properties of the flow. CFD simulation has possibility to closely predict the characteristics of a turbulent flow.

In nature, the air and gas flows inside the tunnel kiln are turbulent; hence to analyse the flow inside the kiln, the characteristics of turbulence are used. However, flows from turbulent to laminar or from laminar to turbulent (i.e. transitional flow) are difficult to simulate accurately [40]. If the flow has no change at a point with time is defined as steady flow. On the other hand a flow that is not steady is known as unsteady flow, whereas developing flows are considered as transient flow [41].

The fluid flow in tunnel kiln is not steady at the initial stage of firing, but with the course of time the flows become stable and temperature distribution inside the kiln becomes steady quickly.

Single phase flow consists of gas-gas or liquid-liquid systems.

In case of single-phase laminar flow, CFD can provide very accurate results, while it gives satisfactory results in most cases of turbulent flow.

The main problem is usually simulation of the mixing of reactants for fast reactions in laminar or turbulent flow [40]. When the reaction rate is fast compared to the mixing, a model for mixing along with a chemical reaction must be introduced. Combustion in the gas phase and ion–ion reactions in the liquid phase belongs to this category.

Multiphase flow may consist of gas-liquid, gas-solid, liquid-liquid, liquid-solid or gas-liquid solid systems. For multiphase system containing very small particles that follow the continuous phase closely, reasonably accurate simulation results can be obtained [40]. Systems in which the dispersed phase has a large effect on the continuous phase are more difficult to simulate accurately, and only crude models are available for multiphase systems with a

high load of the dispersed phase. At the moment, the quality of the simulations is limited not by the computer speed or memory, but also by the lack of good models for multiphase flow. An example for multitphase flow is coal particles sprayed in the gaseous fuel.

In this study, only air or gas fuel is considered. Therefore, multitphase flow is not necessary to consider, and single phase flow is adequate for the simulation.

3.3   ANSYS 14.0

ANSYS 14.0, a commercial CFD software package is commonly used in the modelling of combustion, fluid flow and heat transfer. It has a combined advanced solver with powerful pre- and post-processing capabilities. Furthermore, it includes a reliable and robust solver, definition of the problem in full integration, analysis and presentation of the results. Also, it has an intuitive and interactive setup process and uses advanced graphics.

In general, commercial CFD packages contain modules for CAD drawing, meshing, flow simulations and post-processing. In solving a problem using CFD there are many steps that must be defined, as is illustrated in Figure 3.2.

3.3.1 Geometry Modelling

The geometry of the fluid domain where the analysis performed is drawn by ICEM CFD 14.0. The geometries can be drawn in other CAD software and then can be imported in ANSYS 14.0 (Fluent). However, the geometries drawn in other CAD software may contain details that cannot be included in CFD simulation drawing and may require correction, as this CAD program is not designed for CFD. Therefore, it is better to use built-in drawing software ICEM CFD 14.0 for modelling the geometry.

Geometry modelling
Define gemetry
Define boundaries

Grid generation
Divide the geometry into small computational
cells

Defining models
Add models for turbulence, chemical reactions
etc.

Set properties
Density, viscosity etc.

Set boundary and intet conditions
The intial conditions, inlet and outlet conditions and conditions at
the walls are set

Solve
Choose solver, iteration methods, transient or steady state,
convergence requirement

Post-processing
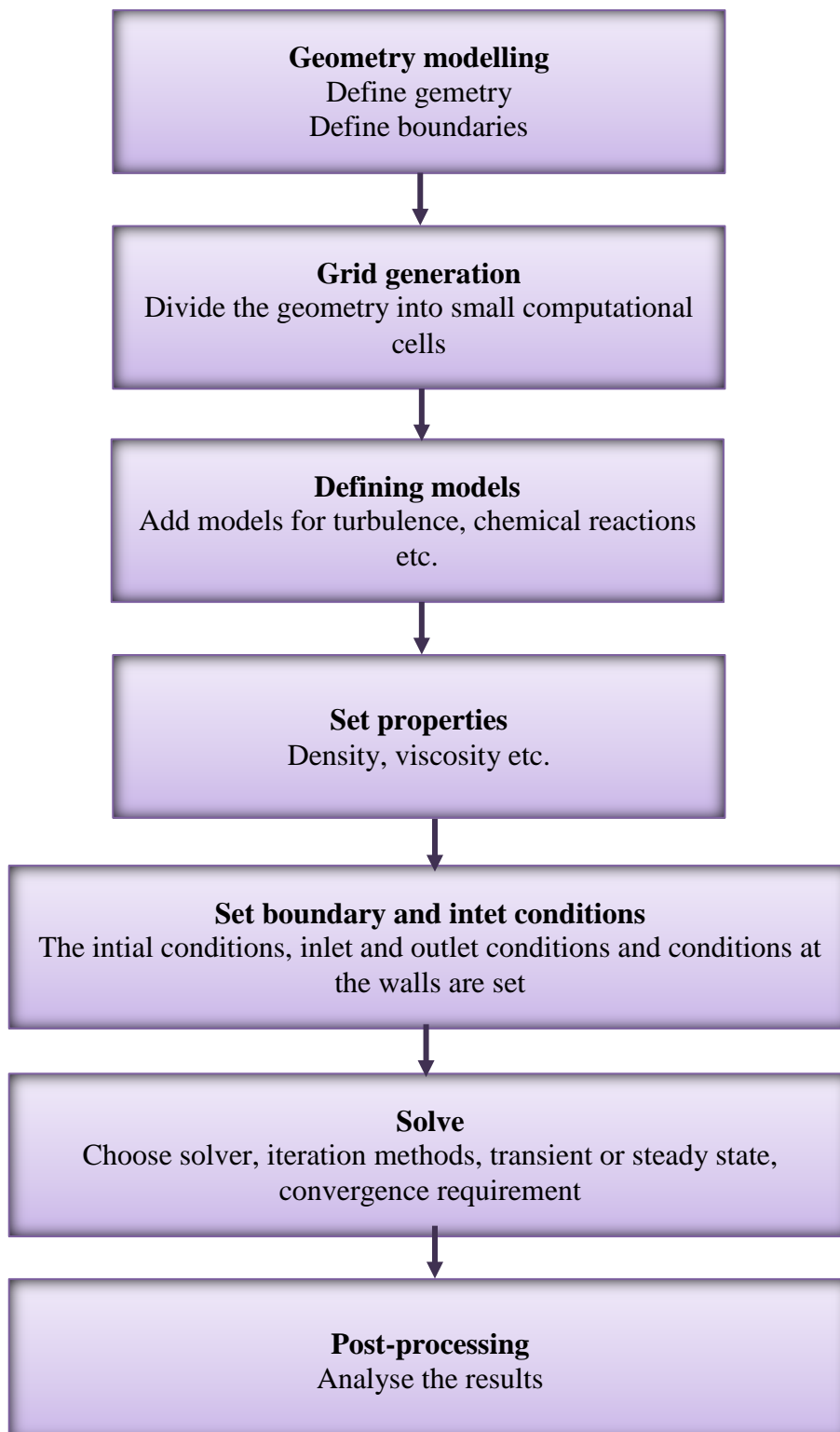Analyse the results

Figure 3.2: Steps in CFD simulations

3.3.2 Meshing process

The computational domain must be created before solving a problem. So, after drawing the geometry. It is divided into small cells using ICEM CFD 14.0. This software supports both 2D and 3D geometries, also can be used to define boundary types. Structured and Unstructured meshes can be created in this software. The typical cell shapes are shown in Figure 3.3.

- 2D

Triangle **("tri")**   2D prism (quadrilateral or **"quad"**)

- 3D

Tetrahedron **("tet")**   Prism with quadrilateral base

(**hexahedron** or **"hex"**)

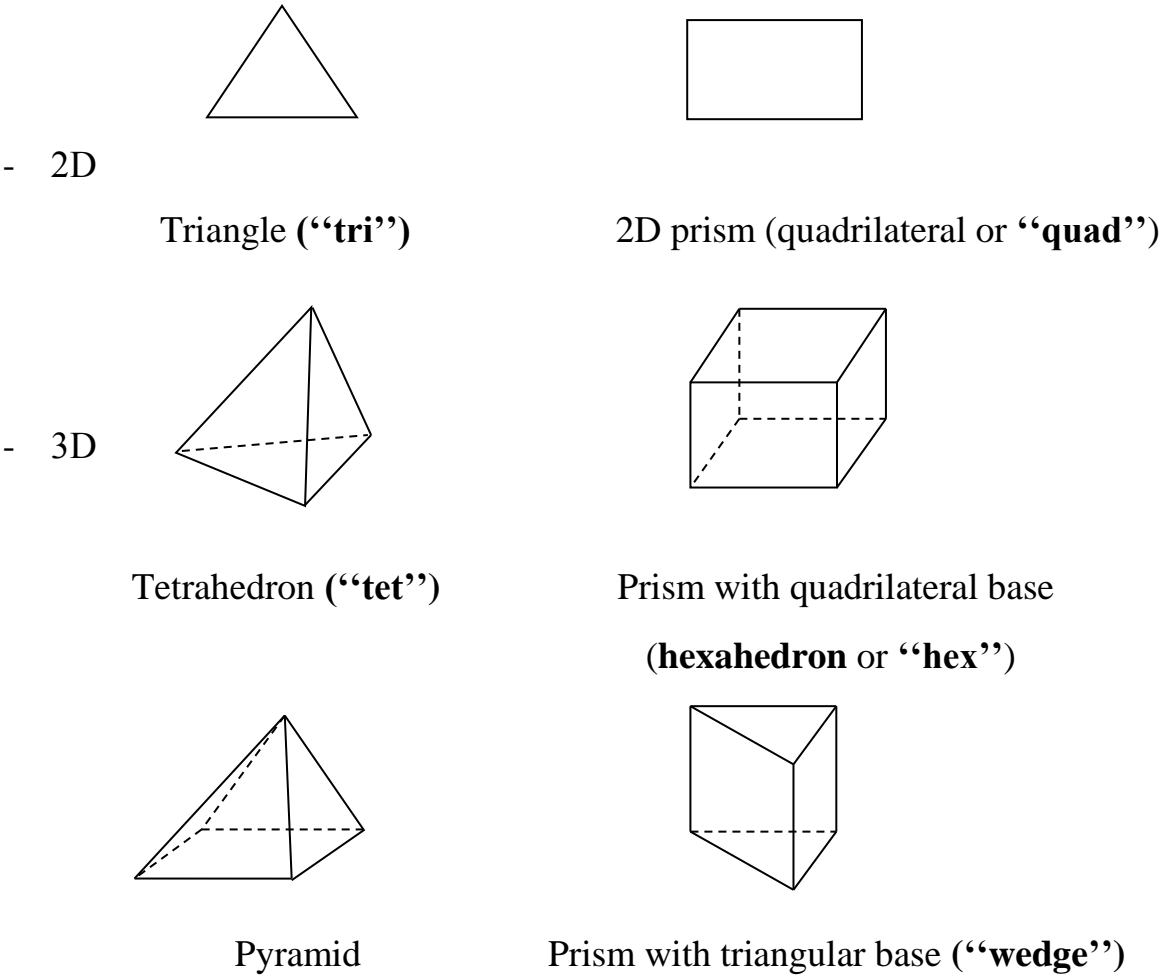Pyramid   Prism with triangular base **("wedge")**

Figure 3.3: 2D and 3D typical cell or element formed by meshing methods

The meshing method needs to be chosen at the beginning, and the global mesh setting has to be specified, which means the type of mesh is going to be generated in the overall geometry.

In general, the computational domain descriptors by choosing between structured, unstructured and hybrid mesh. The decision depends on the specific advantages, shortcomings and also the complexity of the geometry [44]. The local mesh setting is interested if required and that means the higher spatial resolution at the important part of the geometry. The higher resolution is achieved by subdividing the larger elements at the particular part and that leads

to an increased number of local elements. The purpose of this section is to give an overview of structured meshes which used to carry out this work.

- **Structured meshes**

Structure meshes are a definition of mesh set out in a regular repeating pattern called a block. The quadrilateral elements in 2D and hexahedral elements in 3D in a computationally rectangular array are used.

Even though the cell topology is fixed, the mesh can be shaped to fit the geometry, through stretching and twisting of the block. The mesh can consist of multi blocks and can be connected together, as shown in Figure 3.4.
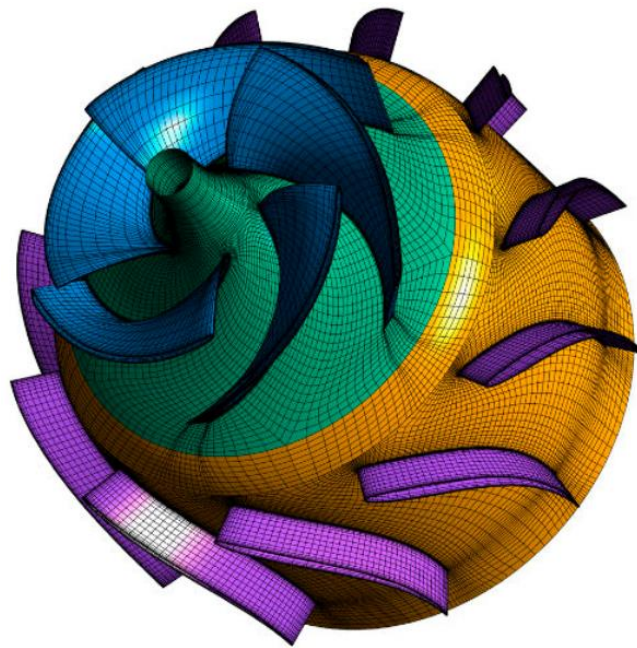

Figure 3.4: An example of a structured multiblock mesh [42]

The structured meshes have an advantage over another grid method (unstructured meshes) in that they allow the user a higher degree of control. Hexahedral cells are very efficient at filling space and support a high amount of skewness and stretching before affecting solution. In addition, the grid is flow aligned, which helps the solver to converge and make post processing easier as logical grid acts as excellent reference points for examining the flow field.

The weakness of structured mesh is known as it takes excessive time producing the mesh compared to unstructured mesh. Some geometries don't allow structured topology due to the high skewness angles and stretch of cells that are required. In general, there are three basic topologies used to adapt structured mesh [43]:

- **H meshing**

H type meshing is the standard meshing method used in ANSY-ICEM CFD. H mesh can achieve good results in a simple geometry, as well as in a geometries have a symmetry segment. However, to maintain accuracy for complex shapes the blocking becomes quite complex.

- **O meshing**

The O type mesh is ideally suited for circular or curved surfaces. Figure 3.5 shows the difference between H and O meshes. It can be seen that when an H mesh is used on a circular geometry, highly skewed elements exist at angles of 45° around the geometry, while an O type mesh removes this skewness.

Figure 3.5: H mesh and O mesh

- **C meshing**

C mesh is a blend of an O and H mesh. It has the benefit of the O mesh, thus, it gets accurate for a curved surface. Furthermore, it allows for refinement of the mesh in the leeward edge of the geometry. The C mesh is characterized to reduce H mesh at the bluff leading edge and small finite to infinite trailing edge, such as foils and wings, allowing for mesh edges to fully capture the geometry of these critical regions. Therefore, in general the C type meshing is suited for flows where a wake need to be captured. Figure 3.6 shows C type mesh.
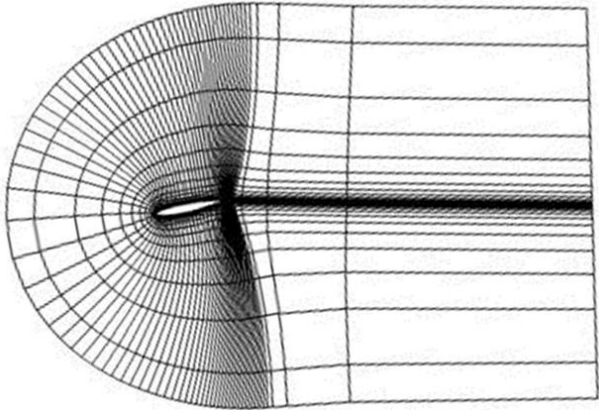

Figure 3.6: C type mesh. [43]

3.4   Equations in ANSYS Fluent

3.4.1 Continuity, momentum and energy equations

The momentum and continuity equations need to be solved for CFD simulation. The equation of the conservation of mass or continuity can be written as follows:

$$\frac{\partial \rho}{\partial t} + \nabla(\rho \vec{v}) = S_m \qquad (3.1)$$

Conservation of momentum in an internal refernce fram is given by:

$$\frac{\partial}{\partial t}(\rho \vec{v}) + \nabla(\rho \vec{v} \vec{v}) = -\nabla p + \nabla(\tau) + \rho \vec{g} + \vec{F} \qquad (3.2)$$

where ρ is the density, v is the velocity, S_m is the source term, p is the static pressure (Pa), τ is the stress, F is the external body force, g is the gravity, t is the time [45].

The stress tensor is given by

$$\tau = \mu \left[(\nabla \vec{v} + \nabla \vec{v}^T) - \frac{2}{3} \nabla \vec{v} I \right] \qquad (3.3)$$

where μ is the molecular viscosity, I is the unit tensor and the second term on the right-hand side of the equation (3.3) is the effect of volume dilation.

Energy equation needs to be solved if heat transfer is included in the problem. As this research is a heat transfer related issue, so the energy equation needs to be incorporated. Heat transfer in a fluid domain is governed by the energy equation given below:

$$\frac{\partial}{\partial t}(\rho E) + \nabla(\vec{v}(\rho E + \rho)) = \nabla \left(k_{eff} \nabla T - \sum h \vec{J} + (\tau_{\text{eff}} \vec{v}) \right) + S_h \qquad (3.4)$$

where E is the energy term, v is the velocity, ρ is the density, k_{eff} is the effective turbulent kinetic energy, T is the local temperature in Kelvin, h is the enthalpy for ideal gas, J is the diffusion flux, τ_{eff} is the effective stress tensor, S_h is the volumetric heat source term, t is the time [45].

The first three terms on the right-hand side of the equation (3.4) represent an energy transfer because of conduction, species diffusion, and viscous dissipation, respectively, and the term E is defined as:

$$E = h - \frac{p}{\rho} + \frac{v^2}{2} \qquad (3.5)$$

where

$$h = \sum_j Y_j\, h_j \qquad\qquad h_i\ \int_{T_{ref}}^{T} c_{p.j}\, dT \qquad\qquad (3.6)$$

where T_{ref} is 298.15 K.

3.4.2 Turbulence model equations

Turbulent flows are characterized by fluctuating velocity fields, and these fluctuations mix transported quantities such as momentum, energy, and species concentration. Practically all technically relevant flows are indeed turbulent. Computationally too expensive to simulate directly in practical engineering calculations, and that because of the fluctuations can be of small scale and high frequency.

In numerical simulations the turbulence models are used to predict the effects of turbulence in fluid flow. There is no turbulence model that has universal acceptability for dealing with all problem areas. Some of these have very specific applications, while others can be applied to a wider class of flows. The choice of turbulence model depends upon various considerations such as flow characteristics, level of accuracy, available computational resource, and availability of time for the simulation. To make the most appropriate choice of model for an application. At the beginning, it is necessary to understand the capabilities and limitation of these various models. The turbulence models available in Fluent ANSYS are: Standard k-ϵ model, k-ω model and Shear Stress Transport (SST) model, etc.

- **Standard k $-\,\epsilon$ model**

The standard k-ϵ model is a semi-empirical model based on model transport equations for the turbulence kinetic energy (k) and its dissipation rate (ϵ). The model transport equation for k is derived from the exact equation, while the model transport equation for ϵ was obtained using physical reasoning and bears little resemblance to its mathematically exact counterpart [46]. In the derivation of the k-ϵ model, it is assumed that the flow is fully turbulent, and the effects of molecular viscosity are negligible. The standard k-ϵ model is therefore valid only for fully turbulent flows. The limitations of this model are due to inaccuracies with swirl flows and flows with strong streamline curvature [46].

For this particular study k-ϵ model has been used to carry out this work. The k-ϵ model equations can be expressed as follows:

$$\frac{\partial}{\partial t}(\rho_m k) + \nabla(\rho_m \vec{v}_m k) = \nabla\left(\frac{\mu_t}{\sigma_k}\nabla k\right) + G_{k,m} + G_b - \rho_m \epsilon \tag{3.7}$$

$$\frac{\partial}{\partial t}(\rho_m \epsilon) + \nabla(\rho_m \vec{v}_m \epsilon) = \nabla\left(\frac{\mu_{t,m}}{\sigma_\epsilon}\nabla \epsilon\right) + \frac{\epsilon}{k}(C_{1\epsilon}G_{k,m} - C_{2\epsilon}\rho_m \epsilon) \tag{3.8}$$

where:

$$G_{k,m} = \mu_{t,m}(\nabla\vec{v}_m + (\nabla\vec{v}_m)^T)\nabla\vec{v}_m \tag{3.9}$$

$$G_{b,m} = -g\frac{\mu_t}{\rho_m \sigma_h}\nabla\rho \tag{3.10}$$

$$\mu_t = \rho G_\mu \frac{k^2}{\epsilon}\nabla\rho \tag{3.11}$$

The model constant $G_{1\epsilon}$, $G_{2\epsilon}$, G_μ, σ_k and σ_ϵ Have the following default values [46]:
$G_{1\epsilon}$=1.44 $G_{2\epsilon}$= 1.92 G_μ = 0.09 σ_k=1.0 σ_ϵ =1.3

where, ρ_m is the mixture density, v_m is the velocity, μ_t is the turbulent viscosity, $G_{k,m}$ is the production of turbulence kinetic energy, G_b is the production of turbulence kinetic energy, k is the turbulent kinetic energy, ϵ is the turbulent dissipation rate, C is the linear anisotropic phase function coefficient, σ_k and σ_ϵ is the scattering coefficient for k and ϵ, and t is the time [45].

- **k-ω model**

This model is used for low-Reynolds number computation. It has few advantages among which are the near wall treatment. Computation of flows involving low Reynolds numbers requires a fine mesh near the wall in order to resolve the laminar part of the boundary layer which is very close to the wall.

- **Shear Stress Transport (SST) model**

This model is based on the k-ω model and has the same automatic wall treatment like k-ω model. It properly calculates the transport of the turbulent shear stress and gives highly accurate predictions. Furthermore, it can also predict the amount of flow separation.

3.5   Modelling reacting flows using fluent
3.5.1 Introduction

In Fluent there are a five approaches available for modelling gas phase reacting flows which are: i) species transport model, ii) non- premixed combustion model, iii)   premixed combustion model, iv) partially premixed combustion model and v) composition PDF transport model.

The first step in solving any problem involving species transport and reacting flow is to determine which model is appropriate. In an industrial combustion process generally there are three combustion models a) Non-Premixed Combustion: Fuel and oxidizer come in separate streams, an example of non-premixed combustion include pulverized coal furnaces, diesel internal-combustion engines and pool fires. b)   Premixed combustion: Fuel and oxidizer are already mixed at the molecular level prior to entry into system & ignition. c) Partially Premixed combustion: Reacting systems with both non-premixed and premixed fuel/oxidizer streams.

The purpose of section is to give an overview of non-Premixed and Premixed models, which are used to carry out this work.

3.5.2 Non-premixed combustion model

Non-premixed modelling approach is specifically developed for the simulation of turbulent flames (fast reaction combustion).

Moreover, the turbulence non-premixed flames are commonly used in a large number of industries. That is because burner of turbulent non-premixed flame gives the ability to regulate the quantity of air and possible to use with different kinds of fuel [47]. In non-premixed model approach certain assumptions are that the instantaneous thermochemical state of the fluid is related to a conserved scalar quantity known as the mixture fraction f. The mixture fraction can be written in terms of the atomic mass fraction as [46].

$$f = \frac{Mass\ of\ Material\ having\ its\ origin\ in\ the\ fuel\ stream}{mass\ of\ mixture} \qquad (3.12)$$

$$f = \frac{Z_i - Z_{i,ox}}{Z_{i,fuel} - Z_{i,ox}} \qquad (3.13)$$

where
Z_i = elemental mass fraction for element i.
The subscript ox denotes the value at the oxidizer stream inlet and the subscript fuel denotes the value at the fuel stream inlet.
The mass fraction is unity i.e. f = 1, in the fuel stream and zero in the oxidizer stream; and within the flow field it takes a value between 1 and 0.

3.5.3 Premixed combustion model

In premixed flames, the fuel and oxidizer are intimately mixed before they enter the combustion device. In many industrial premixed systems, combustion takes place in a thin flame sheet. As the flame front moves, combustion of unburnt reactants occurs, converting unburnt premixed reactants to burnt products.

Therefore the premixed combustion model considers the reacting flow field to be divided into regions of burnt and unburnt species, separated by the flame sheet. The flame front propagation is modelled by solving a transport equation for the density-weighted mean reaction progress variable, denoted by $\overline{c}$ [46].

$$\frac{\partial}{\partial t}(\rho \overline{c}) + \nabla * \left(\frac{\mu_t}{Sc_t}\nabla \overline{c}\right) + \rho Sc \qquad (3.14)$$

where

    $\overline{c}$ = mean reaction progress variable

    Sc_t = turbulent Schmidt number

    Sc = Reaction progress source term (s^{-1})

The value of $\overline{c}$ is defined as a boundary condition at all flow inlets. It is usually specified as either 0 (unburnt) or 1 (burnt) [46].

3.6 Porous media model

The porous media model is used for a wide variety of single phase and multiphase problem, an example of a porous zone includes flow through packed beds, filter papers, perforated plates, flow distributors, and tube banks [46]. Cell zones in ANSYS Fluent consist of fluids and solids zones, porous zone is treated as a fluid zone with pressure loss in the flow.

In this work, the porous media model is used to define the stack of bricks. The momentum source term is added to the standard fluid flow equations for modelling porous media and the source term is composed of two parts, a viscous loss term and an inertial loss term.

In this work, it is assumed that porous media is homogeneous (isotropic media) heat transfer in porous zone is not considered. The definition of viscous and inertial resistance can be written as [46]

$$S_i = -\left(\frac{\mu}{\alpha}v_i + C_2\frac{1}{2}\rho|v|v_i\right) \qquad (3.15)$$

where S_i is the source term for the i th (x, y, or z) momentum equation, $|v|$ is the magnitude of the velocity, α is the permeability and C2 is the inertial resistance factor.

Or as pressure drop per unit length can be written as [46]

$$\frac{\Delta P}{L} = - \left(\frac{\mu}{\alpha} v_i + C_2 \frac{1}{2} \rho |v| v_i \right)$$

(3.16)

3.7   2D simulation of the annular ring burner

The annular ring burner has been proposed in this research, it is a ring tube which consists of an inner fuel nozzle and outer air nozzle, as shown in figure 3.10. The aim of the present work, is to carry out numerical simulations on the turbulent flame based on annular ring burner. It focuses on studying the effect of different ambient conditions and various burner inlet conditions on the flame length and temperature distribution.
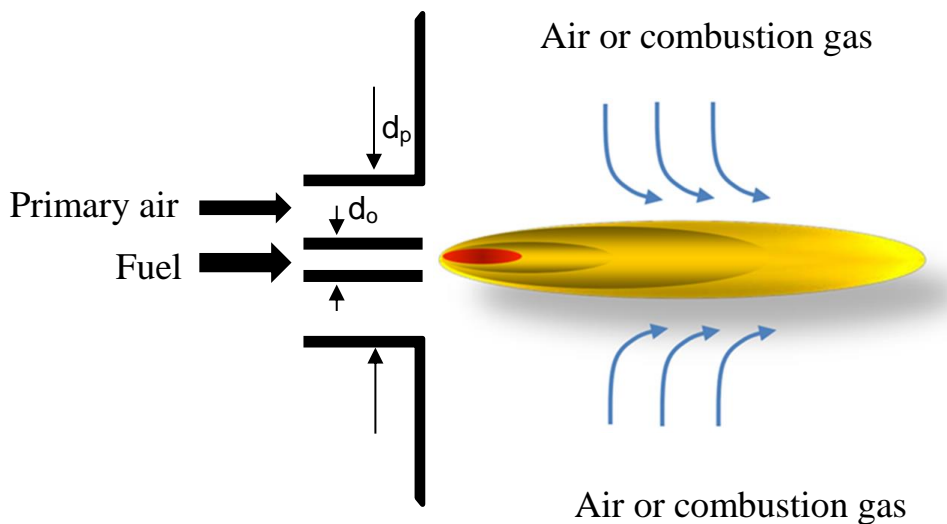
Figure 3.10: Showing the annular ring burner

3.7.1 Geometry and process simplification of annular ring burner

The geometry was created in ICEM CFD, as it has been mentioned before, the annular ring burner is a ring tube burner. In this study, it consists of an inner fuel nozzle with $0.005m$ diameter and outer air nozzle with alterable diameter.

To simulate large space, we proposed a container has $20\ m$ length and $10\ m$ diameter. In this work, the full geometric domain is considered as a symmetrical cylinder ($20\ m$ length and $5\ m$ diameter) to minimize the computational time. The surrounding is defined in two methods (a) ambient is air, (b) ambient is combustion gas.

Figure 3.11a shows the half portion of the cylinder has been considered for simulation as a studying domain, as the flame and the container are cylindrical and symmetrical.
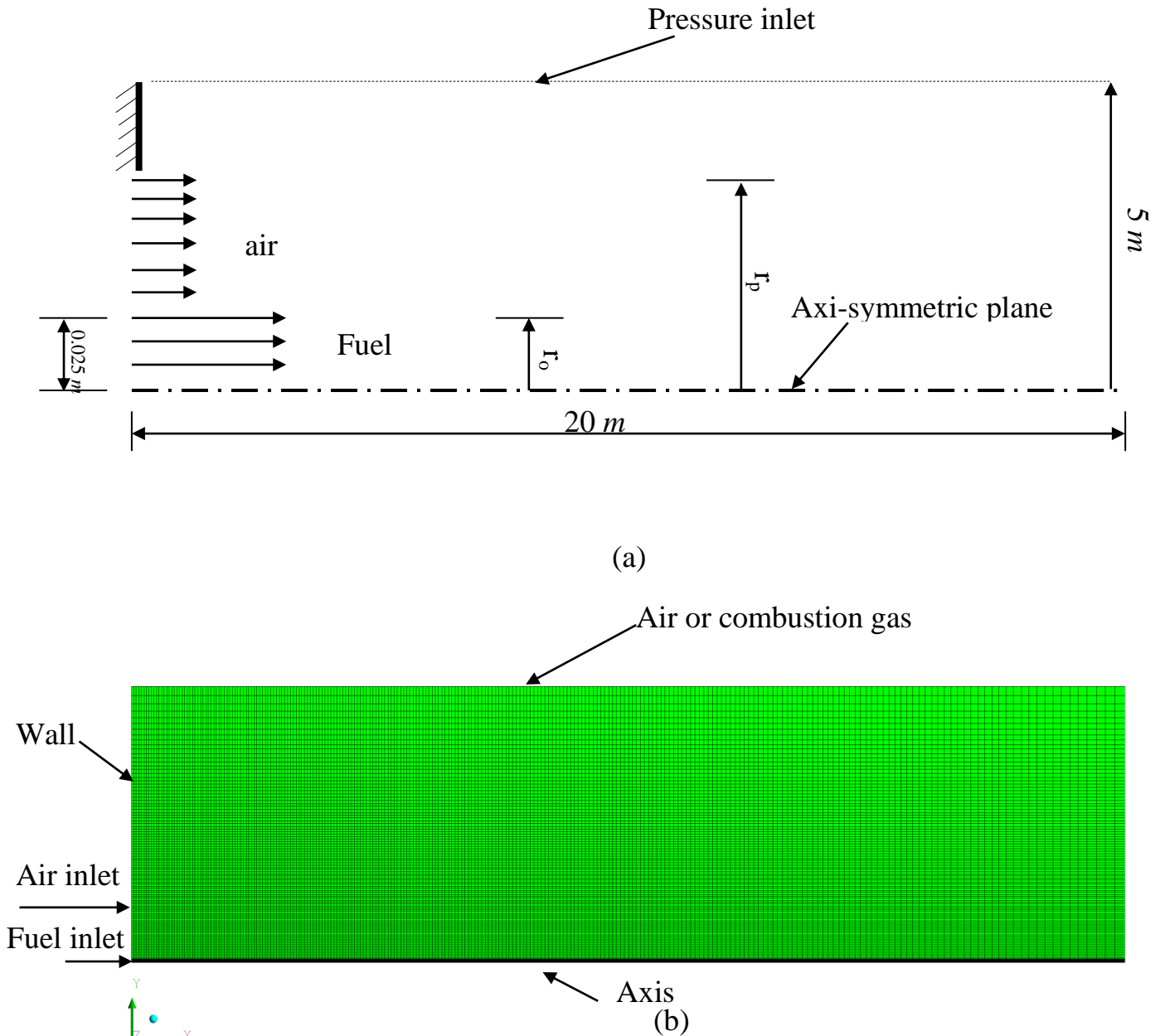
(a)

(b)

Figure 3.11: 2D domain geometry and mesh for annular ring burner (a) geometry (b) mesh

3.7.2 Mesh generation and mesh independence study

A two dimension structured mesh (quadrilateral mesh) is used to simulate non-premixed flame. To make sure that the flame length converges as the grid number increases, the mesh independence study should be studied first. This also ensures accuracy greater of results in a short time.

Figure 3.12 shows the dimensionless flame length related to the cell number. It can be seen that, the mesh number varied from 5,000 to 100,000 cells, where the coarse grids are associated with a large variation of the dimensionless flame length. Moreover, the figure demonstrates that the utilizing grids more than 30,000 cells lead to a relative variation in dimensionless flame length, less than 0.22%. Consequently, in order to minimize the simulation time and keep high-accuracy, the grade with 30,000 cell has been selected to carry out all cases of the non- premixed flame simulations.
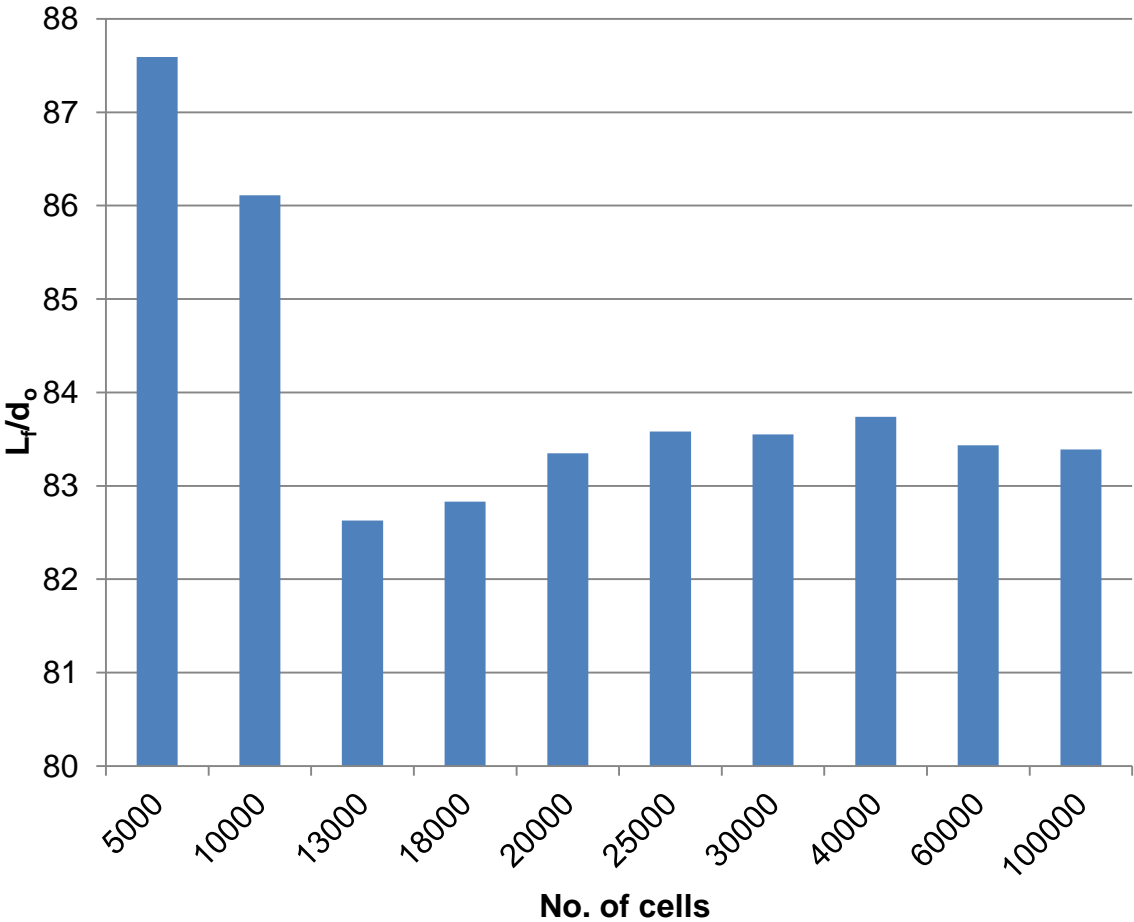
Figure 3.12: Mesh independence study for jet dimensionless flame length

3.8   3-D Modelling of the flow mixing in a part of tunnel kiln

3.8.1 Geometry and process simplification of tunnel kiln

The geometry of tunnel kiln is approximated to a cuboid shape has a length between 35 m and 250 m and width between 1m to 6m [16]. Because of the complexity of the kiln geometry, a huge number of cells should be used to find fundamental results. Therefore, in a first step the empty part in between two kiln cars has been used instead of the complex structure of the kiln with the product. Figure 3.13 shows the schematic description in longitudinal direction of a part of tunnel kiln with the location of the CFD model.
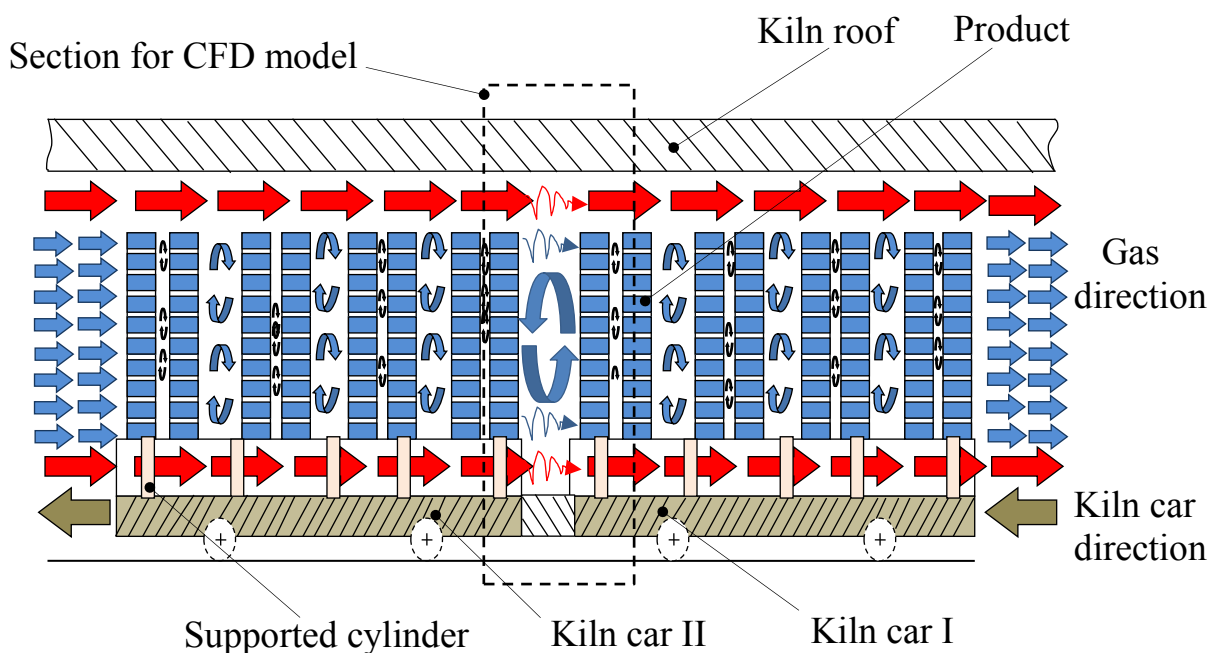
Figure 3.13: Schematic diagram of tunnel kiln

As mentioned before, ICEM CED 14.0 is used to draw the geometry of the fluid domain. Four different kiln geometries with same volume has been studied. The main dimensions of the kiln; kiln height (H_k), kiln width (B_k), ware height (h_w) and ware width(b_w) are listed in table 1, length of the domain is 20 m, is chosen depending on the stability of the simulation.

Table 3.1: Kiln geometrical parameters

Geometry	B_K (m)	H_K(m)	$G_{K,R}$	b_w	h_w
I	4	3.3	1.2	3	2.2
II	5	2.64	1.9	3.75	1.76
III	6	2.2	2.73	4.69	1.41
IV	7	1.88	3.72	5.86	1.13

The main flow of the inlet is divided into two zones with equal area, so that possible to control two streams (gas zone and ware zone) as shown in figure 3.14. The temperature of the gas zone is 400 ^{o}C, and the ware zone temperature is 300 ^{o}C, volume flow rate constant in two zones. After one meter from the main inlet there is a side injection (third stream), velocity, mass flow rate and temperature of the side injection is changed depending on the boundary condition. The flow in this work is considered as incompressible flow. The walls are assumed to be adiabatic, i.e. There is no heat loss through the walls.
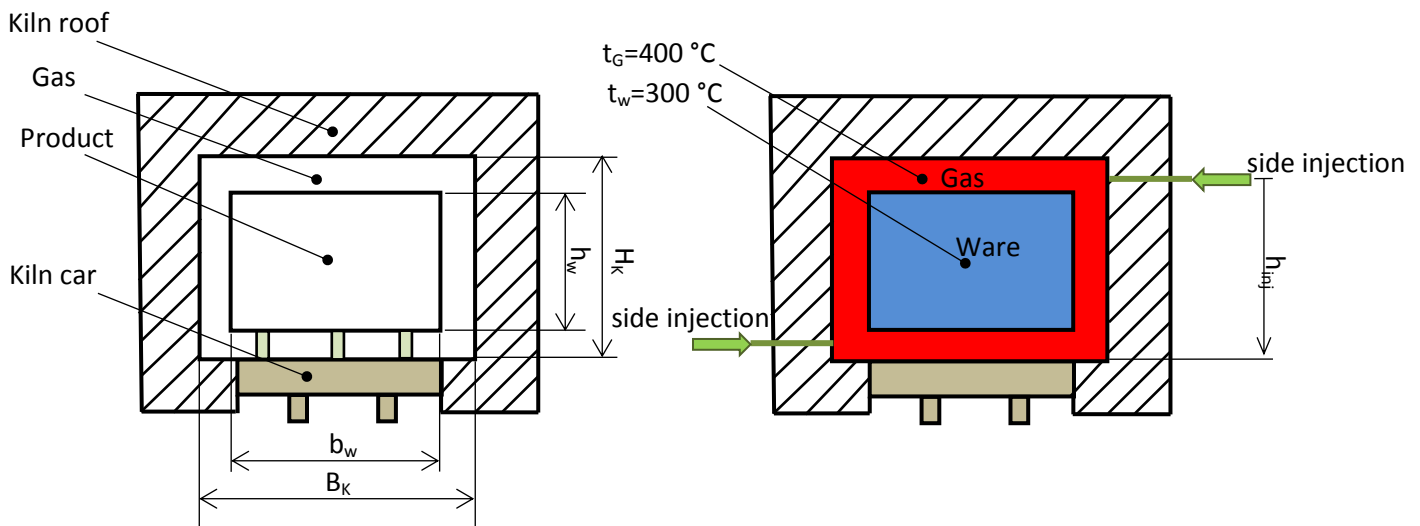
Figure 3.14: Transverse section without and with proposal respectively

Figure 3.15 shows the principals schematic diagram for proposed geometry (I) and boundary types, in this model, there is two nozzles installed after one meter from the main flow.
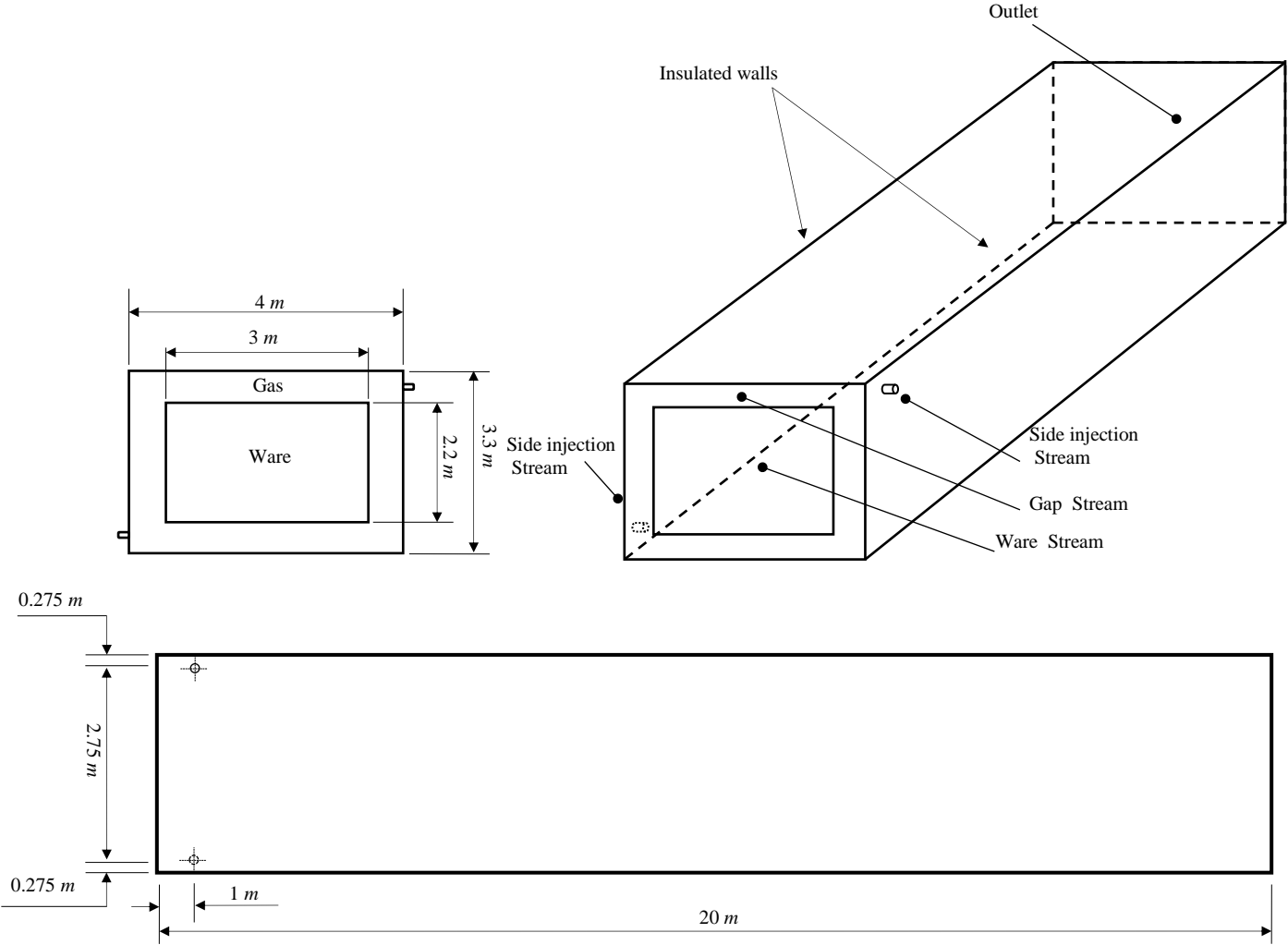
Figure 3.15: Cavity Geometry (I)

3.8.2 Mesh generation and mesh independence study

Structured mesh (Hexahedral mesh) is used in 3D object – based multi-block structured volume mesh, with O-grid mesh generation at the orifice of the side injection.

In order to calculate the temperature distribution for the mixture through the kiln, the mesh must be fine enough. Therefore, it is important and necessary to conduct a mesh independence study to ensure better accuracy results in short time. Therefore, in the present study, a number of 3D meshes with increased density are used to insure the average temperature converges as the mesh size increases.

In the present study, the Reynolds number of the main inlet flow is 31190 and for the flow from side nozzles varied from (58189.9-130021.2) which leads to turbulent flow. The standard k-ε turbulence model is employed to calculate the temperature distribution as a result of flow mixing between the two flows. The flows are taken to be incompressible. Default schemes are selected to compute the field variables.

Eight different sets of grids (HEXAS cell) are built as shown in figure 3.16. The temperature is measured after 1 m from the side injection. The results show that utilizing grids more than 6,7572,506 cells lead to a relative variation in temperature less than 0.001%. Consequently, in order to minimize the simulation time and keeping high- accuracy. The grads with the 6,757,506 cells has been selected to carry out this work.
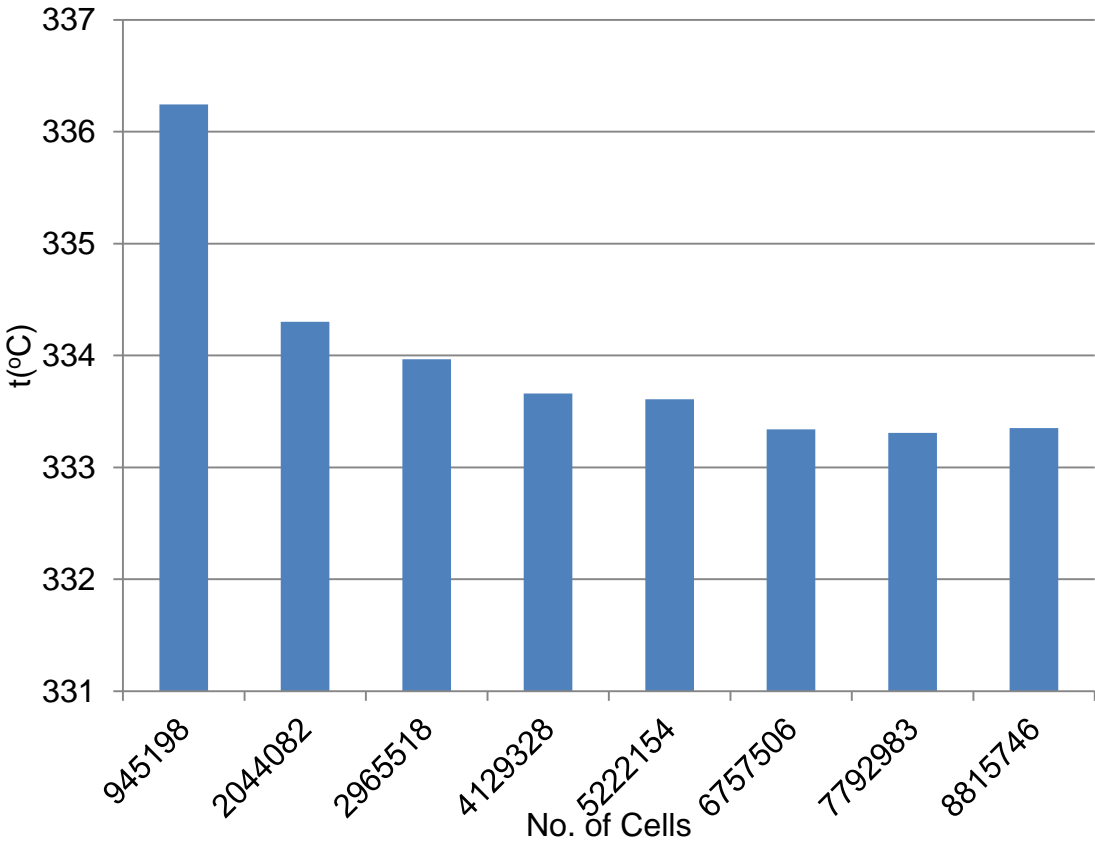
Figure 3.16: Grid independence study for the computational domain

Figure 3.17 shows that the mesh used to model the gap between tunnel kiln car. It is shown that, all the elements are Hxahedral element, and O grid has been used in the side injection. The grids are fine enough to calculate the temperature.
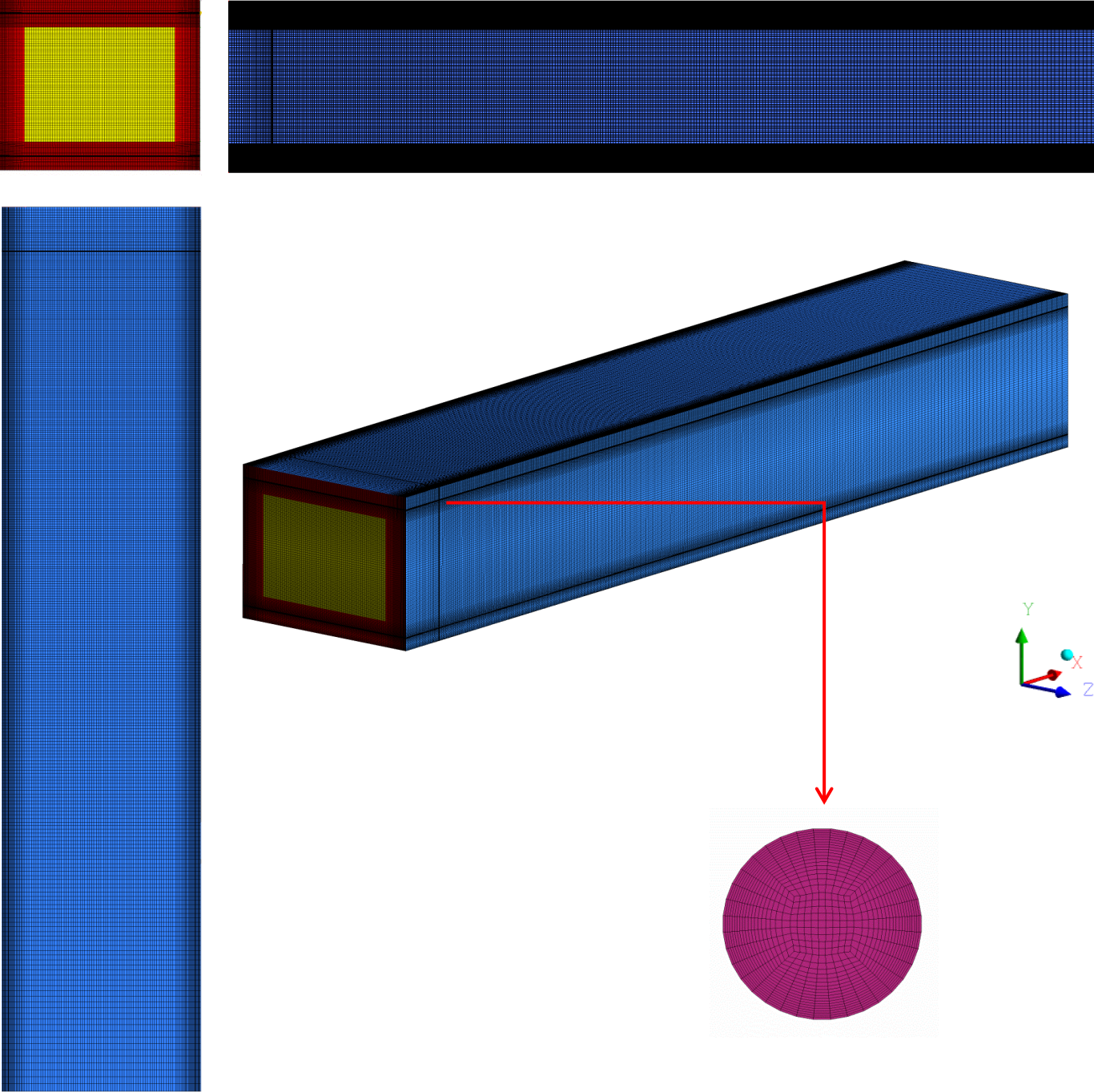
Figure 3.17: Modeling done by ANSYS ICME 14.0

3.8.3 Model verification

Three streams are used in this work; gas stream (gab stream) at temperature 400^oC, ware stream at temperature 300^oC and side injection with 20^oC. The temperature of the mixture is related to the mixing ratio of side injection.

The assumptions used during the present CFD simulations were steady state, incompressible flow and adiabatic (walls insulated). For verification of calculating temperature, temperature is calculated analytically using equation 3.30 [48].

More than Fifteen different models have been carried out for the used domain with different boundary condition (velocity and mass flow rate of the side injection), with different mixing ratios. The results show a good agreement between the numerical and analytical solution with maximum error of 0.5 % as shown in Figure 3.18. Number of elements and approaches of mesh are considered as reference for other models in this work

$$t_{mixing} = \frac{\dot{M}_{inj}*c_{p,inj}*t_{inj}+\dot{M}_{ware}*c_{p,ware}*t_{ware}+\dot{M}_{gap}*c_{p,gap}*t_{gap}}{\dot{M}_{inj}*c_{p,inj}+\dot{M}_{ware}*c_{p,ware}+\dot{M}_{gap}*c_{p,gap}} \qquad (3.17)$$
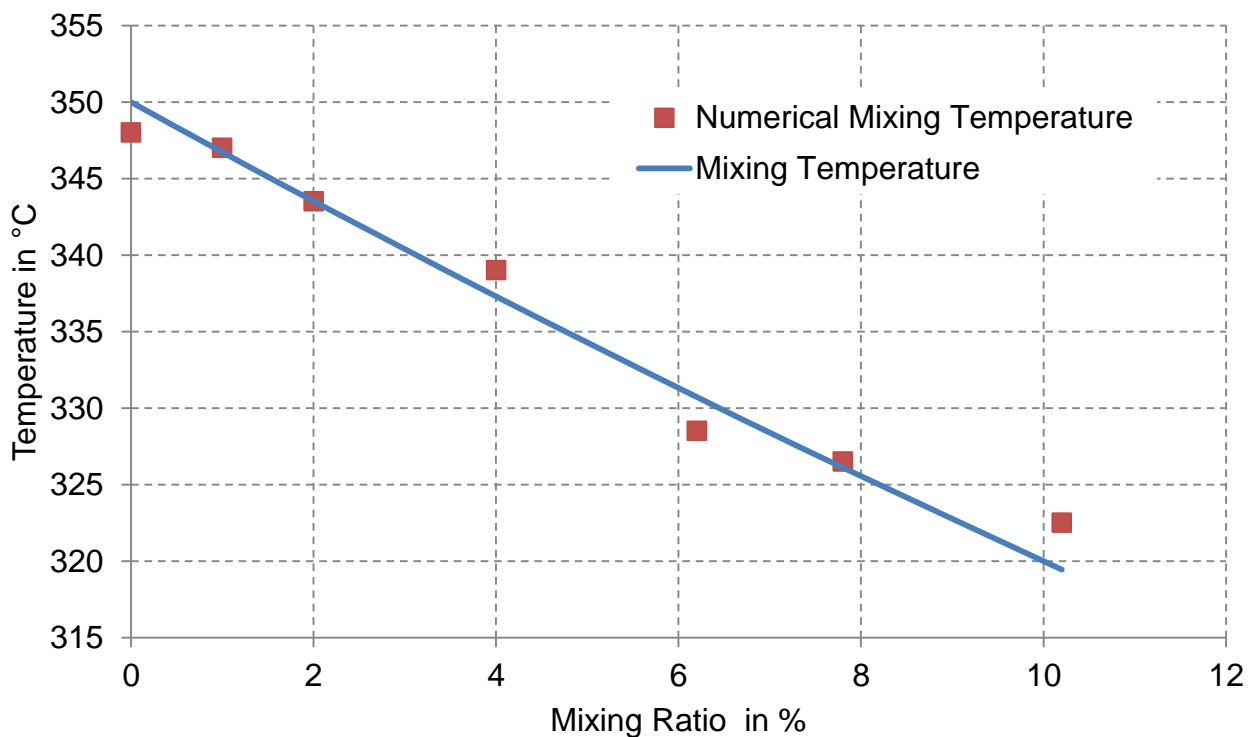
Figure 3.18: Comparison between mixing temperature and numerical mixing temperature

3.9 3-D Modelling flow mixing in a part of tunnel kiln with ware

In this part, the ware (stack of bricks) is considered for studying the influence of stacks of bricks on the quality of the mixing. Furthermore, the influence of cross-section area of the ware is also studied.

3.9.1 Geometry and process simplification

Three different models have been studied for this work. In this section, the height and width of the tunnel kiln are considered constant with different product dimensions as shown in Figure 3.19.

Geometry (I) ($A_{ware}=0.5A_{total}$)

Geometry (II) ($A_{ware}=0.75A_{total}$)   Geometry (IV) ($A_{ware}=0.81A_{total}$)
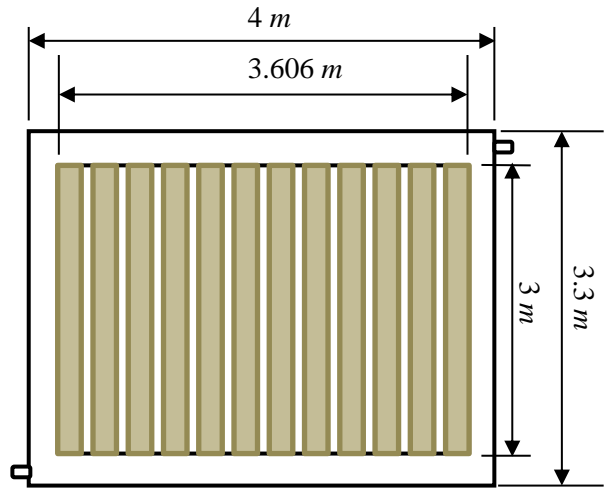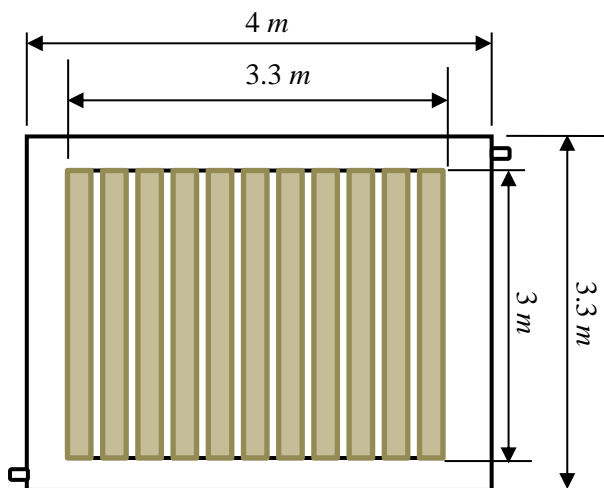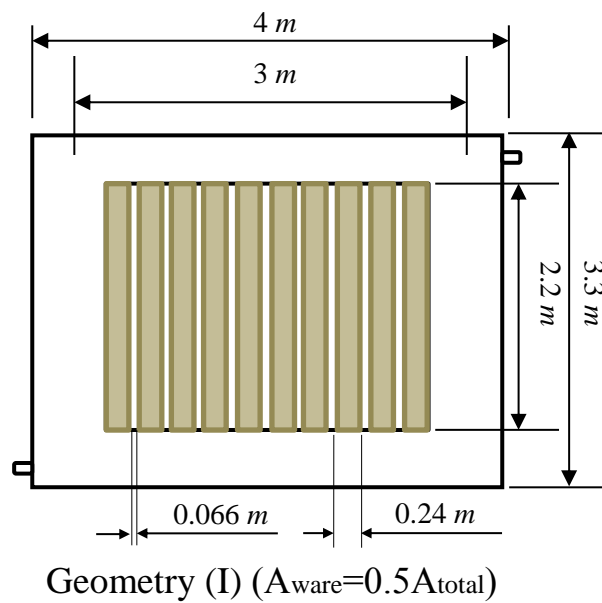
Figure 3.19: Show the different A_R shapes

The standard brick dimension is 0.24x0.12x0.071 m. The width of the blade of bricks is dependent on the width of a brick. For geometry (I) the stack dimension is 3.5 m length, 0.24 m width and 2.2 m height. The blade has 3.5 x 0.24x 2.2 m, as shown in figure 3.20.

The number of bricks for each blade is 702 brick, so that, by using equation 3.18 the porosity for each blade of bricks is 0.22.
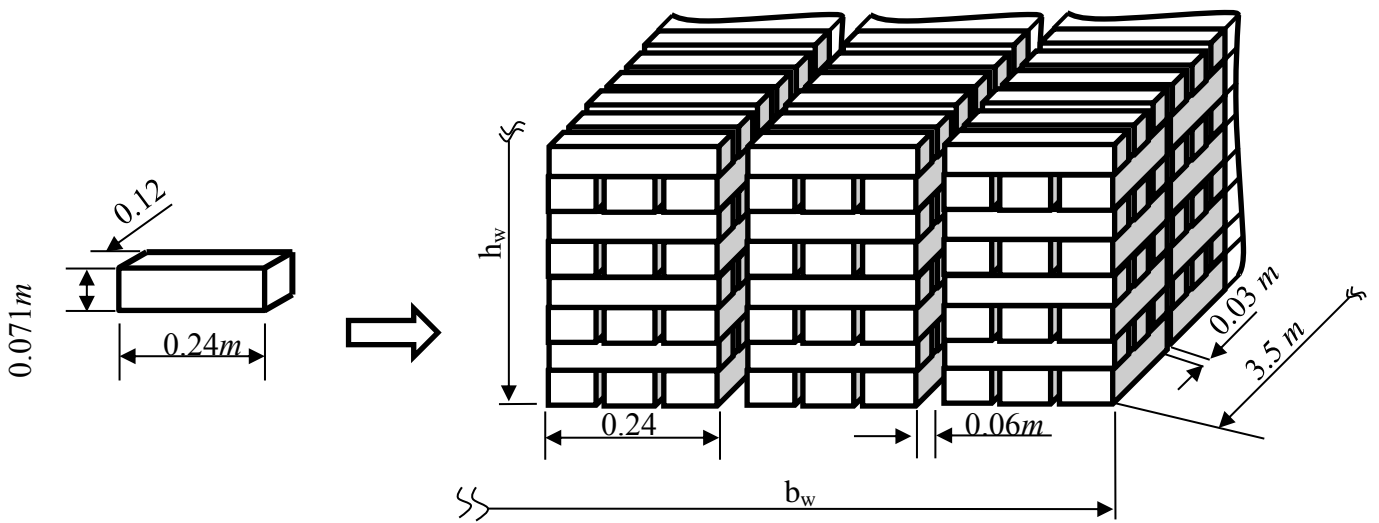

Figure 3.20: Dimensions of the single standard brick and stacks of the bricks

$$\varphi = \frac{total\ pore\ volume}{bulk\ volume} \qquad (3.18)$$

Where

φ is the porosity,

Total pore volume $= total\ bulk\ volume - (No.\ of\ brick\ *\ brick\ volume)$

The permeabity and intertnal resistance can be found by using equation 3.19 and 3.20 [46].

$$\alpha = \frac{d_p^2 - \varphi^3}{150 * (1-\varphi)^2} \qquad (3.19)$$

$$C_2 = \frac{3.5 - (1-\varphi)}{d_p * \varphi^3} \qquad (3.20)$$

$d_{par.}$ is the equivalent diameters of particle (brick), and it can be calculated from equation 3.21 [49].

$$d_p = \left(\frac{6}{\pi} V_{par.}\right)^{1/3} \qquad (3.21)$$

3.9.2 Mesh generation and mesh independence study

In this section of the study a structured mesh (Hexahedral mesh) is used in 3D object based multi-block structured volume mesh, with O-grid mesh generation at the orifice of the side injection.

Six different sets of grid structured mesh (Hexahedral mesh) are built. Figure 3.21 shows the temperature measured after 0.9 m from the side injection with different mesh elements. The results show that, the utilizing grids with more than 7,777,974 cells lead to a relative variation in temperature less than 0.09%. Consequently, the grade of the 7,777,974 cells has been selected to carry out this work.
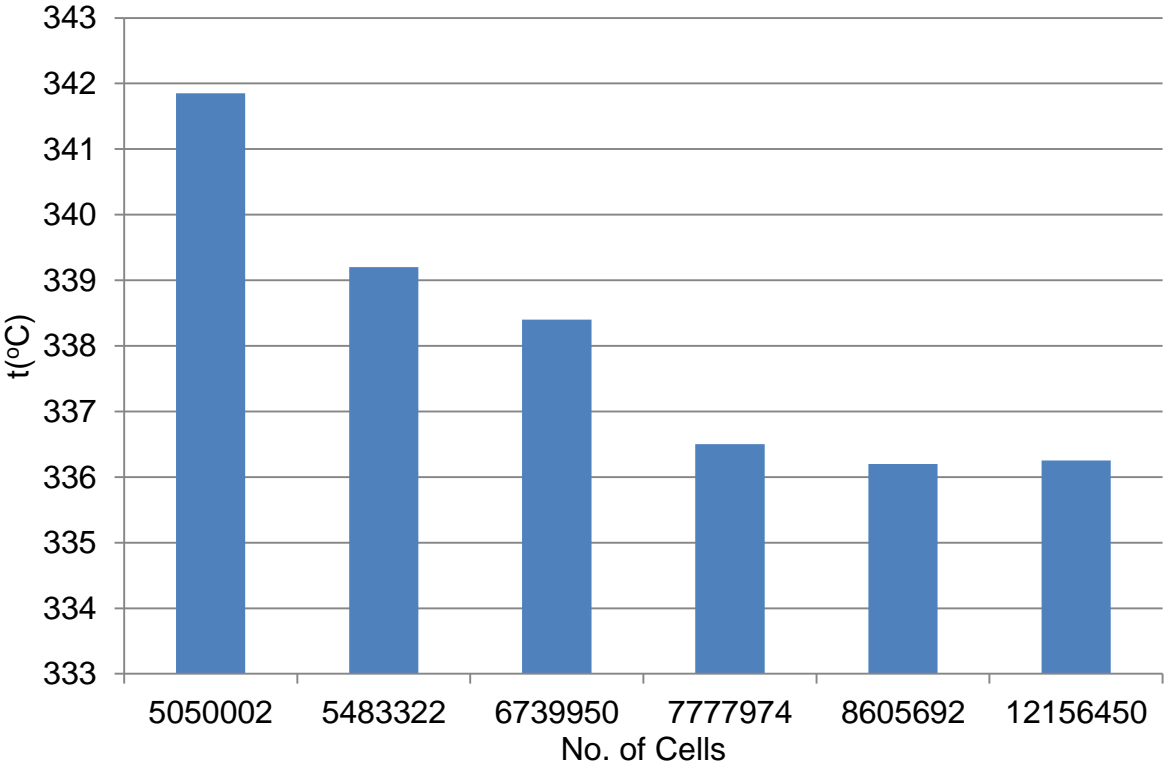
Figure 3.21: Grid independence study for the computational domain

Figure 3.22 shows the hexahedral mesh that used in simulation of mixing in tunnel kiln, also the figure show the distribution of mesh.
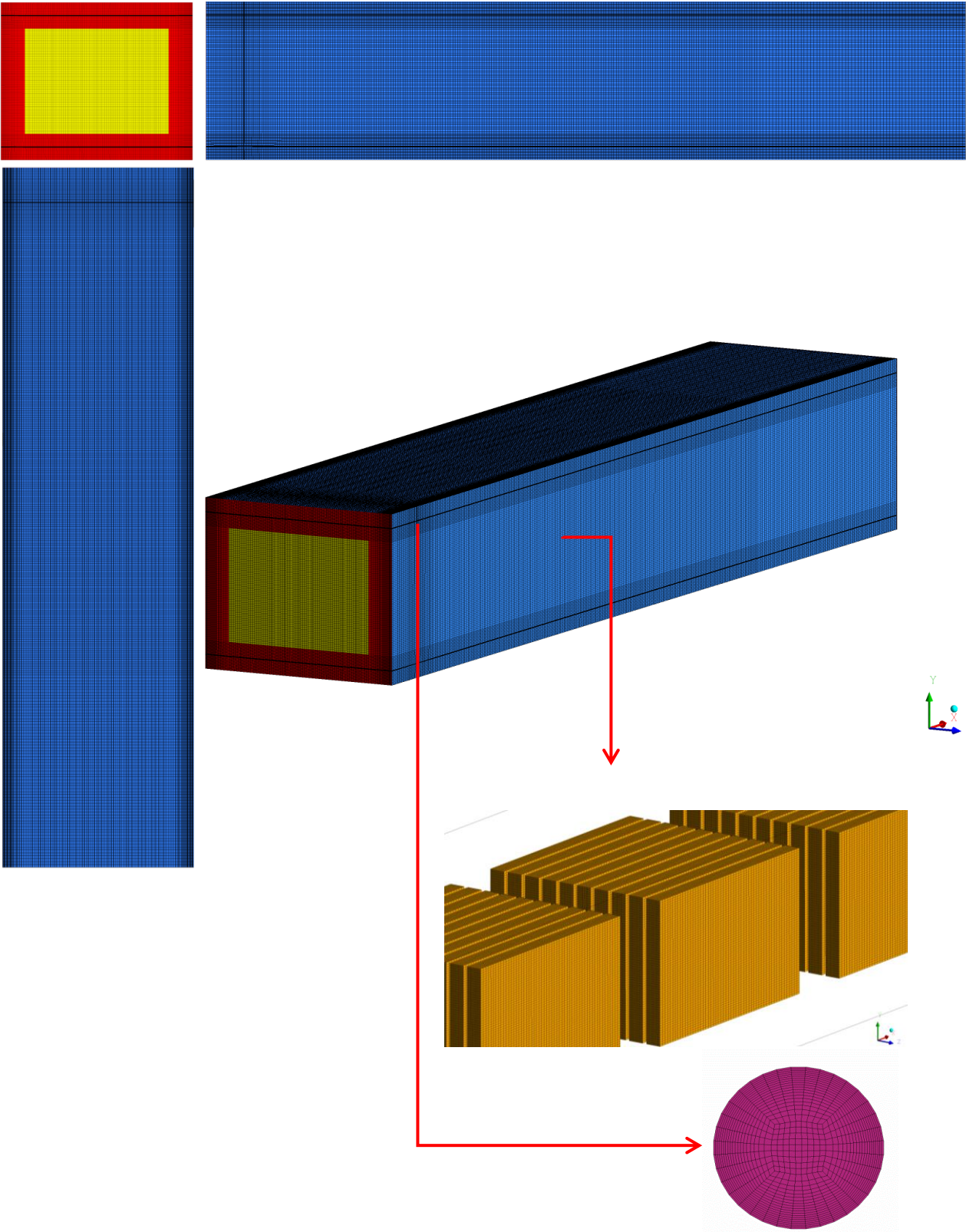
Figure 3.22: Modelling with ware done by ANSYS ICME 14.0

3.10   3-D models of roller kiln and burner design

The main purpose of this part of the study, is to find the direction of stream line of the burner (without combustion), quantity of the sucked air in addition to finding the influence of the cone length. The second purpose is to find the temperature distribution at the outlet (with combustion), in two different cases, the first one when the burner fixed against the direction of the main flow and the second one when the burner fixed in the same direction of the main flow.

3.10.1 Geometry and process simplification of roller kiln

The typical roller kiln has $126m$ length, 1.45 m width and 0.872 m height [50]. This kiln is used for producing tiles. The typical tile dimensions are $0.045x0.045x0.007$ m. In this study, the sample of roller kiln has four burners with premixed combustion. These burners are supported on the roof of the roller kiln. As shown in Figure 3.23, a half portion of the total width of the kiln has been taken as a studying domain to minimize the simulation time.
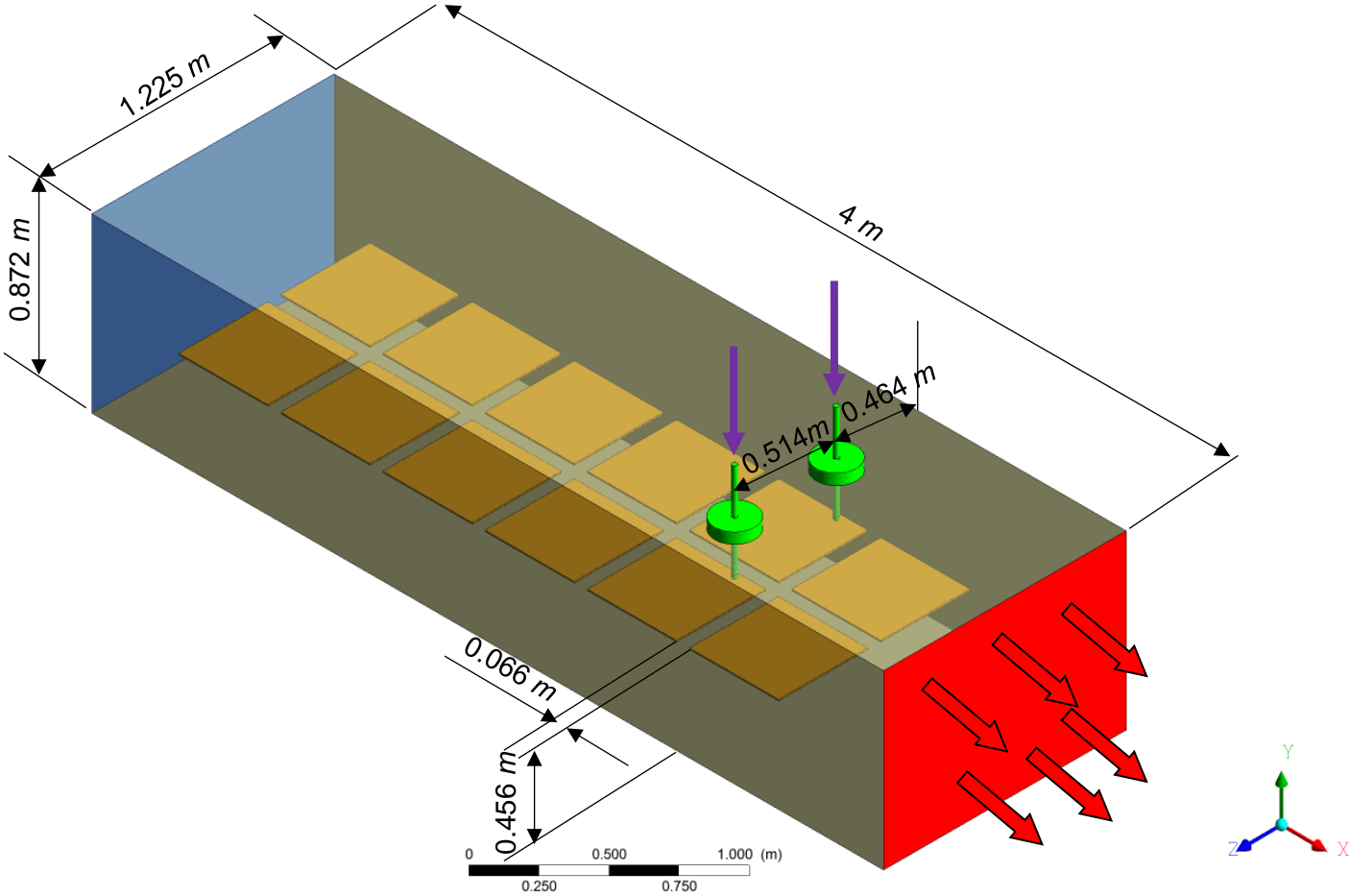

Figure 3.23: Model of the roller kiln and burner

There is a bore hole in the roof insulation, which allows the injector to suck air from inside of the kiln channel to use it in the combustion process.

The burner dimensions are 0,024 m diameter, 0.5 m length, 0.034 m output diameter with 28.3° slope and 0.044m diameter of the orifice to suck the air. The cone dimensions are 0.006 outlet diameter and 0.031 *m* length, as shown in Figure 3.24.
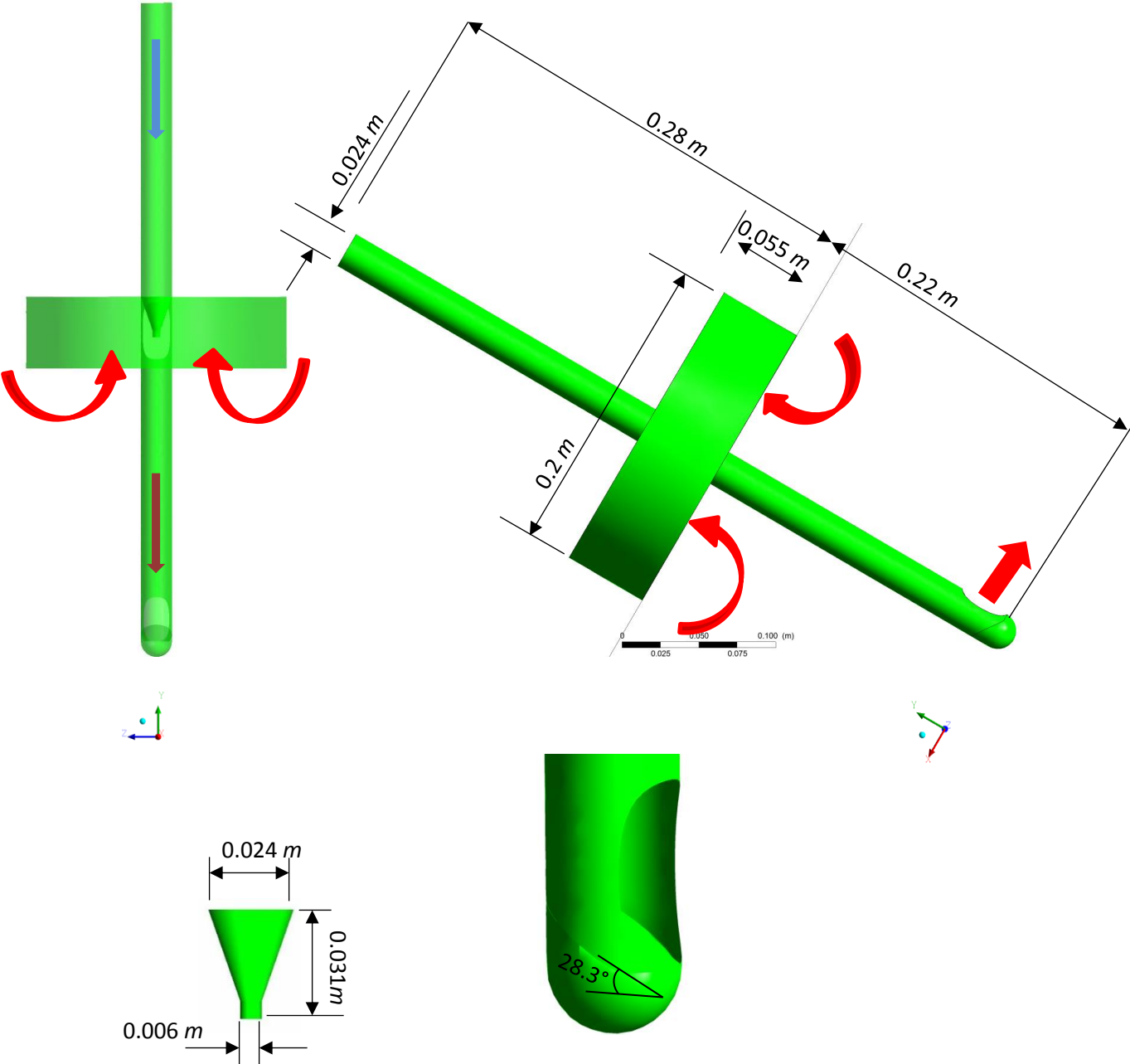

Figure 3.24: Model of the burner system

The second object as mentions above, is to find the temperature distribution at outlet in two cases (burner fire against the main flow or the same direction like

the main flow). Consequently, it created the new geometry to decrease the computation time with accurate results. The empty cube with orifice at the mid length of the kiln is proposed. The slop of the burner is not considered here. The unborn mixture is injected from the ending edge of the burner, as shown in Figure 3.25. Non adiabatic premixed combustion (Zimont) model, 10% fuel (Methane) and 90 % air stoichiometric combustion with k-ϵ model has been used to carry out this work.
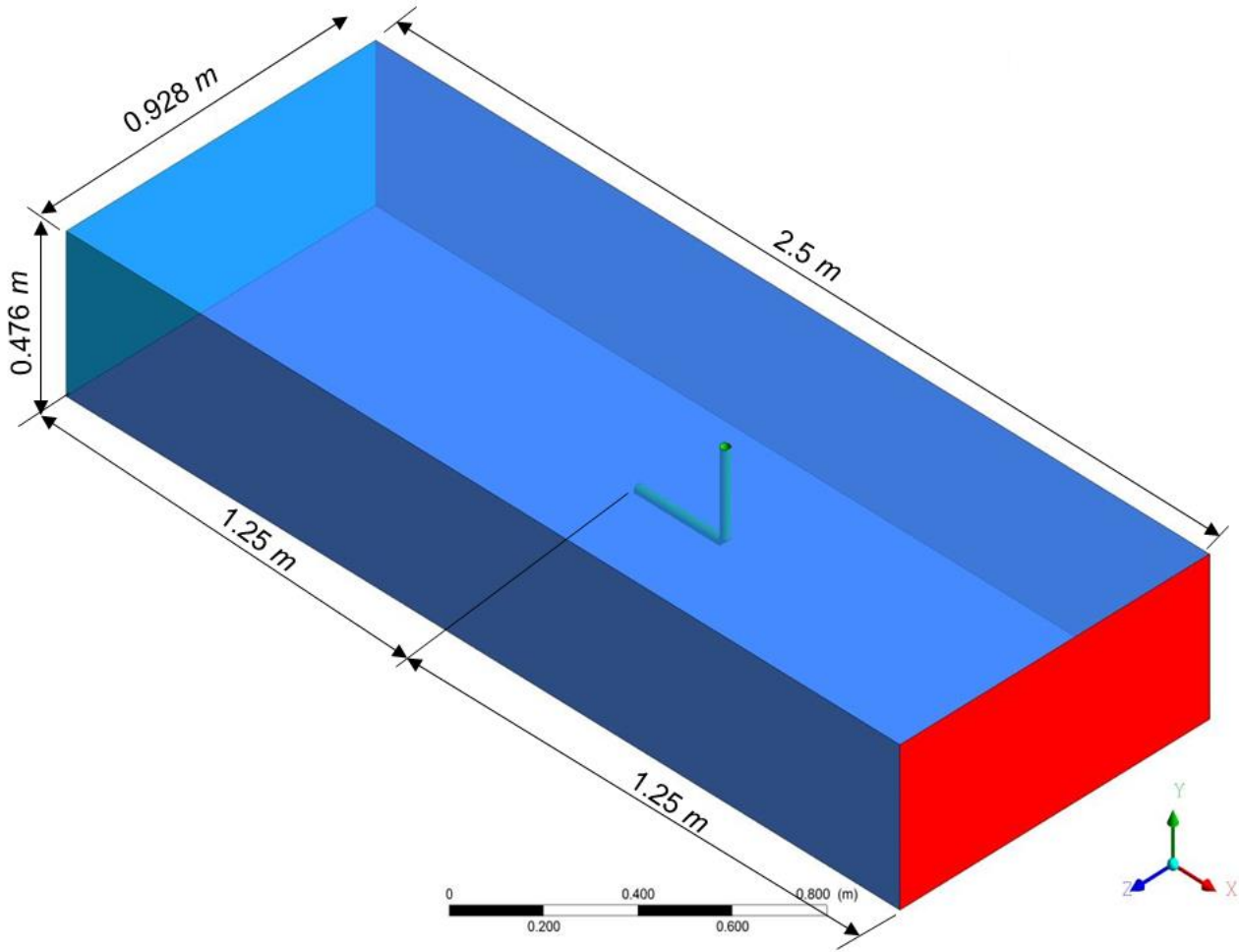

Figure 3.25: Modelling of the combustion chamber

3.10.2 Grid design and mesh independence study

Various meshes are generated in the combustion chamber to study mesh independence. The mesh is generated using the tetra/mixed method (Delaunary) with prism layer. In general, the Delaunary method is considered more suitable for CFD simulations. This method roots from the surface and making it way up to fill the whole geometry.

Five different meshes are generated by applying the maximum size element, the mesh in the region that in front the burner is maintained fine by using density region method. Therefore, The density region is not a part of the geometry, but only used to refine the mesh in a volumetric zone as shown in figure 3.26a. Figure 3.26b shows three of different grid settings. The details about different mesh sitting are listed in table 3.2:

Table 3.2: Detals of the mesh setting

Mesh No.	Max size	Cells number
1	0.1	2641966
2	0.07	2645324
3	0.04	2751402
4	0.03	2888541
5	0.02	3674289

The global element scale factor is 1, and the maximum size for the burner and density region is 0.003, 0.007 respectively.

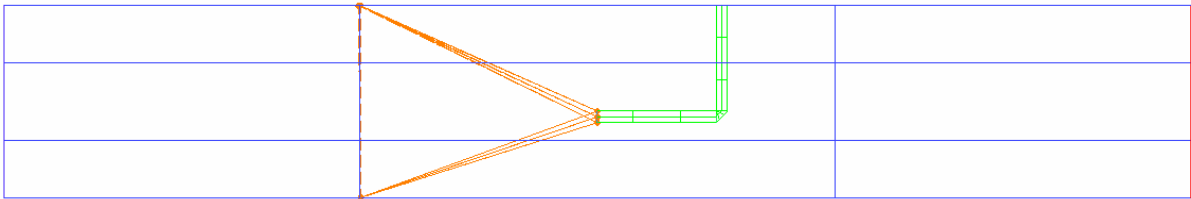Figure 3.26a: show location of the density region

Grid No. 3

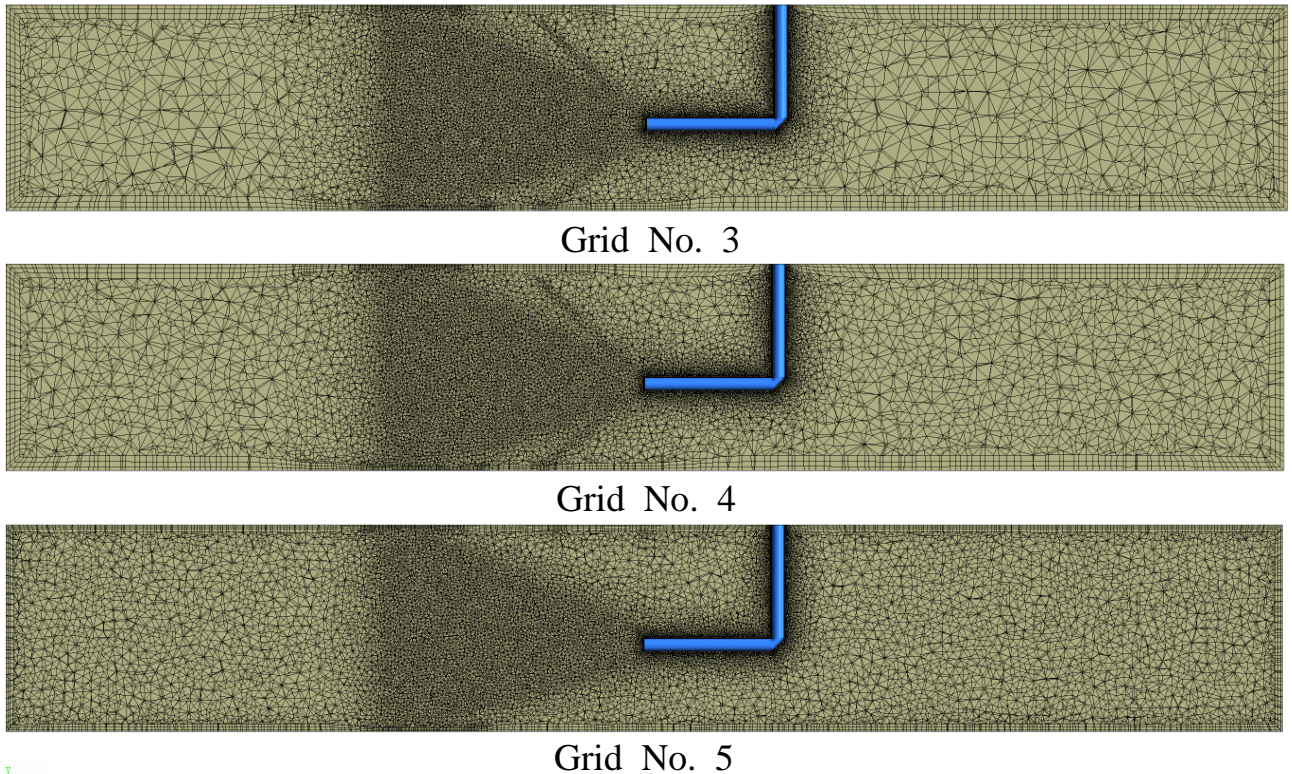Grid No. 4

Grid No. 5

Figure 3.26b: Mesh with the prism layer at different size element

The influence of the grid number is described as the temperature. Figure 3.27, shows the peak temperature, which   depends upon the grid number. It can be seen that by increasing the number of elements, the peak temperature increases. After the grid number increase   to   2888541cells the temperature distribution curve is becoming constant also peak temperature remains constant at 1144.22 °C. According to the above description, the results of simulated temperature distribution obtained from model No.4. Figure 3.28 shows the chosen mesh in 3D model for simulation of the combustion chamber.
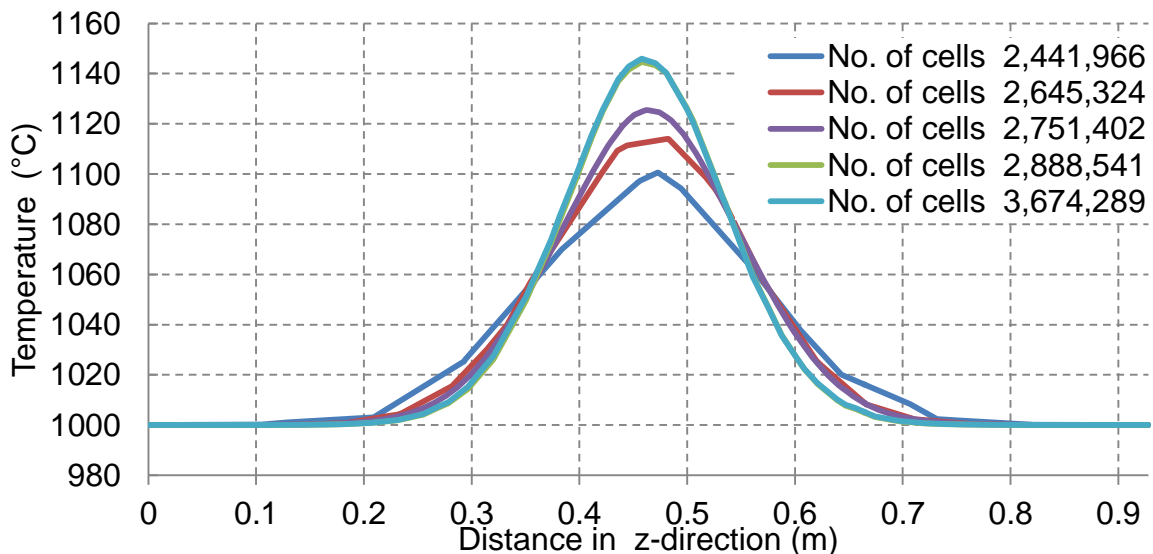

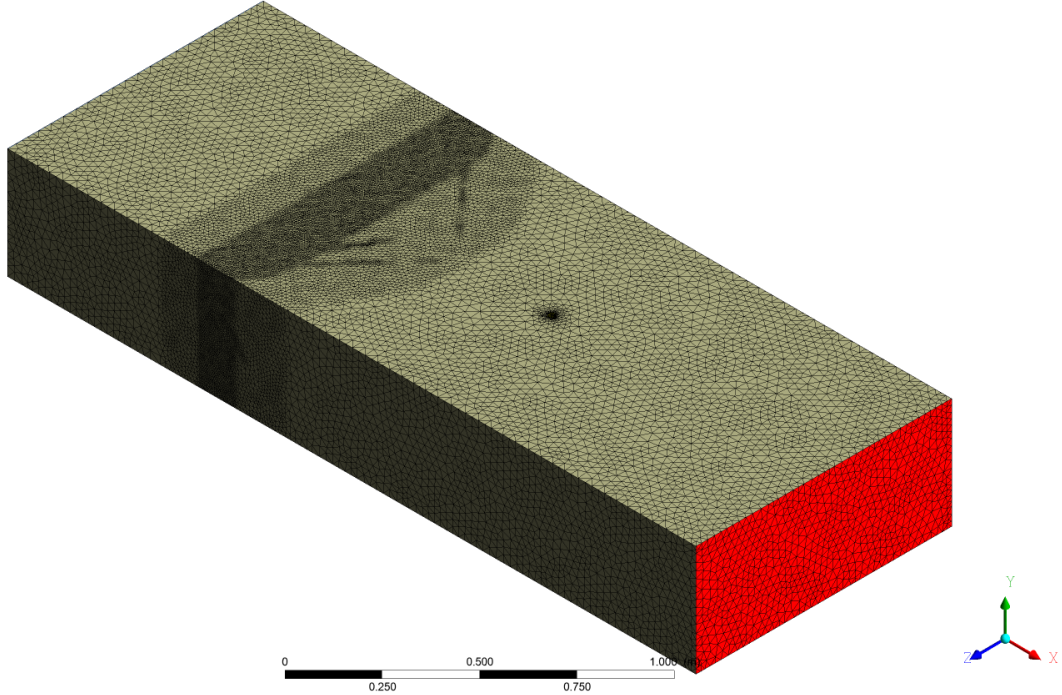Figure 3.27: Grid independence study for the computational domain

Figure 3.28: 3D modelling of combustion chamber

The computational mesh represents the geometry of the region of interest. Therefore, The burners mesh is extremely fine with 0.003 maximum element size. It is used to study the direction of streamline, the quantity of air sucked and maximum velocity for different burner designs. The maximum element size for whole geometry and the perimeter of the tiles is 0.1 and 0.04 respectively. The total element is 5413676. Figure 3.29 shows the mesh of roller kiln.
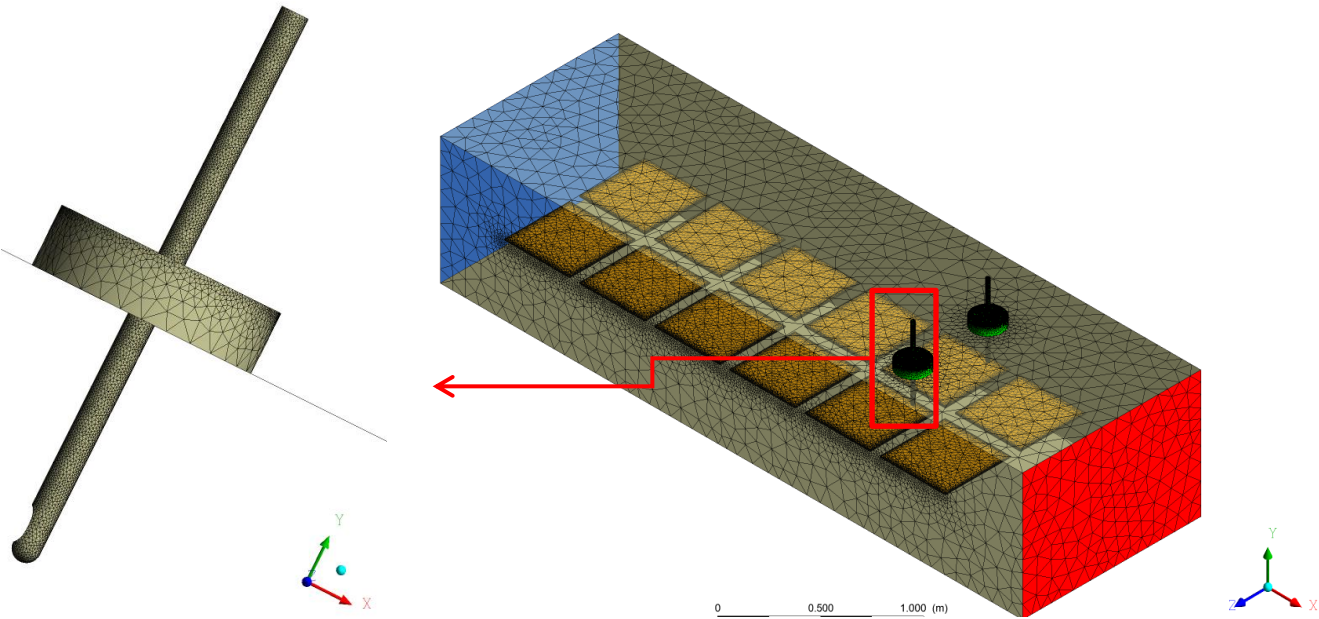

Figure 3.29: 3D modelling of the roller kiln and burner

3.11 Summary

This chapter is devoted to the introduction of the fundamentals of the computational fluid dynamics. Theories of ANSYS Fluent 14.0 of some models used in this work. In addition, the meshing process in ANSYS-ICEM CFD 14.0 includes an introduction to mesh types, theories of mesh quality.

A structured mesh is used to represent the geometry of the 2D annular ring burner model and also used to simulate a 3D   model of a part of the tunnel kiln (gap between cars). Unstructured mesh (Tetrahedral mesh) is used for the roller kiln. Standard k- ϵ model is used to solve the turbulent situation for this work. The thermal energy option is selected to simulate the temperature distribution in a tunnel kiln (gap between cars). The porous zone model is used to define the stack of bricks. The non Premixed combustion model (Equilibrium and non-Adiabatic models) is used to simulate 2D annular ring burner with axisymmetric method. The Premixed combustion model (C Equation with non-adiabatic model) used in roller kiln. Furthermore, the simulation of a series of grids with different grid density is carried out.

4 Side injection of air jets

4.1 Introduction

This chapter is dedicated to the discussion on results of temperature distribution inside a part of tunnel kiln when side injections are used perpendicular to the main flow. It was proposed in section (3.8) that with this assembly the improved temperature distribution inside the tunnel kiln could be expected. This investigation is related to a segment somewhere in the preheating zone where exists a typical temperature difference of 100°C between gas and ware zone.

The total main volume flow rate is (1.663 m³/s) with velocity (0.126 m/s). Ambient air is injected at 20°C, by using jet is located at the side position of tunnel kiln. Here, a single nozzle or one nozzle per side is considered. Beside the injection velocity and the injected mass flow rate, the influence of the nozzle position, the nozzle diameter and nozzle shape have been studied in geometry (I). The nozzle position is defined by the distance (h) between nozzle and kiln top or kiln bottom as shown previously in chapter three Figure 3.14. Table 4.1 shows the different arrangements with side nozzles for geometry (I). In the first arrangement (i), a side injection nozzle is located at the level (h=0. 9 H_k). Then by changing (h) and number of side injection nozzles, the other three arrangements are obtained. The dimensionless position of the nozzles is called height ratio, which is defined as follows

$$H_R = \frac{h}{H_K} \qquad\qquad 4.1$$

Which H_R is the ratio between the nozzle position to the kiln height. The injected mass flow rate is defined through the mixing ratio (M_R)

$$M_R = \frac{\dot{M}_{inj}}{\dot{M}_{main}} * 100\% \qquad\qquad 4.2$$

Where $\dot{M}_{inj}$ is the mass flow rate of air from the side injection and $\dot{M}_{main}$ is the mass flow rate of the main flow containing gas zone and ware zone.

Table 4.1: Nozzle arrangements for geometry (I)

Nozzle Arrangements	Number of nozzles	Velocity in m s⁻¹	M_R in %	H_R
i	1	34 - 203	1	0.9
ii	2	26 - 331	1 - 10	0.9
iii	2	53	2	0.5
		106	4	
iv	2	53	2	0.7
		106	4	
v	2	53	2	0.8
		106	4	

The actual assessment area begins at the axial nozzle position (x = 0) and extends over 1 m (x = 1 m). So, the mixing behaviour in relation to the distance from the location of air injection can be studied. The mixing behaviour will be quantified with the cross sectional temperature difference of the gas at different axial positions. Whereby this temperature difference is $\Delta T_o = 100\,°C$ at the main inlet of the domain.

In general, three different methods are used to present the degree of the mixing in tunnel kiln. These three methods are listed below.

1. Comparison of temperature fields (contour plot of temperature)
2. Plotting frequency distributions of temperature.
3. Calculation of maximum temperature difference of the mixture.

Figure 4.1 shows the location of the assessment area.
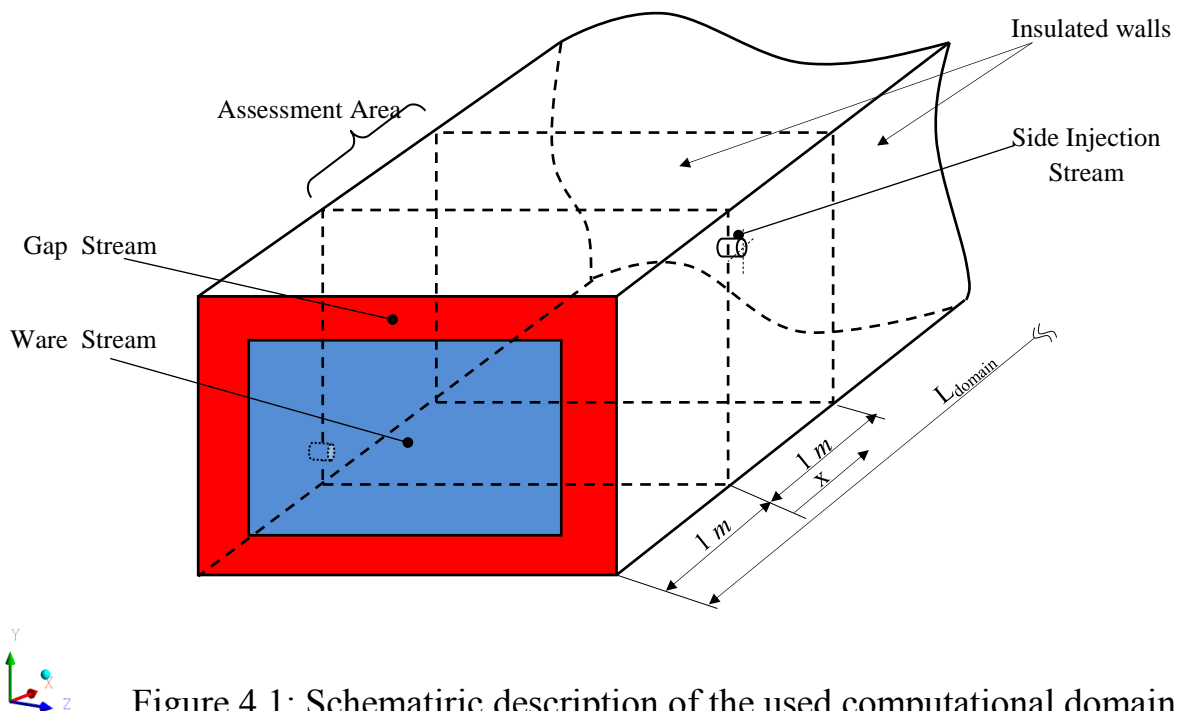
Figure 4.1: Schematiric description of the used computational domain

In this chapter, the results of 3 D simulation of a part of tunnel kiln will be presented in two cases; with and without ware. Thus, these results are divided into two main sections according to the proposed confinements.

4.2   3-D Modelling flow mixing without ware

4.2.1 Effect the velocity of side injection

The influence of the velocity of side injection for arrangements (I) and (II) is studied by different arrangements of the nozzles. At first, it is considered that:

One nozzle is established on one side, which means one side injection. In this section, the mixing ratio is constant (1%). The nozzle diameter is reduced to increase velocity of side injection. Figure 4.2 represents the influence of different injection velocities (34, 53, 94, 203 m/s) on the temperature profile.

Contours of temperature for the different velocities at the same cross sectional plane (x=0 *m*) are shown in Figure 4.2a. It can be seen that, the temperature in ware zone remains constant i.e. (300°C)

Furthermore, the effect of injection velocity is limited to gap stream. As a consequence, the gas zone region decreases with increasing the velocity of side injection. Which it can observe the alterable gap stream for the better mixing by increased the velocity from 34 m/s to 203 m/s.

To quantify the temperature homogenization more precisely. In ANSYS provides tools for computing and reporting integral quantities at surfaces and boundaries, and it could create a histogram plot (frequency distribution) of solution data (temperature). Therefore the frequency distribution of the temperature in percentage form is used.

The frequency distribution of the temperatures at x = 1 *m* is shown for the four different injection velocities in Figure 4.2b. The principle of this approach is that the frequency of temperature at the main inlet is divided between 300°C and 400°C. The side injection makes the frequency of temperature distributed between 300°C and 400°C. Therefore, if the gas zone is affected by side injection, the frequency of temperature at 400 is decreased. On the other hand, the frequency of temperature that is close to the mixture temperature is increased. An ideal mixing of the kiln atmosphere would lead the peak (frequency approaching 100%) to be at mixing temperature of 350°C. But as observed in Figure 4.2b, when the side injection velocity increases from 34 m/s to 203 m/s, the frequency of temperature drops sharply at the 400°C edge (about 25% to 0%), and rise slightly at 350°C. On the other hand, it can be seen that, a slight change in 300 °C edges.
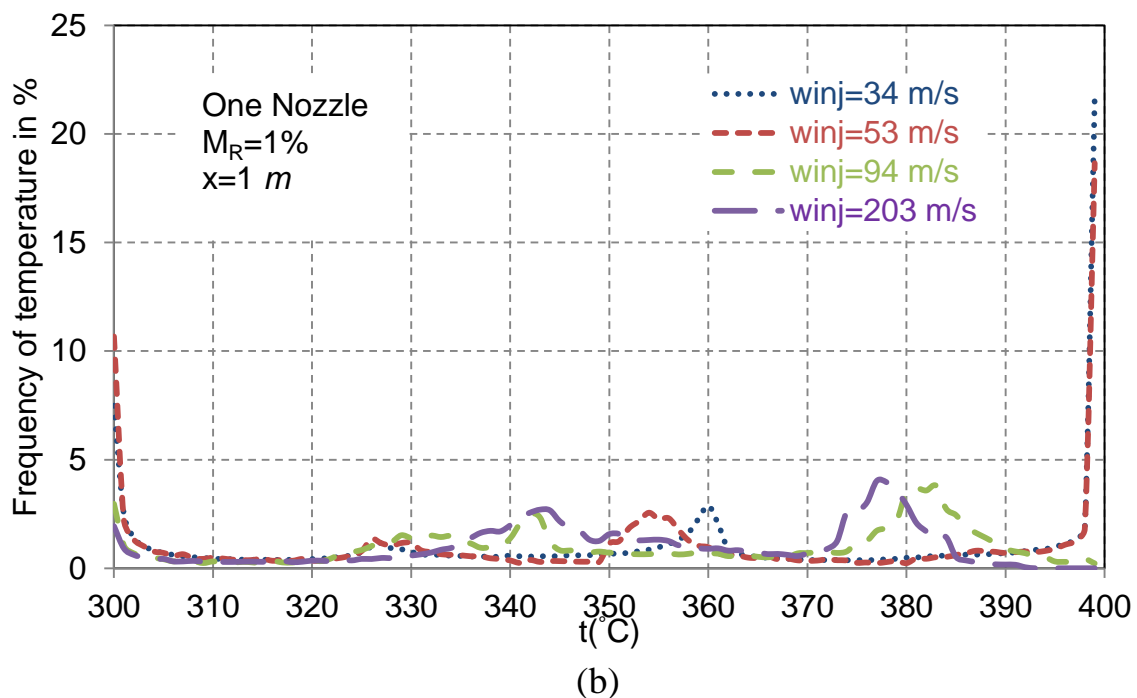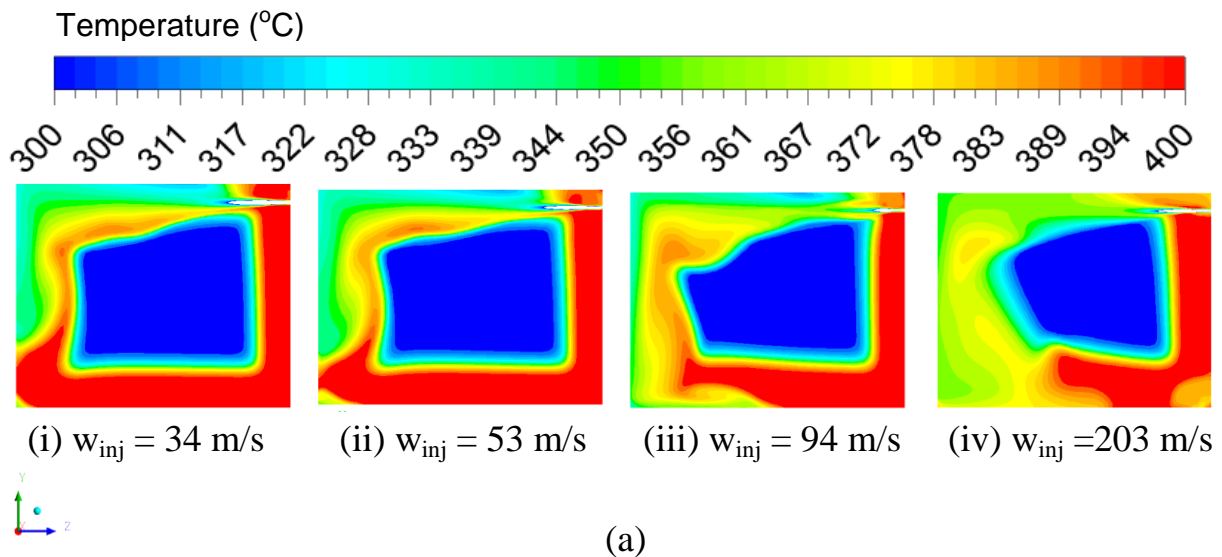
Temperature (°C)

(i) w_{inj} = 34 m/s (ii) w_{inj} = 53 m/s (iii) w_{inj} = 94 m/s (iv) w_{inj} =203 m/s

(a)

(b)

Figure 4.2: Temperature distribution as a function of w_{inj} with 1% mixing ratio and one nozzle (a) contours at x=0m (b) Temperature distribution after 1 m from side injection (x=1m)

Secondly, the influence of two nozzles at the same axial position is investigated. Figure 4.3a represents the temperature field at the position of side injection. The injection velocities 26, 47,102 and 166 m/s are studied with constant total mixing ratio M_R (1%). It can be noted that, by increasing the injection velocity, the temperature of the gas zone stream becomes closer to the average temperature, but there is a limited effect on the ware zone. As a consequence the centre (ware zone) still has the same temperature as initial. Figure 4.3b represents the frequency distribution of temperature for these velocities after1m

of side injection. It can be observed that, the width of curve decreases as the peak of the curve increasing, at the same time, it shifts closer to the average temperature of the mixture with increasing the injection velocity.
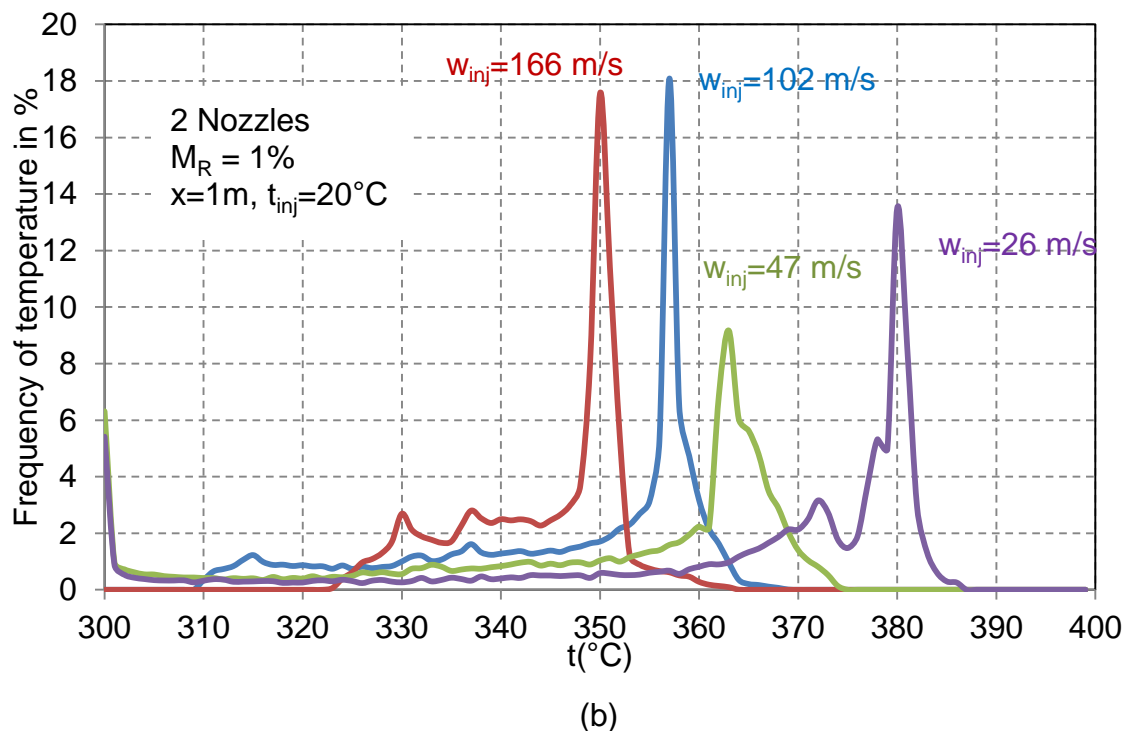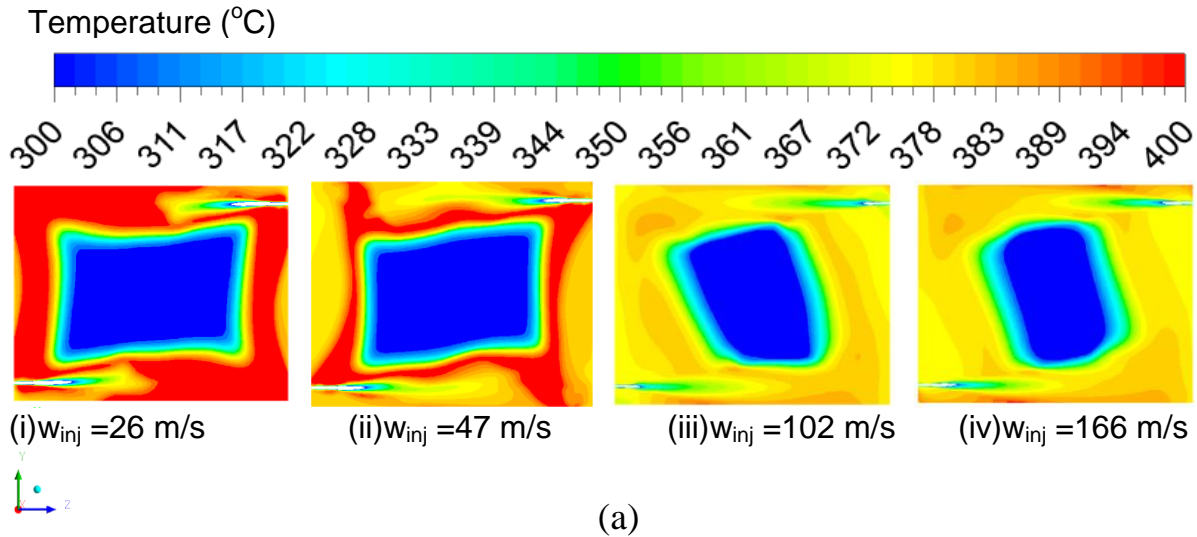
Temperature (°C)

(i)w$_{inj}$ =26 m/s   (ii)w$_{inj}$ =47 m/s   (iii)w$_{inj}$ =102 m/s   (iv)w$_{inj}$ =166 m/s

(a)

(b)

Figure 4.3: (a) Contours of temperature distribution at mixing ratio of 1%, x = 0
(b) Temperature frequency distribution, x = 1 m

In the following, the width of the temperature range will be used to express the quality or efficiency of the mixing. So, a dimensionless temperature difference θ is defined as

$$\theta = \frac{t_{max} - t_{min}}{\Delta t_o} \qquad\qquad 4.3$$

Where t_{max} and t_{min} are maximum and minimum temperature respectively and Δt_o is the initial temperature difference between gas and ware zone at the entry of the computational domain (100K).

In general, mixing depends on injection velocity and the amount of injected air. These influencing parameters can be combined with the impulse flow rate (IFR), which is defined by

$$IFR = w_{inj} * \dot{M}_{inj}. \qquad 4.4$$

Figure 4.4, represents the dimensionless temperature difference for every 25 cm from the side injection in the longitudinal direction with a mixing ratio of 1% for different impulse flow rate (IFR). From the figure, it can be noted that by moving away from the side injection in the longitudinal direction, the dimensionless temperature difference decreases, and the values of dimensionless temperature difference reduction depend on the impulse. Thus, the dimensionless temperature decreases up to $\sim$ 14% when IFR increases up to 0.22N (26-47m/s), while it becomes $\sim$31% with IFR increases up to 0.8N (26-102 m/s).
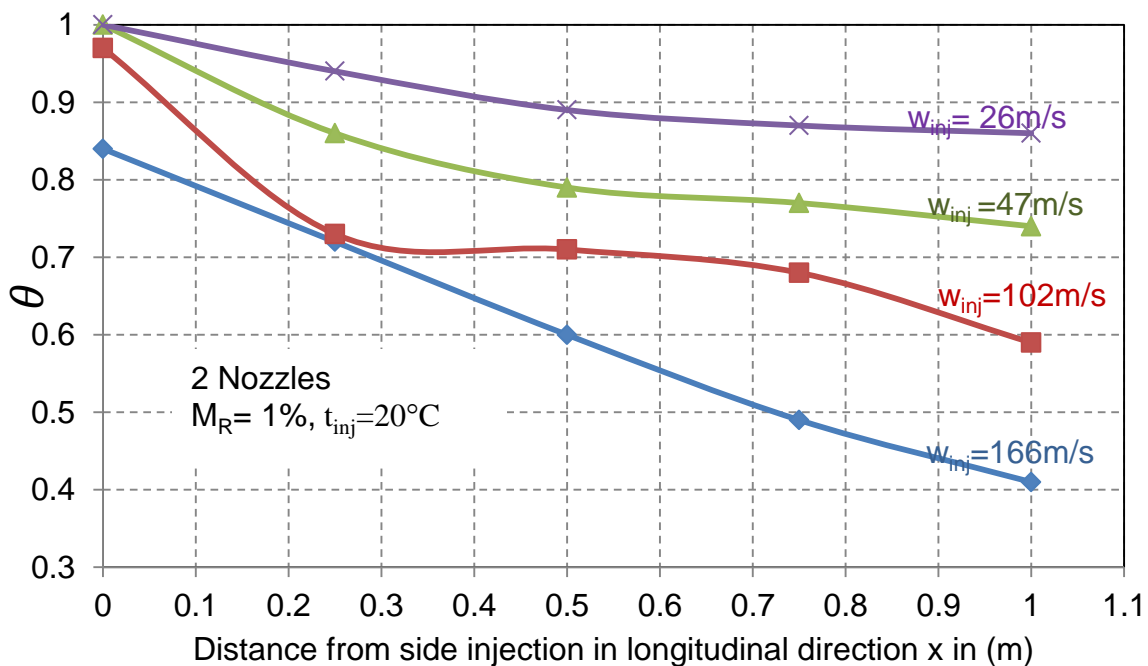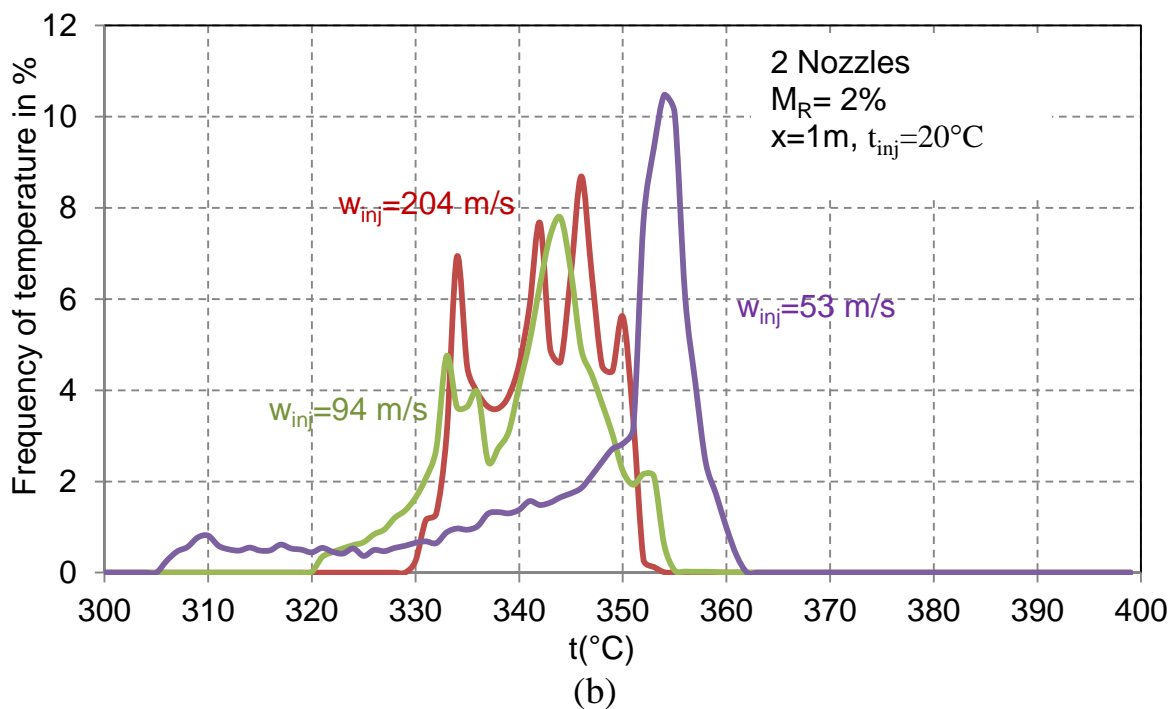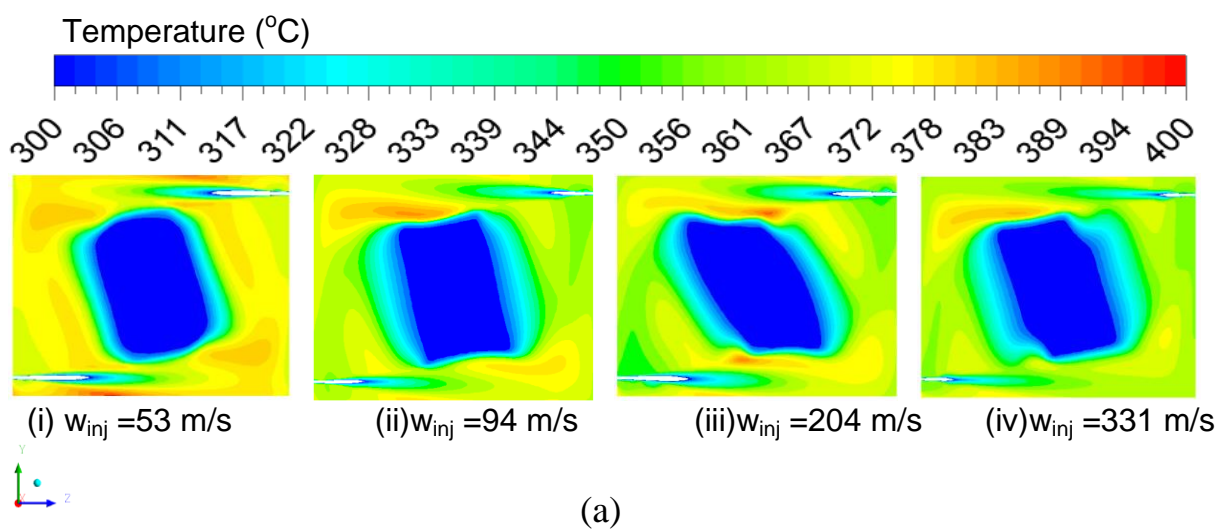

Figure 4.4: Temperature difference at mixing ratio 1%

Figure 4.5 shows the effect of injection velocity on the temperature distribution. In this part of the study, the velocity of side injection is doubled. As a consequence the mixing ratio becomes 2%. Therefore, the velocity values of side injection are 53, 94, 204 and 331 m/s. From Figure 4.5.a, It can be observed

that, the gas zone disappears with the increasing velocity of side injection, while the ware zone (core) remains at 300°C.

Figure 4.5b represents the frequency of temperature after one meter from side injection. It can be observed that for an injection velocity of 53 m/s the width of the curve is larger compared to the width of curve for other injection velocities. Furthermore, the peak is shifted to gas side. But by increasing the injection velocity, the peak is shifted to the around 350 °C and the width of the curve is decreased. By increasing the injection velocity, the peak becomes closer to the average temperature. From Figure 4.3 and Figure 4.5, it can be noted that the mixing is better in case of higher velocities.

Temperature (^{o}C)

(i) w_{inj} =53 m/s   (ii)w_{inj} =94 m/s   (iii)w_{inj} =204 m/s   (iv)w_{inj} =331 m/s

(a)

(b)

Figure 4.5: (a) Contours of temperature distribution at mixing ratio of 2%, x = 0
(b) Temperature frequency distribution, x = 1 m

Figure 4.6 represents the dimensionless temperature difference for every 25 cm from the side injection in the longitudinal direction. By moving away from the side injection in the longitudinal direction, the dimensionless temperature difference decreases. Also, it can be noted that the behaviour of temperature difference is similar to the case of 1% mixing ratio (M_R) (see Figure 4.4). The dimensionless temperature difference at velocity 53 m/s (IFR 1.14 N) and 2% M_R is 55. On the other hand, it is 59 at velocity 102 m/s (IFR 1.1N) and 1% M_R (see Figure 4.4). Although, the velocity in case of 2% M_R ratio is a half of the velocity in case of one percent mixing ratio. It can be concluded that, the dimensionless temperature difference (θ) in the previous cases is very close. And similar goes with the dimensionless temperature difference (θ) in case when velocity 94 m/s (IFR 2 N, 2%MR) and in case when the velocity 47 m/s (IFR 1.77 N, 1%MR).

Hence, the dimensionless temperature difference θ or the quality of mixing does not depend only on the velocity of the side injection but it is also related to mass flow rate.
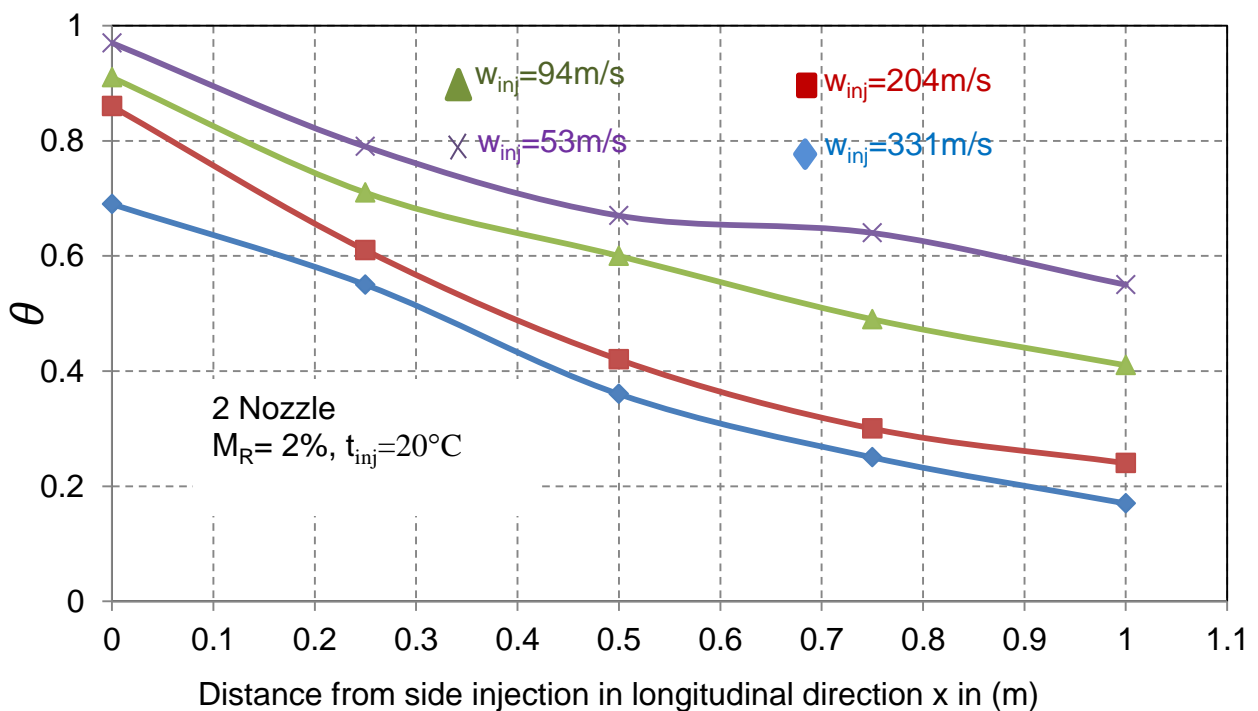

Figure 4.6: Temperature difference at mixing ratio 2%

4.2.2 Effect of mixing ratio

Figure 4.7 represents the temperature distribution be a function of the mixing ratio after 1 m from the side injection. It can be observed that, the peak of temperature distribution varies and ranges between one summit to two summits.

The peak is one summit at 1% M_R. The second summit start to grow by increasing mixing ratio till 7.8% M_R, then the peak comes back to one summit. Therefore, it is related to the mixing ratio. The width of the curve decreases with increasing the mixing ratio. The average temperature decreases at the same time due to more injected ambient air at 20 °C. Therefore, the mixing temperature of the main flow and the injected air is less than 350 °C.

In the figure, there are two peaks up to about 95 % on each side. These peaks belong to the initial temperature profile at the entry of the computational domain. The first one at 300 °C represents the temperature profile of the ware zone and the second peak at 400 °C represents the temperature profile of the gas zone. In addition, two small peaks at 350 °C represent the boundary zone between the two zones, which is related to the CFD solution.

Figure 4.8 represents the dimensionless temperature difference for every 25 cm from the side injection in the longitudinal direction with different mixing ratio and constant velocity (106m/s). The behaviour of the rate of temperature difference same as described in the Figure 4.6 (mixing ratio constant and different velocity). It can also noted that the dimensionless temperature difference is decreasing ∼14% by increasing IFR 2.5N (4%-6.2M_R). Thus the reduction ration is increased to ∼86% by increasing IFR 10.5 (1%-10.2%M_R).
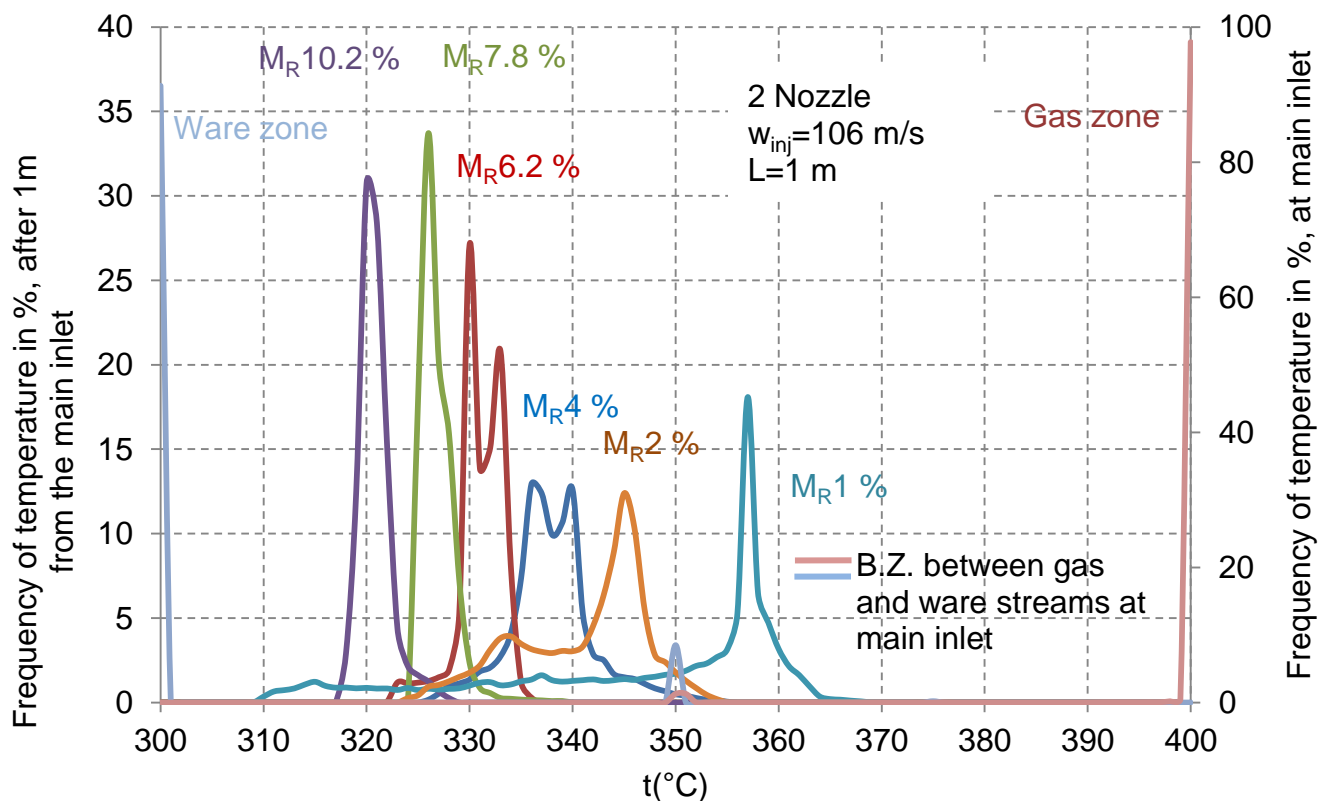

Figure 4.7: Temperature distribution at main inlet and after 1m from the side injection with constant velocity (w_{inj}=106 m/s) as a function of mixing ratio
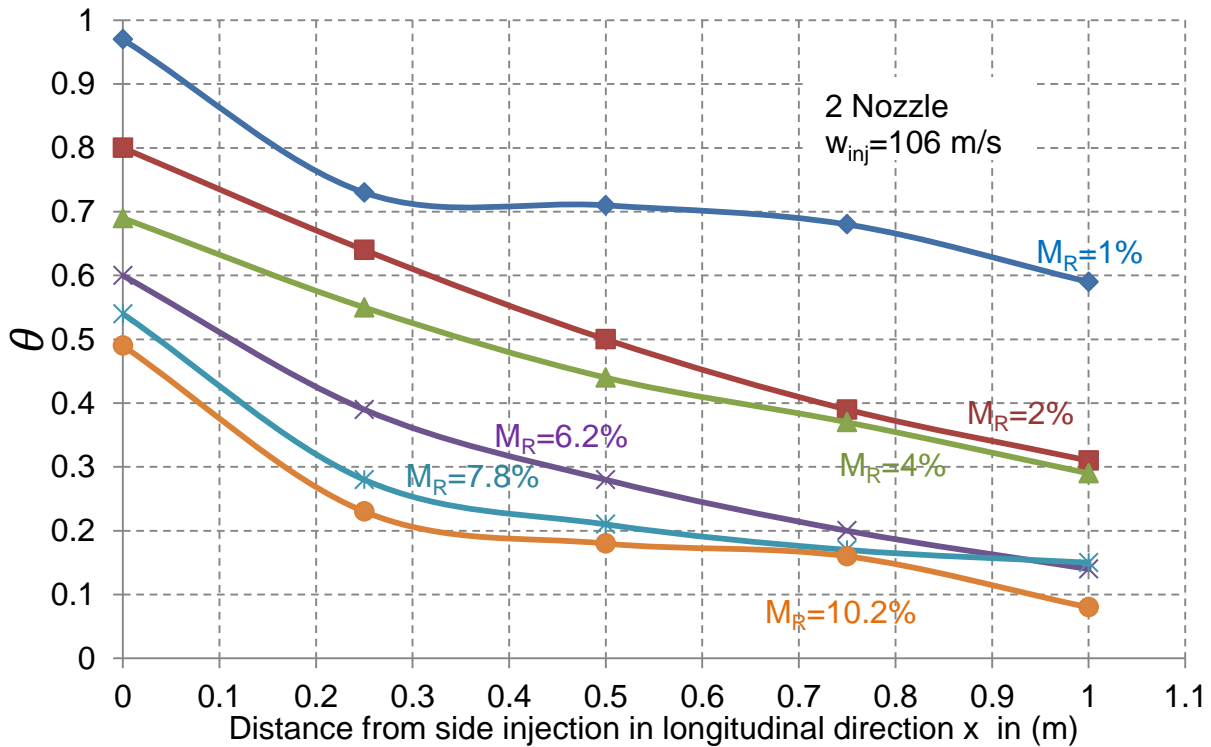
Figure 4.8: Temperature difference at constant velocity (106 m/s) as a function of mixing ratio

Figure 4.9 shows the contours of temperature distribution at the position Y=1.65m (top view). The velocity of side injection is constant 106m/s, the mixing ratio are (1%, 2%, 4%, 6.2%, 7.8%, and 10.2%).

From the Figure 4.9 (i) can be seen that, the last range of the contour line is 345 °C (colour frontier 25) at 1% M_R. The colour range (25) varies with increasing mixing ratio. It is moving in the direction of the main inlet by increasing mixing ratio. At the same time, the last contour line is decreasing till 322°C (colour frontier 13) at M_R 10.2%. As a consequence, the temperature of the mixture is decreasing with increasing mixing ratio. Furthermore, the contours of temperature have shown that, the temperature distribution becomes more homogenous with increasing M_R.
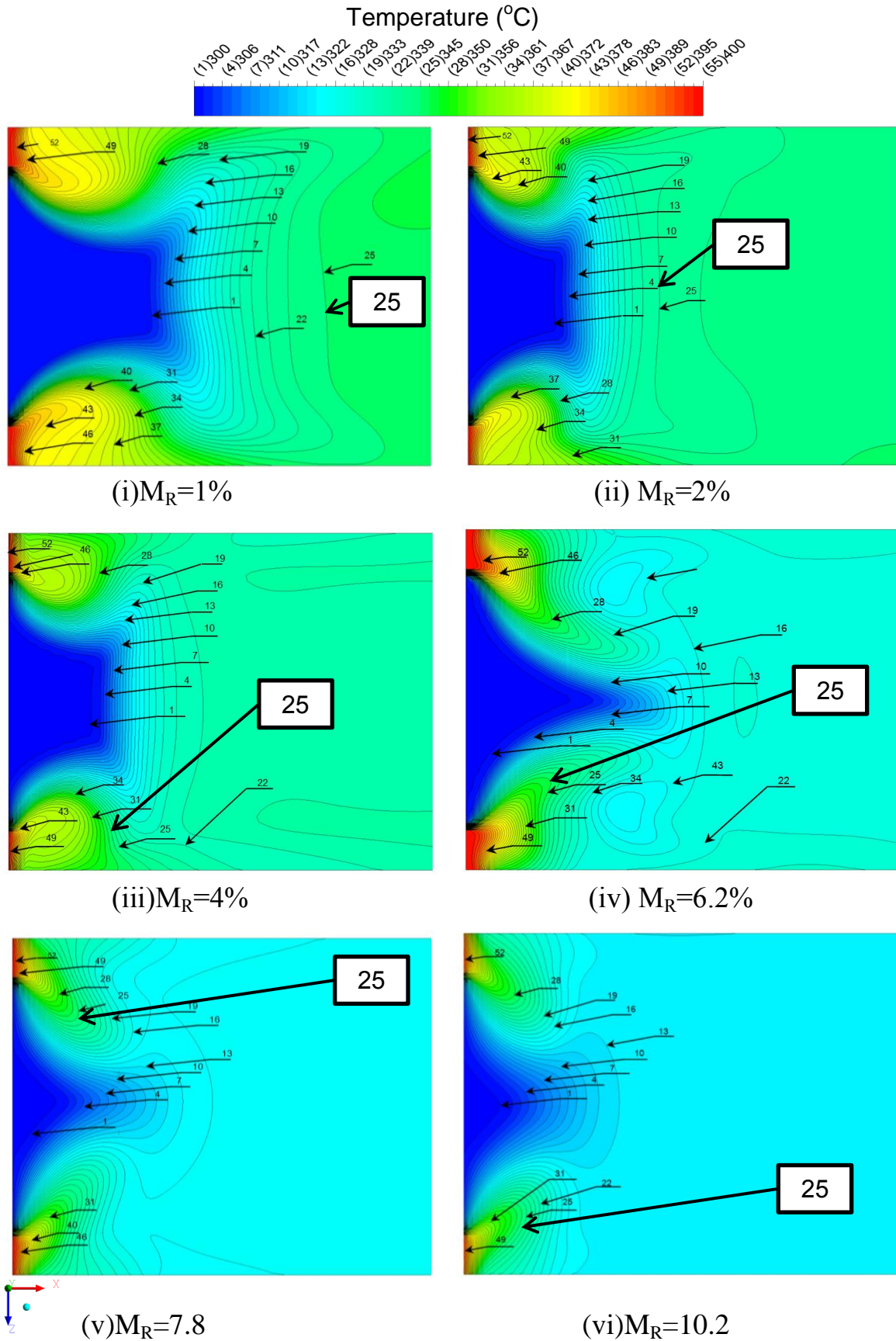
Figure 4.9: Contours of temperature distribution at Y=1.65m(top view), with constant velocity of side injection (w_{inj}=106 m/s) and different M_R

4.2.3   Effect of impulse

According to what is mentioned above (effect of velocity and mass flow rate). The mixing quality does not depend on the velocity only or on mass flow rate of the side injection. But velocity and mass flow rate complementary to each other, i.e. it always depends on the impulse of side injection.

Figure 4.10 describes the quality of the mixing terms of the dimensionsless temperature difference as a function of the IFR. Results are shown at positions x = 0.5 m and x = 1 m. The mixing ratio varied from 1 to 10.2 %. So, the Figure combined almost all previously presented results. There is a progressive decrease in the temperature difference with increasing IFR. When the IFR is less than 4 N, the curve falls sharply and the effect of the injection on the temperature homogenization is significant. For IFR more than 4 N, the curve is relatively flat and the influence of the injection decreases. If there is no injection (IFR = 0), the dimensionless temperature difference θ is 1. Thus, the maximum temperature difference between the gas stream and ware stream zone at the inlet of the domain is not reduced.
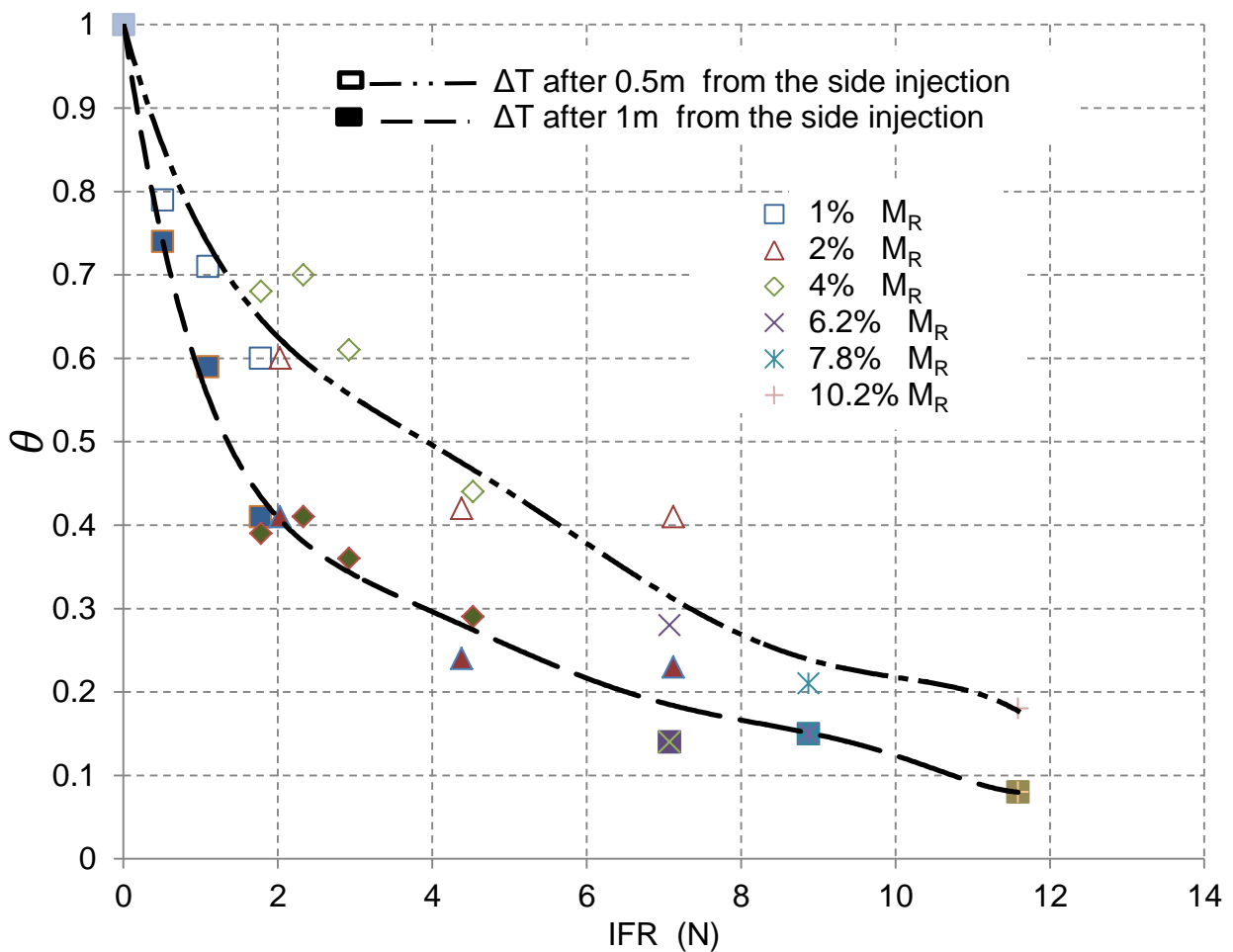

Figure 4.10: Temperature difference as a function of impulse flow rate after half, and one meter from side injection at 0.9 H_R

4.2.4 Effect of nozzle position, for constant flow velocity

The influence of the nozzle position is studied by two different ways. Here, the velocity of the ware zone is equal to the velocity of the gas zone ($w_{ware}=w_{gas}$). The position of the two nozzles at the different height ratio (H_R) is investigated with constant velocity (53 m/s) and mixing ratio (2%).

Figure 4.11 represents the contours of temperature in the cross section at the position of the side injection (x = 0). In the first arrangement, two side injection nozzles are located opposite at the same level (h=0.5 H_k), then by increasing (h), the other three arrangements are obtained. The figure demonstrates that the nozzle position has a big influence on the temperature distribution. Furthermore, it is obvious that, there is always a region with 300 °C. By increasing H_R, the gas temperature becomes more homogeneous, especially in the gas zone.

Temperature (°C)

(i) H_R=0. 5   (ii)H_R=0.7   (iii) H_R=0.8   (iv) H_R=0.9
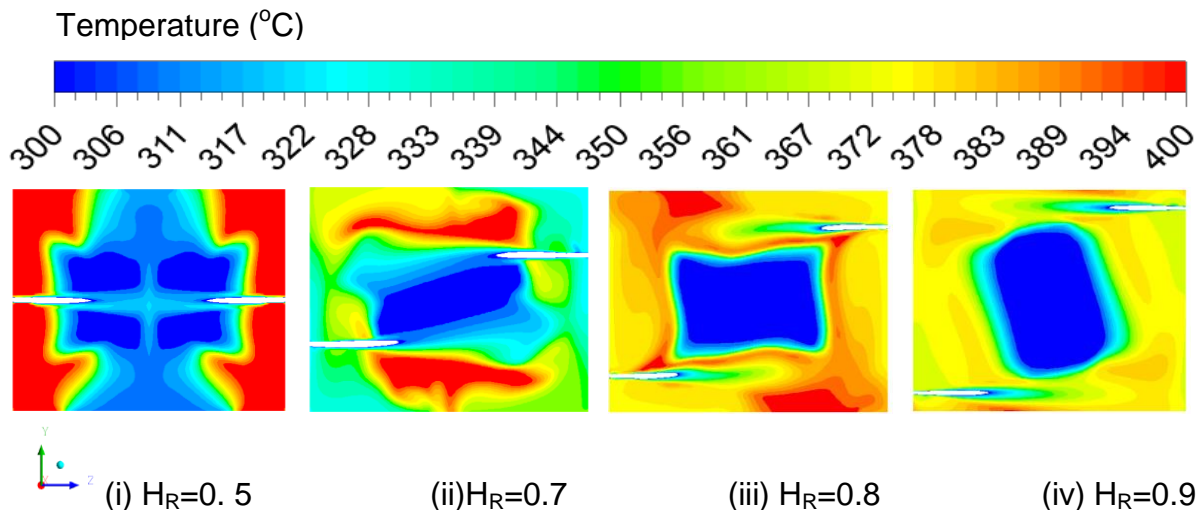
Figure 4.11: Contours of temperature distribution at (x=0m) for different H_R at 2% M_R

The frequency distribution of the temperature after 1 m from the side injection is shown in Figure 4.12. If the nozzles are located opposite at the same height (H_R=0.5), the profile shows a peak close to 400 °C. So, the gas zone is not touched everywhere and shows an area with the initial temperature of 400 °C. Only the ware zone is affected. But, related to the flat region of the curve below 400 °C, the temperature is still non homogeneous. In general, the mixing seems to be bad. By increasing the value of H_R, the maximum peak of the profiles will be shifted closer to the average temperature of about 350 °C. Moreover, the width of the curve becomes smaller and has one peak in the case of high value of H_R. As a consequence, the mixing becomes better.
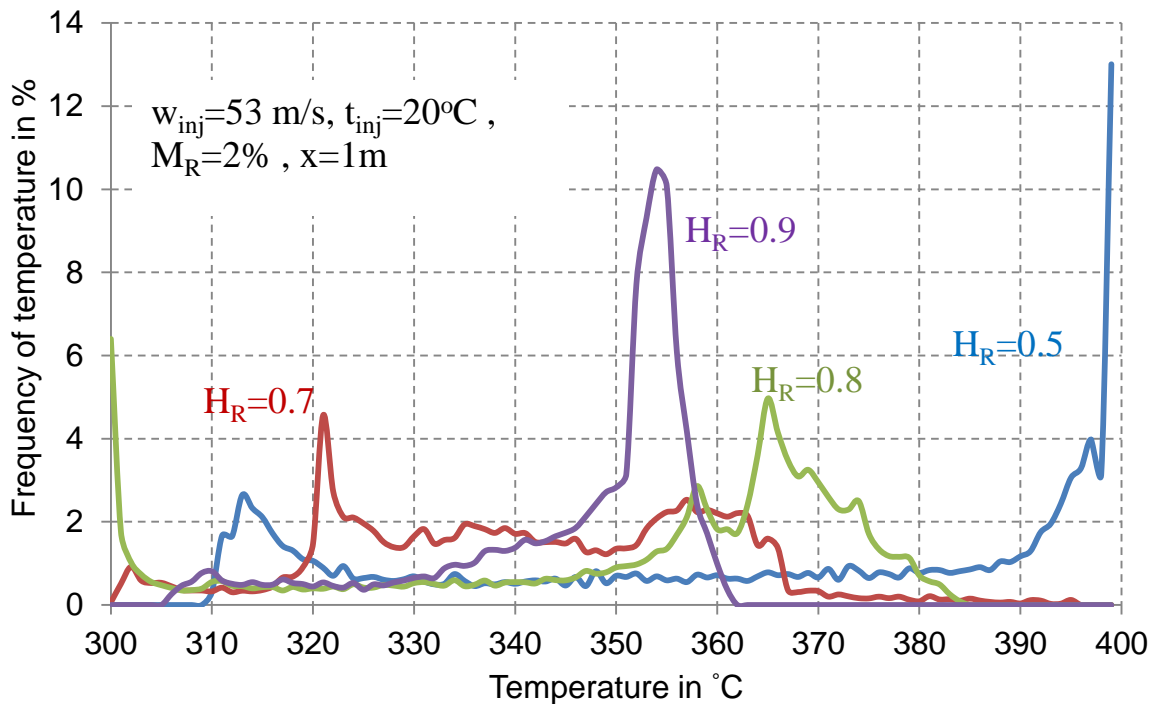
Figure 4.12: Temperature distribution after 1 m from side injection (x=1) as a function of H_R

Figure 4.13 shows the dimensionless temperature difference θ for different axial positions after the side injection while varying the height ratio. By increasing the height ratio the dimensionless temperature difference θ increases slowly till $H_R = 0.7$ and drops sharply afterwards. So, the mixing becomes more efficient with a high value of H_R. This trend is nearly the same at all axial positions.
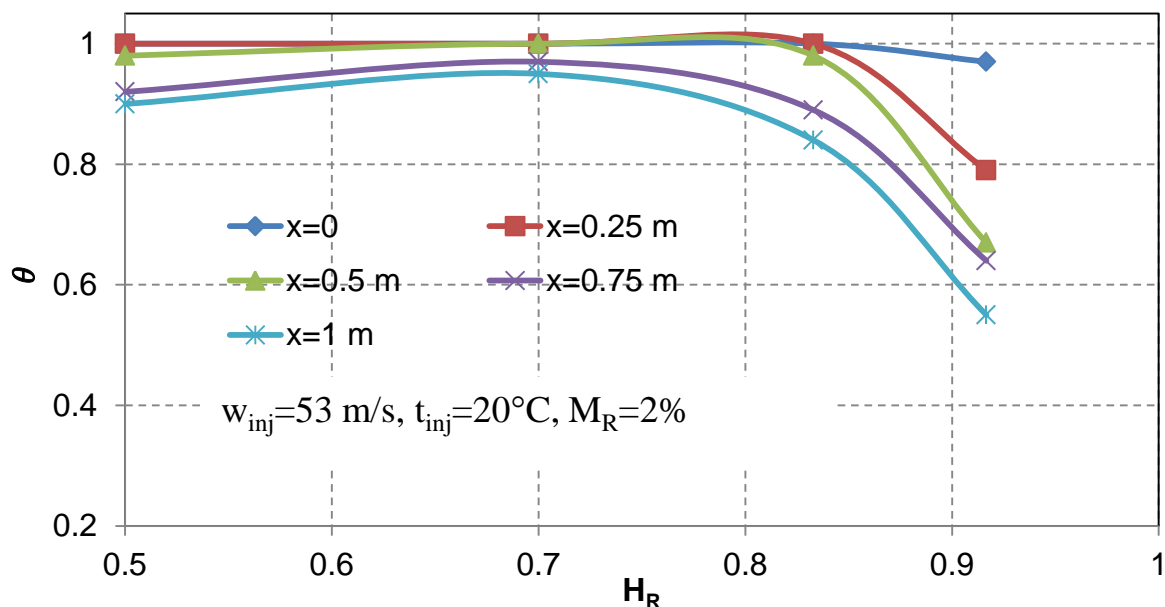
Figure 4.13: Dimensionless temperature difference as a function of H_R at different axial positions

The two nozzles with same direction are investigated and compared with opposite two nozzles (H_R=0.9) as shown in Figure 4.14 and Figure. 4.15.

Figure 4.14a show the contours of temperature distribution at x=0. It can be noted that, the region with temperature 400°C is clear at using two parallel nozzles, while it is disappeared completely at using two opposite nozzles.

Figure 4.14b shows the frequency of temperature distribution after 1m from side injection (x=1). It can be observed that, one peak is achieved by using opposite nozzles, and it is between 350 °C and 360°C. The two parallel nozzles are cause to create two summits between 320°C and 350°C. The width of the frequency curve when two opposite nozzles are used is smaller than in the case of use parallel nozzles. The temperature difference for every 25cm is shown in figure 4.15. From this figure, it can be observed that using two parallel nozzles, the temperature difference remains constant till 0.5m from the side injection (x=0.5) then it starts to decline, while, it decreases directly after the side injection with case of opposite nozzles.
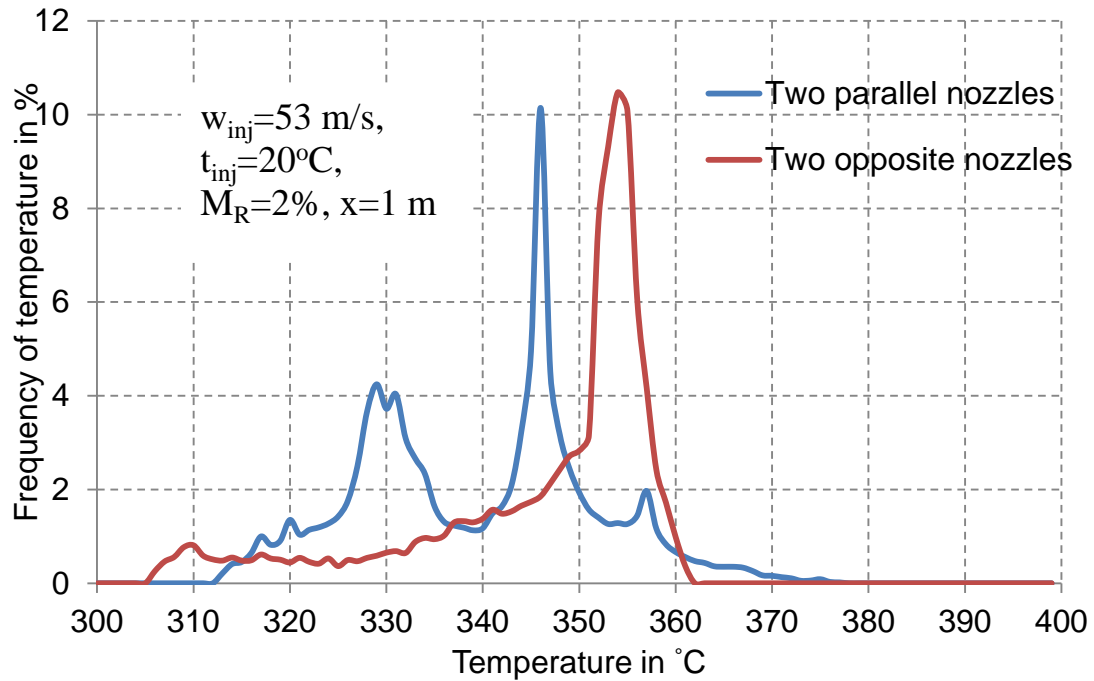
Temperature (°C)
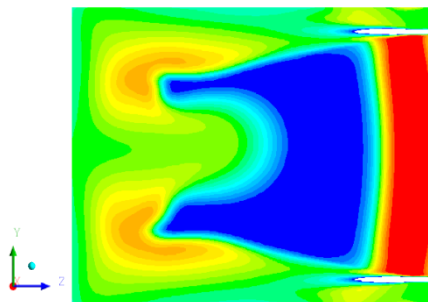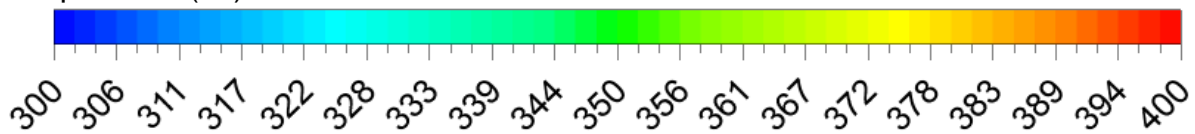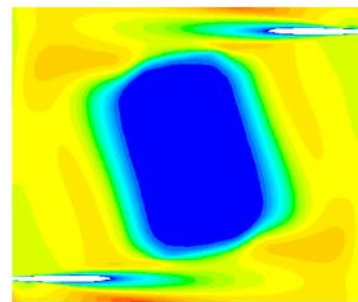
(i)Parallel nozzles   (ii) Opposite nozzles

(a)

(b)

Figure 4.14: Temperature distribution after 1 m from side injection (x=1) as a function of the direction of the side injection
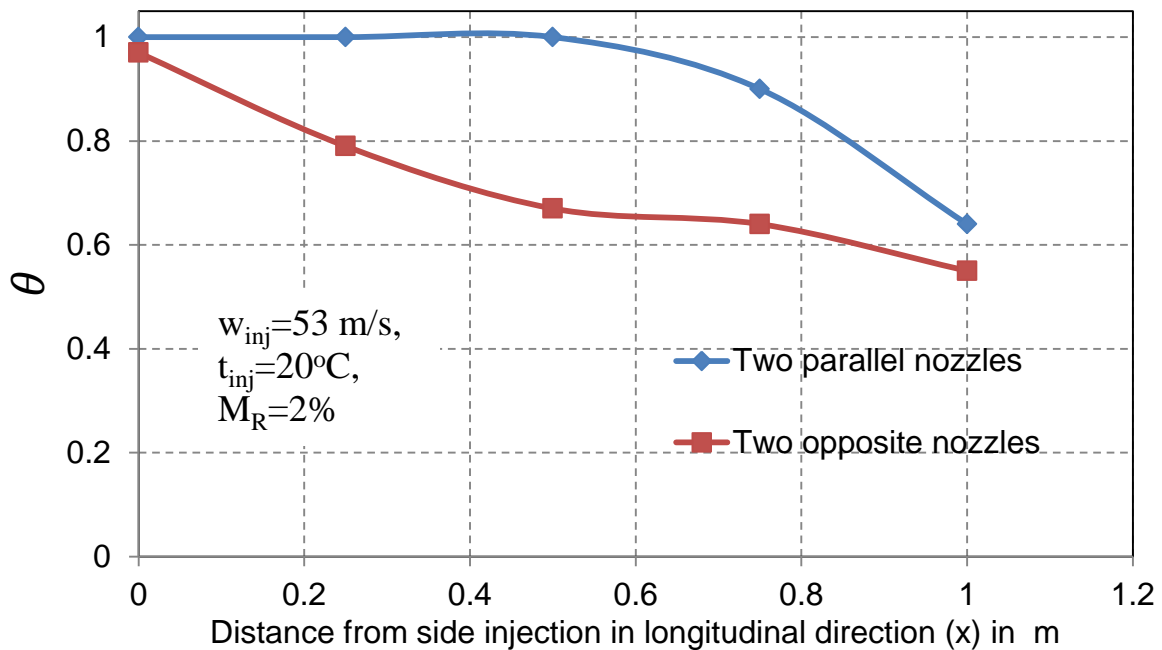

Figure 4.15: Dimensionless temperature difference as a function of the direction of the side injection at different axial positions

4.2.5 Effect of nozzle position, for different flow velocity

In this part of the study, the velocity of the ware zone is decreased to the half. The cross section area of the ware zone is equal to that of gas zone. As the total main flow rate is constant (1.663 m^3/s) in all studies, the velocity of the gas zone should be increased as same as the decreases of the velocity of the ware zone. Therefore, the velocity of ware zone is one third of the velocity of the gas zone (w_{ware} =1/3w_{gas}). Moreover, the temperature of the mixture is increased by decreasing the volume flow rate of the ware zone as shown in figure 4.16.

In general, the width of the curves decreases with increasing height ratio. As a consequence, one peak starts to grow. The mixture became more homogeneous with one peak around 370 ^{o}C, and that clearly with the highest position of side injection (H_R=0. 9).
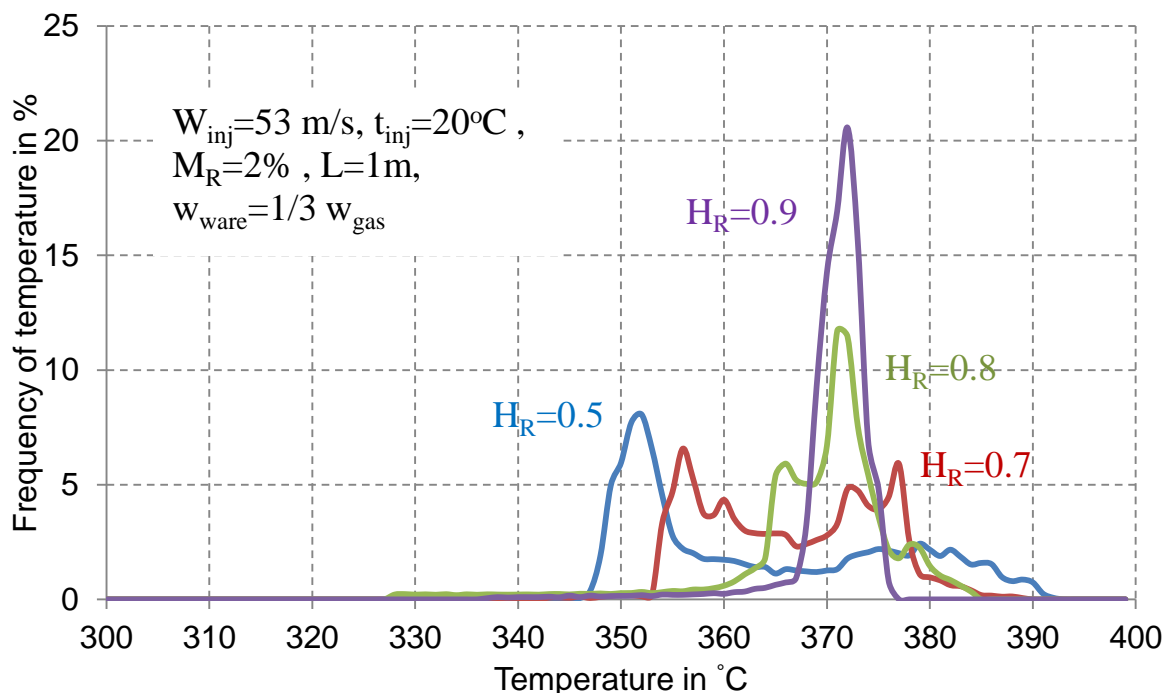

Figure 4.16: Temperature distribution after 1 m from side injection (x=1) as a function of direction of side injection

The contours of temperature distribution are represented in Figure 4.17. By comparing this figure with Figure 4.11 (w_{ware}=w_{gas}) it can be noted that the contours of temperature are divided into four regions, except in case of the last arrangement (H_R=0.9), which is divided into two regions. In this arrangement (H_R=0.9), the gas zone is disappeared for both cases. Regarding the ware zone disappears in the first (H_R=0.5) and in the fourth (H_R=0.9) arrangement when w_{ware}=1/3w_{gas}.
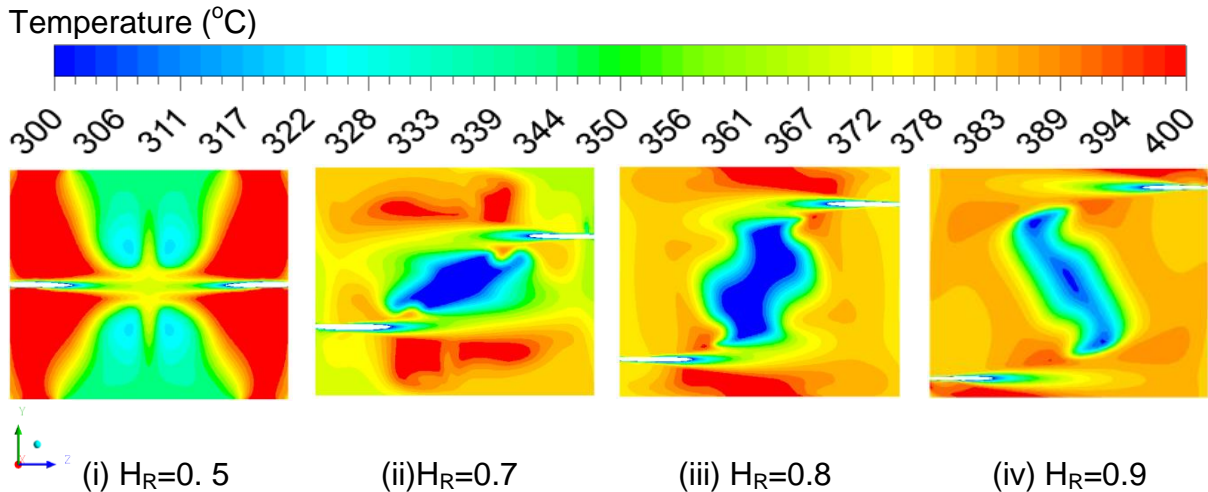
Temperature (^{o}C)

(i) H_R=0. 5   (ii)H_R=0.7   (iii) H_R=0.8   (iv) H_R=0.9

Figure 4.17: Contours of temperature distribution at (x=0m) for different H_R at 2% M_R and w_{ware}=1/3w_{gas}

Figure 4.18 represents the dimensionless temperature difference θ for every 25 cm from the side injection in the longitudinal direction with different height ratio (H_R). In general,it could be realized that the behaviour of the dimensionless temperature difference θ improves in the longitudinal direction by comparing with Figure 4.13 (w_{ware}=w_{gas}). Furthermore, from Figure 4.18, it can be noted that, the height of side injection (H_R) has a small effect in this case (w_{ware}=1/3w_{gas}), but still the higher position of side injection (H_R=0.9) gives the better mixing with taking the consideration of the slight changing.
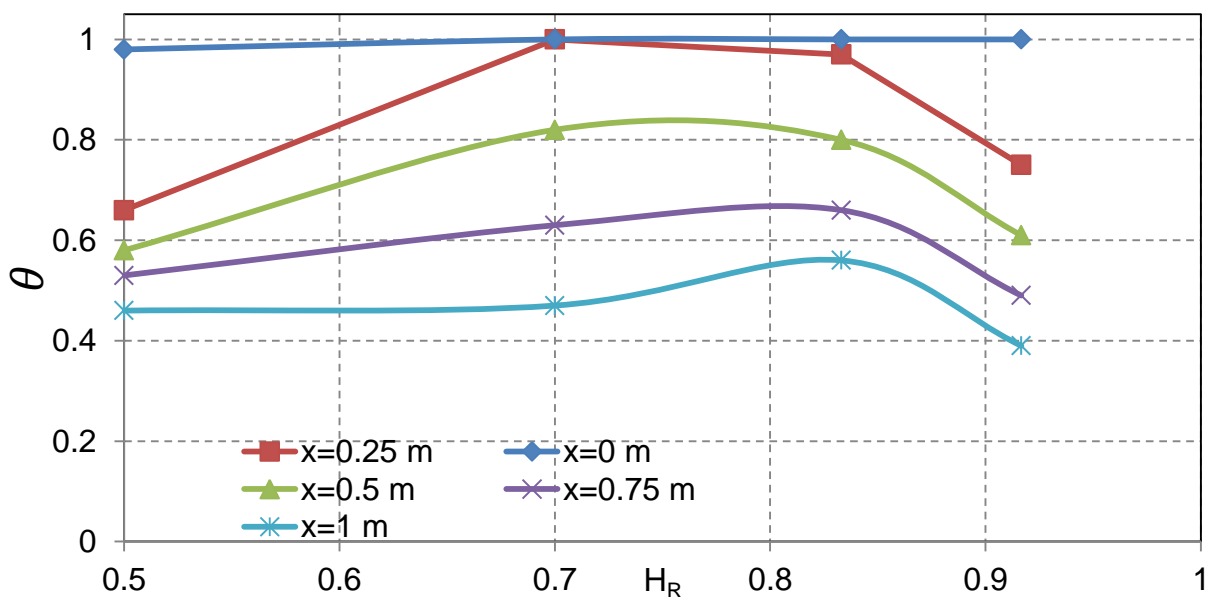

Figure 4.18: Dimensionless temperature difference as a function of H_R at different axial positions at w_{ware}=1/3w_{gas}

4.2.6 Effect of relative velocity of ware zone to gas zone (w$_r$)

Figure 4.19 demonstrates four contour plots for the different relative velocity of ware to gas zone(w$_r$). The volume flow rate (1.663 m^3/s) and the mixing ratio (2%M$_R$) are constant. This figure shows that, for small w$_r$ there is a good mixing. The ware zone starts to be more clear with increasing relative velocity.
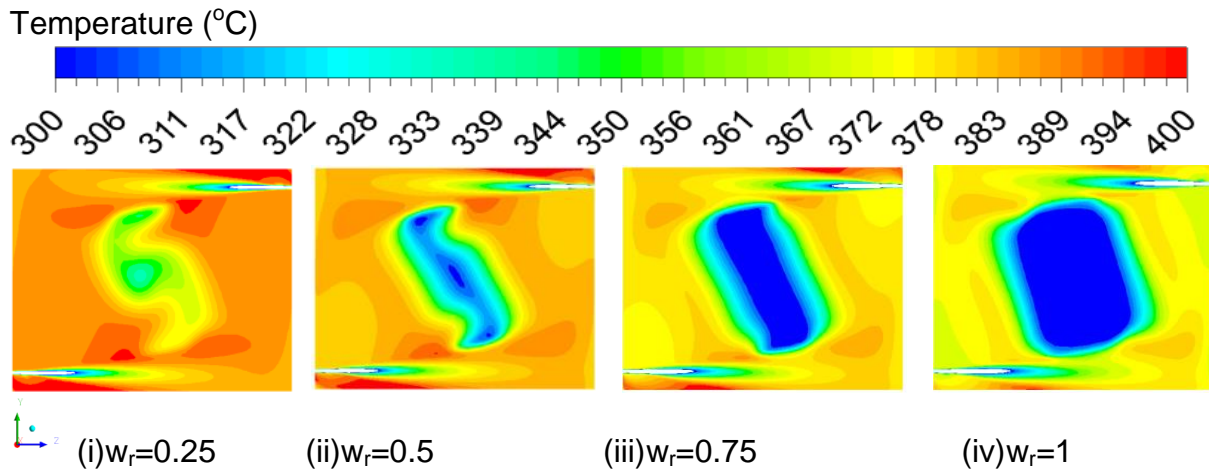
Temperature (°C)

(i)w$_r$=0.25   (ii)w$_r$=0.5   (iii)w$_r$=0.75   (iv)w$_r$=1

Figure 4.19: Contours of temperature distribution for different Wr with 2%M$_R$

Figure 4.20, shows the frequency of temperature distribution after 1 m from side injection with different w$_r$. This figure shows that as the value of w$_r$ increases the peak value decreases and it shifts to ware side. Thus the mixture temperature decreases. Furthermore, the width of the curve increases with increasing the value of w$_r$. This means that the mixing is better for the small value of w$_r$.
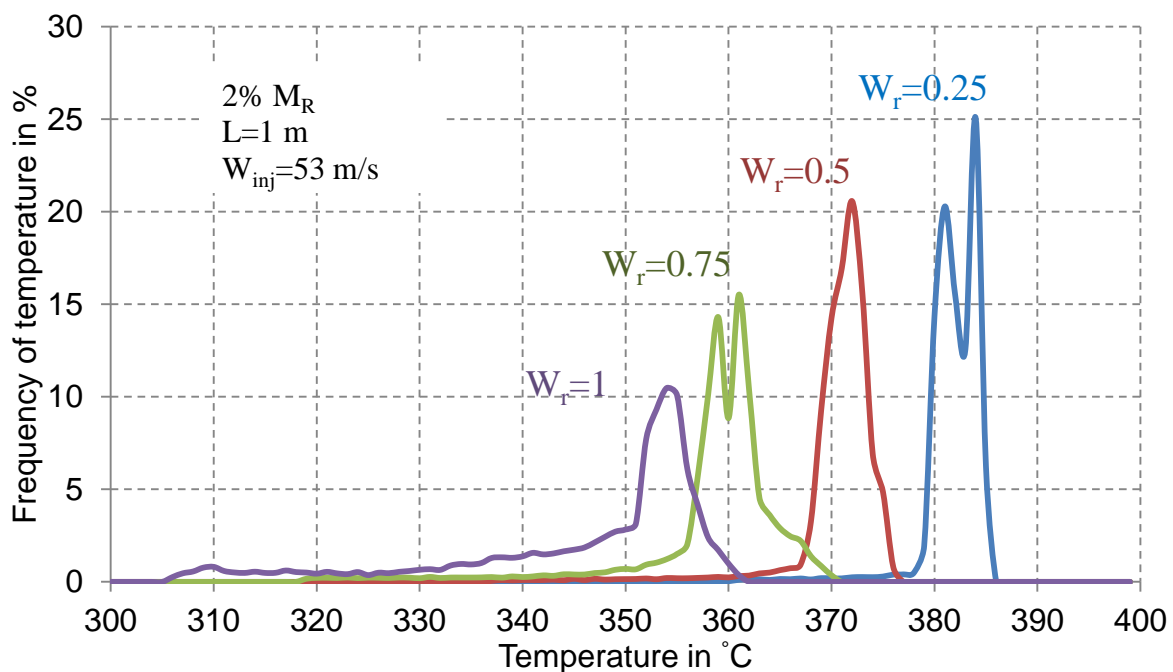

Figure 4.20: Temperature distribution after 1 m from side injection, with M$_R$= 2%.

Figure 4.21, represents the dimensionless temperature difference θ for every 25 cm from the side injection in the longitudinal direction with different w_r. In general, by increasing the w_r, the temperature difference increases. The curves have the same tendency for all values of w_r except at x=0. Also, it can be concluded that, the rate of temperature difference decreases with moving away from the side injection and the minimum occurred at w_r=0.25 and x=1 m which indicated there is good mixing.
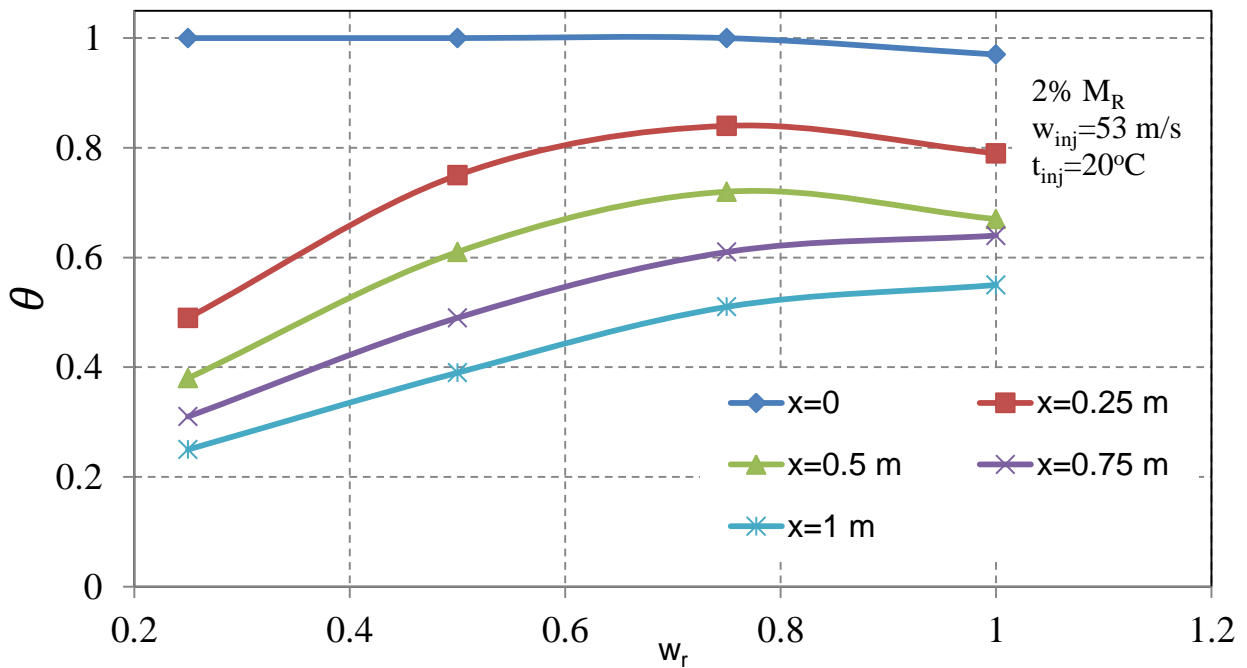

Figure 4.21: Effect of ware to gas relative velocity on the temperature difference with M_R 2%

4.2.7 Effect of injection temperature

Two different injection temperature low and high 20°C and 350°C respectively have been studied. The first temperature (20°C) represents the ambient temperature, while the second (350°C) represents the average temperature of the mixture. The mixing ratio (M_R) is constant 4% and the impulse flow rate (IFR) is also constant 4.54 N.

Figure 4.22 shows contour plots of the temperature distribution at a height of 1.65 m (top view). It is clearly obvious from the Figure 4.22(a) that the last range of the contour line is $\sim$ 350°C (28), while it is moving in the direction of the main inlet by injecting air at temperature 20°C. Figure 4.22b shows the last range of the contour line is $\sim$337°C (21). This is a proof that the mixture temperature is decreasing with increasing temperature of the side injection. Regarding the quality of the mixing, it has the same behaviour for the both injection temperatures.
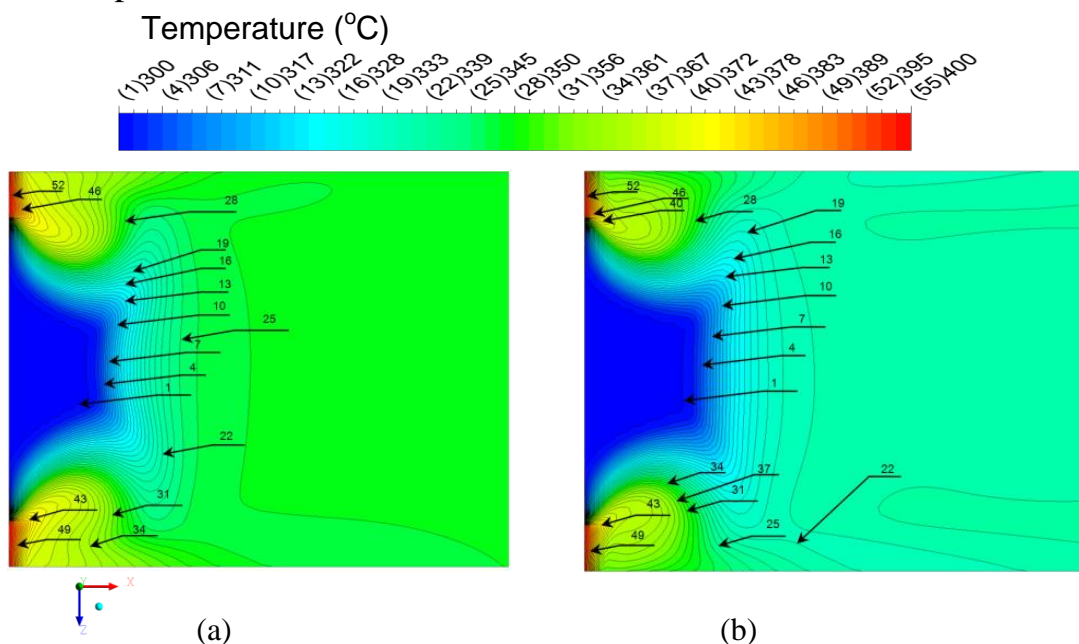

Figure 4.22: Contours of temperature distribution at Y=1.65m, with M_R=4% and IFR =4.54 N (a) t_{inj}=350 ^{o}C,(b) t_{inj}=20°C

Figure 4.23, represents the frequency of temperature distribution after 1 m from side injection for two different temperature injection (t_{inj})with the same impulse. This Figure shows that as the injection temperature increases, the peak of frequency of temperature distribution increases. Furthermore, the width of the curve is nearly the same for the both cases. In other words, it can be concluded that the injection temperature does not affect on the mixing quality.
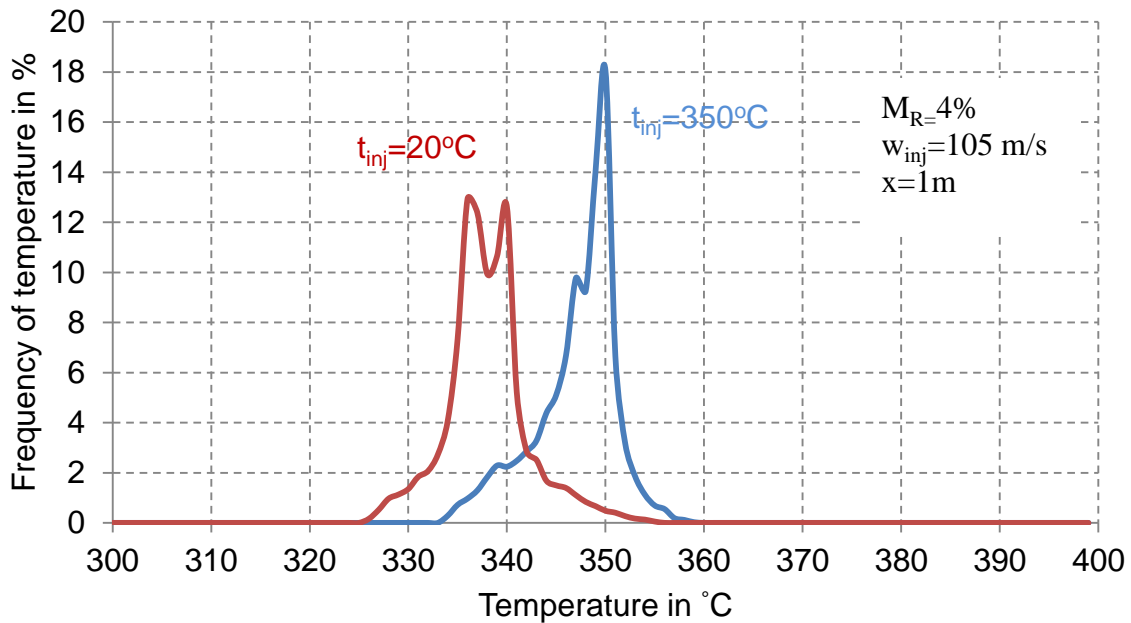
Figure 4.23: Temperature distribution after 1 m from side injection with
$M_R=4\%$ and IFR $=4.54$ N

Figure 4.24 represents the dimensionless temperature difference θ as a function of temperature of side injection in the longitudinal direction from the side injection with a constant mixing ratio and impulse flow rate. By moving away from the side injection in the longitudinal direction, the ratio of temperature difference decreases. Moreover, there is no effect of the injection temperature on the temperature difference.
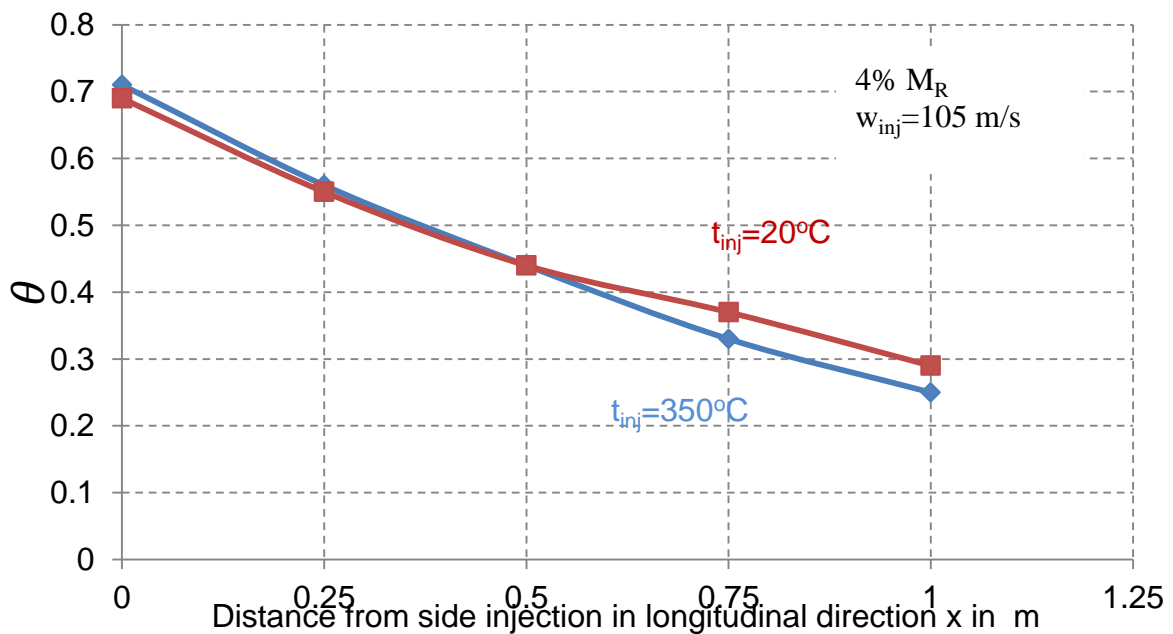

Figure 4.24: Temperature difference for every 25 cm from side injection with
$M_R=4\%$ and IFR $=4.54$ N

4.2.8 Effect of cross section area

The effect of cross sectional area is divided in two sections, the first section is the effect of the cross section area of the ware zone on the mixing quality. This effect will be studied and discussed in the section 4.3.

The second section is the influence of kiln geometry. A four different kiln geometries with same volume has been proposed, the geometric dimensions are mentioned before in chapter three sections 3.10.1 table 3.1.

Figure 4.25, represents four different kiln geometries to study its effect on the gas mixing when mixing ratio is 2%. In this figure, the total volume of the kiln is constant in all cases. Therefore, the ratio between kiln width and height ($G_{k,R}$= kiln geometrical ratio=B_k/H_k) is changing for this purpose. Furthermore, the ratio between height and width depend on the product shape. Four kiln geometries with ($G_{k,R}$ = 1.2, 1.9, 2.73 and 3.72) have been studied. The first plot for ($G_{k,R}$ =1.2) shows that the mixing is more homogeneous in the whole cross section. By increasing the ratio ($G_{k,R}$), the mixing is getting better in the middle of the kiln cross section, but it is worst near the side walls. On the other hand, by increasing the $G_{K,R}$, the ware zone starts to demise, but at the same time, a high temperature region is established in the gas zone, and that lead to the increased temperature difference inside the kiln.
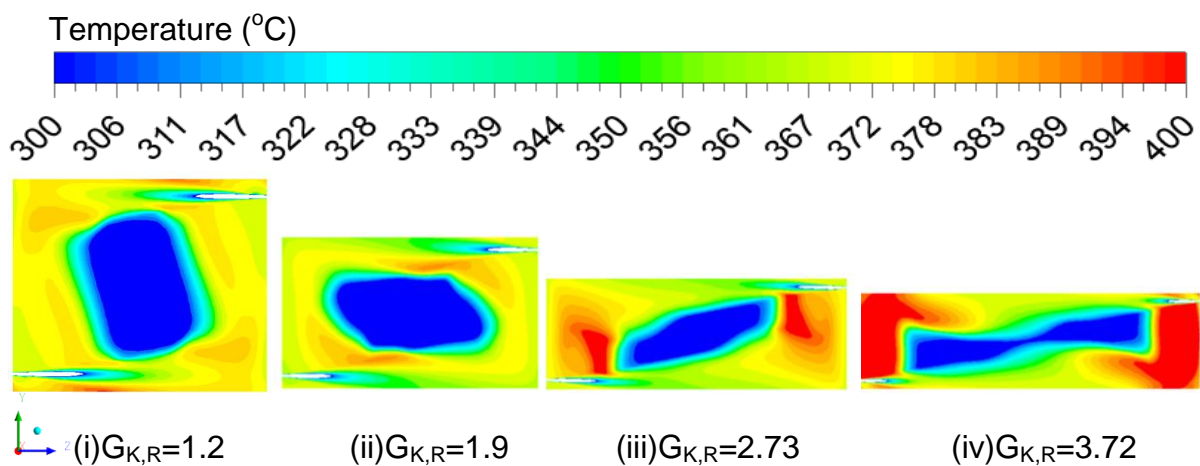

(i)$G_{K,R}$=1.2   (ii)$G_{K,R}$=1.9   (iii)$G_{K,R}$=2.73   (iv)$G_{K,R}$=3.72

Figure 4.25: Contours of temperature distribution for different $G_{k,R}$, with 2% M_R

Figure 4.26 shows the frequency of temperature distribution after 1 m from side injection (x=1m) with different $G_{k,R}$. The figure shows that as the value of $G_{k,R}$ increases the peak value decreases. Furthermore, the width of the curve is increasing with the increasing value of $G_{k,R}$. This means that the mixing is better for the small value of $G_{k,R}$.
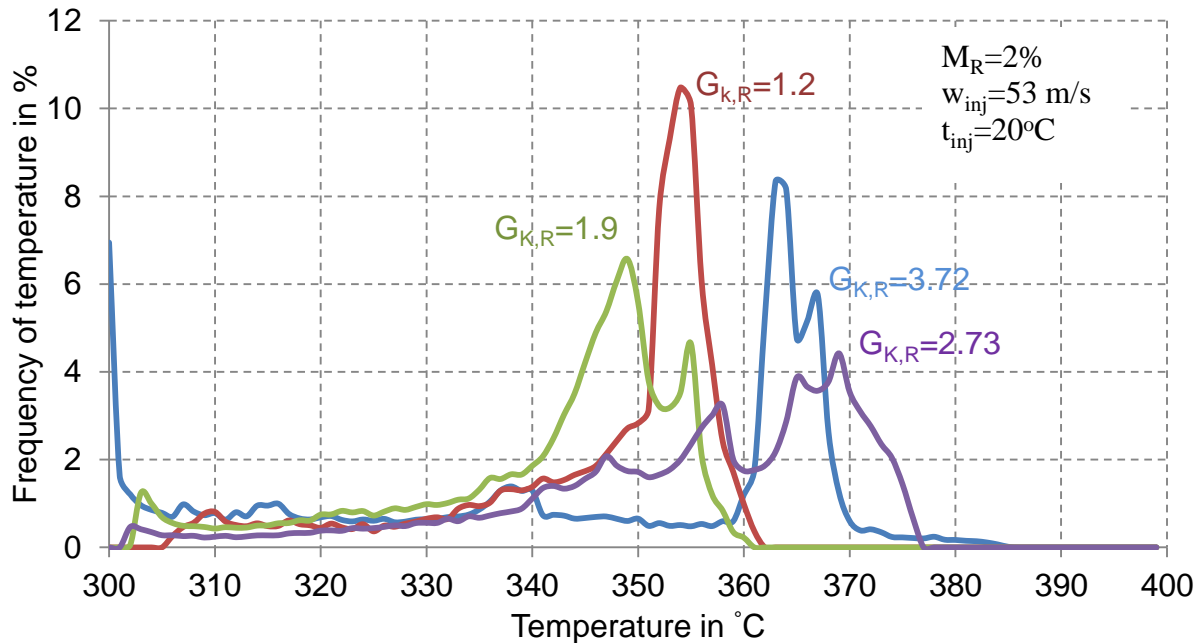

Figure 4.26: Temperature distribution after 1 m (x=1m) from side injection with different $G_{k,R}$

Figure 4.27 represents the dimensionless temperature difference θ for every 25 cm from the side injection in the longitudinal direction with different $G_{k,R}$. By increasing the $G_{k,R}$ values, the temperature difference ratio increases and the curves nearly have the same tendency. Also, it can be concluded that, the rate of temperature difference ratio decreases with moving away from the side injection and the minimum occurred at $G_{k,R}$ =1.2 and x=1 m.
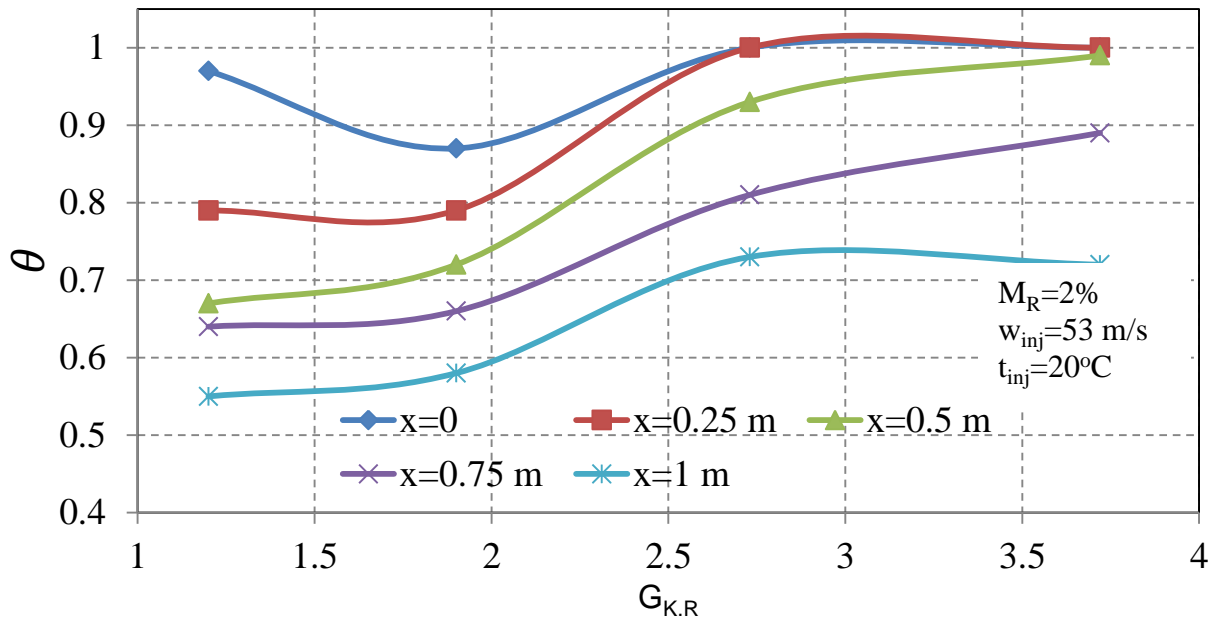
Figure 4.27: Temperature difference for every 25 cm from side injection with mixing ratio 2% as a function of width to the height ratio ($G_{k.R}$)

4.2.9 Nozzle geometry

In addition to dimensions kiln, two different nozzle geometries have been studied by changing the shape of the cross section area of side injection from circle to square with keeping the cross section area constant. Figure 4.28 shows the effect of nozzle geometry on frequency of temperature distribution for two different mixing ratios. It can be concluded that the shape of the nozzle cross section area has no influence on the mixing quality.
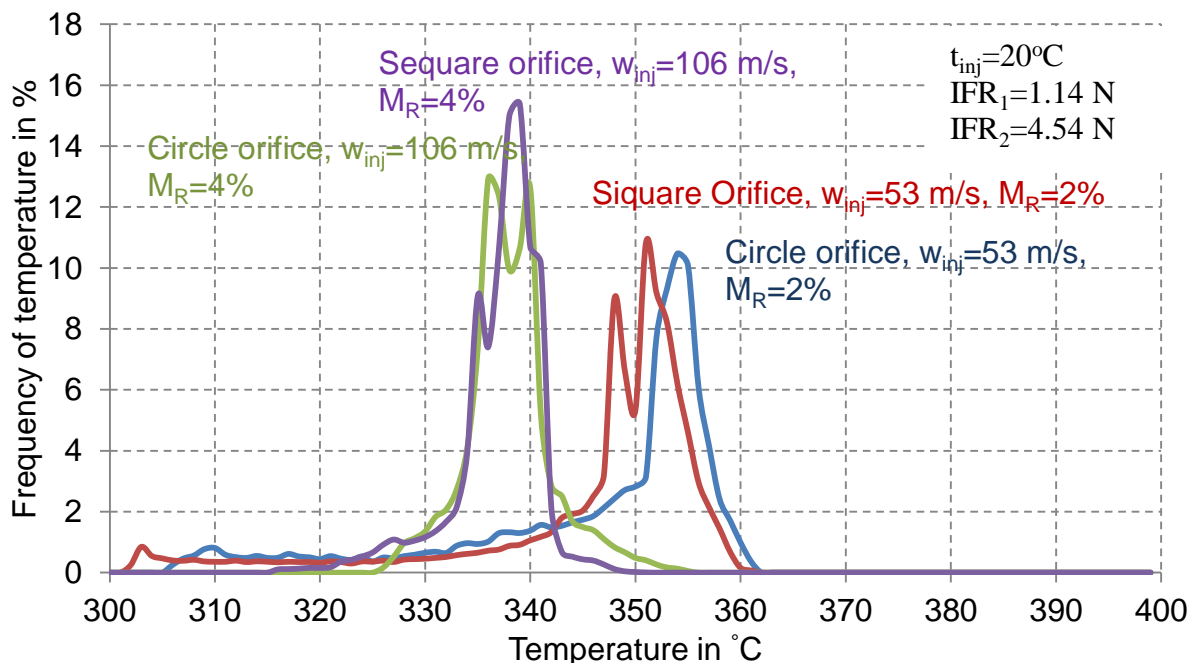

Figure 4.28: Temperature distribution after one meter from side injection (x=1m) as a function of shape of side injection, with impulse IFR=1.14 N and IFR=4.54 N

4.3 3-D Modelling of flow mixing with ware

4.3.1 Introduction

The effects of ware on the quality of the mixing has been studied in this section. The first stack of bricks are placed after one meter from the side injection. There are two other stacks which are placed with one meter between each one of them. The stacks are proposed as porous zone and the porosity for each blade of bricks is 0.22. The cross-section area of the stack always is equal to the cross-section area of the ware zone at the main inlet. Therefore, the number of the blades are variable and are always related to cross-section area of the ware zone. Two opposite nozzles are used in this study. The area of assessment starts directly after side injection. Figure 4.29 shows the schematic description of the used computational domain with ware.
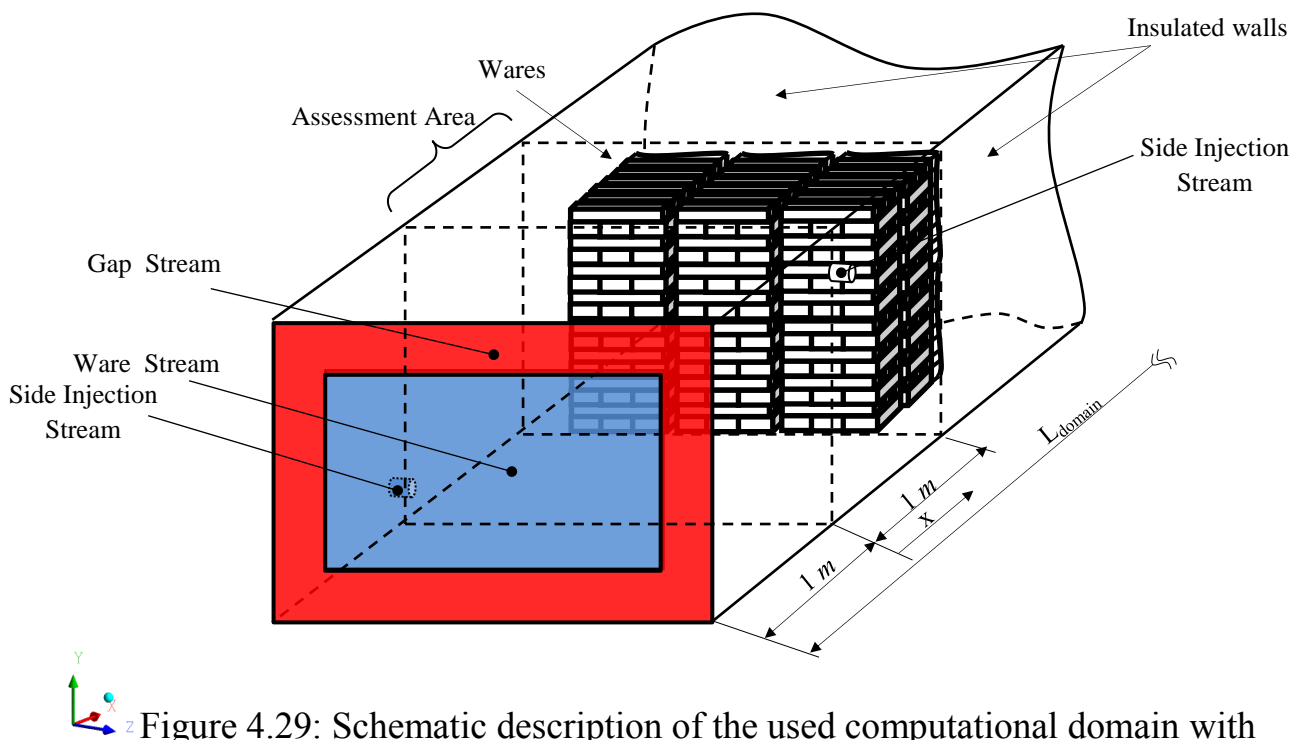

Figure 4.29: Schematic description of the used computational domain with ware

4.3.2 Effect of cross-sectional area of the ware zone

Three different product dimensions for geometry (I) have been studied as listed in table 4.2. In the first arrangement, area of ware and gas zone is equal ($A_{ware}=0.5A_{total}$). Then by increasing the product dimensions the other two arrangements are obtained. The volume flow rate of the main flow and side injection are 1.663 m^3/s and 0.033 m^3/s respectively. As a consequence of   the increasing cross section area of ware by keeping the main flow constant, the velocity of ware zone will decrease at the same time as the velocity of gas zone increased.

Table 4.2: Kiln Geometrical (I) Parameters

Geometry	b_w, m	h_w, m	A_R
i	3	2.2	0.5
ii	3.3	3	0.75
iii	3.606	3	0.81

Figure 4.30 demonstrated the velocity distribution along different height (Y level) with 2% mixing ration and 53m/s velocity of side injection. From the figure it can be noted that, the lowest velocity distribution around the product is found at Y level =1.65 m. Therefore, it is adopted to show the influence of the parameters.
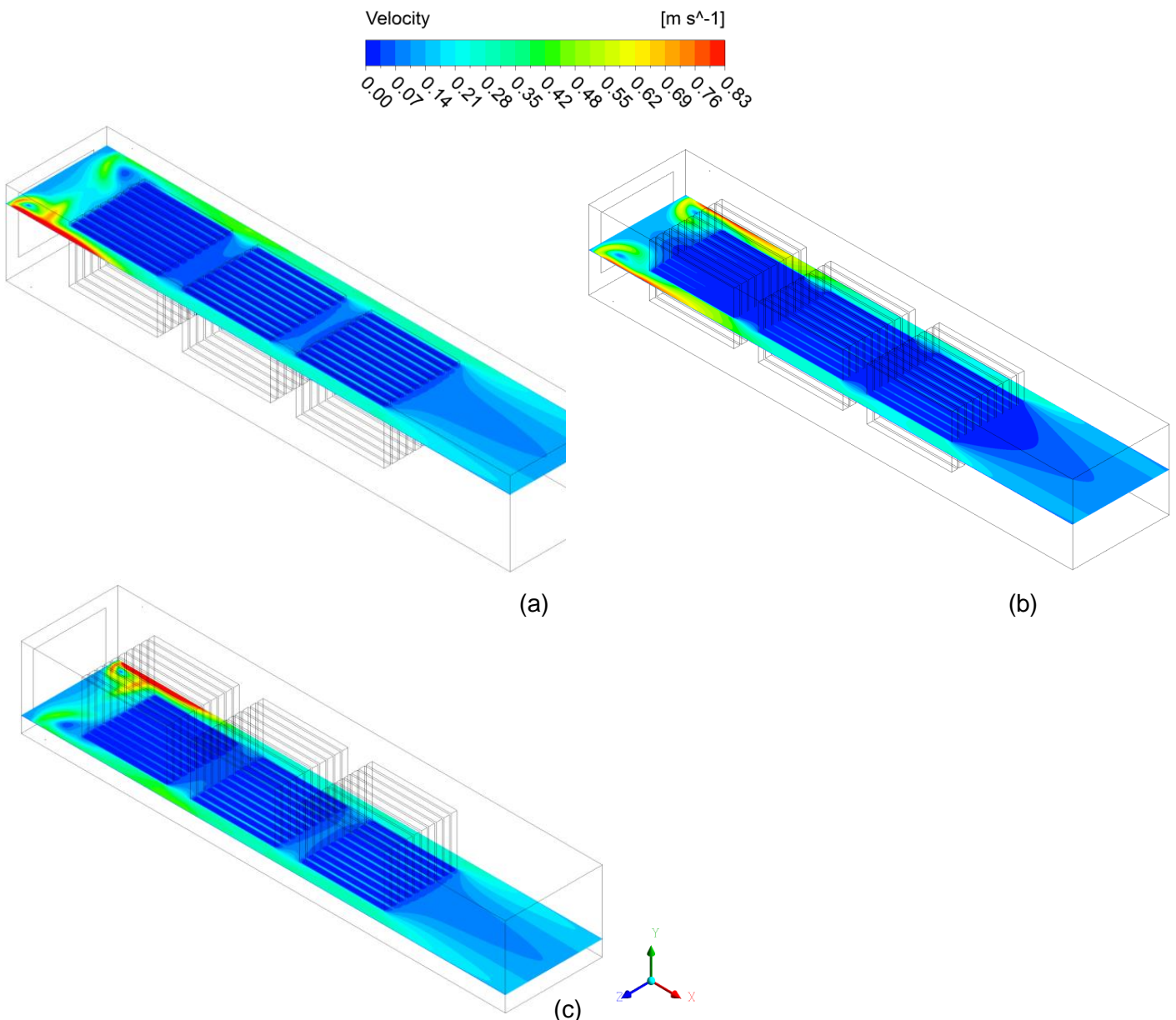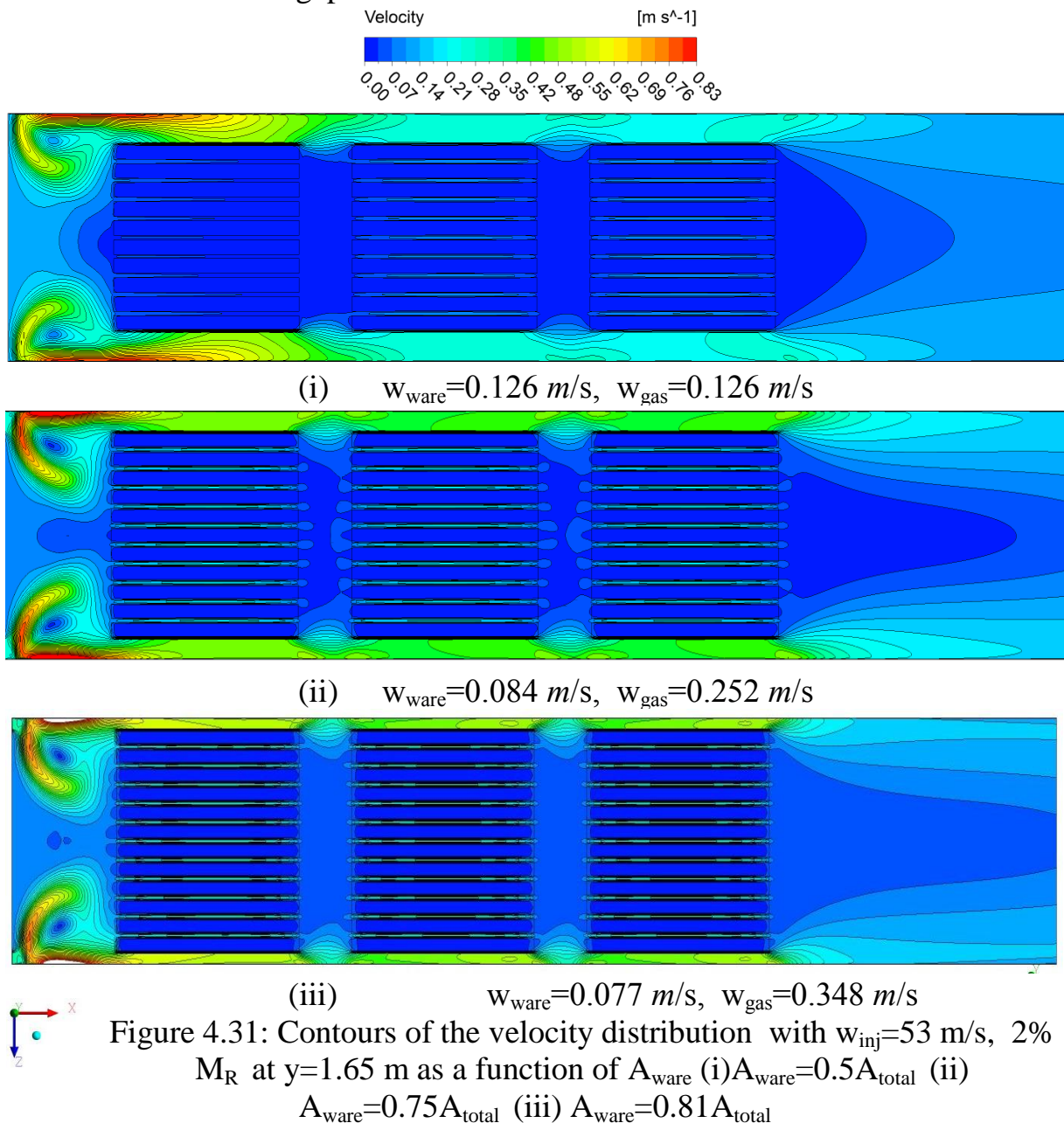

Figure 4.30: Contours of the velocity distribution with w_{inj}=53 m/s, 2% M_R A_{ware}=0.5A_{total} at (a) Y=2.65 m, (b) Y=1.65 m (c) Y=0.65 m respectively

Figure 4.31, shows the velocity contours along the kiln for three different geometries. For the first geometry, the product width is 2.2 m. There is a wide gap between the product and kiln walls. Therefore, the flow goes with large amount trough this gap and not between the products itself. It is due to the high resistance for the flow to pass in the channels between the products. On the other hand, the second and third geometry, it is clearly obvious from figure 4.31 that there is a high velocity in the channel between the products compared to the first geometry. Although, the gap between blades has the same dimensions. As a consequence, as the gap between the walls and products is reduced, the flow will be forced to pass in between the products. Which means a good heat transfer will occur in between gas and products. Furthermore, the mixing of gases is much better when the gap is reduced.

(i) $w_{ware}=0.126$ m/s, $w_{gas}=0.126$ m/s

(ii) $w_{ware}=0.084$ m/s, $w_{gas}=0.252$ m/s

(iii) $w_{ware}=0.077$ m/s, $w_{gas}=0.348$ m/s

Figure 4.31: Contours of the velocity distribution with $w_{inj}=53$ m/s, 2% M_R at y=1.65 m as a function of A_{ware} (i)$A_{ware}=0.5A_{total}$ (ii) $A_{ware}=0.75A_{total}$ (iii) $A_{ware}=0.81A_{total}$

The effect of product geometry on the frequency of temperature distribution at 0.9 m from the side injection is shown in the figure 4.32. As the cross sectional area of ware inlet increases, the width of the curve decreases. This means that the mixing is being better. Furthermore, the peak gets closer to the average temperature of the mixture as the cross sectional area of the ware increases.
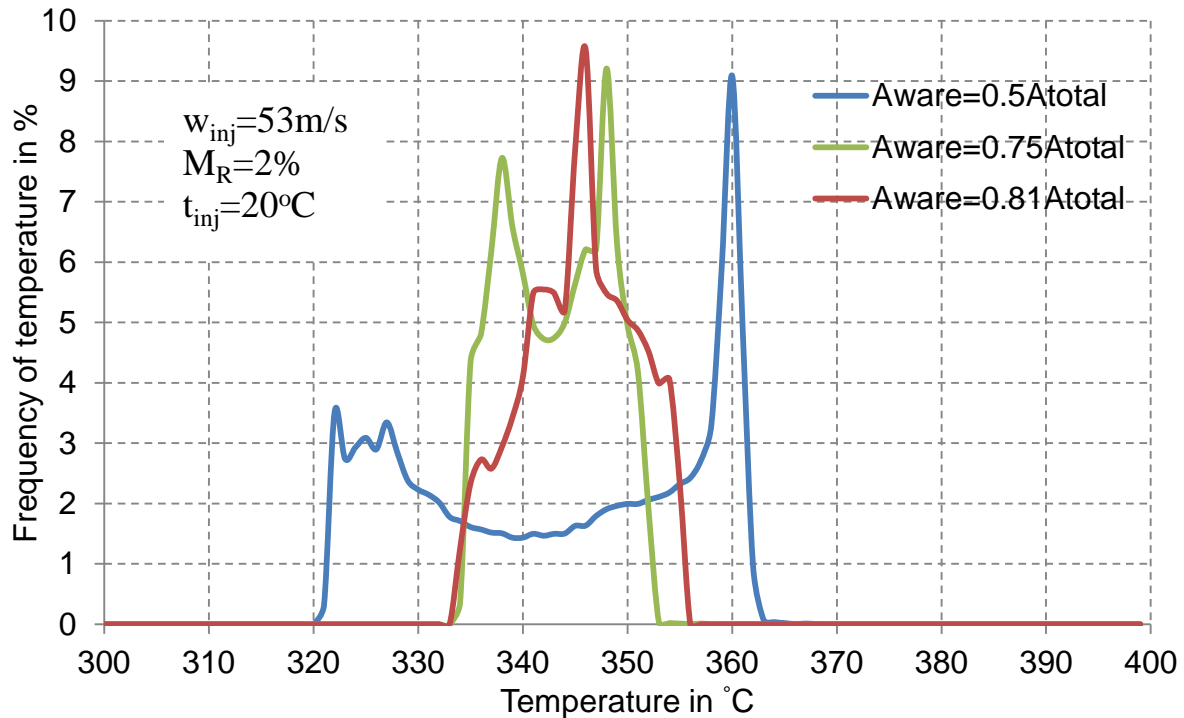

Figure 4.32: Temperature distribution after 0.9 meter from side(x=0.9m), with 2%M_R and 53m/s w_{inj}, as a function of ratio of area of ware to the total area

Figure 4.33 represents the dimensionless temperature difference θ along cross sectional planes ranging from x=0 to x=0.9 m in the longitudinal direction. The temperature difference ratio decreases as moving away from the side injection. It has a value equal to one at x=0 when the cross-section area of the ware is a half of the total cross-section (A_{ware}=0.5A_{total}). It is shifted to 0.86 in case of A_{ware}=0.81A_{total}, and its value is in between them in case when A_{ware}=0.75A_{total}. The same behaviour persists with other values of x. Therefore, it can be concluded that as the cross sectional area of the ware increases, the temperature difference decreases.
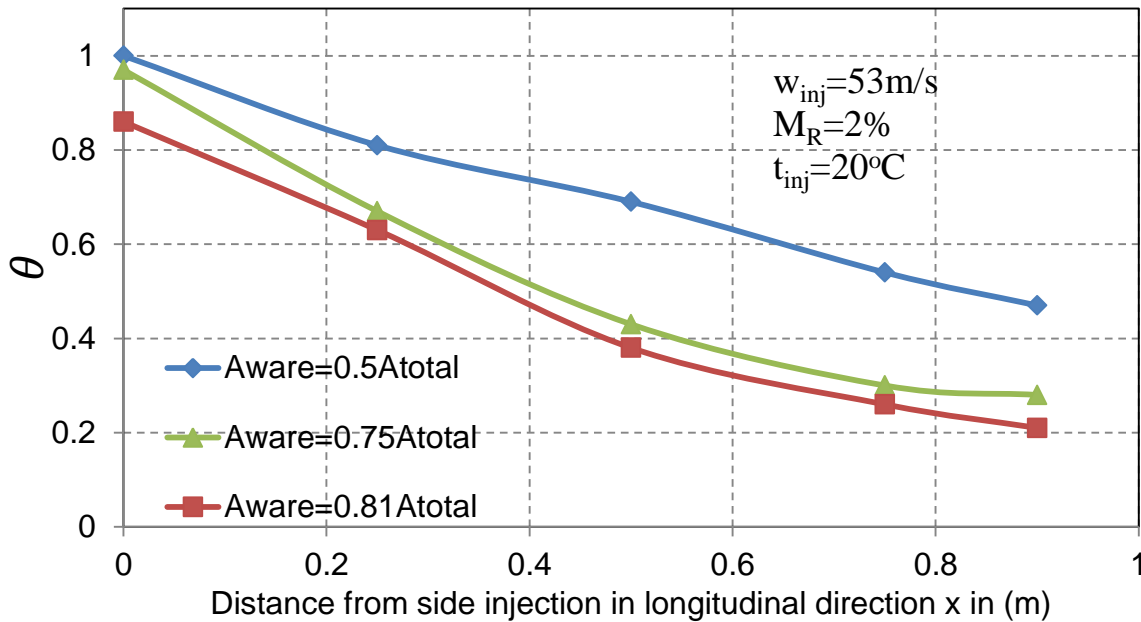
Figure 4.33: Temperature difference for every 25 cm from side injection, with $2\%M_R$ and 53m/s w_{inj}, as a function of ratio of area of ware to the total area

4.3.3 Effect of the ware on the mixing

In this part of the work, the influence of product on the quality of the mixing is studied. The comparison between two different cases, with and without ware has been used to show how the product can influence on the quality of the mixing. Furthermore, three different geometries have been used in this study. Table 4.2 shows the kiln dimensions and the area ratio.

Figure 4.34, represent three different ware zone arrangements in two different cases (a) with product (b) without product, at constant mixing ratio M_R 2% and velocity w_{inj} 53 m/s. As mentioned before, the main flow rate remains constant in all cases, Therefore, the velocity of ware decreases with the increasing cross sectional area, at the same time the velocity of gas zone increases to maintain the main flow constant.

By comparison, between (a) and (b) in the first arrangement ($A_{ware}=0.5A_{total}$). It can be noted that, the core region (ware zone stream) is fading faster in case (a). As a consequence, the mixing became better and faster in the longitudinal direction. That is due to the products as they offer some resistance against the flow of the air. This resistance has led to force flow of the air to pass through the products in case of the increased cross section area of the ware (less gap).

Therefore, the turbulence inside the kiln increases, and that makes the mixing more homogeneous. The same behaviour can be observed in the second arrangement when $A_{ware}=0.75A_{total}$ and third arrangement when $A_{ware}=0.81A_{total}$ respectively.
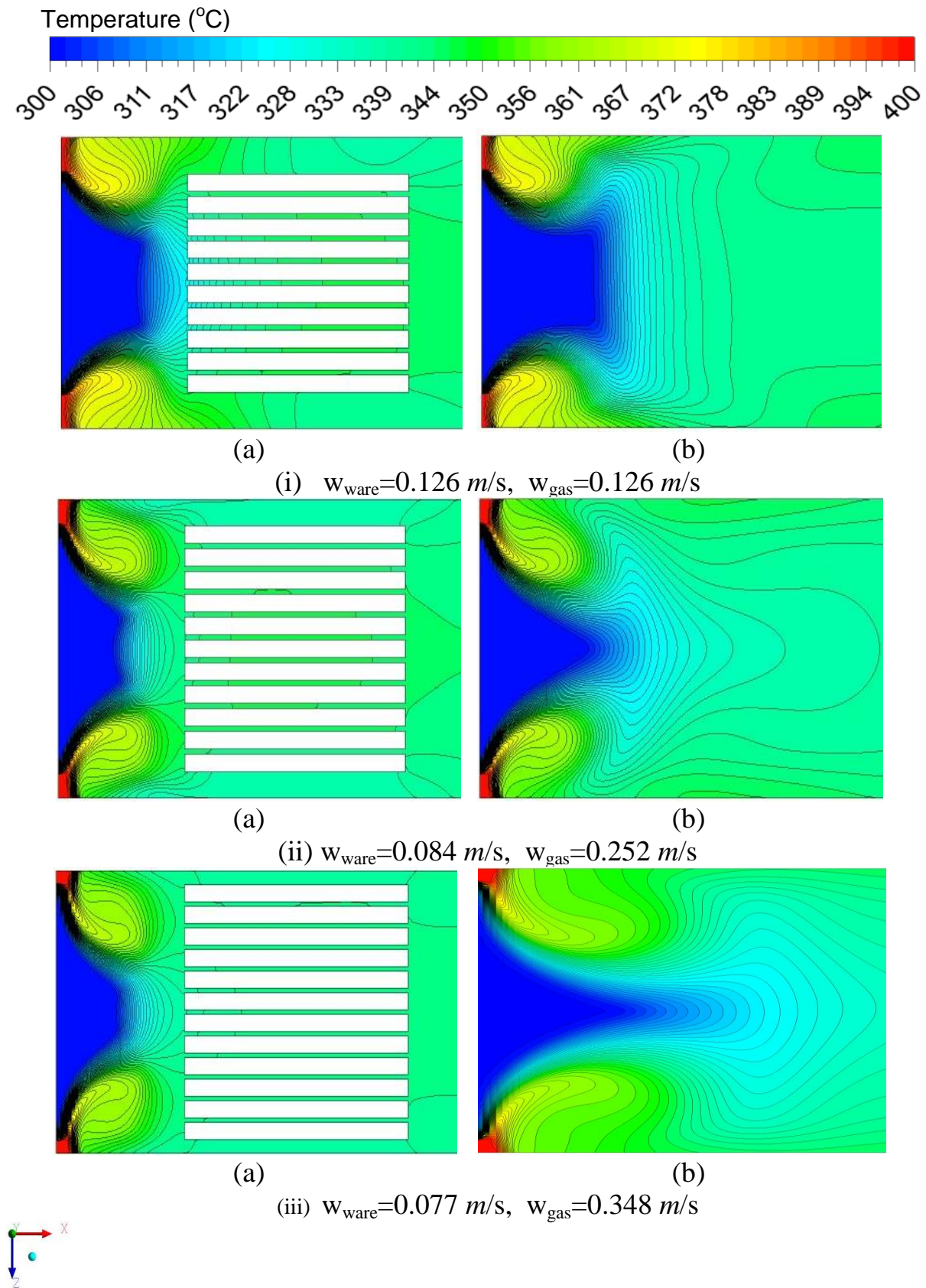
Figure 4.34: Contours of the temperature distribution at Y=1.65 m with w_{inj}=53 m/s and 2% M_R as a function of ratio of the area of ware zone to the total area, (a) with load (b) empty (i)A_{ware}=0.5A_{total} (ii) A_{ware}=0.75A_{total} (iii) A_{ware}=0.81A_{total}

The effect of cross-section area of the ware in two cases (with and without products) on the frequency of temperature distribution at a position 0.9 m from the side injection is shown in Figure 4.35.

GI, GII and GIII (without product) with GI, GII and GIII (with product) are compared. The geometries with product have a smaller width of temperature curves. That means, the mixing is better in the case of the kiln with product compared to empty kiln. In addition, by comparing GI, GII, and GIII (with and without product)   with each other, it is seen that, the width of the curve decreases as the cross sectional area of the ware increases. The peak gets closer to the average temperature of the mixture as the cross sectional area of the ware increases.
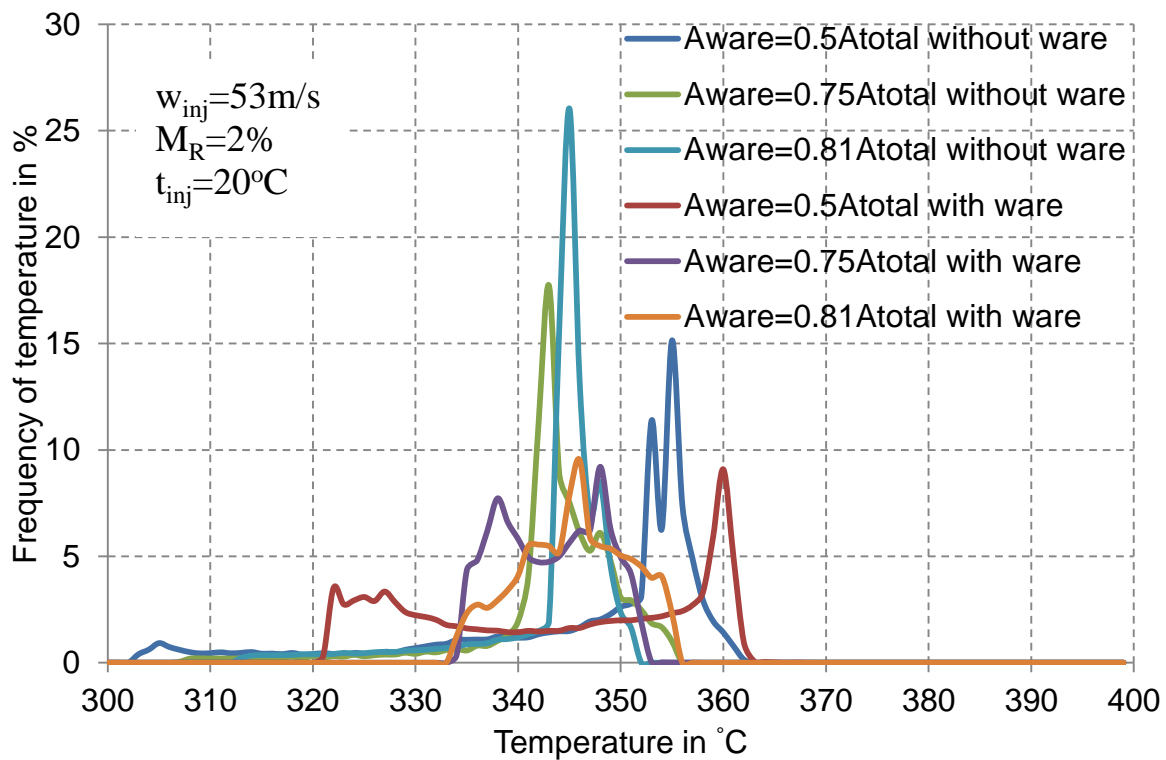

Figure 4.35: Effect of geometry on the temperature distribution at 0.9 m from the injection (x=0.9m)

Figure 4.36 represents effect of kiln geometry (cross-section area of the ware) in two cases (with and without products) on the dimensionless temperature difference θ. Four points are chosen with distance of 25cm between each other, except last point which is 20cm. In general, the temperature difference decreases with moving away from the side injection for all geometries. The effect of the product on the quality of the mixing is positive. This effect could be observed clearly after $\sim$ 0.5m from side injection (x=0.5m).

The dimensionless temperature difference θ is $\sim$0.67 at x=0.5 and $A_{ware}=A_{gas}$ in both cases (with and without products). It decreases with the rate of $\sim$13.5% in case of without product, while it decreases in the rate of $\sim$30% in the case when the products are inside the domain. The temperature difference decreases with the increasing the cross-section area of the product (or ware zone stream).

Thus, with the increased cross-section area the influence of products could be observed even at a short distance (x< 0.5) from the side injection. The temperature difference is 0.86 at x=0 and $A_{ware}=0.81A_{total}$ in both cases (with and without products). After that, it is affected by the presence of products indicated by a bigger slope of the temperature difference profiles than the slope in case of without products. Therefore, the effect of the product is positive (better mixing) on the quality of the mixing.
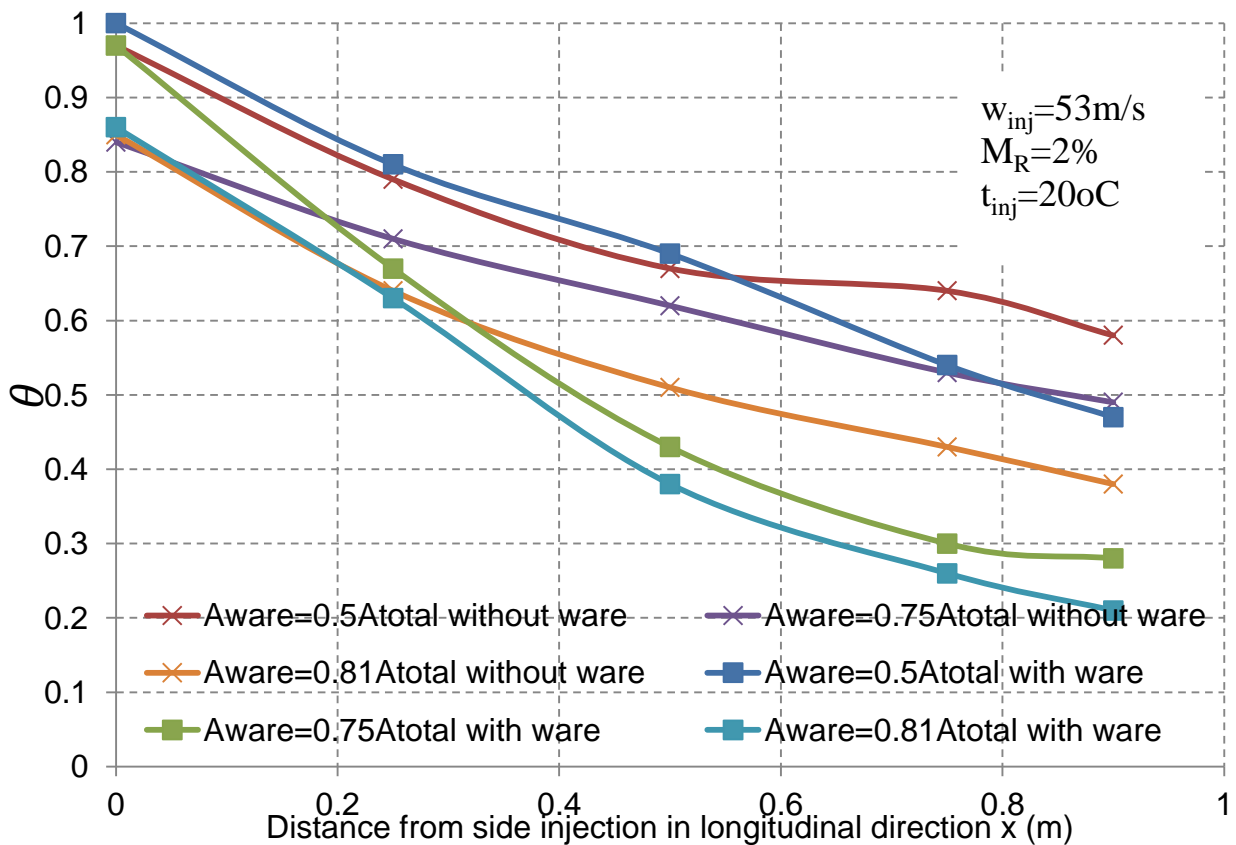

Figure 4.36: Temperature difference in longitudinal direction from side injection, with mixing ratio 2%, w_{inj}=53 m/s, as a function of ratio of the area of ware to the total area in two cases with and without products

5 Annular ring burner

5.1 Introduction

The annular ring burner is a typical non-premixed fuel burner. Where fuel and oxidizer injected into the combustion chamber through different pipes. This chapter is dedicated to establishing a better understanding of non-premixed flame behaviour and its characteristics. The surroundings of the combustion chamber are defined in two methods (a) ambient is air, (b) ambient is combustion gas. The results of numerical solutions are divided into three main sections according to the proposed surroundings of the combustion chamber and definition of reacting flow.

5.2.1 Analytical modelling

The fuel-oxidizer mixing mechanism plays a crucial role in calculating the velocity and fuel mass fraction in axial direction. In annular ring burner, the fuel and air propagate in axial direction. During this propagation the mixture draws gas from the environment and the speed of the fuel decreases continuously. Figure 5.1 shows a schematic diagram of the annular ring burner and flow field.
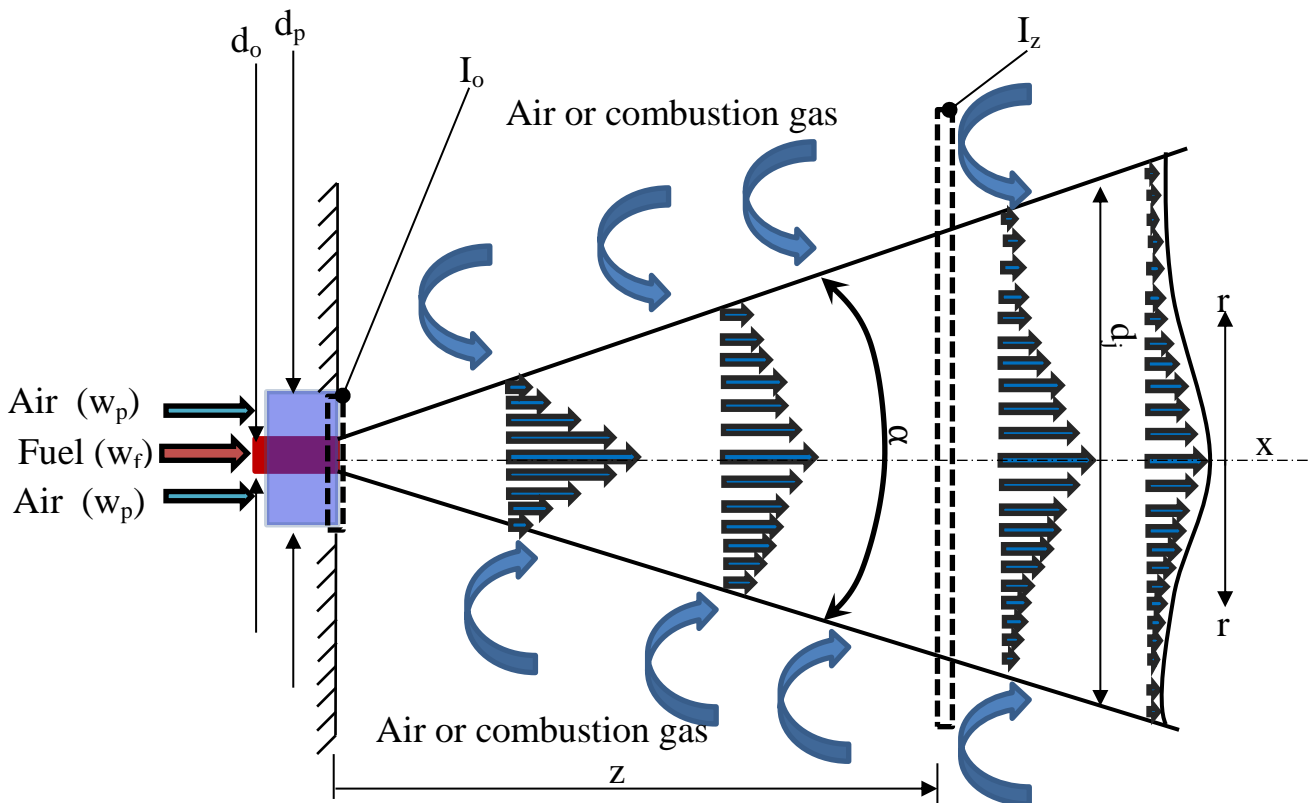

Figure 5.1: Schematic diagram of the flow field

Along the flame direction, there are no external effective forces. The pressure is constant, so the momentum flow remains constant [47]. The following shall apply:

$$I_o = I_z \qquad (5.1)$$

Where

I_z is the momentum flow of nozzle after (z) distance from the inlet,

I_o is the initial momentum flow of the nozzle (z=0) (see Figure 5.1).

$$I_o = I_f + I_p \qquad (5.2)$$

I_f and I_p are the fuel and air flow momentum respectively.

Therefore, the equation (5.2) can be written as:

$$I_o = \dot{M}_f * w_f + \dot{M}_p * w_p \qquad (5.3)$$

where

w is flow velocity

$\dot{M}$ is mass flow, subscripts f and p is the fuel and the primary air respectively (see Figure 5.1).

$$\dot{M}_f = \rho_f * \frac{\pi}{4} * d_o^2 * w_f \qquad (5.4)$$

$$\dot{M}_p = \rho_p * \frac{\pi}{4} * (d_p^2 - d_o^2) * w_p \qquad (5.5)$$

where

ρ is the density, subscripts f and p is the fuel and the primary air respectively

d is the diameter, subscripts o and p is the fuel and the primary air respectively

By compensating equations 5.4 and 5.5 in eq. 5.3 gives:

$$I_o = \rho_f * \frac{\pi}{4} * d_o^2 * w_f + \rho_p * \frac{\pi}{4} * (d_p^2 - d_o^2) * w_p \qquad (5.6)$$

The momentum flow of nozzle after (z) distance from the inlet can defined as follows:

$$I_z = \dot{M}_J * \overline{w} \qquad (5.7)$$

where

I_z is the momentum flow of nozzle after (z) distance from the inlet

$\dot{M}_J$ is the mass flow of the jet

$\overline{w}$ is the mean flow velocity of the jet flow

The mass flow of the jet is defined as follows:

$$\dot{M}_J = \rho_j * \frac{\pi}{4} * d_j^2 * \overline{w} \tag{5.8}$$

d_j is the jet flow diameter and ρ_j is mean jet flow density.

The diameter of jet flow d_j can be determined from the following equation:

$$d_j = d_o + 2 * z * \tan\frac{\alpha}{2} \tag{5.9}$$

The jet flow gets wider by the angle α (the calculation approaches of jet angle α is described in section 5.1.2)

By substituting equations 5.8 and 5.9 in equation 5.7 gives:

$$I_z = \rho_j * \frac{\pi}{4} * \left(d_o + 2 * z * \tan\frac{\alpha}{2}\right)^2 * \overline{w}^2 \tag{5.10}$$

By Substituting equations 5.6 and 5.10 in equation 5.1, the conversation of momentum can written as:

$$\rho_f + \rho_p * \left(\frac{d_p^2}{d_o^2} - 1\right) * \frac{w_p^2}{w_f^2} = \rho_j * \frac{\left(d_o + 2*z*tan\frac{\alpha}{2}\right)^2}{d_o^2} * \frac{\overline{w}^2}{w_f^2} \ . \tag{5.11}$$

The mass flow of primary air can also define as:

$$\dot{M}_p = \dot{M}_f * L * \lambda \tag{5.12}$$

where L is air demand, λ is excess air number

From equations (5.5) and (5.6) equation 5.12 can be written as:

$$\frac{w_p}{w_f} = \frac{\rho_f}{\rho_p} * \frac{L*\lambda}{\left(\frac{d_p}{d_o}\right)-1} \qquad . \qquad (5.13)$$

From the above equations (5.11) and (5.13), the speed reduction in axial direction can be written as:

$$\frac{w_f}{\overline{w}} = \left\{\left(1 + 2 * \frac{z}{d_o} * \tan\frac{\alpha}{2}\right) * \left[\frac{\rho_f}{\rho_j} + \frac{\rho_f}{\rho_j} * \frac{\rho_f}{\rho_p} * \frac{\left(\lambda L*\frac{d_o}{d_p}\right)^2}{1-\left(\frac{d_o}{d_p}\right)^2}\right]^{-\frac{1}{2}}\right\} \qquad . \qquad (5.14)$$

The velocity along the centreline of the jet decreases inversely with distance from the virtual source as shown in Figure 5.2. Therefore the mean flow velocity of the jet flow ($\overline{w}$) is a half axial flow velocity [52] i.e.
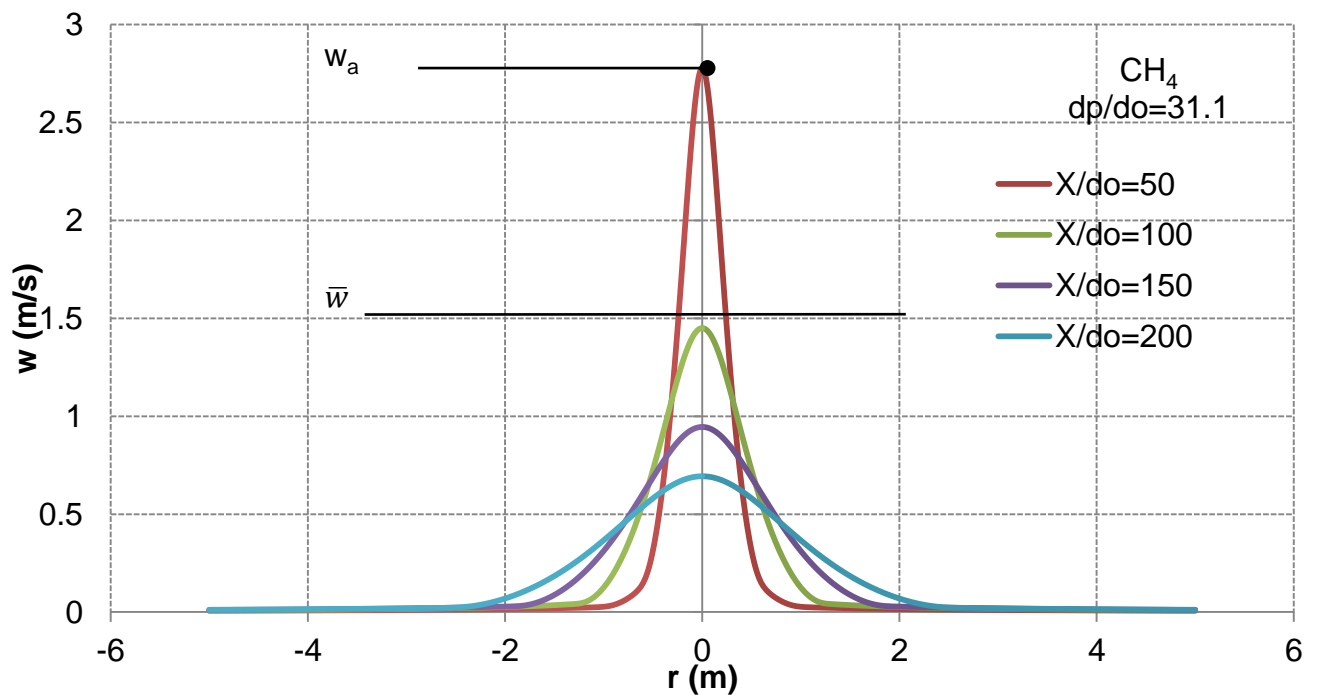
$$\overline{w} = 0.5w_a \qquad (5.15)$$

Figure 5.2: The radial profiles of axial velocity

Therefore, the speed reduction in axial direction can be written as:

$$\frac{w_f}{w_a} = 0.5 \left\{ \left(1 + 2 * \frac{z}{d_o} * \tan\frac{\alpha}{2}\right) * \left[\frac{\rho_f}{\rho_j} + \frac{\rho_f}{\rho_j} * \frac{\rho_f}{\rho_p} * \frac{\left(\lambda L * \frac{d_o}{d_p}\right)^2}{1 - \left(\frac{d_o}{d_p}\right)^2}\right]^{-\frac{1}{2}} \right\} \quad (5.16)$$

In case of $d_p >>> d_o$ ➡ $\frac{d_o}{d_p} \approx 0$ (free jet)

The equation (5.16) could be written as:

$$\frac{w_f}{w_a} = 0.5 \left\{ \left(1 + 2 * \frac{z}{d_o} * \tan\frac{\alpha}{2}\right) * \left[\frac{\rho_f}{\rho_j}\right]^{-\frac{1}{2}} \right\}. \quad (5.17)$$

Regarding the reduction of mass fraction in axial direction, the conversation of fuel mass can be written as:

$$\dot{M}_f = \dot{M}_J \quad (5.18)$$

where

$\dot{M}$ is mass flow, subscripts f and j is the fuel and the jet respectively.

The mass flow can written as:

$$\dot{M}_f = \rho_f * \frac{\pi}{4} * d_o^2 * w_f * x_o \quad (5.19)$$

$$\dot{M}_J = \rho_j * \frac{\pi}{4} * d_j^2 * \overline{w} * \overline{x} \quad (5.20)$$

where

ρ is the density, subscripts f and j is the fuel and the primary air respectively

d is the diameter, subscripts o and j is the fuel and the primary air respectively

x_o is the initial mass fraction, $\overline{x}$ is the mean mass fraction

w is flow velocity and $\overline{w}$ is the mean flow velocity of the jet flow.

By substituting equations 5.19 and 5.20 in equation 5.18 gives:

$$\frac{\bar{x}}{x_o} = \frac{\rho_f}{\rho_j} * \left(\frac{d_o}{d_j}\right)^2 * \frac{w_f}{\bar{w}} . \qquad (5.21)$$

The diameter of jet flow (d_j) is described above in equation (5.9).

By substituting equations 5.9 and 5.14 in equation 5.21, the reduction of fuel mass in axial direction can be written as:

$$\frac{x_o}{\bar{x}} = \left\{ \frac{\rho_j}{\rho_f}\left(1 + 2 * \frac{z}{d_o} * \tan\frac{\alpha}{2}\right) * \left[\frac{\rho_f}{\rho_j} + \frac{\rho_f}{\rho_j} * \frac{\rho_f}{\rho_p} * \frac{\left(\lambda L * \frac{d_o}{d_p}\right)^2}{1-\left(\frac{d_o}{d_p}\right)^2}\right]^{\frac{1}{2}} \right\} . \qquad (5.22)$$

The behaviour of reduction of the mass of fuel in the axial direction the same as the behaviour of reduction of axial velocity as shown in Figure 5.3. Therefore the mean mass fraction can written as:

$$\bar{x} = 0.5x_a \qquad (5.23)$$

where

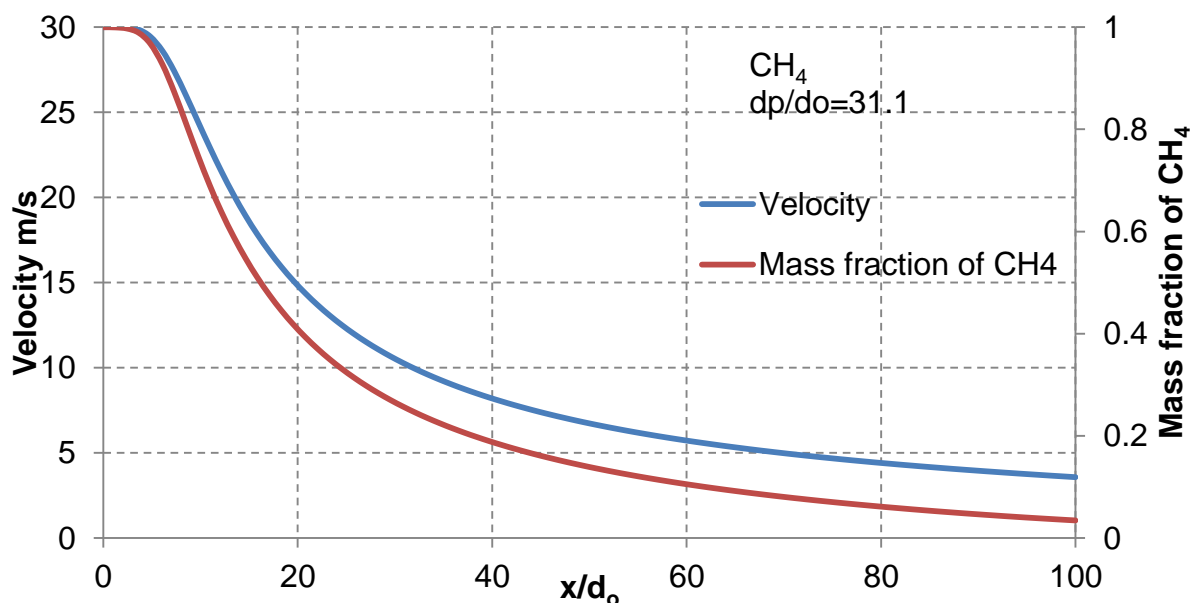x_a is the axial mass fraction

Figure 5.3: The profiles of axial velocity and axial mass fraction of fuel

Therefore, from equation (5.23) the reduction of fuel mass in axial direction can be written as:

$$\frac{x_o}{x_a} = 0.5 \left\{ \frac{\rho_j}{\rho_f}\left(1 + 2 * \frac{z}{d_o} * \tan\frac{\alpha}{2}\right) * \left[\frac{\rho_f}{\rho_j} + \frac{\rho_f}{\rho_j} * \frac{\rho_f}{\rho_p} * \frac{\left(\lambda L * \frac{d_o}{d_p}\right)^2}{1 - \left(\frac{d_o}{d_p}\right)^2} \right]^{\frac{1}{2}} \right\}$$ (5.24)

In case of $d_p \ggg d_o$ ⟹ $\frac{d_o}{d_p} \approx 0$ (free jet)

The equation (5.24) could be written as:

$$\frac{x_o}{x_a} = 0.5 \left\{ \left(1 + 2 * \frac{z}{d_o} * \tan\frac{\alpha}{2}\right) * \left[\frac{\rho_j}{\rho_f}\right]^{\frac{1}{2}} \right\}.$$ (5.25)
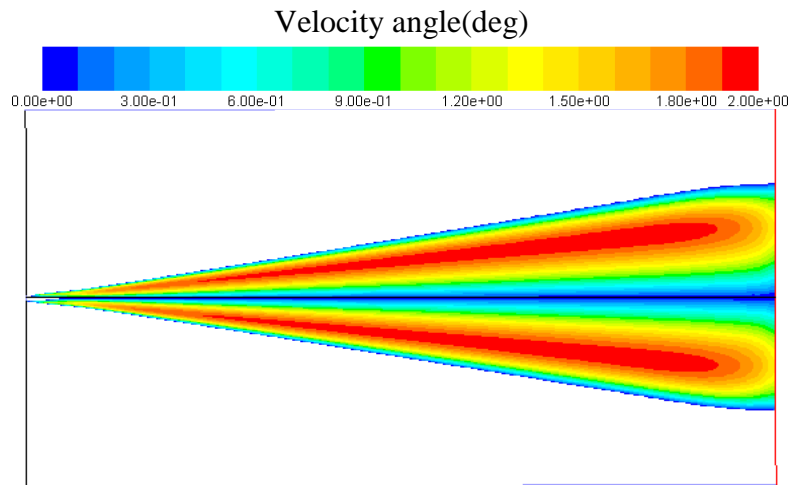
5.2.2 Jet angle

The angle of the non-premixed flame is important to solve the analytical model. When the fuel and air are injected into the combustion chamber, the original kinetic energy of the mixture dispersed gradually in the turbulent mixing. Surrounding of the combustion chamber is entrained by the jet so that the velocity of the jet decreases. While the mass of fluid increases, the momentum remaining constant. In this way the jet spreads in the form of a cone.
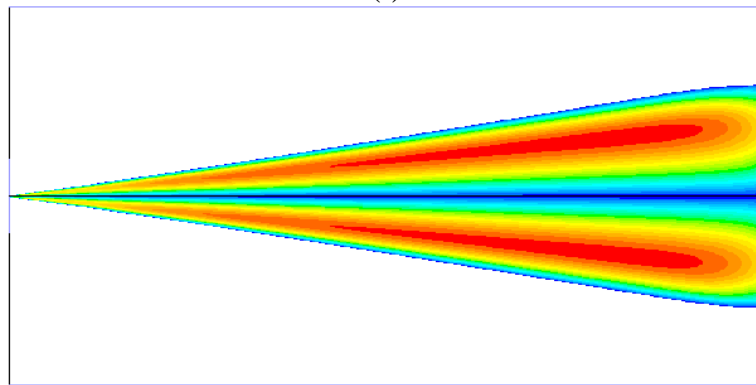
The boundary layer between surroundings of the combustion chamber and jet can identified by using velocity angle. The definition of angle of the velocity is [46]

$$velocity\ angle = \tan^{-1}\left(\frac{radial\ velocity\ component}{axial\ velocity\ component}\right).$$ (5.26)
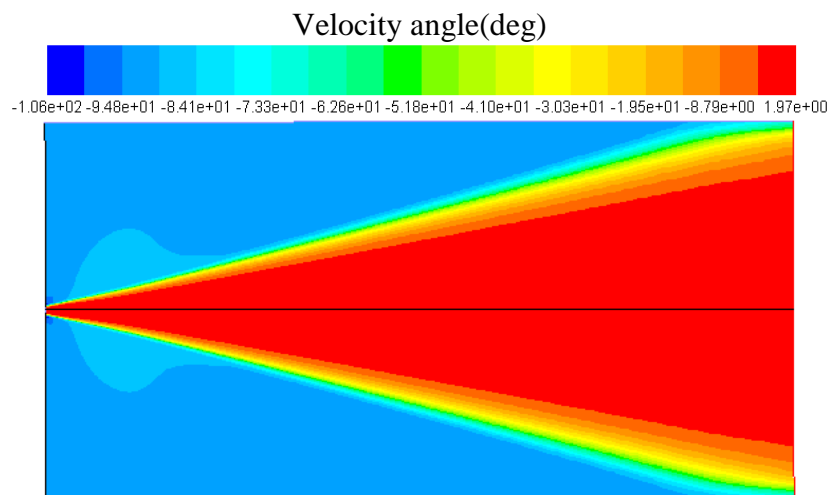
In general, the angle of velocity ranges between positive and negative values ($0 \geq$ velocity angle < 0). From Figure 5.4 (i) and (ii), it can be noted that the angle of velocity is zero at the r=0 and increases with increasing (r) up to the peak. Then, it reduces to zero again at the sides of the jet border. That it refers to the direction of the velocity component between surroundings of the combustion chamber and the stream of the jet. Where the angle of the velocity has negative values around the boundary layer of the jet as shown in Figure 5.4 (iii)and (iiii). The angle of the jet can be calculated directly from the contours of the velocity angle by using a protractor. It ranges between 18-20° for different annular diameter ratios.

Velocity angle(deg)

0.00e+00   3.00e-01   6.00e-01   9.00e-01   1.20e+00   1.50e+00   1.80e+00 2.00e+00

(i)

(ii)

Velocity angle(deg)

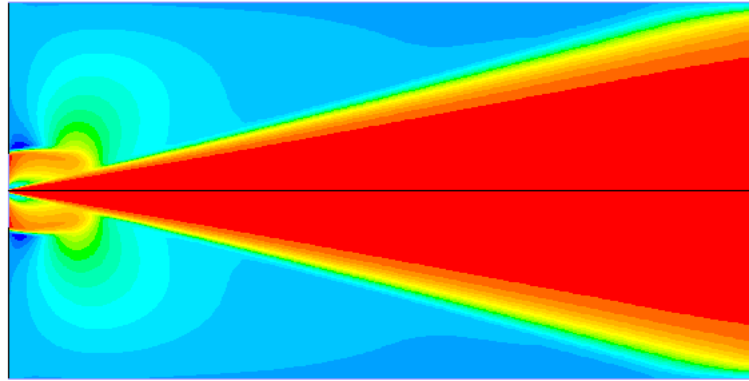-1.06e+02 -9.48e+01 -8.41e+01 -7.33e+01 -6.26e+01 -5.18e+01 -4.10e+01 -3.03e+01 -1.95e+01 -8.79e+00 1.97e+00

(iii)

(iiii)

Figure 5.4: The angle of velocity in different annular diameter at 1:200 drawing scale: (i), (ii) the scale range of the angle of velocity ≥ 0 at dp/do =3.7 and dp/do=40 respectively, (iii) and (iiii) at the scale range (0$\geq$velocity angle<0) and dp/do =3.7 and dp/do=40 respectively

5.3 Simulation of annular ring burner without gas phase reaction

The simulations are carried out to see the influence of air inlet diameter on axial velocity and mass fraction of fuel considering gas phase without reaction (without combustion). The simulation results are compared with the results obtained through analytical solutions. A species transport model without volumetric reactions is chosen. These comparisons give the purpose of verification of the simulations.

5.3.1 Influence of air inlet diameter on axial velocity

The influence of air inlet diameters on axial velocity is calculated analytically. Then, it is compared with a numerical result. The dimensionless annular diameter considered, ranges from 3.7 to 40 are proposed. The velocity of fuel is 30m/s. The excess air number (λ) is constant and equals to 1.3. The primary air inlet flow rate is also constant. Therefore, the primary air inlet velocity will decrease with the diameter increasing. The primary air to fuel velocity ratio (w_p/w_o) is changing from 0.975 to 0.007 according to variation of d_p/d_o, as shown in table 5.1.

Table 5.1: Primary air to fuel velocity ratio of different annular diameters

d_p/d_o	w_p/w_o
3.7	0.975
5.1	0.495
7.4	0.230
10.6	0.111
15.9	0.049
31.1	0.013
35.0	0.010
40.0	0.007

Figure 5.5 describes the effect of air diameter on dimensionless axial velocity in case of methane (CH_4) as a fuel. The dimensionless axial velocity increases with the increasing air inlet diameter. Where, it can be observed the dimensionless axial velocity at z/do=150 is increased from ~8 to~ 18 (increasing ratio ~ 125%) with increasing the dimensionless diameter from 3.7 to 10.6. While it increases from ~32 to~ 34 (increasing ratio ~ 6.25%) with increasing the dimensionless diameter from 31.1 to 40. Moreover, the dimensionless diameter increases by ~6.9 in case of increasing 3.7 to 10.6, while it increases by~9 in case of increasing the dimensionless diameter from 31.1 to 40. After the above discussion, the annular ring burner works as free jet after increases the dimensionless diameter more than 31.1. This behaviour can be noted at different positions (different z/do).

Figure 5.6 and Figure 5.7 show the effect of air diameter on the dimensionless axial velocity at using Biogas and CO as a fuel respectively. The same behaviour persists in case of using Biogas and CO as a fuel. Here the dimensionless axial velocity increases by ~112.5% and ~3.5% with increasing dimensionless annular diameter from 3.7 to 10.6 and from 31.1 to 40 respectively at using Biogas as a fuel. And it increases by ~114% and ~1.1% with increasing dimensionless annular diameter from 3.7 to 10.6 and from 31.1 to 40 respectively at using CO as a fuel. That it conforms of the annular ring burner works as free jet after increases the dimensionless diameter more than 31.1.
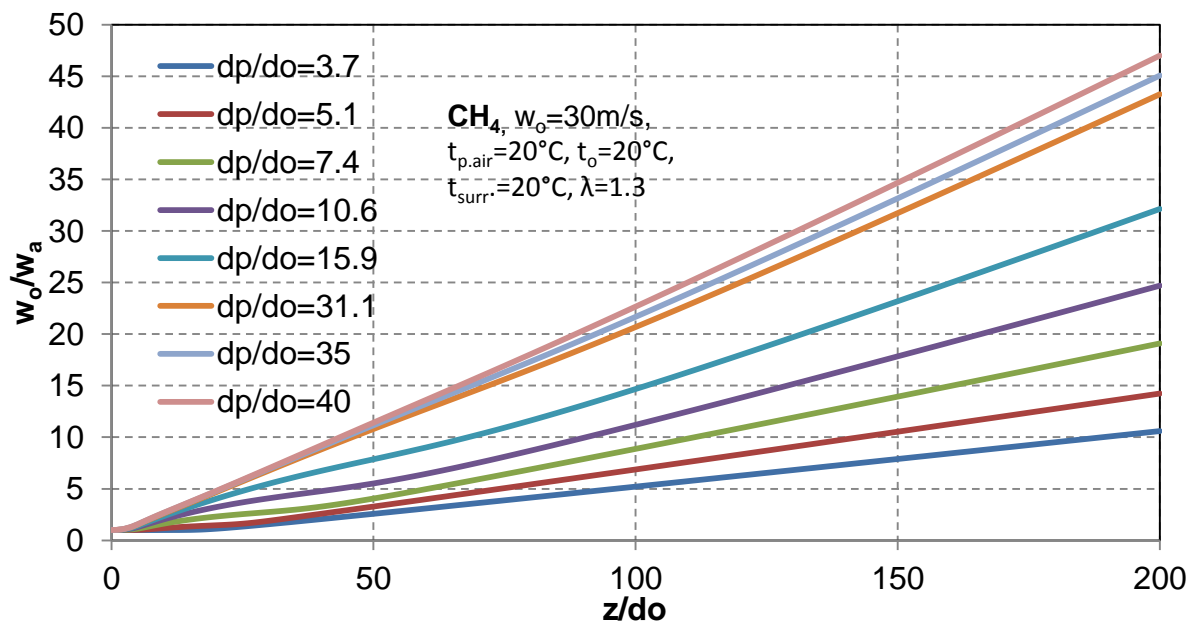

Figure 5.5: Dimensionless axial velocity as a function of dimensionless annular diameters at using CH4 as a fuel
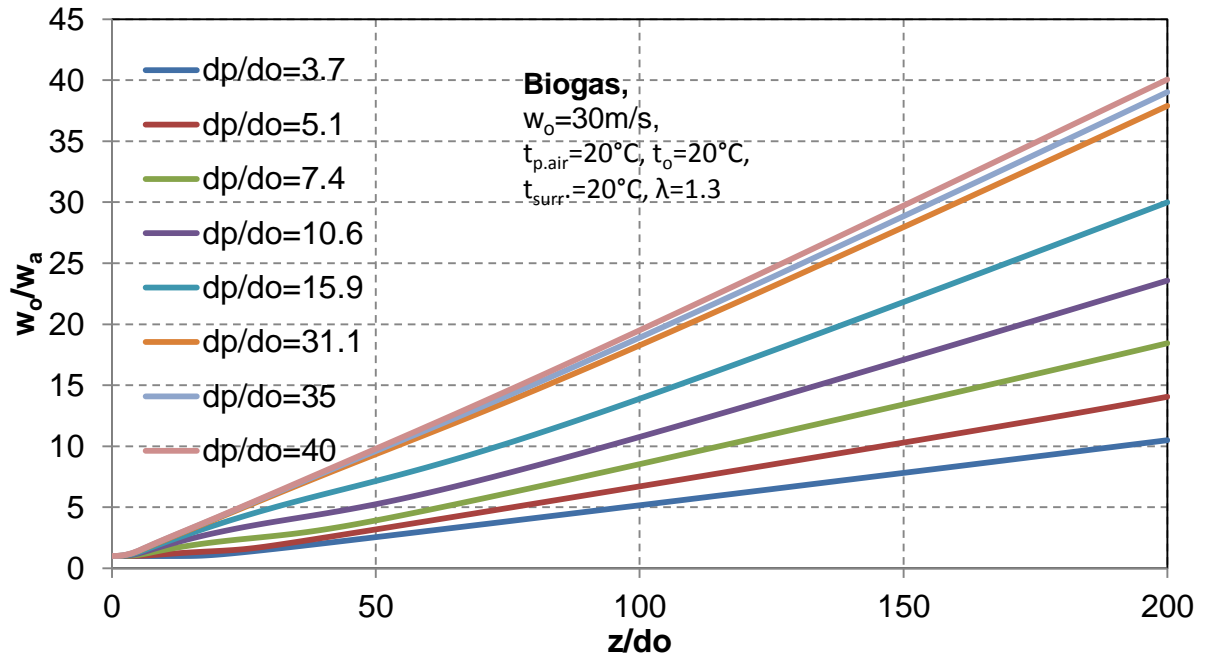
Figure 5.6: Dimensionless axial velocity as a function of dimensionless annular diameters at using Biogas as a fuel
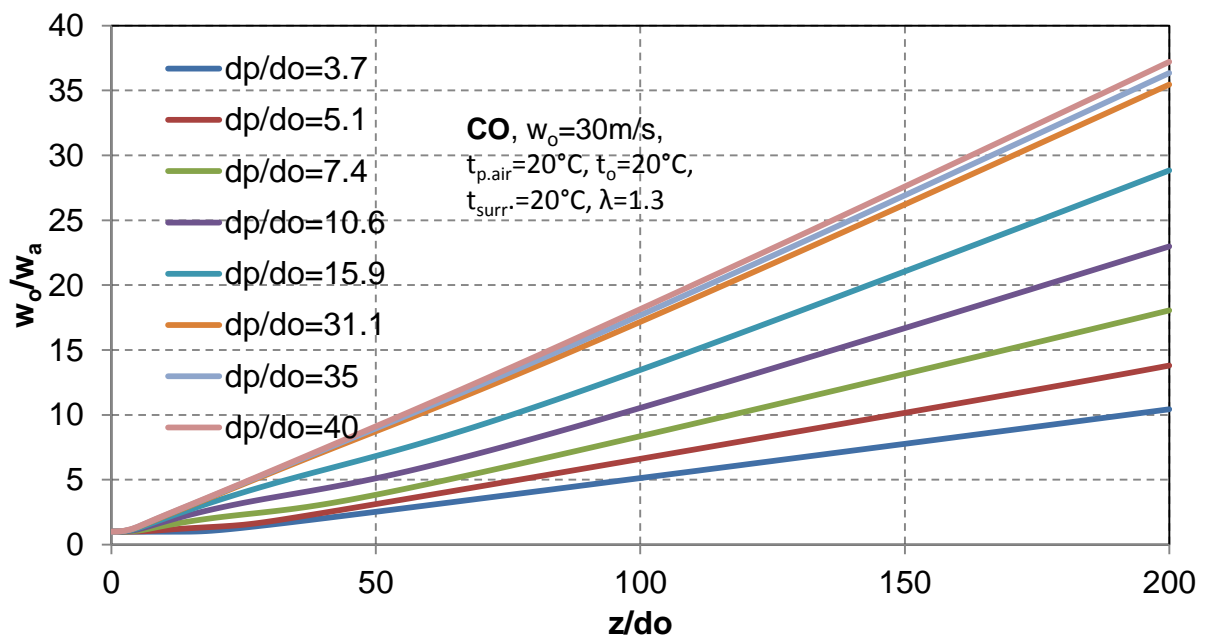

Figure 5.7: Dimensionless axial velocity as a function of dimensionless annular diameters at using CO as a fuel

The velocity contours with different air diameters are shown in Figure 5.8. The air inlet velocity decreases clearly with the dimensionless annular diameters increasing. But the effect of diameter of air inlet is disappearing after the dimensionless diameter more than 31.1.
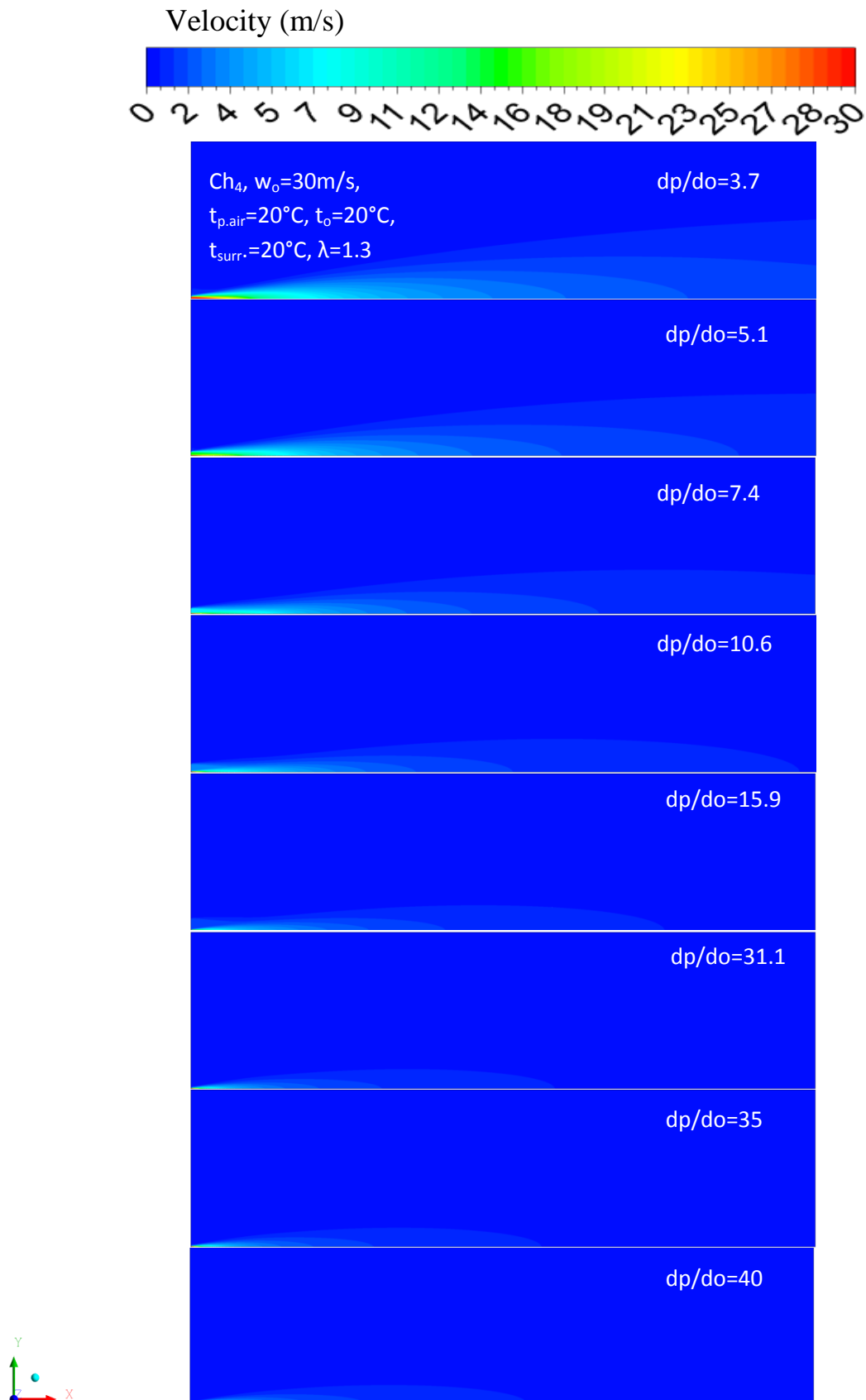
Fig. 5.8:Contours of velocity as a function of dimensionless annular diameter at using methane as a fuel

The reduction of velocity in the axial direction as a function of the dimensionless annular diameters for three different gaseous fuels (CH4, Biogas and CO) is calculated analytically by using equation (5.16) and it is shown below.

$$\frac{w_f}{w_a} = 0.5 \left\{ \left(1 + 2 * \frac{z}{d_o} * \tan\frac{\alpha}{2} \right) * \left[\frac{\rho_f}{\rho_j} + \frac{\rho_f}{\rho_j} * \frac{\rho_f}{\rho_p} * \frac{\left(\lambda L * \frac{d_o}{d_p} \right)^2}{1 - \left(\frac{d_o}{d_p} \right)^2} \right]^{-\frac{1}{2}} \right\}$$

The dimensionless annular diameters, velocities and the excess air number are same as mentioned above.

Figure 5.9 shows the results of analytical solutions for reduction of velocity in axial direction. The dimensionless axial velocity increases with increasing air inlet diameter, which increasing dimensionless annular diameters at using CH4 as a fuel. Where the dimensionless velocity at z/do=20 is increased from ~1.1 to ~4.8 (increasing ratio ~ 336%) with increasing the dimensionless diameter from 3.7 to 31.1. While it increases from 4.8 to 5 (increasing ratio ~ 4%) at z/do=20 with increasing the dimensionless diameter from 31.1 to 40.

It is evident that dimensionless axial velocity at z/do=200 increases with the increasing air inlet diameter. Where it increases from 10 to 43 (increasing ratio ~ 330%) with increasing the dimensionless diameter from 3.7 to 31.1. While the increasing ratio, reduced to ~4.6% by increasing the dimensionless diameter from 31.1 to 40. Here it expects the behaviour of annular ring burner change to the free jet flame after d_p/d_o =31.1.

From Figure 5.10 it can be noted at using Biogas as a fuel. The dimensionless axial velocity takes the same behaviour which mentioned above. It increases by 267 % with increasing the dimensionless diameter from 3.7 to 31.1. Also the increasing ratio, reduced to ~5% by increasing the dimensionless diameter from 31.1 to 40.

The effect of dimensionless annular diameters on the dimensionless axial velocity at using CO as a fuel is shown in Figure 5.11. Here the dimensionless annular diameters has effect on dimensionless axial velocity relatively higher than in case of CH_4 and Biogas as a fuel. It increases by ~442% with increasing the dimensionless annular diameters from 3.7 to 31.1 at z/do=20. The same as before the increasing ratio, reduced to ~5% by increasing the dimensionless diameter from 31.1 to 40. Therefore, the behaviour of annular ring burner change to the free jet after dp/do =31.1(w_p/w_o=0.013) and that independence on kind of gaseous fuel.
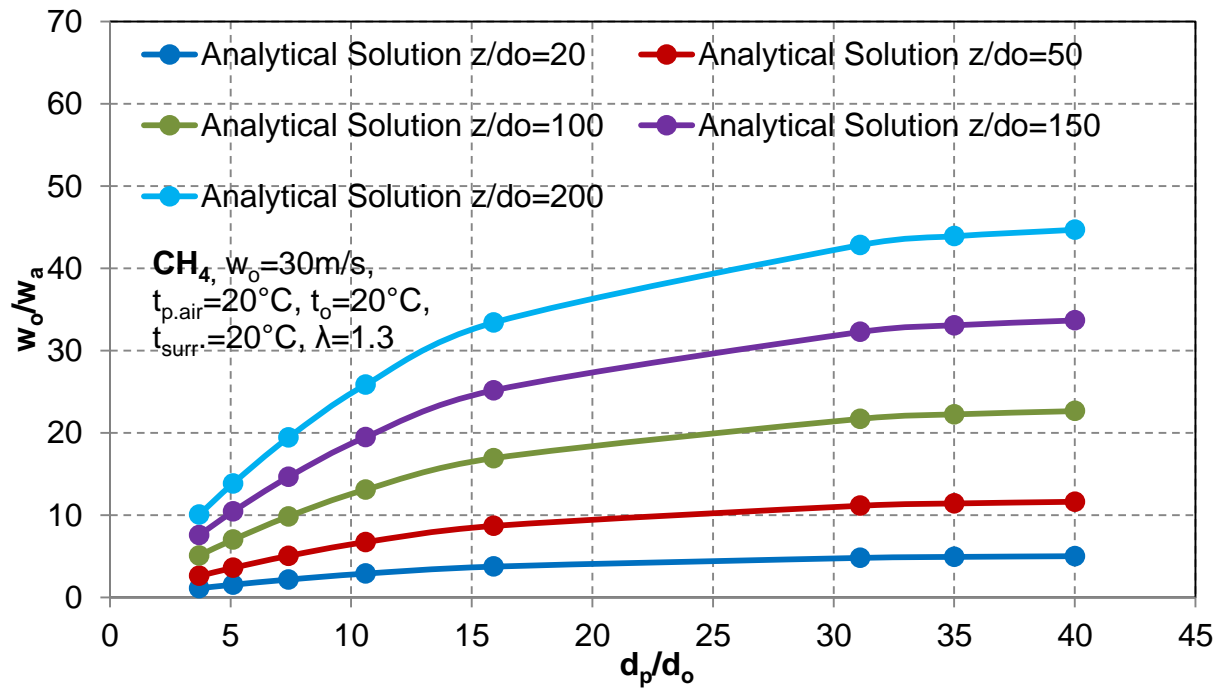
Figure 5.9: Analytical solution of dimensionless axial velocity as a function of dimensionless annular diameters at different dimensionless axial positions, at using CH4 as a fuel
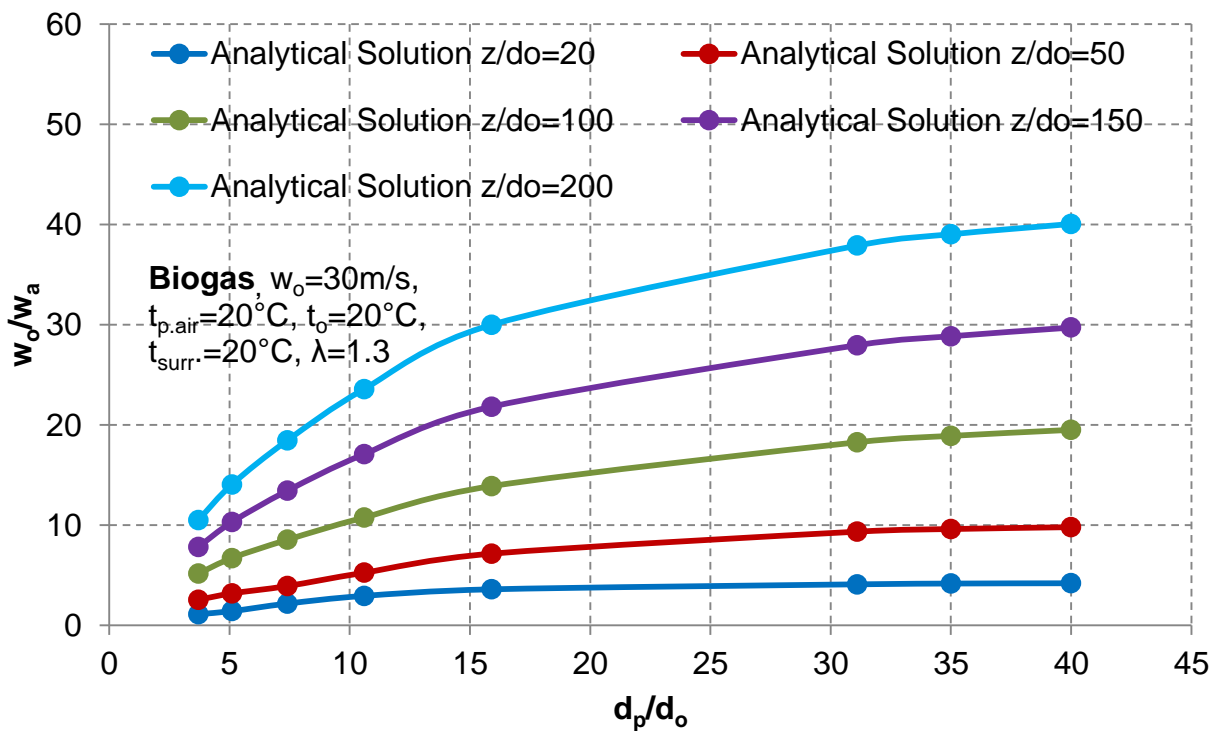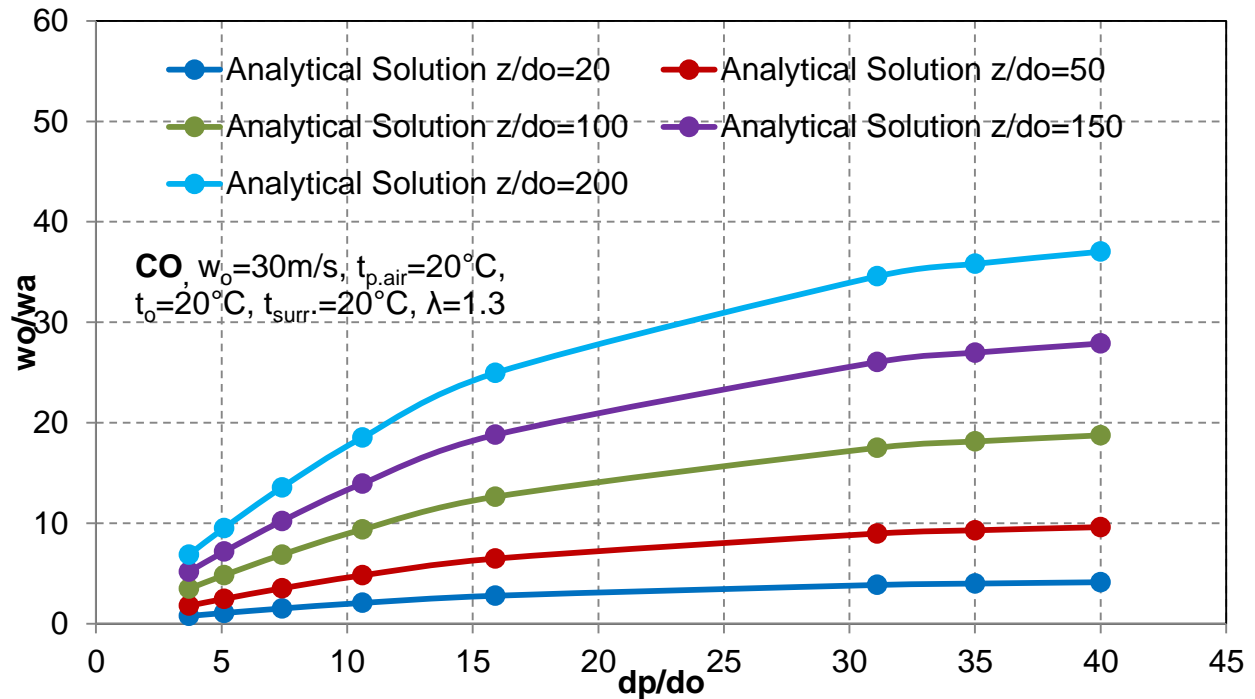

Figure 5.10: Analytical solution of dimensionless axial velocity as a function of dimensionless annular diameters at different dimensionless axial positions, at using Boigas as a fuel

Figure 5.11: Analytical solution of dimensionless axial velocity as a function of dimensionless annular diameters at different dimensionless axial positions, at using CO as a fuel

The comparison between the numerical and the analytical results of the axial velocity for three different gaseous fuels are shown in figure 5.12, 5.13 and 5.14. Figure 5.12 describes the influence of dimensionless annular diameter on the dimensionless axial velocity in case of methane (CH_4) as a fuel. It can be noted that the numerical results for different positions (z/do) are identical with analytic results. Moreover. The maximum relative error is ~11% at d_p/d_o=15.9 and z/do=100. Also, the dimensionless velocity at z/do=20 is increased from ~1.1 to ~5 (increasing ratio ~ 400%) with increasing the dimensionless diameter from 3.7 to 40. While it increases from 10 to 45 (increasing ratio ~ 350%) at z/do=200. It means the increase ratio of the dimensionless velocity is relatively independent of the position (z/do). Figure 5.13 and 5.14 show the comparison between the numerical and the analytical solution for the axial velocity at using Biogas and CO as a fuel respectively. The same behaviour persists for dimensionless axial velocity as mentioned above. The numerical and analytical results are identical with maximum relative error ~23% and ~19% for Biogas and CO respectively. As the density of Biogas and CO is higher than the density of CH4, the dimensionless axial velocity for Biogas and CO is relatively lower than the dimensionless axial velocity of Methane (CH_4).
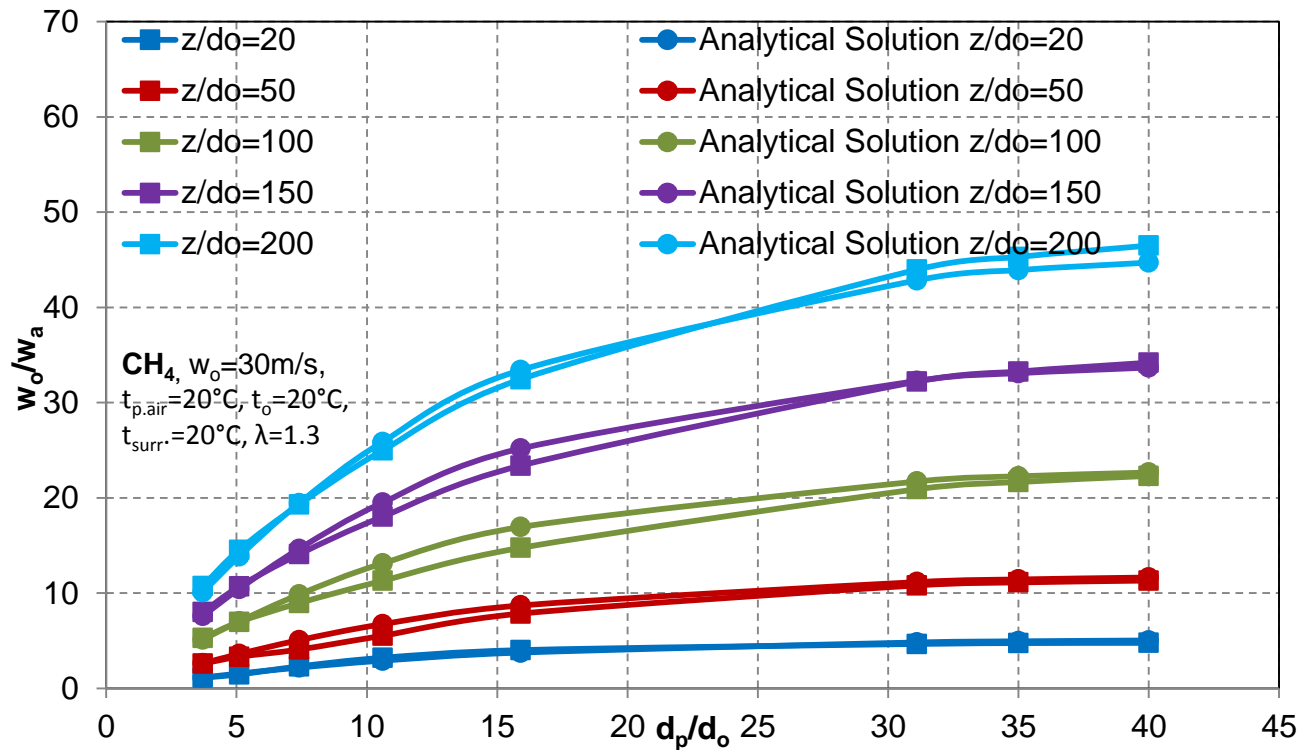
Figure 5.12: Numerical and analytical solution of dimensionless axial velocity as a function of dimensionless annular diameters at different dimensionless axial positions at using CH4 as a fuel
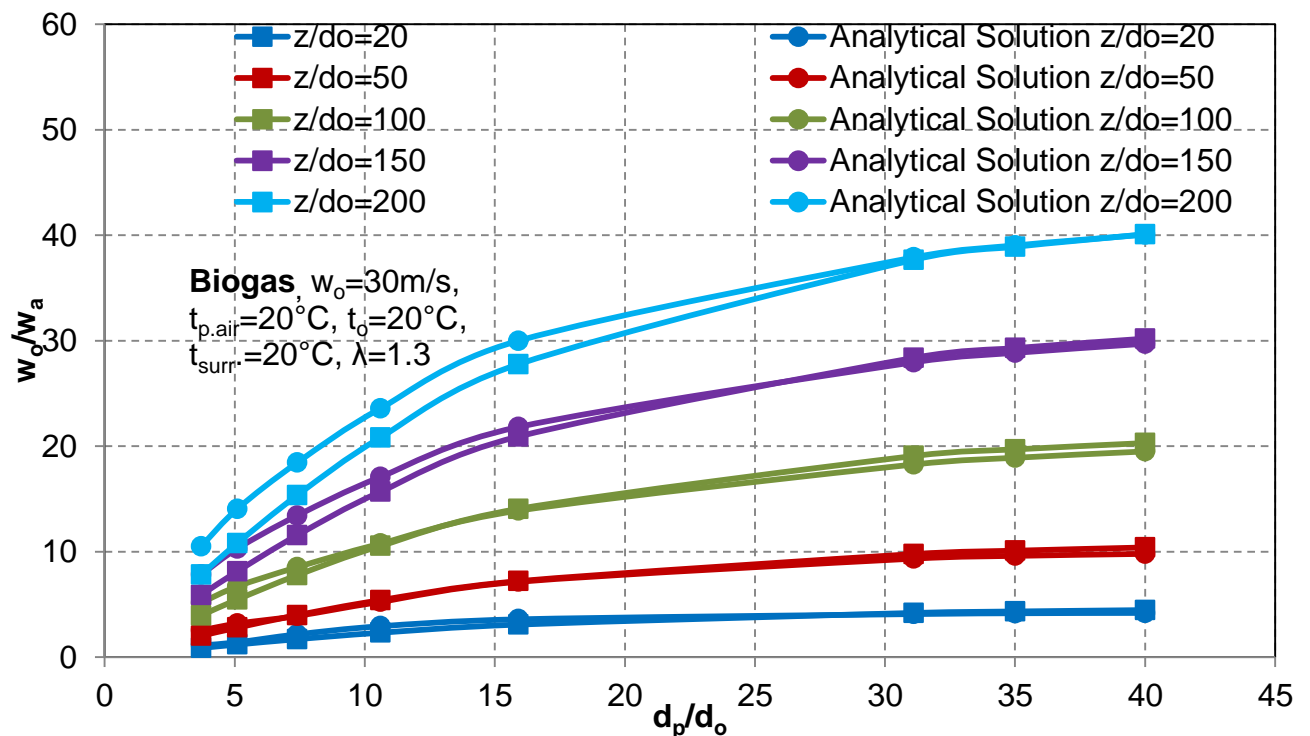

Figure 5.13: Numerical and analytical solution of dimensionless axial velocity as a function of dimensionless annular diameters at different dimensionless axial positions at using Biogas as a fuel
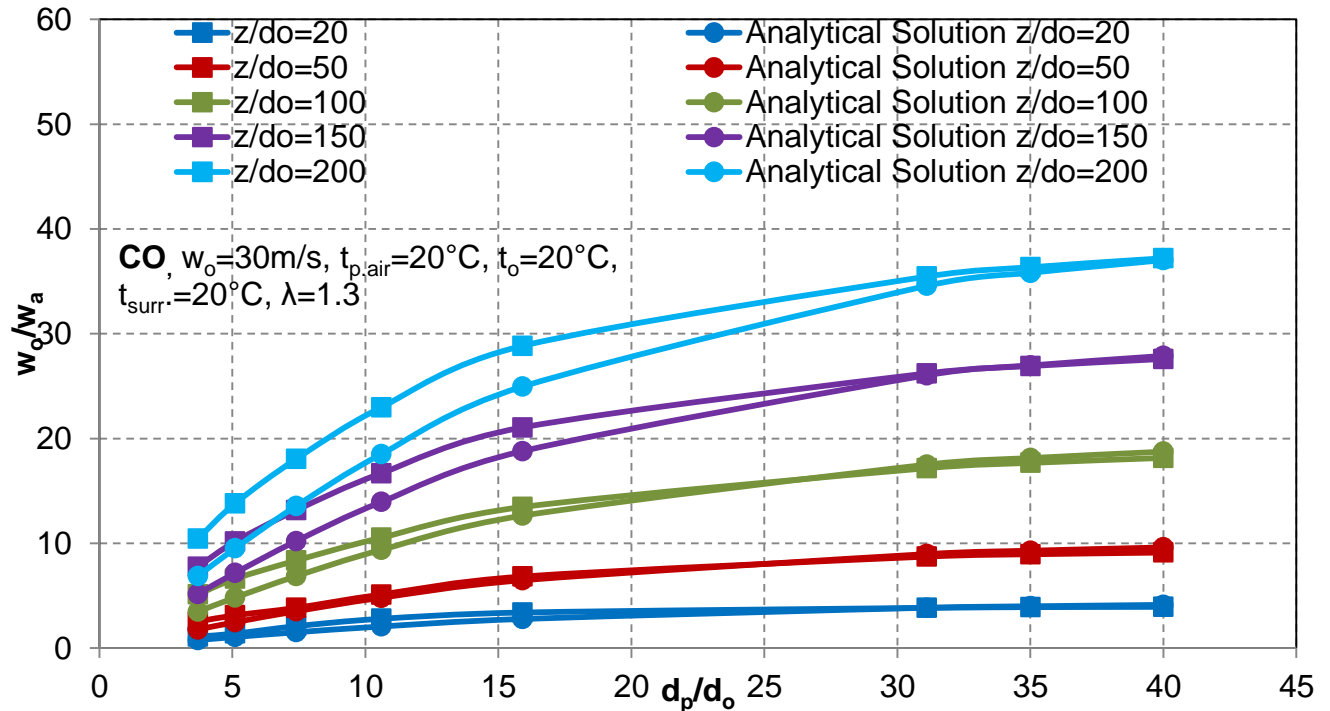
Figure 5.14: Numerical and analytical solution of dimensionless axial velocity as a function of dimensionless annular diameters at different dimensionless axial positions at using CO as a fuel

5.3.2 Influence of air inlet diameter on mass fraction of fuel

The dimensionless mass fraction of different gaseous fuels (CH_4, Biogas and CO) as a function of the air inlet diameters is studied.

The dimensionless annular diameters, velocities and the excess air number are same as mentioned above (section 5.31).

Figure 5.15 describes the influence of dimensionless annular diameter on the inverted dimensionless axial mass fraction (x_o/x_a) at using CH_4 as a fuel.

It can be noted that the dimensionless axial mass fraction decreases with increasing dimensionless annular diameter. It decreases by 76% with increasing dp/do from 3.7 to 15.9 at z/do=100. While it does not change anymore with increasing dimensionless annular diameter after dp/do=31.1. At z/do=100, it decreases by 74% with increasing dp/do from 3.7 to 15.9. In this case also it does not change anymore with increasing dimensionless annular diameter after dp/do=31.1.

Figure 5.16 and Figure 5.17 describes the influence of dimensionless annular diameter on the inverted dimensionless axial mass fraction (x_o/x_a) at using Biogas and CO as a fuel respectively. In general, it can be noted that the dimensionless axial mass fraction decreases with increasing dimensionless annular diameter. Here also it does not change anymore with increasing

dimensionless annular diameter more than dp/do=31.1. Which means the behaviour of annular ring burner change to the free jet after dp/do =31.1(w_p/w_o=0.013) and that independence on kind of gaseous fuel.
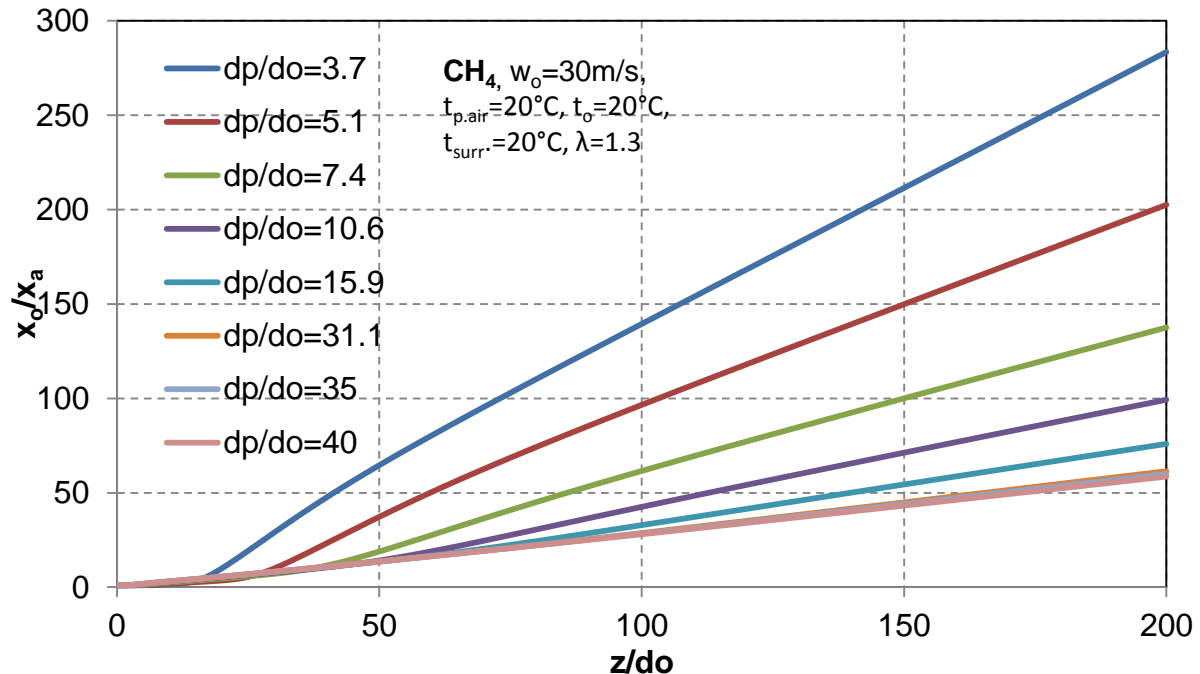

Figure 5.15: The dimensionless axial mass fraction of fuel as a function of dimensionless annular diameters at different dimensionless axial positions, at using CH4 as a fuel
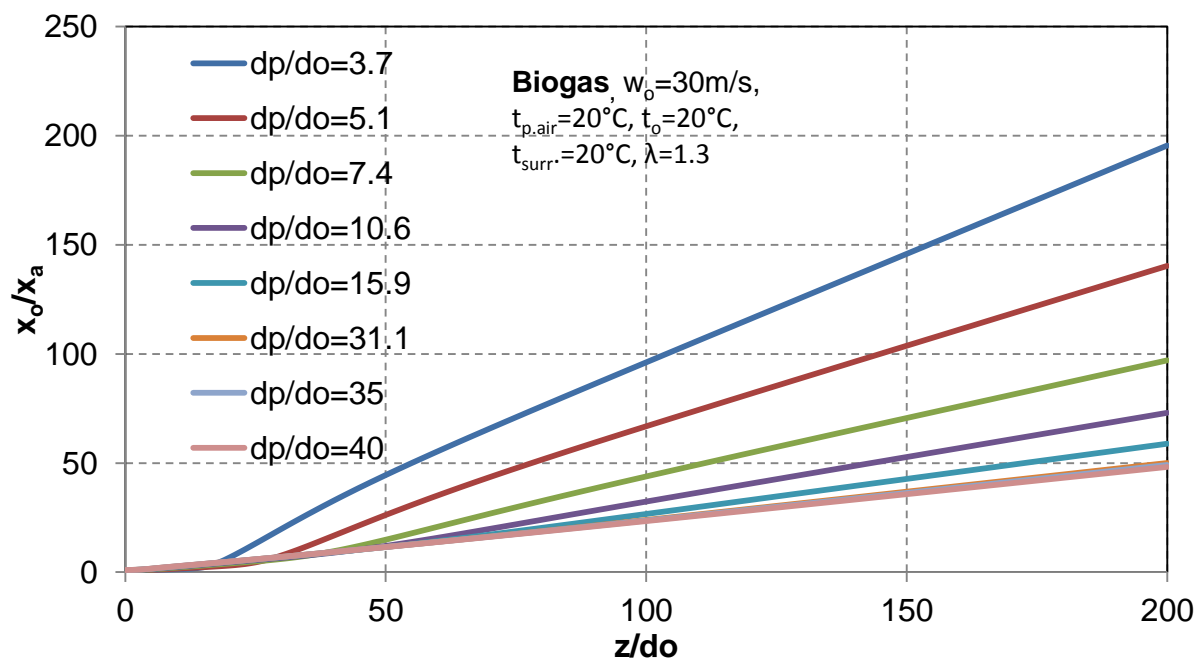

Figure 5.16: The dimensionless axial mass fraction of fuel as a function of dimensionless annular diameters at different dimensionless axial positions, at using Biogas as a fuel
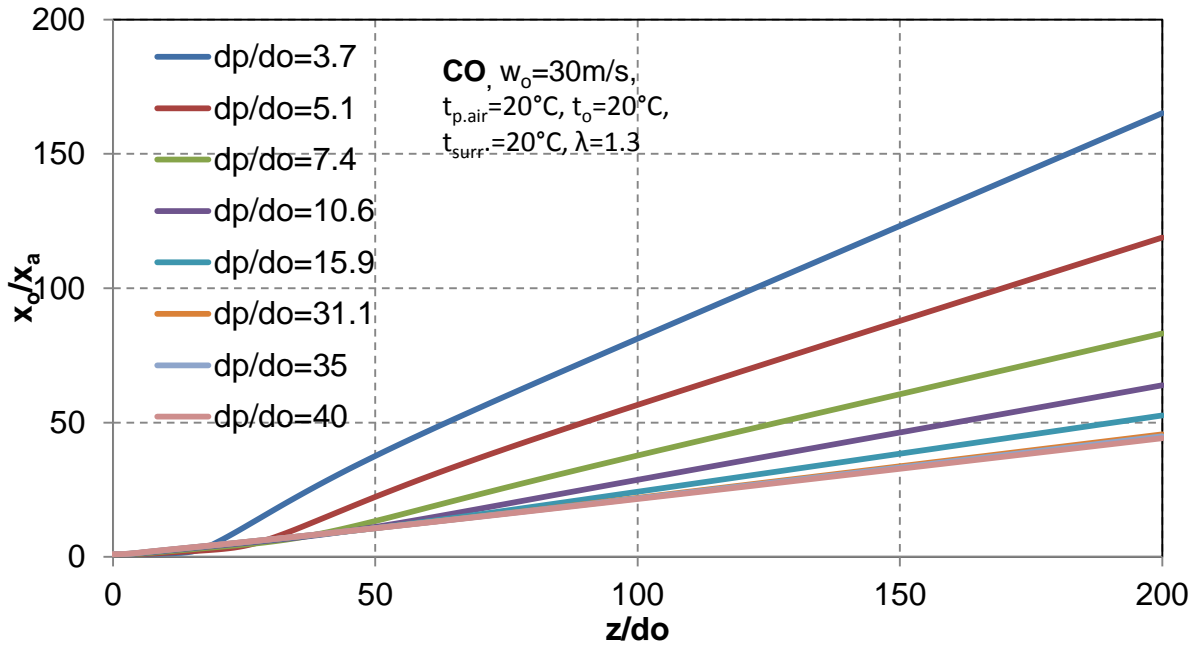
Figure 5.17: The dimensionless axial mass fraction of fuel as a function of dimensionless annular diameters at different dimensionless axial positions, at using CO as a fuel

The dimensionless mass fraction of fuel (CH_4, Biogas and CO) as a function of The dimensionless annular ring burner diameter is calculated analytically by using equation (5.24) as it is shown below

$$\frac{x_o}{x_a} = 0.5 \left\{ \frac{\rho_j}{\rho_f}\left(1 + 2 * \frac{z}{d_o} * \tan\frac{\alpha}{2}\right) * \left[\frac{\rho_f}{\rho_j} + \frac{\rho_f}{\rho_j} * \frac{\rho_f}{\rho_p} * \frac{\left(\lambda L * \frac{d_o}{d_p}\right)^2}{1 - \left(\frac{d_o}{d_p}\right)^2}\right]^{\frac{1}{2}} \right\}.$$

Then the analytical results is compared with the numerical results. The boundary condition, i.e., annular diameters, velocities and the excess air number are same as mentioned above (section 5.3.1).

Figure 5.18 describes the influence of dimensionless annular diameter on the dimensionless axial mass fraction (x_o/x_a) at using Methane as a fuel. It also shows the comparison between the numerical and analytical results. In general, both solutions (the numerical and analytical results) the dimensionless axial mass fraction (x_o/x_a) decrease with increasing the dimensionless annular diameter. But the rate of decrease is decreasing upto 22.6% with increasing dp/do from 15.1 to 31.1. After that, it can note the dimensionless annular diameter has no effect on dimensionless axial mass fraction.

Figure 5.19 and Figure 5.20 shows the influence of dimensionless annular diameter on the dimensionless axial mass fraction (x_o/x_a) at using Biogas and CO as a fuel respectively. In general, the behaviour of dimensionless axial mass fraction as mentioned above (CH_4 as a fuel). The numerical results in the different positions (z/do) are identical with analytic results especially at d_p/d_o <15.9. The maximum relative error is ~10% at d_p/d_o=40 and 200 z/do. In case of $d_p/d_o \geq 15.9$, the maximum relative error is ~29.5% of the position z/do=200 at using CO as a fuel. The dimensionless mass fraction of CH_4 at different positions (z/d_o) relatively is higher than the dimensionless mass fraction of Biogas and CO.
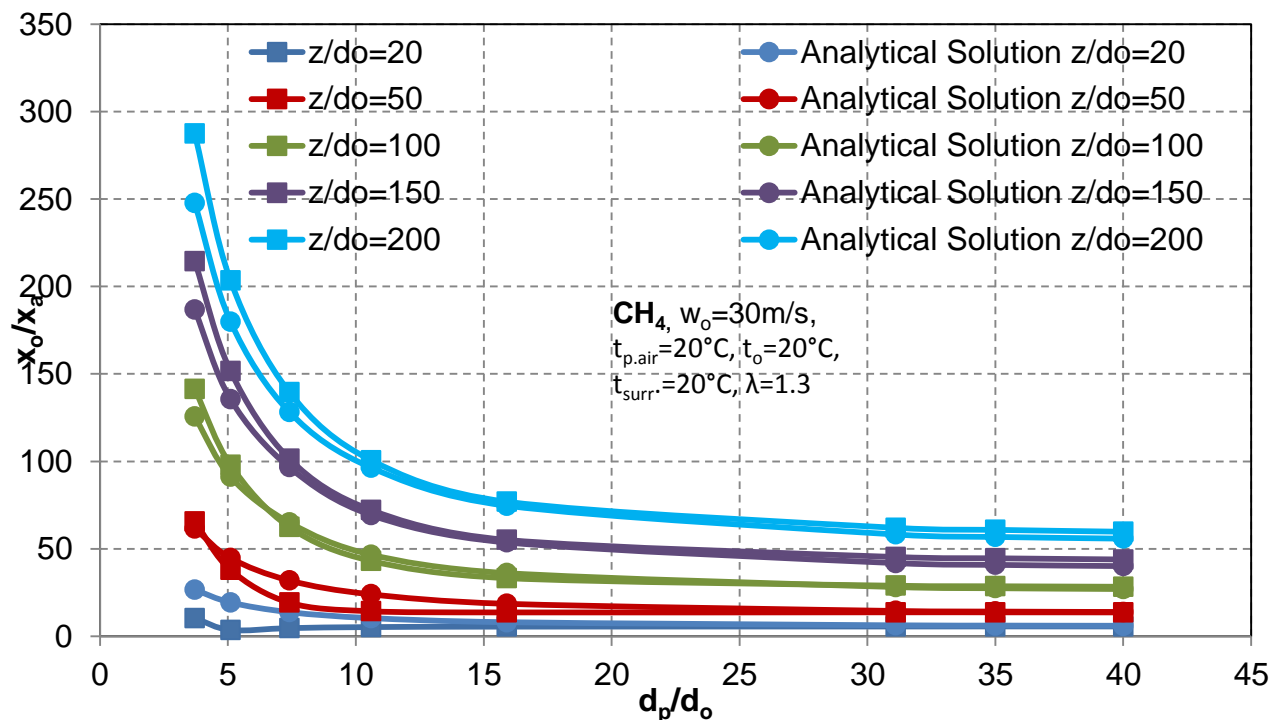

Figure 5.18: Numerical and analytical solution for dimensionless axial mass fraction of fuel as a function of dimensionless annular diameters at different dimensionless axial positions, at using CH_4
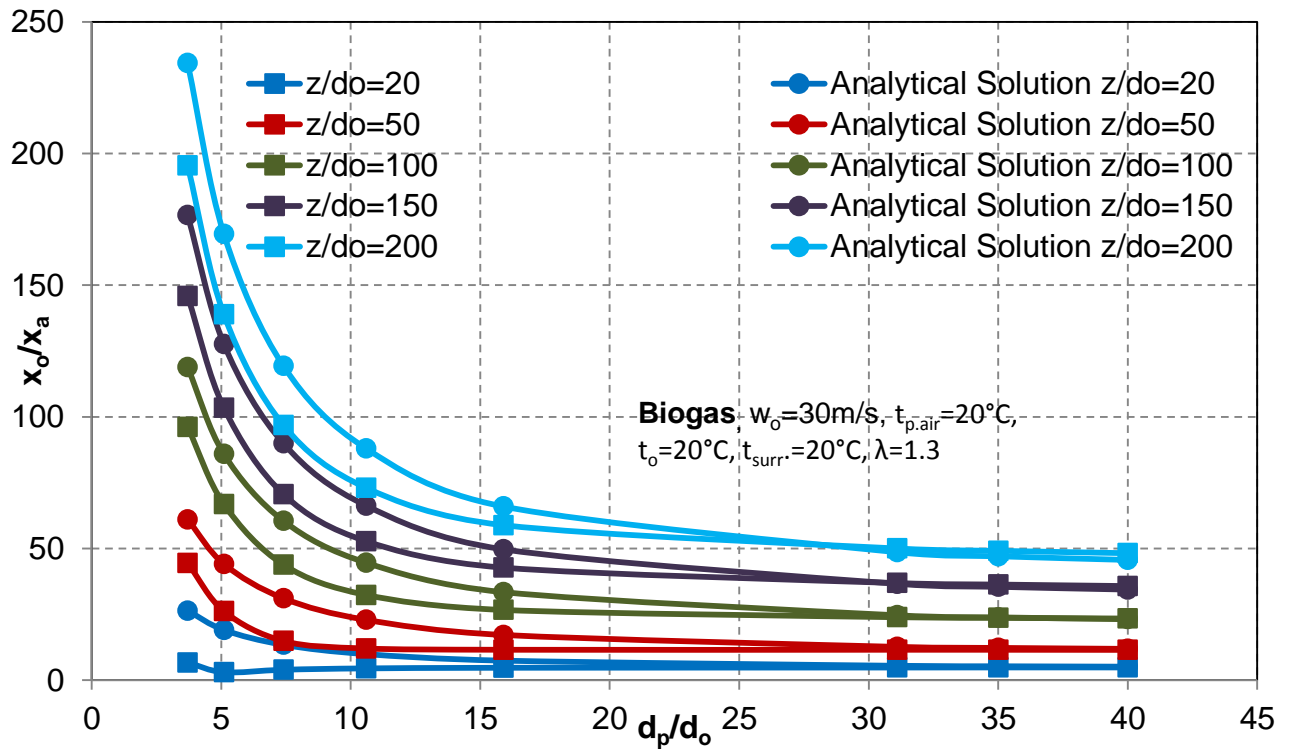
Figure 5.19: Numerical and analytical solution for dimensionless axial mass fraction of fuel as a function of dimensionless annular diameters at different dimensionless axial positions, at using Biogas
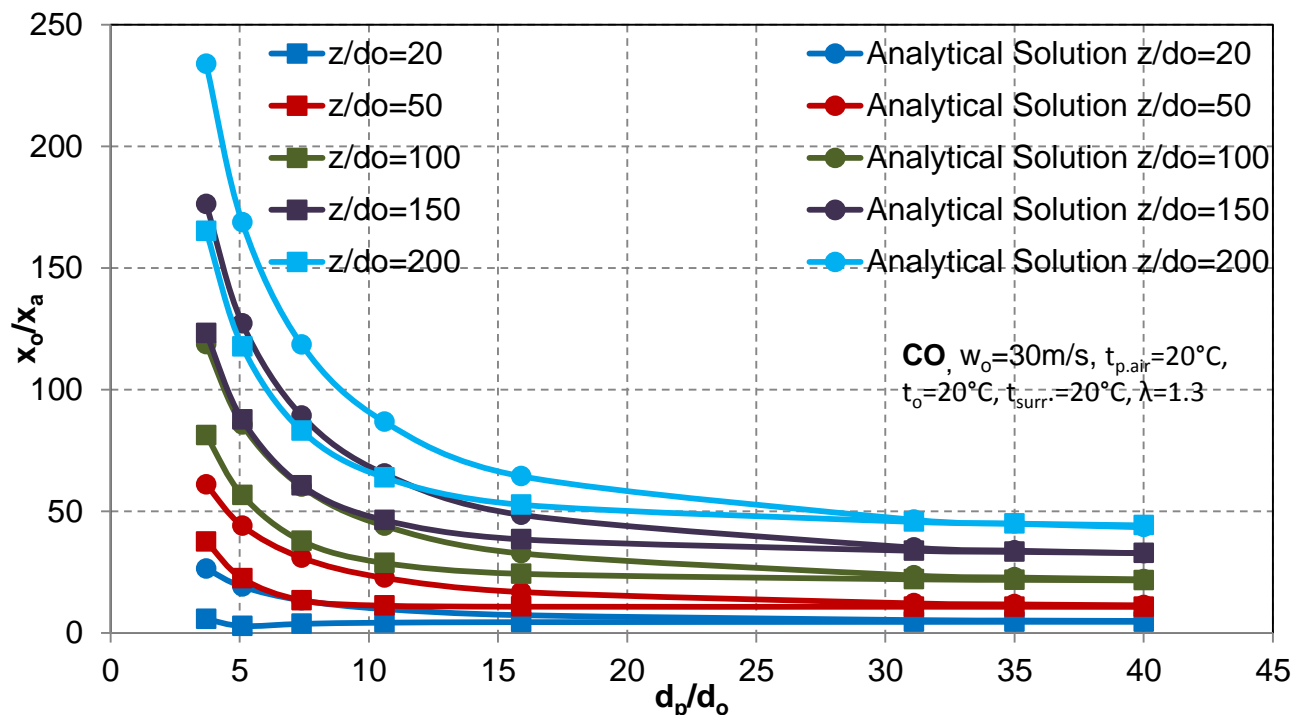

Figure 5.20: Numerical and analytical solution for a dimensionless axial mass fraction of fuel as a function of dimensionless annular diameters at different dimensionless axial positions, at using CO as a fuel

5.4 Flame simulation when the surrounding is air

In this section, the effects of the operating conditions, including primary air inlet velocity and ambient air temperature on flame behaviour are studied, in addition to the effect of geometric parameters (air inlet diameter) also are presented and investigated. The temperature contours are used to visualize the flame, and three different kinds of gaseous fuels (CH4, Biogas, and CO) are employed.

5.4.1 Species distributions

The typical mass fraction profiles of individual species during the combustion of methane along the flame direction and in a radial direction are shown in Figure 5.21. The dimensionless annular diameter is 10.6 and the gas fuel is Methane. In general, the combustion reaction starts at the rim of the burner and methane is converted to CO2 and water vapour along the flame. The mass fraction of methane fuel decreases along the flame, while the oxygen is entirely consumed by the fuel combustion at the beginning and then the concentration of O2 increase along the axial direction. The same behaviour is observed in radial direction.
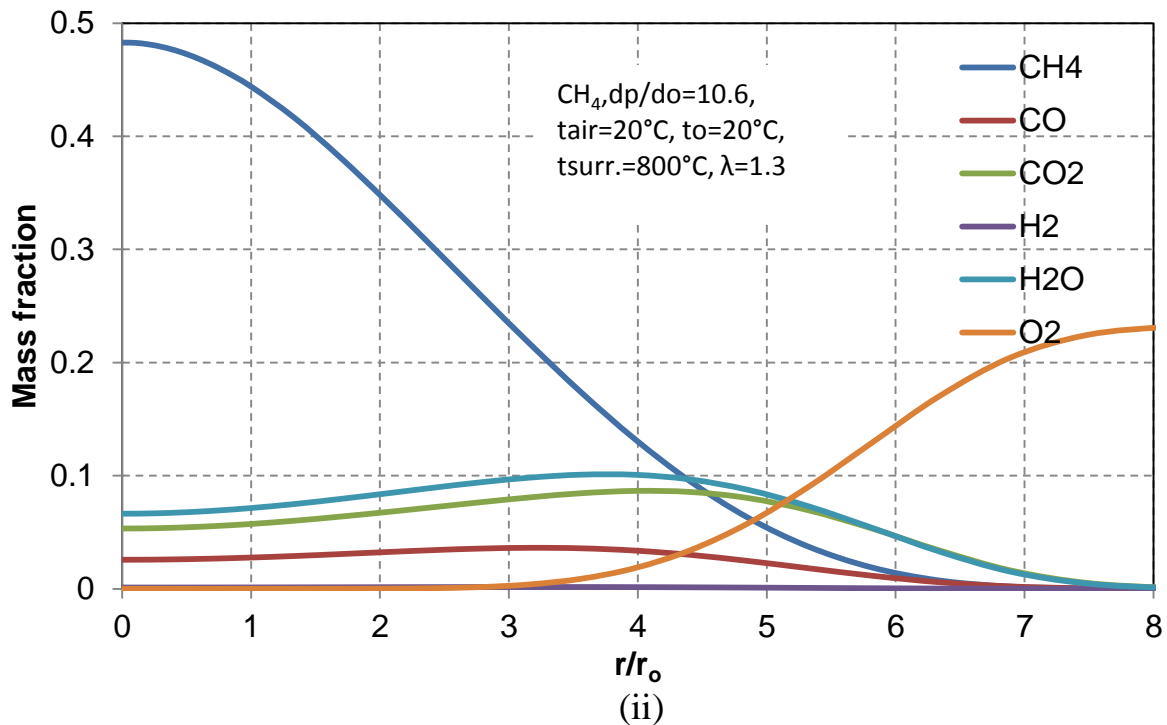

(i)
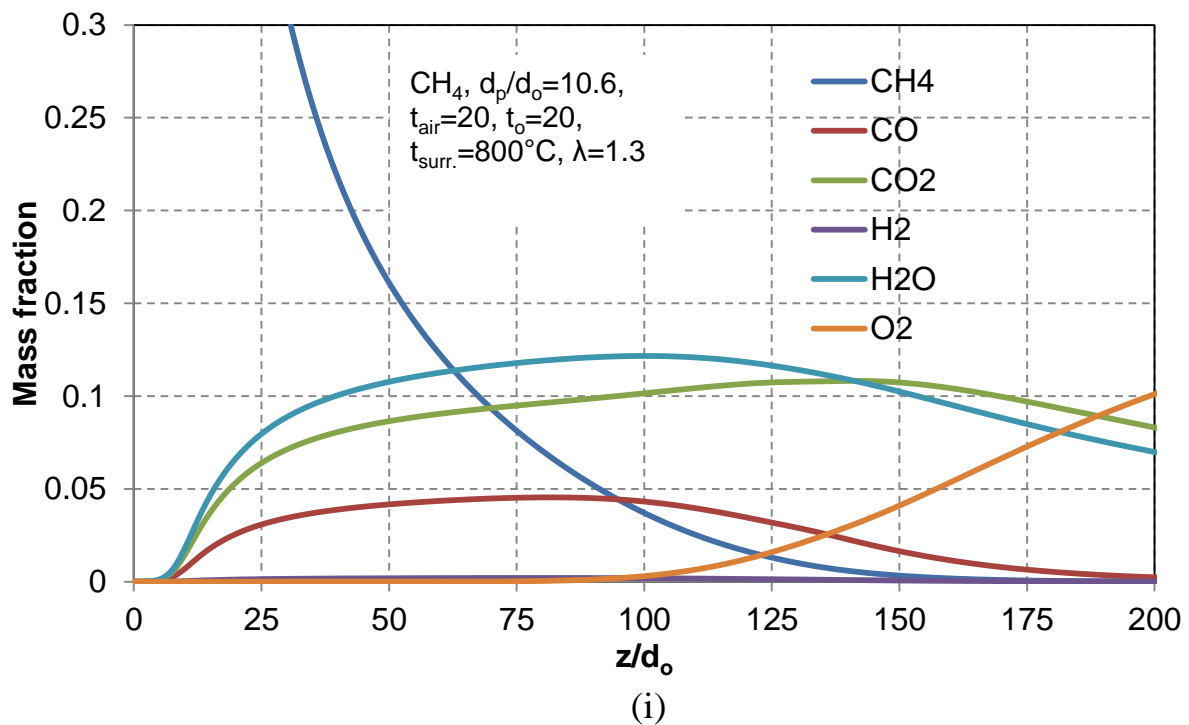
Figure 5.21: Species mass fraction distribution (i) axial distribution, (ii) radial distribution

5.4.2 Influence of air inlet diameter

The results of the influence of air inlet diameter on flame length and flame temperature will be presented and discussed in this section. The dimensionless annular diameter from 3.7 to 40 are proposed. The fuel velocity is always constant (30 m/s). The temperature of the fuel, primary air and the surrounding air is 20℃. The excess air number (λ) is constant and equals to 1.3. The primary air inlet flow rate is also constant. The ratio of velocity of primary air to the velocity of the fuel (w_p/w_o) is shown in table 5.1.

Figures 5.22 and 5.23 demonstrate the influence of dimensionless annular diameter on the axial temperature distribution and on dimensionless axial mixture fraction profiles along the flame direction, respectively. Figure 5.22 shows the temperature profiles. The temperature in all cases increases dramatically near the burner rim and reach to the peak point and then decreases with the same trend to a relatively lower value. The trend is changing gently along the flame direction in the end. The peak temperature of the flame goes up greatly (from nearly 1220°C to 1800°C) with increasing the air inlet diameter. Moreover, the highest temperature point is shifted to the distant site in axial direction. This phenomenon is due to the increase in mixing area between combustion air and fuel with the increasing air inlet diameter. The flame volume

gets larger and also the temperature of the flame increases. On the contrary, the velocity of the primary air increases by decreasing the diameter. This contributes to better mixing between fuel and air. As a consequence, the combustion completes in a short distance. Therefore, peak temperature is always near the burner rim with decreasing the air inlet diameter. Finally, it can be seen clearly that as the diameter ratio increase from 31.1 to 40, the peak temperature value does not change distinctly, and the peak temperature point also do not shift any more again. Consequently, the flame temperature does not increase.
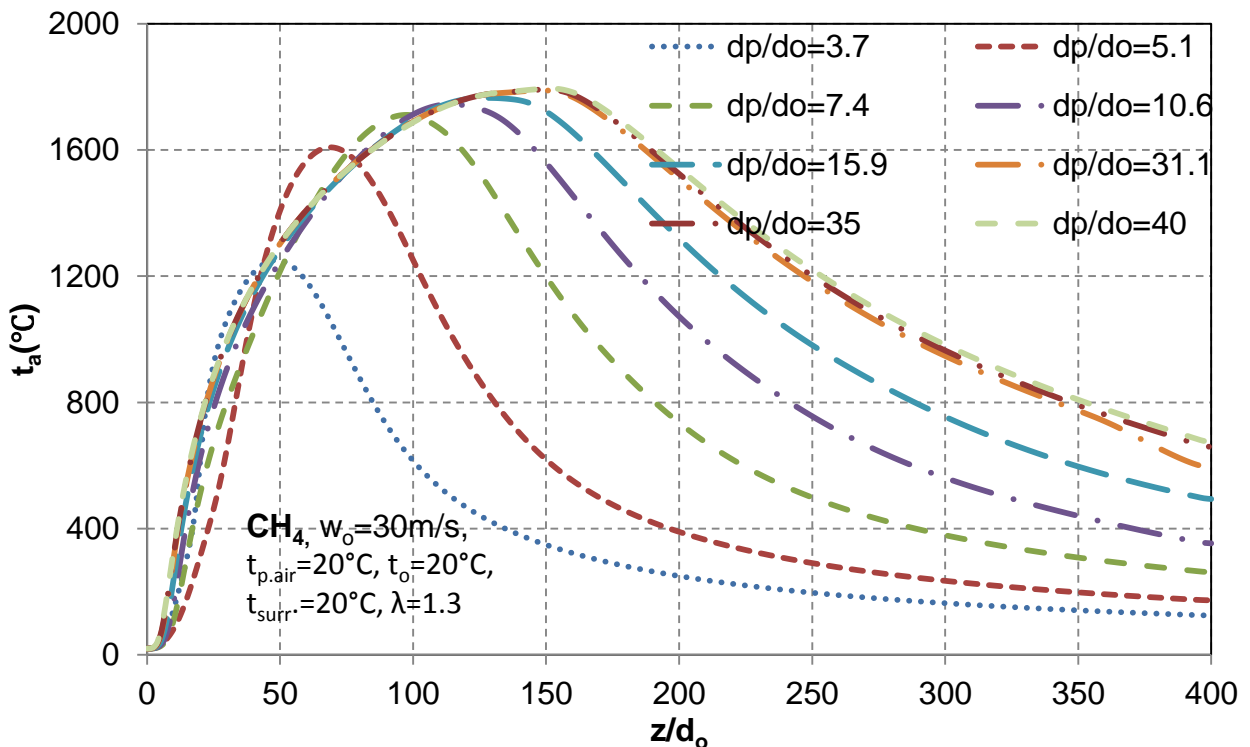

Figure 5.22: Influence of air inlet diameter on axial temperature distribution along the flame.

Figure 5.23 describes the influence of air inlet diameter on the inverted dimensionless axial mean mixture fraction profiles along the flame. The flame length is measured using a conserved scalar quantity; mean mixture fraction. It can be defined that the flame length ends at a point where the simulated mean fraction is the same as the stoichiometric mixture fraction [51]. The values stoichiometric mixture fraction of the studied gaseous are given in table 5.2. The air inlet diameter makes a great influence on the mixture fraction and subsequently on the flame length. It can be observed that the flame length increases from ~50 to more than ~150 with the increasing diameter ratio from 3.7 to 31.1. Moreover, the flame length does not change any more when the diameter ratio is larger than 31.1. Furthermore, It can also be observed, the flame length is directly proportional to the dimensionless annular diameter and

that due to the effect the velocity of the primary air. Which tends to improve the fuel air mixing. The temperature contours of the flame with a different dimensionless annular diameter are shown in Figure 5.24. The flame length and temperature change could be visualized in clearly in there temperature contour.

Table 5.2: Physical and thermal properties of fuels [51]

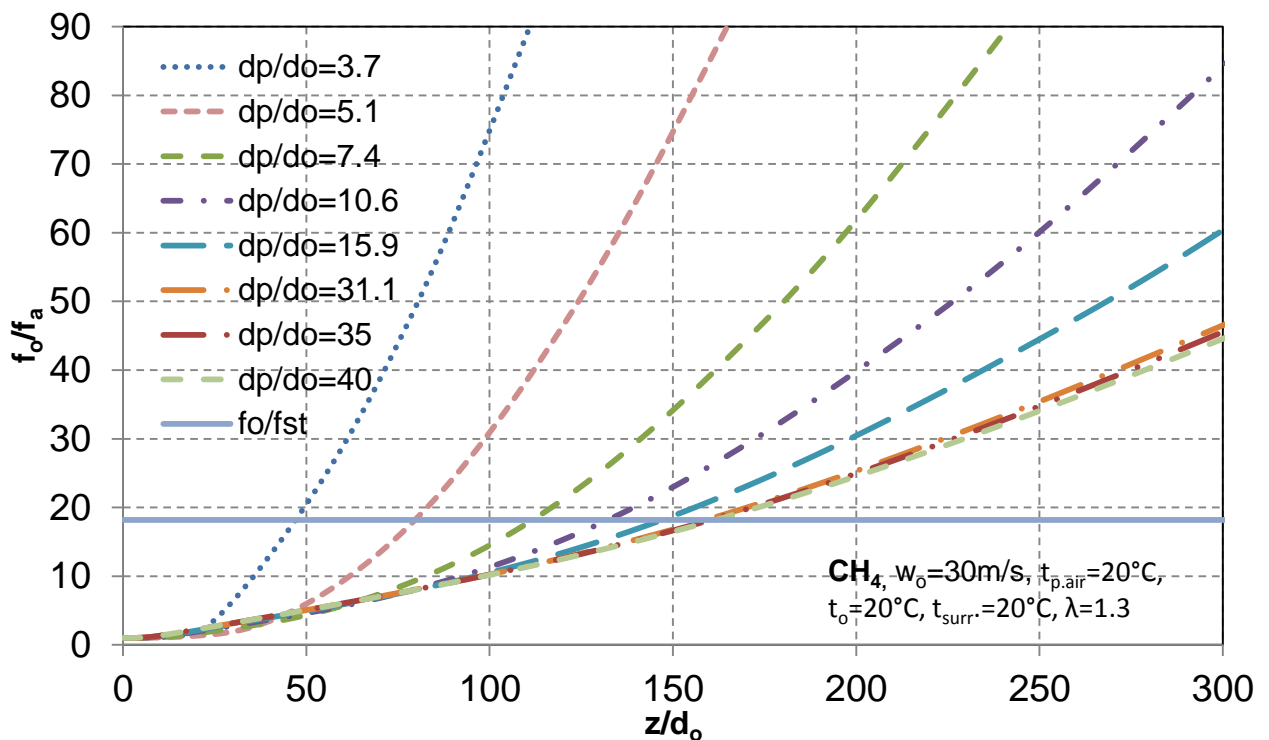| Fuel	L kg$_{air}$/kg$_o$	ρ_o kg/m^3	h$_u$ Mj/kg$_o$	M$_o$ Kg/kmol	$\tilde{L}$ m^3_{air}/m^3_0	f$_{st}$	K (W/m.K)
Ch4	17.3	0.668	50	16	9.52	0.055	0.035
Biogas	5.45	1.248	20.5	30	4.76	0.155	0.0295
CO	2.46	1.165	10.1	28	2.38	0.289	0.024

Figure 5.23: Influence of air inlet diameter on dimensionless axial mixture fraction profiles along the flame

The inverted dimensionless axial mixture fraction along the flame for Biogas and CO as fuels are shown in Figure 5.25 (i)and (ii). The fuel velocity is 30 m/s. Temperatures of the fuel, primary air and the air of the combustion chamber surrounding are 20°C. According to the flame length definition, the flame is disappearing at the point that the mixture fraction is equal to the stoichiometric mixture fraction. As mentioned before. The smaller stoichiometric mixture fraction is the longer the flame length. Consequently, the flame length of CH$_4$ is the longest one (see figure 5.23), while the CO fuel has the shortest flame length, and these independent of the diameter of the air inlet diameter. The flame length is increased by ～ 98% and 16% for   CH4 and Biogas

respectively, with increasing d_p/d_o from 5.1 to 31.1. While it can be observed that the diameter of the air inlet has not a significant impact on the flame length of the CO.
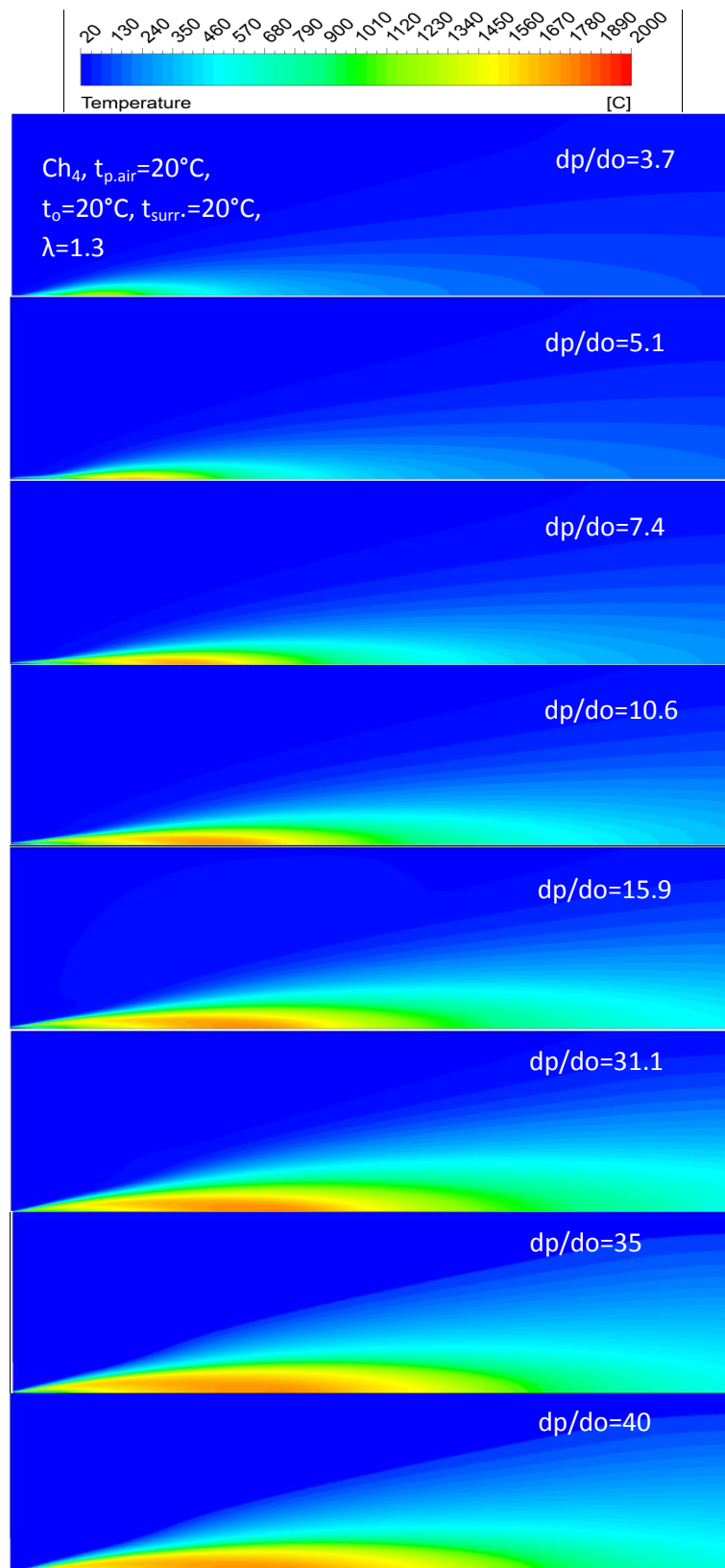

Fig. 5.24: Contours of temperature as a function of dimensionless annular diameter at using methane as a fuel
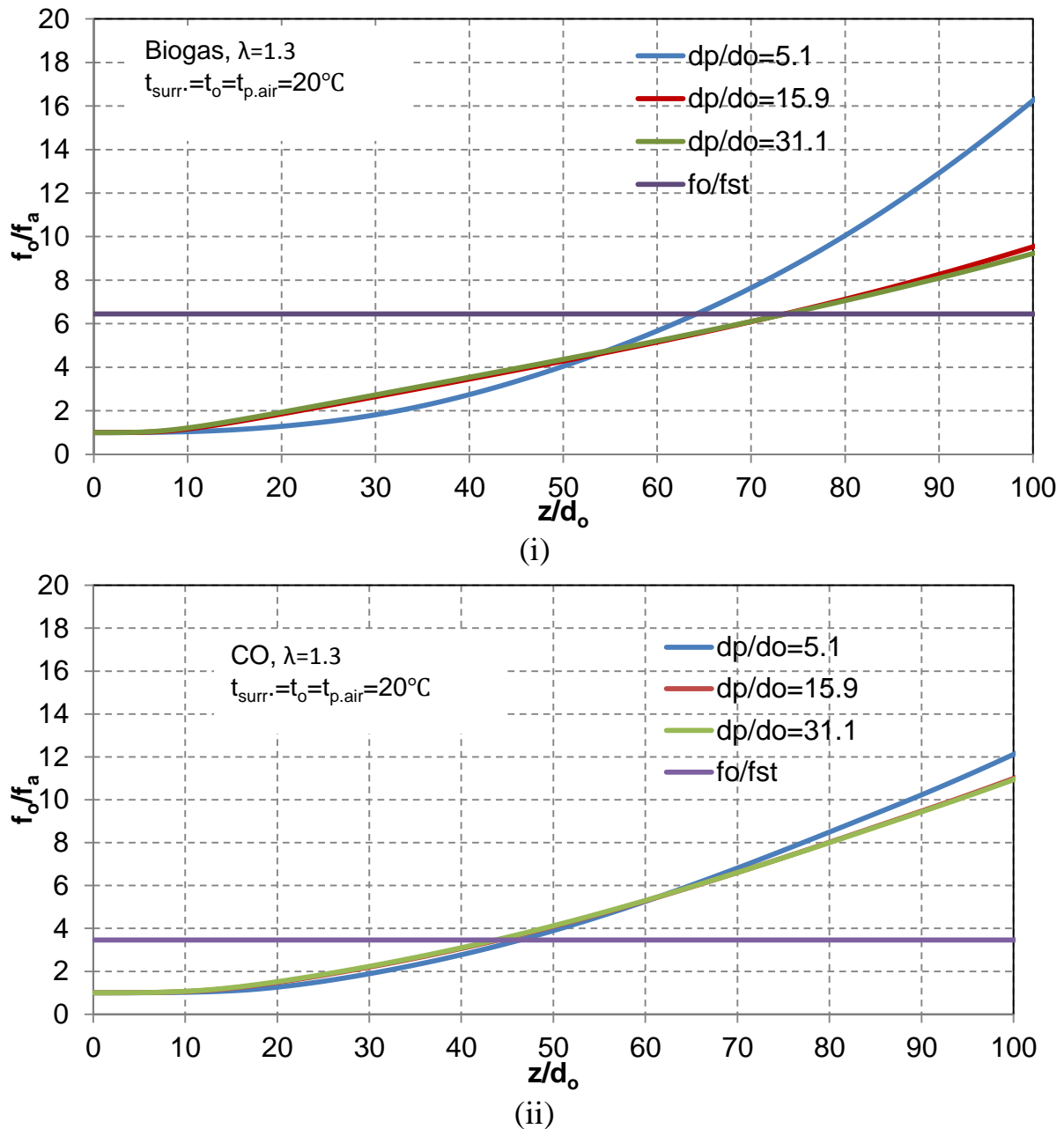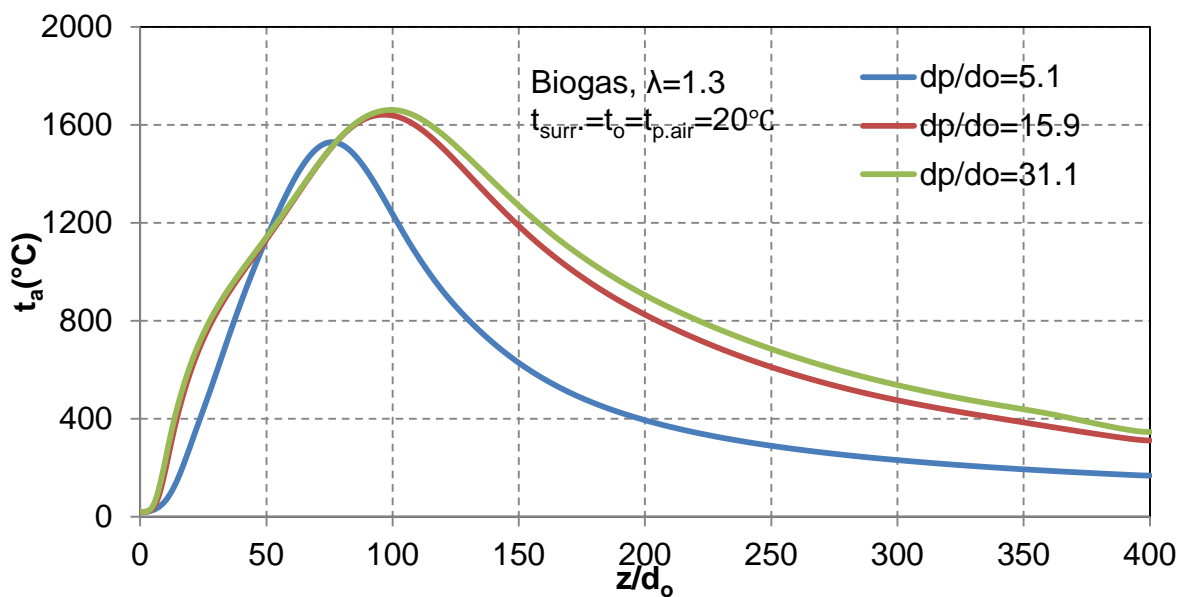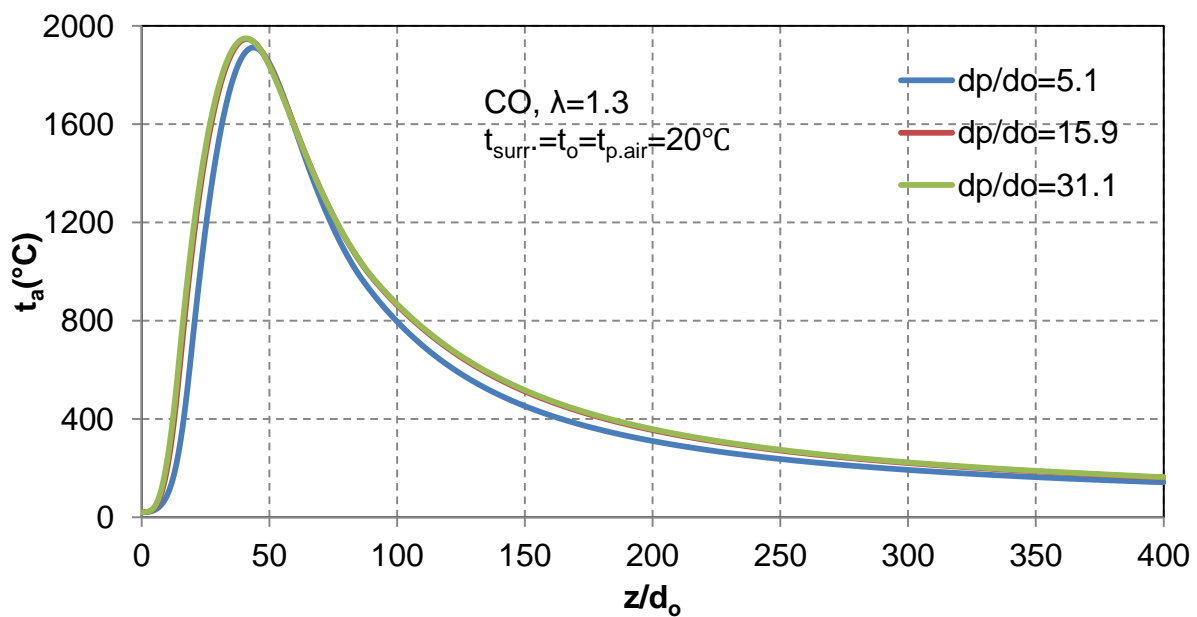
(i)

(ii)

Figure 5.25: Comparison of dimensionless axial mixture fraction along the flame for Biogas and CO fuels with different dimensionless annular diameter

Figure 5.26 (i) and (ii) show axial temperature profiles with different dimensionless annular diameters at using Biogas and CO as a fuel. As displayed in the figure, the CO has a peak temperature while the Biogas is the lowest. This behaviour is observed at different air inlet diameters. The peak temperature of Biogas fuels shift up and also shift to the right with increasing dimensionless annular diameter, while the temperature profiles of CO fuel does not change. Regarding Biogas fuels can be explained this behaviour by that, when increasing the air inlet diameter the mixing area increases and consequently increase the flame volume. On the contrary, decrease the air inlet diameter increases the air

inlet velocity, it contributes to the mixing process. The high air velocity the better mixing between air and fuel. As a result, the combustion process completes in a short distance from the burner rim, which results in a decrease in flame volume and the peak temperature point are closer to the burner rim. In case of using CO as a fuel, the air inlet diameter has a small effect on the flame temperature profiles, and the peak temperature is increased by ～5%. While the peak temperature for CH_4 (see figure 5.22) and Biogas increases by ～ 126% and 35% respectively.


(i)

(ii)

Figure 5.26: Comparison of axial temperature profiles along the flame for Biogas and CO fuels with different dimensionless annular diameter: (i) Biogas (ii) CO

5.4.3 The influence of surrounding air temperature

The effect of secondary or surrounding air temperature is investigated in this work. As a comparison, three kinds of fuels (CH_4, Biogas, and CO) operate in the same conditions are used. The primary air temperature is 20°C, and three different values (20°C, 500°C, and 1000°C) are used for the secondary air temperature. The dimensionless annular diameter 10.6, the excess air number 1.3, and fuel inlet velocity is 30 m/s are used.

The influence of the secondary air temperature on the dimensionless axial velocity for three types of gas fuels is shown in figure 5.27(i),(ii) and (iii). In general, It can be observed that, the dimensionless axial velocity decreases at first, and then the slope is decreased after z/do=60. The trend is similar for all kinds of the fuels at any secondary air temperature. Furthermore, there is no big difference between the axial velocity profiles at z/do<60. After that, it can be noted that the dimensionless velocity increases with the increasing temperature of the secondary air. Furthermore, the dimensionless velocity of CO and Biogas fuel are little bit higher than the dimensionless velocity of CH_4 fuel at the dimensionless axial position (z/do) less than 40. This phenomenon is same in these three velocity profiles. This can be attributed to the density. The highest density the higher velocity profile is. From table 5.2, both of the densities of CO and Biogas are higher than the density of CH4. The dimensionless velocity profile of CO fuel is decreasing at a faster rate than the dimensionless velocity of other two fuels at z/do >40. This is due to the mixing process of CO fuel is complete with a relatively shorter distance than the other two fuels.
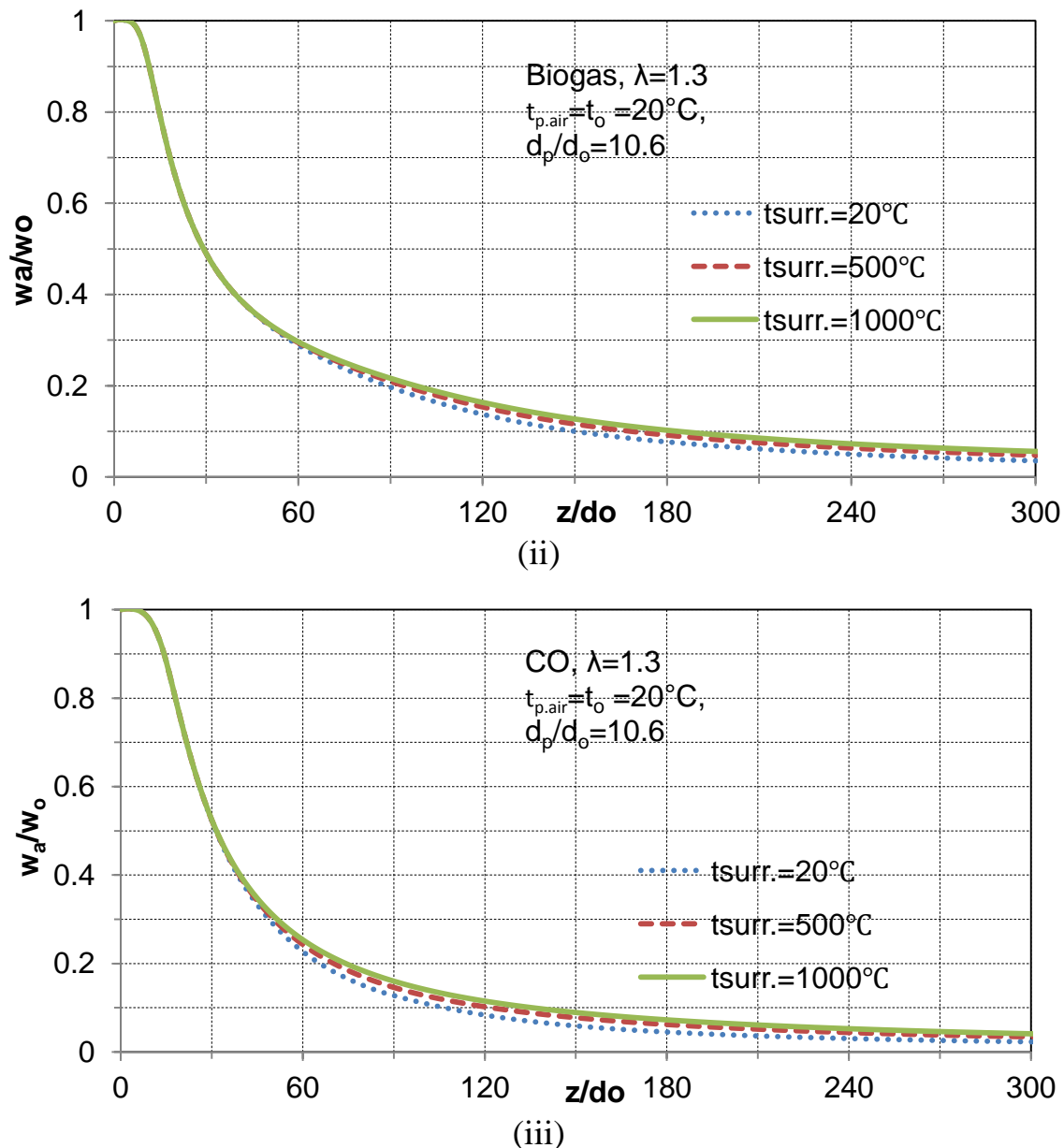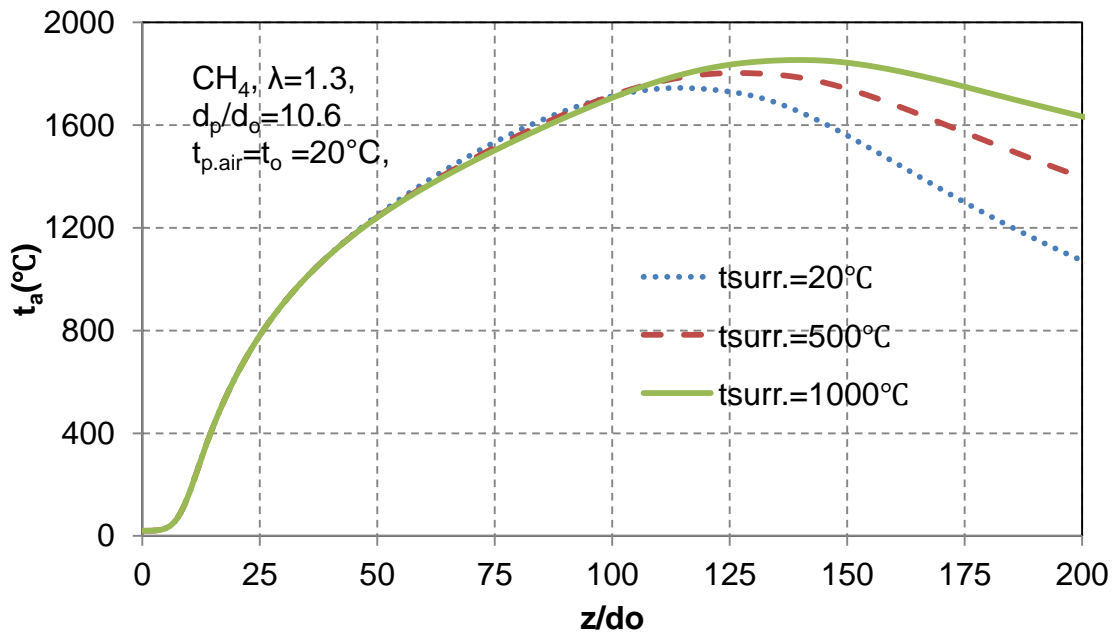

(i)
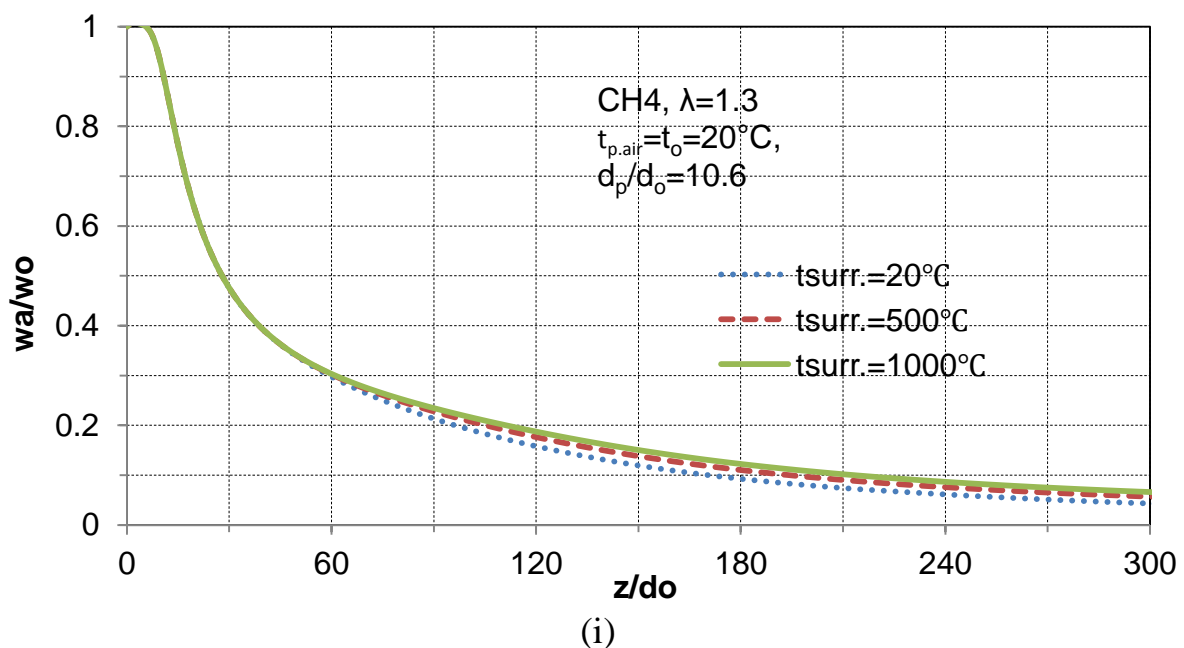
Figure 5.27: Influence of secondary air temperature on dimensionless axial velocity profiles along the flame: (i) CH4, (ii) Biogas and (iii) CO
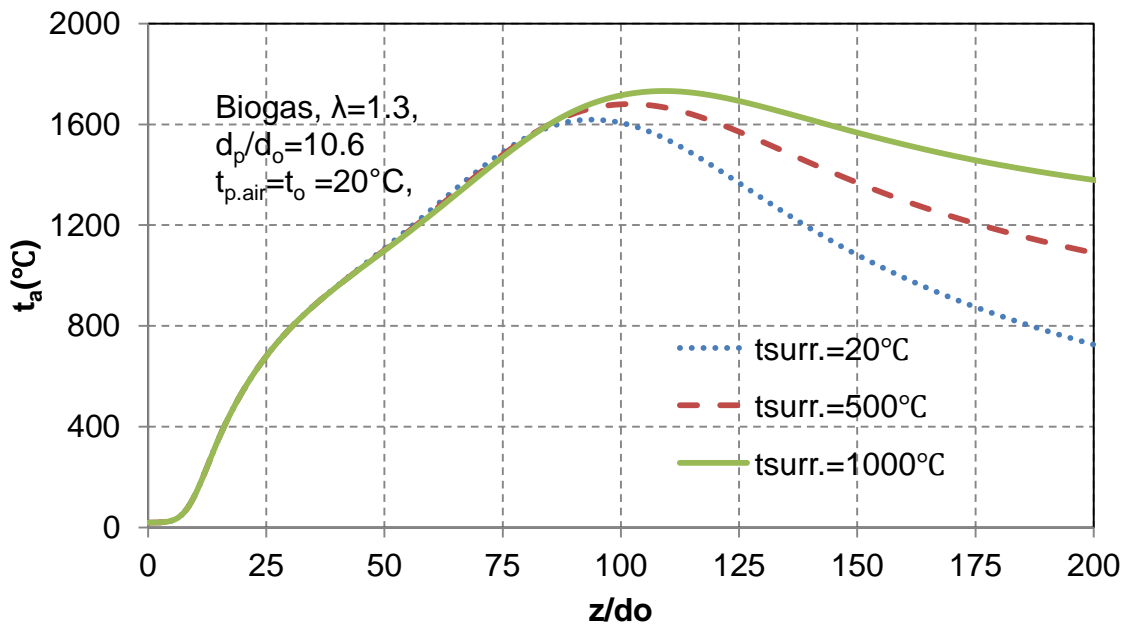
The influence of the secondary air temperature on the axial temperature profiles along the flame direction for different fuels is shown in Figure 5.28(i), (ii) and (iii).

In general, it can be seen that the axial temperature increases with the increasing secondary air temperature. As secondary air temperature increases the primary air temperature and thus increase the mixing temperature between fuel and air. As a consequence, it will increase the disorder of the system and that leads to the increased the available energy. The secondary air temperature has a significant effect on the temperature profiles of the CH_4 fuel and Biogas fuel, while it has a relative smaller effect on the temperature profiles of the CO fuel. Moreover, the

peak flame temperature of the CO fuel is the highest one and the Biogas fuel is the lowest one. The peak temperature point of CH_4, Biogas, and CO always changed within the range of position of z/do~ (120-140), (90-110), and (40-50) respectively with increasing the temperature of air surrounding from 20 to 1000 °C. Consequently, the flame length of CH_4 is longer than the flame length of Biogas, and the CO fuel has the smallest flame length.
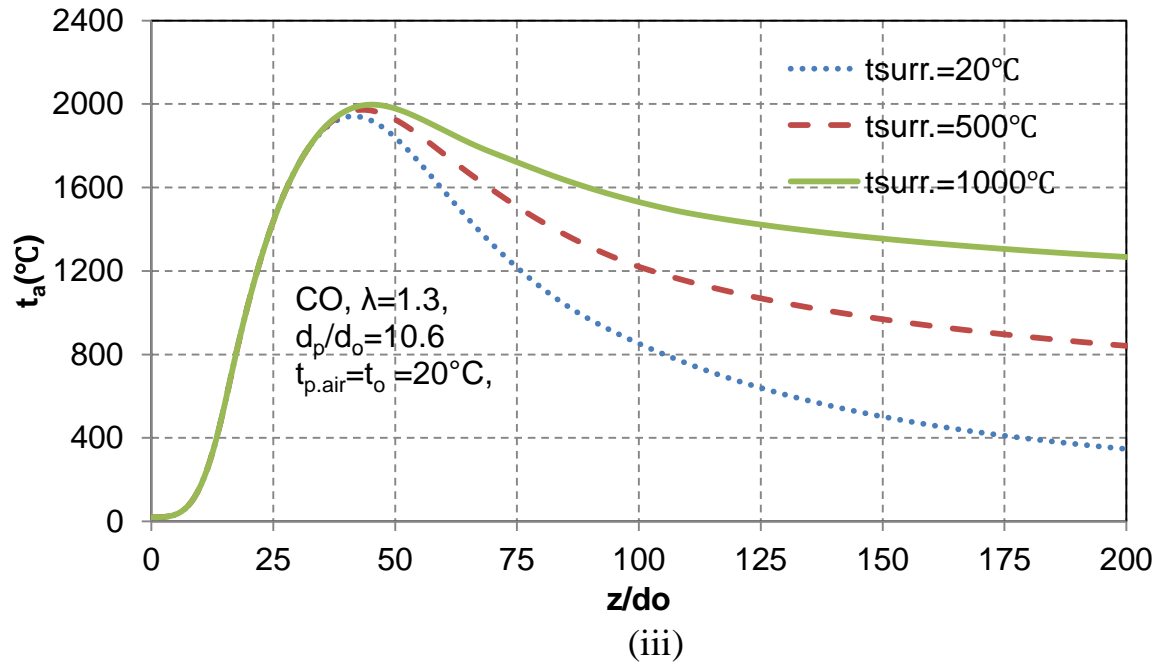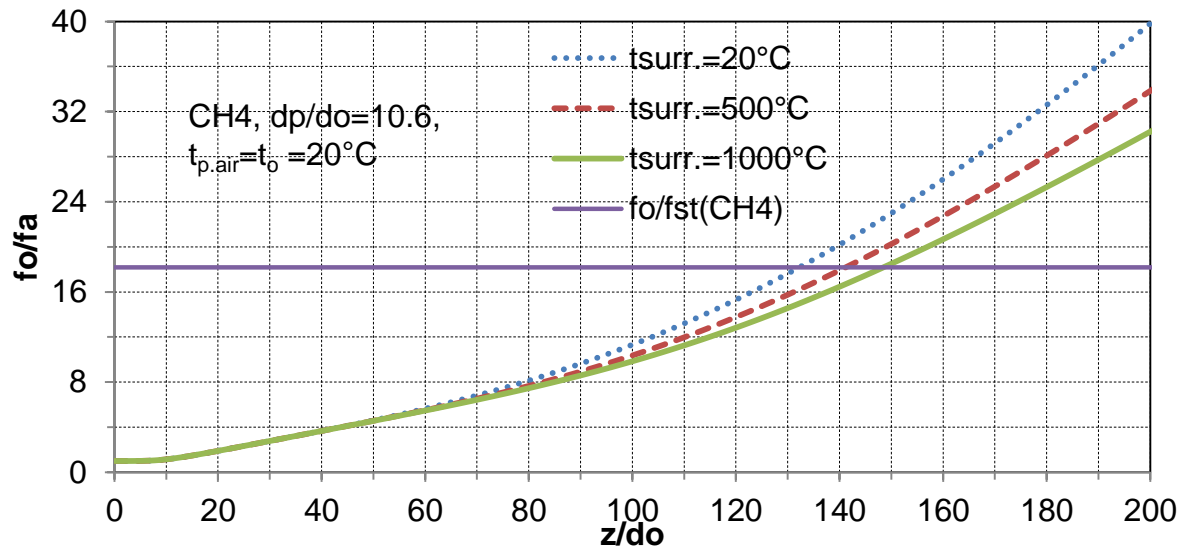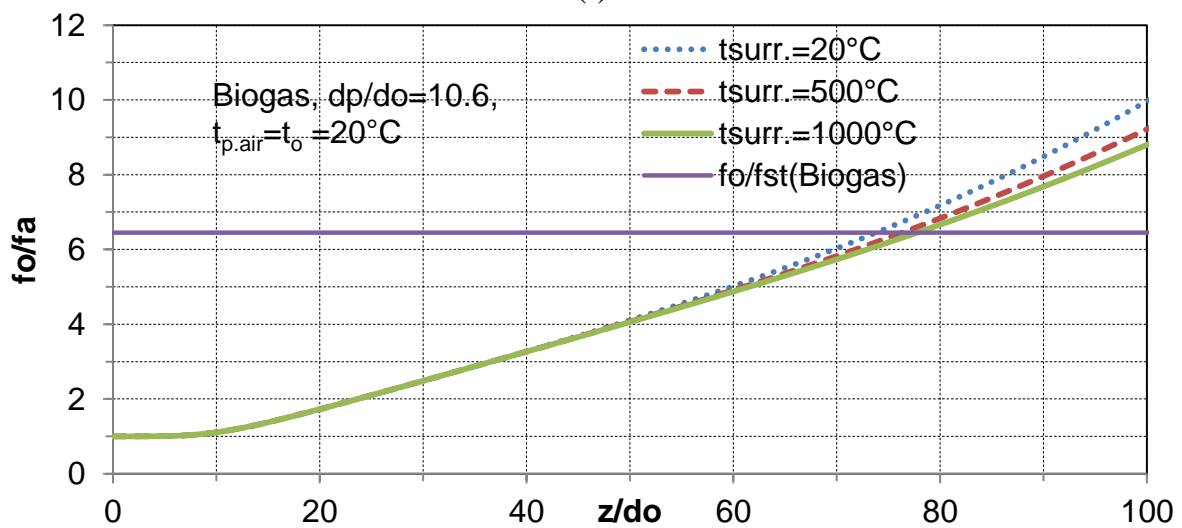

(i)

(ii)

(iii)

Figure 5.28: Influence of secondary air temperature on axial temperature profiles along the flame: (i) CH_4, (ii) Biogas and (iii) CO

The effect of secondary air temperature on the axial mean mixture fraction profiles is presented in the Figure 5.29(i), (ii) and (iii). Three different gaseous fuels are used (CH_4, Biogas and CO), at a different secondary air temperature i.e. 20°C, 500°C, and 1000°C.

The results of this figure demonstrate that the flame length increases with the increasing secondary air temperature and this trend is same for these three kinds of fuels. The influence of the secondary air temperature on flame length of Biogas and CO is smaller in comparison with CH_4. This is because, the stoichiometric mixture fraction of CH_4 fuel is larger than the Biogas and CO fuels, and the CO fuel has the smallest stoichiometric mixture fraction. Thus, the increase ratio of flame length with temperature of secondary air in more precisely are 11%, 7.5% and 4% for CH4, Biogas and CO is respectively. The temperature contours for three different gaseous fuels (CH4, Biogas and CO) with 20℃ secondary air temperature are displayed in figure 5.30. It can be seen from the figure, CO has the smallest flame hot area while the CH_4 has the largest one. In other words, the CO has the shortest flame length and the CH_4 has the longest flame length. And flame length for Biogas has a value in between them.
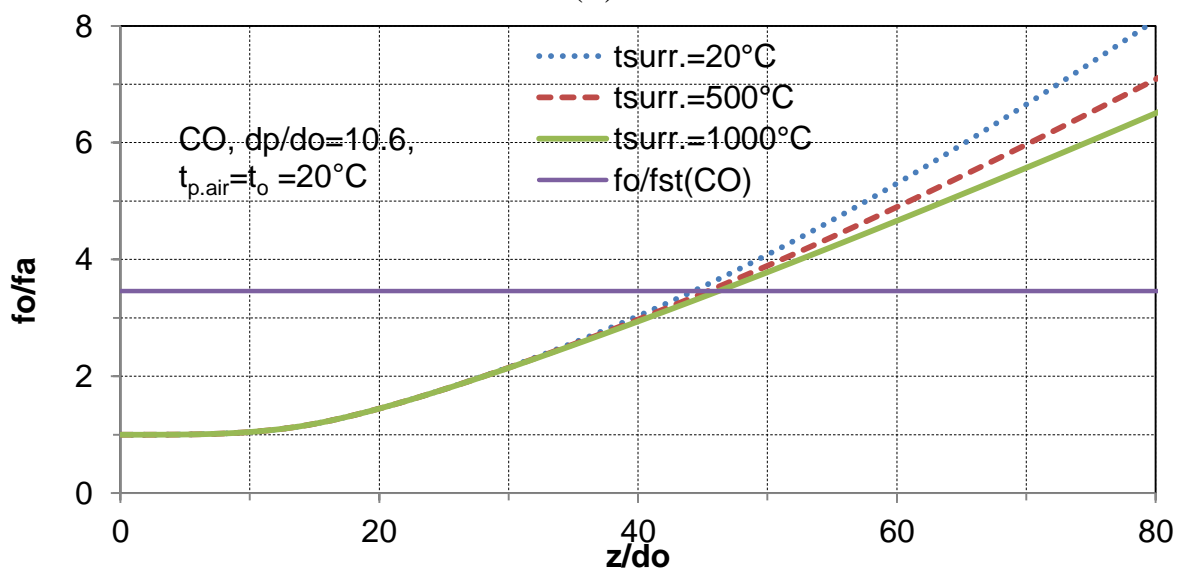
Figure 5.29: Influence of secondary air temperature on inverted dimensionless axial mean mixture fraction profiles along the flame: (i) CH_4, (ii) Biogas and (iii) CO
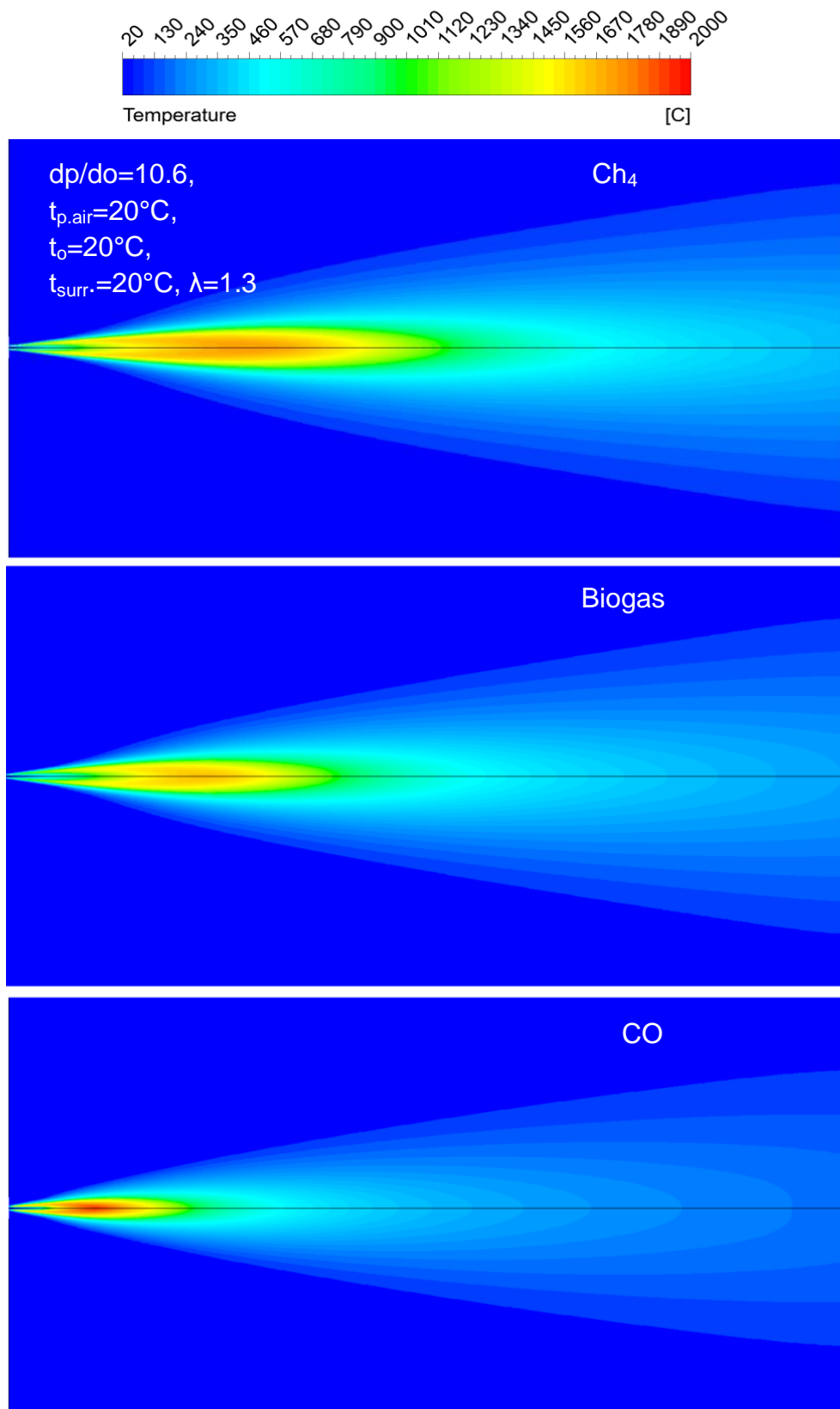
Figure 5.30: Comparison of flame temperature contours for CH4, Biogas and CO fuels at $t_{surr.=}20°C$

5.5 Flame simulation at surrounding is combustion gas

5.5.1 Introduction

In reality, the burner works under the conditions where the atmosphere is a combustion gas. In other words, the gaseous fuel burns in a large space, which is full of combustion gas. Furthermore, when the ambient is air, to discuss the effect of its excess air number is meaningless. Therefore, combustion gas as a surrounding is used in this study. The stoichiometric mixture fraction is used to define the flame length. 2D simulation for annular ring burner flame are carried out in order to understand the flame behaviour under combustion gas environment. The same cylinder with a diameter of 10 m and 20 m length is proposed here to simulate the annular ring burner. Three different fuels are suggested to study (CH_4, Biogas, and CO). The results are used to investigate the effects of geometrical parameters on the flame behaviour. In addition, the effect of operating parameters which include, the velocity of the primary air, combustion gas temperature and the O_2-concentration of combustion gas also is considered.

5.5.2 Species distribution

Figure 5.31 (i) (ii) demonstrates the typical mass fraction profiles of individual species during the combustion of methane along the flame direction and in a radial direction respectively. The temperature of the fuel and air is 20 °C and the temperature of combustion gas is 800 °C. The excess air number is 1.3 and the ratio between annular diameter and fuel inlet diameter is 10.6. As it is shown in the figure, the individual species distribution in annular ring burner with the combustion gas environment is similar to the distribution in case of air environment (see figure 5.21). But the mass fraction of CH_4 is higher in the combustion gas environment at the position far away along the axis than the air environment. On the other hand, it can be noted that the mass fraction of O_2 is lower than the mass fraction of O_2 in case of air is the environment. This can be attributed to the fact that the air environment has a large quantity of air that contributes to the high O2 concentration at position far away along the axis. Moreover, the higher oxygen concentration will be helpful to the fuel combustion and this is the reason why the mass fraction of methane will decrease dramatically to zero at a shorter distance than that in case of the combustion gas environment. While a small difference in radial direction.
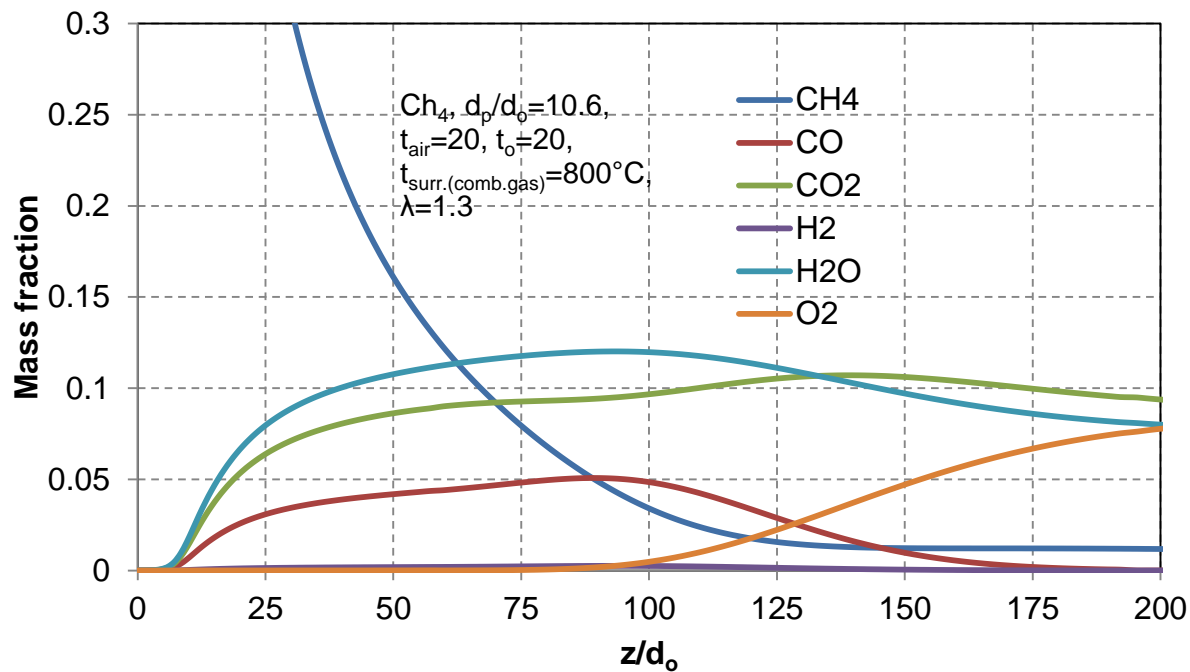
(i)
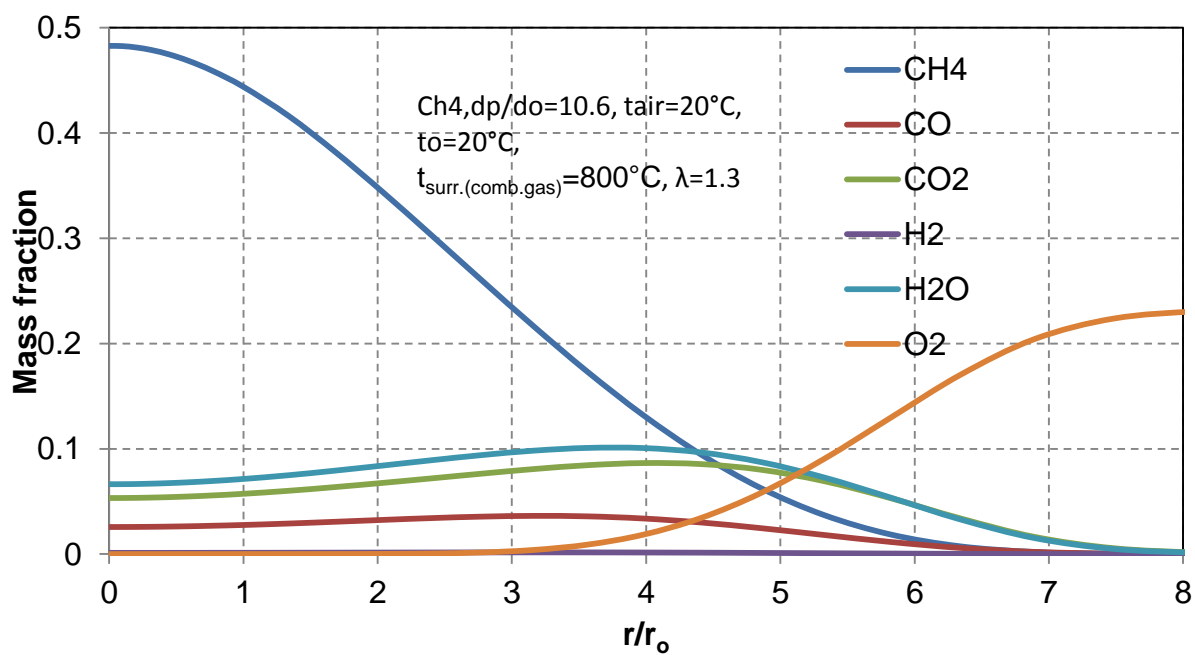
(ii)

Figure 5.31: Species mass fraction distribution (i) axial distribution, (ii) radial distribution
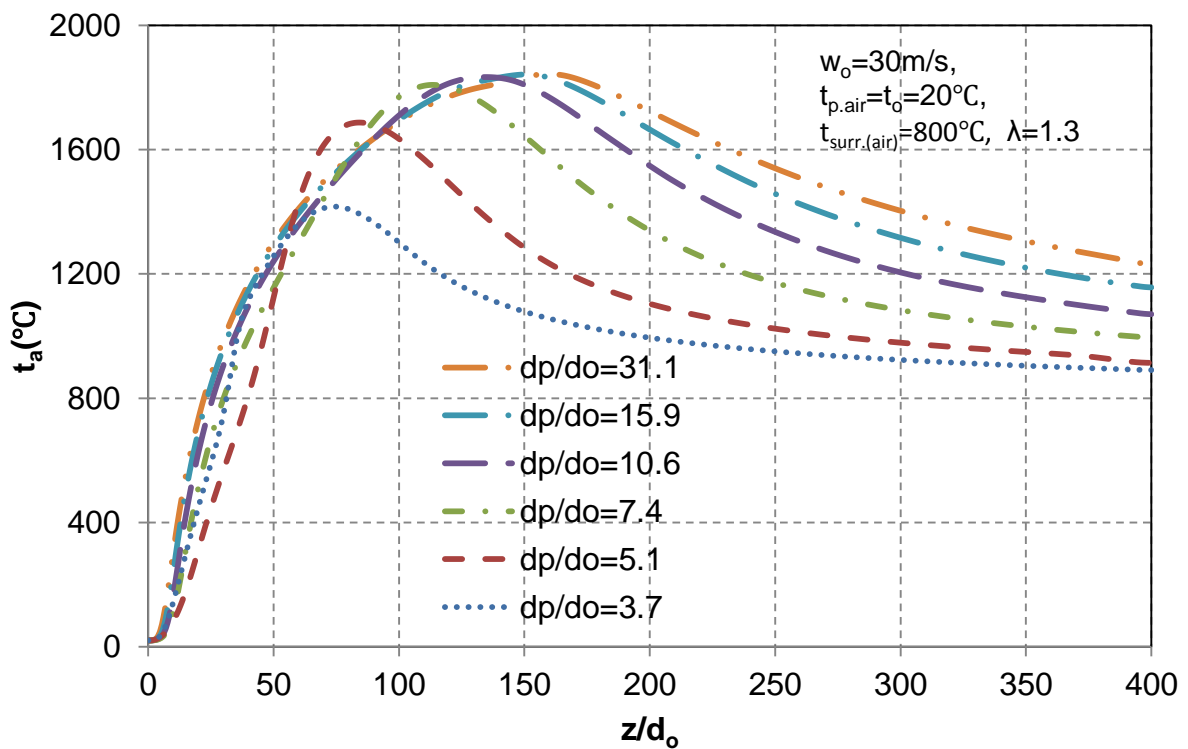
5.5.3 The influence of air inlet diameter

The influence of air inlet diameter on the flame length and axial flame temperature will be presented and discussed in this section. The outlet velocity of the air depends on the diameter (air inlet diameter) and the excess air number of the oxidizer under the constant flow rate of the gas fuel. Figures 5.32 (i), (ii) show the influence of annular diameter on axial temperature distribution along the flame direction in two different cases (i) when the surrounding is combustion gas and (ii) at the surrounding is air. The initial temperature of fuel and air is 20°C and the temperature of the surrounding is 800 °C. The different annular diameters are used 3.7 to 31.1. From figure 5.32 (i) it can be noted that, the temperature profiles in all cases are increasing directly with increasing annular diameter. Furthermore, the peak temperature of the flame increases from nearly 1050°C to 1720°C with increasing annular diameter. Moreover, the highest temperature point shifted to the distant site in axial direction. Comparison of 5.32 (i) and (ii) shows that, the temperature increases to the maximum value and then decreases to a certain value depending on the annular diameter. The axial temperature distribution in the case of the surrounding is air relatively more widespread than when the surroundings is combustion gas.

The dimensionless axial mixture fraction profiles along the flame direction in two different cases (i) when the surrounding is combustion gas and (ii) at the surrounding is air are shown in Figure 5.33 (i) and (ii). In general, it can be noted that, the conditions of the surrounding has a slight effect on the tendency of the mixture fraction. On the other hand, the flame length increases dramatically with increasing the annular diameter in both cases.
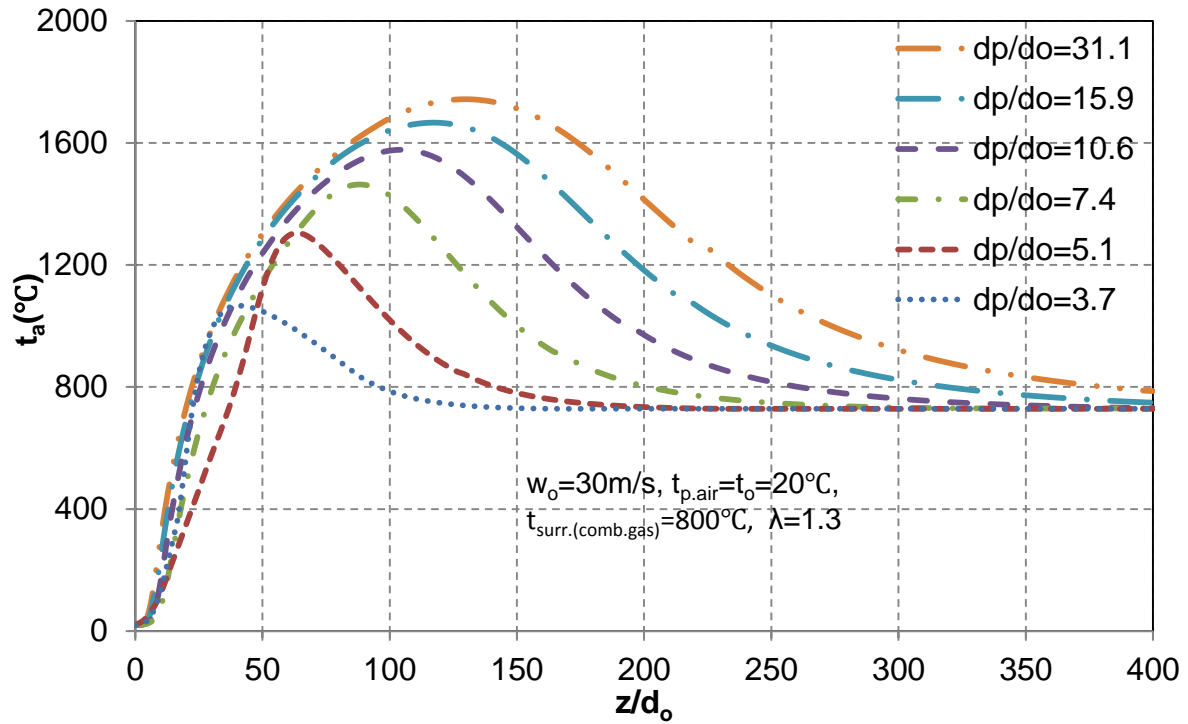
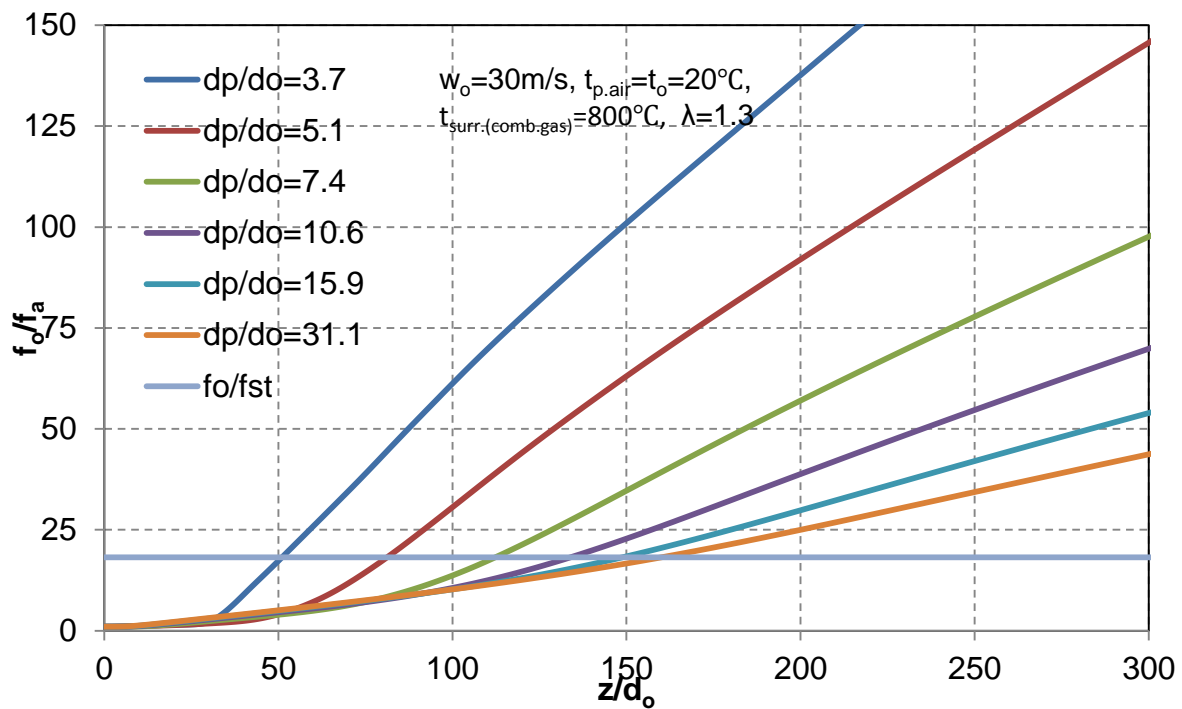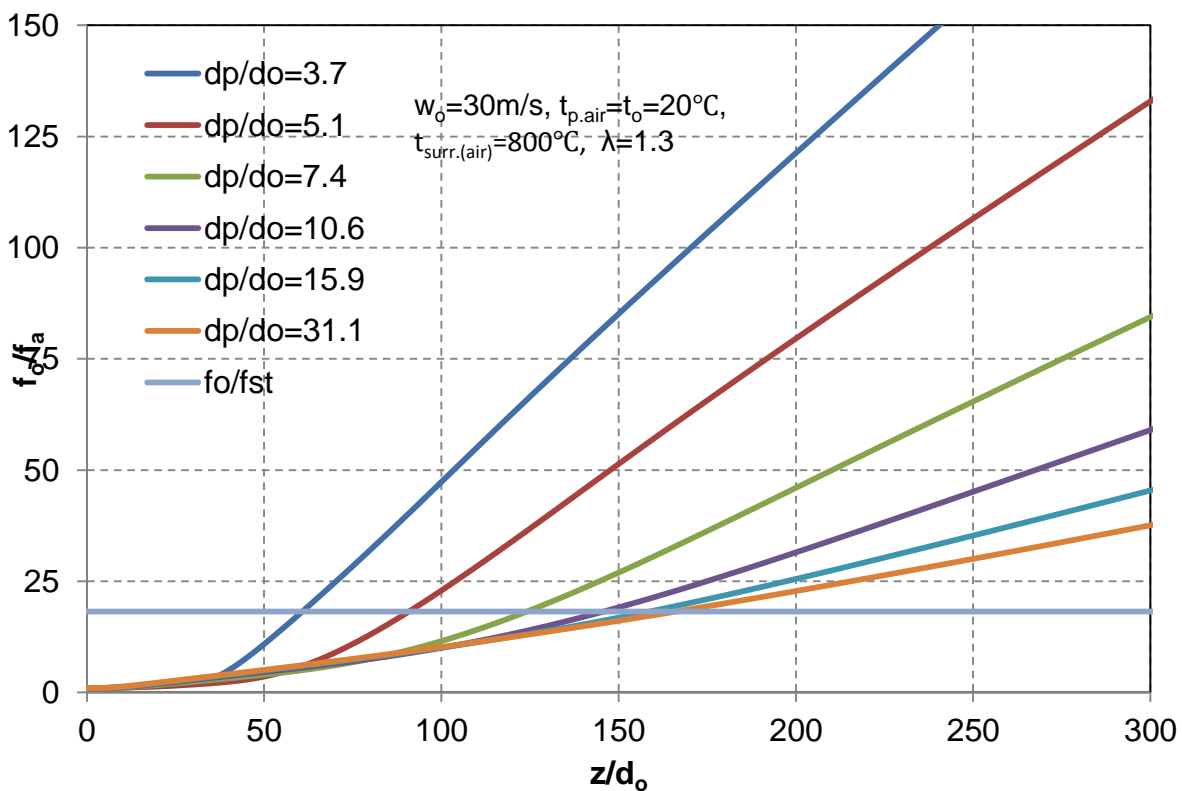Figure 5.32: Influence of air inlet diameter on axial temperature distribution along the flame of Methane fuel, the surrounding temperature is 800°C (i) ambient is combustion gas (ii) ambient is air
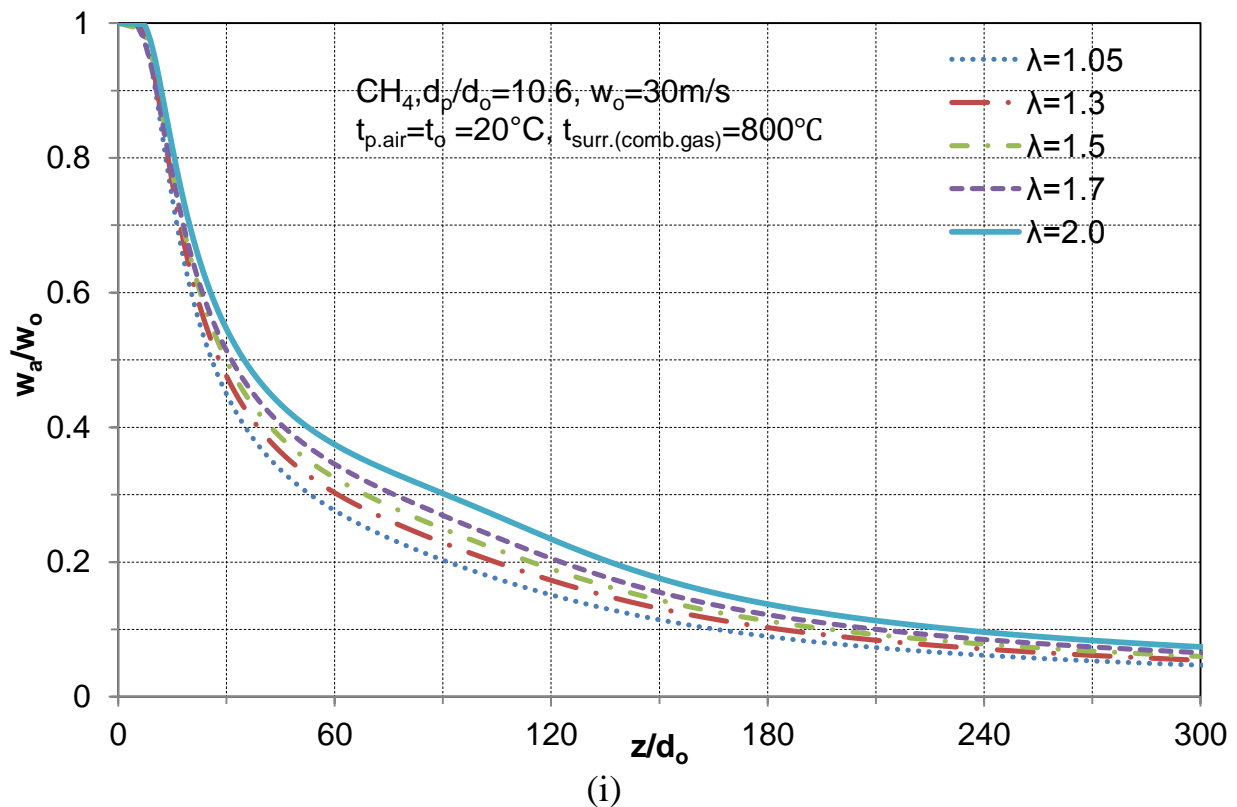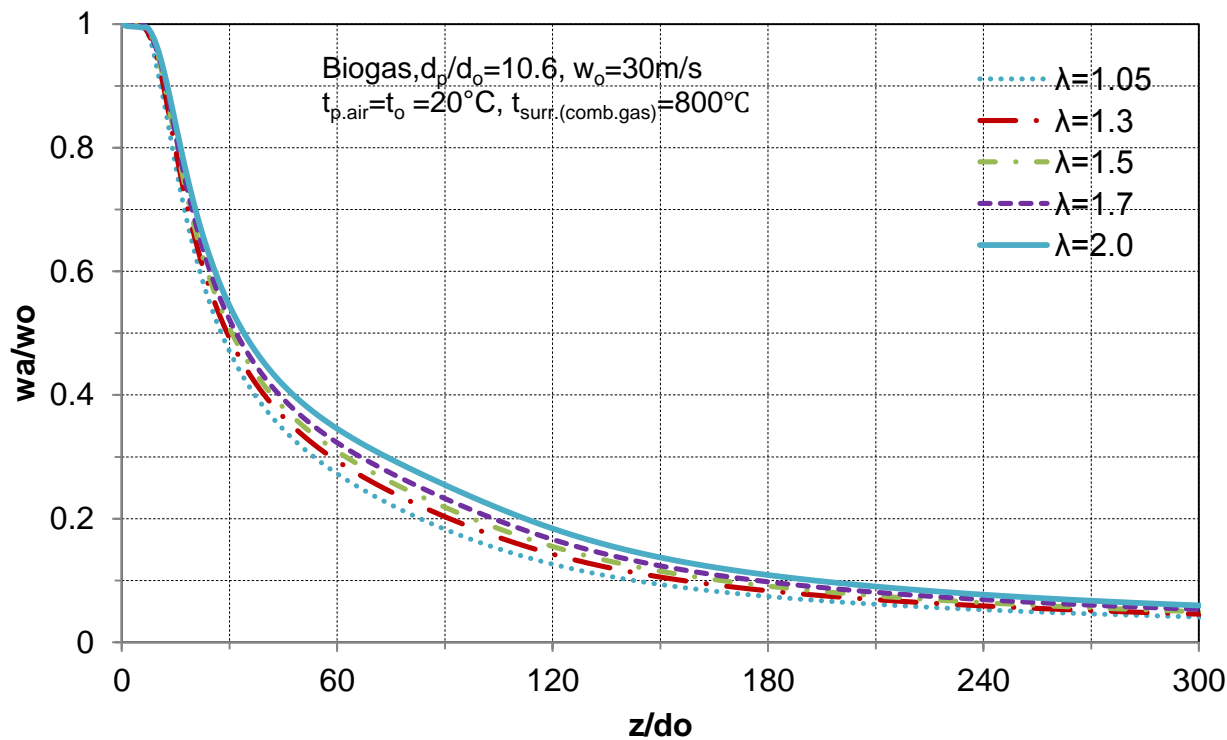
(i)

(ii)

Figure 5.33: Influence of air inlet diameter on inverted dimensionless axial mixture fraction profiles along the flame for Methane fuel CH_4(i) ambient is combustion gas (ii) ambient is air

5.5.4 The influence of excess air number

Figures 5.34 (i), (ii) and (iii) demonstrate the influence of excess air number on axial velocity profiles for CH$_4$, Biogas, and CO respectively. The excess air number 1.05, 1.3, 1.5, 1.7 and 2 are considered. The axial velocity is decreasing along the flame for all fuels. The excess air number has a considerable effect on the axial velocity profiles, especially on the position in the range $z/do \sim 50$-250 for CH$_4$ and Biogas fuels. While the effect of an excess air number on the axial velocity profiles of CO fuel is relatively smaller than the axial velocity profiles of CH$_4$ and Biogas.

Regarding figure 5.35 (i) and (ii) describe the influence of excess air number on the axial temperature distribution when Methane is used as fuel. The temperature increases and then it decreases along the flame direction for all the excess air numbers. There is no big difference of the temperature distribution near the burner rim and at the flame end for different excess air number. However, the lower excess air number, the lower peak flame temperature. Figure 5.35 (ii) shows that there is about 100°C temperature difference between the largest excess air number and the smallest one.

CH$_4$;d$_p$/d$_o$=10.6, w$_o$=30m/s
t$_{p.air}$=t$_o$ =20°C; t$_{surr.(comb.gas)}$=800°C

λ=1.05
λ=1.3
λ=1.5
λ=1.7
λ=2.0

(i)

(ii)
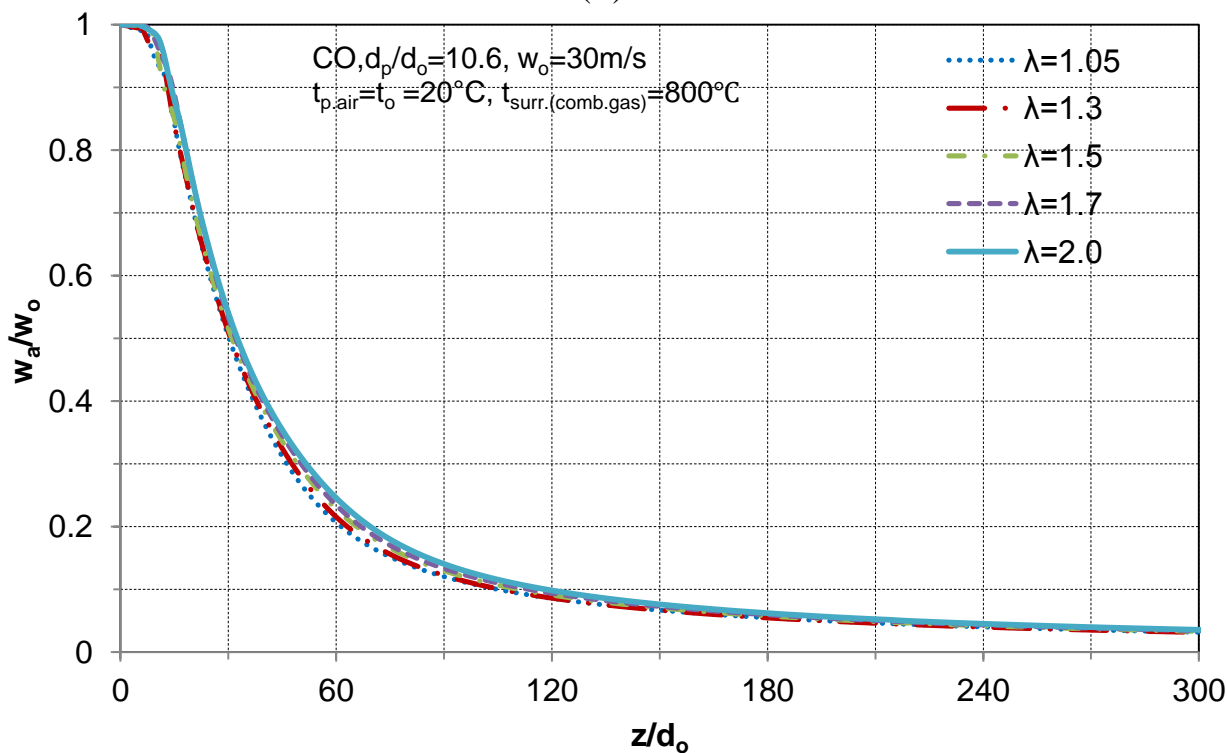
(iii)

Figure 5.34: Influence of excess air number on dimensionless axial velocity profiles along the flame (i) CH4, (ii) Biogas, (iii) CO.

Figure 5.35: (i) influence of excess air number on the axial temperature distribution for Methane fuel (ii) exploded view of the maximum temperature part
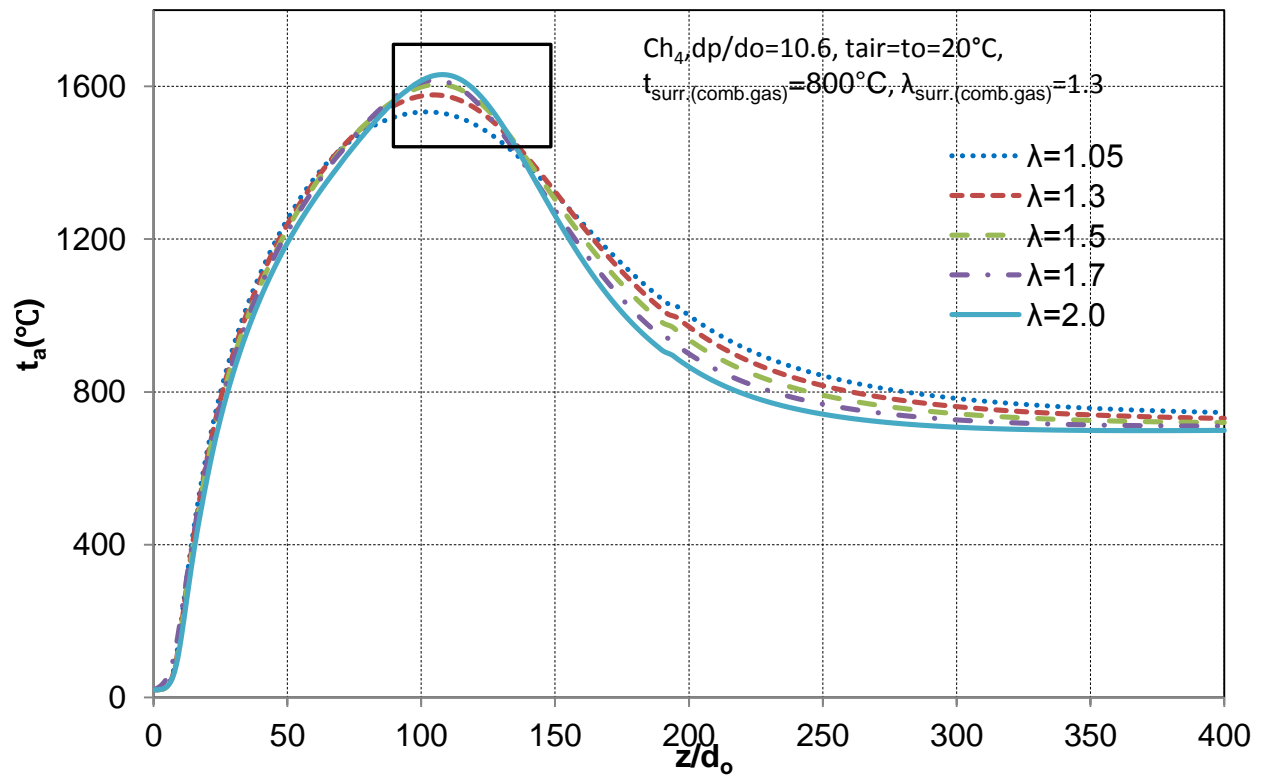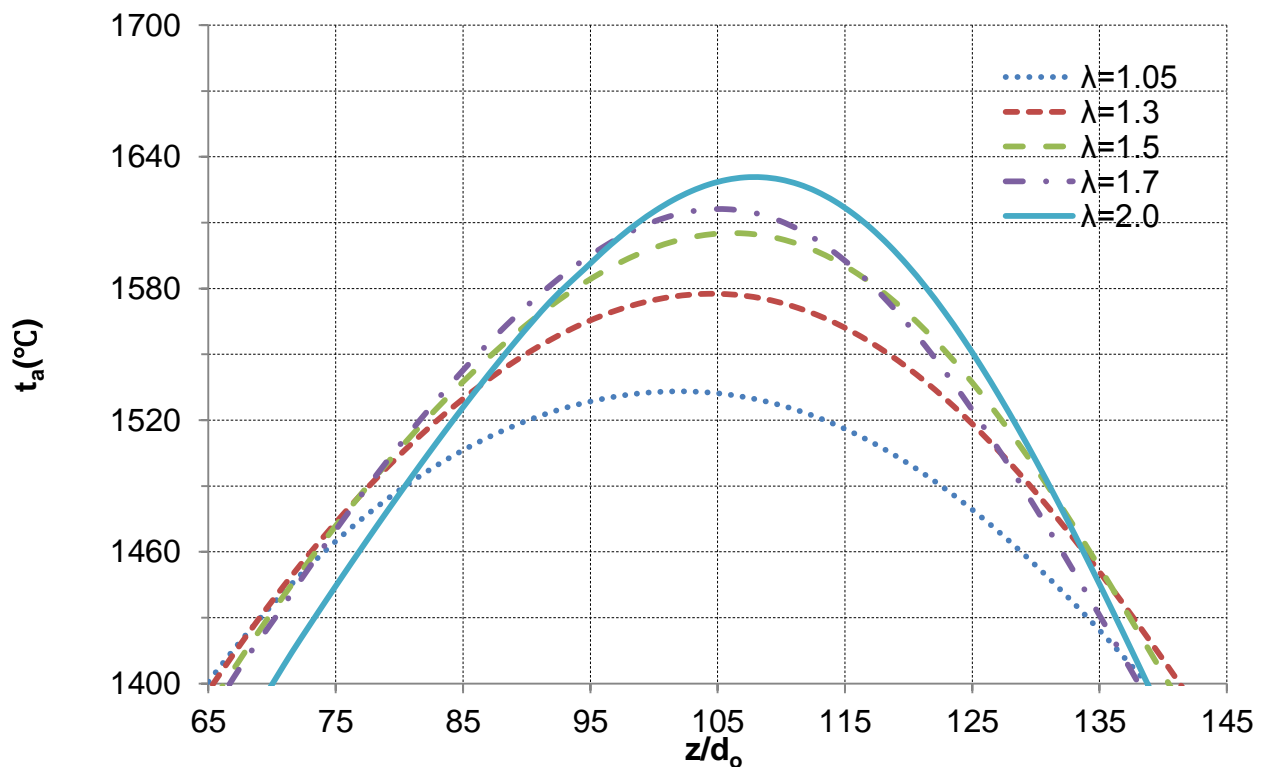
### 5.5.5 The influence of the oxygen concentration in the combustion gas

The influence of the O_2-concentration in the combustion gas on the flame temperature and flame length are presented in this section. Increase the O_2-concentration in the combustion gas means the increasing of the excess air number in the combustion gas. Consequently, instead of the O_2-concentration, the effect of an excess air number of the combustion gas is studied in this section. At first, Methane is used as a fuel with different excess air numbers ranged between 0.1 and 10. Then three different excess air number are chosen to study the influence of excess air number of combustion gas on the flame temperature for three different fuels (CH_4, Biogas, and CO). Table 5.3 shows the relationship between the excess air number and the O_2-concentration in the combustion gas.

Table 5.3: Relationship between excess air number and the O_2-concentration in the combustion gas

Ch_4, d_p/d_o=10.6, $t_{air}=t_o$=20°C, $t_{surr.(comb.gas)}$=800°C, λ= 1.3	
Excess air number in the combustion gas ($\lambda_{surr.comb.gas}$)	O2- concentration in the combustion gas (%)
0.1	6.0
0.3	7.5
0.7	10.0
1.0	11.0
1.3	12.0
1.5	13.0
2.0	14.0
3.0	16.0
4.0	17.0
6.0	18.0
10.0	19.0

Figure 5.36 shows the influence of excess air number of the combustion gas on axial temperature profiles along the flame. All of the temperature profiles show the similar trend, while the only difference lies in the peak temperature region. The maximum temperature increases with the increasing excess air number, but among these peak temperature values. The difference between the maximum and the minimum is around 100°C (Figure 5.36 (ii)). Consequently, it can be concluded that the O_2-concentration in the combustion gas has a little influence on the axial flame temperature.

Regarding figure 5.37 shows the influence of excess air number of combustion gas on axial temperature profiles along the flame for different fuels. It can be observed from figures 5.37(i),(ii) and (iii) the peak temperature is increased by $\sim$ 5.6% for both CH_4 and Biogas, while is $\sim$3% for CO.
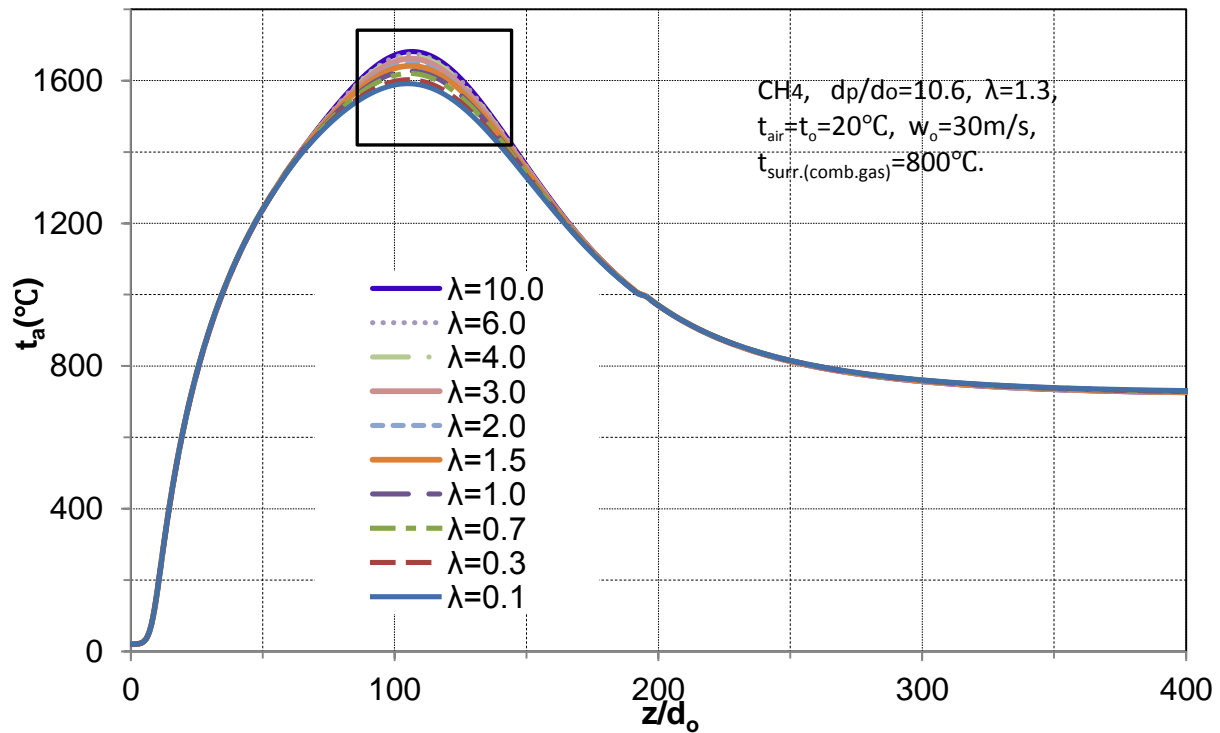
(i)
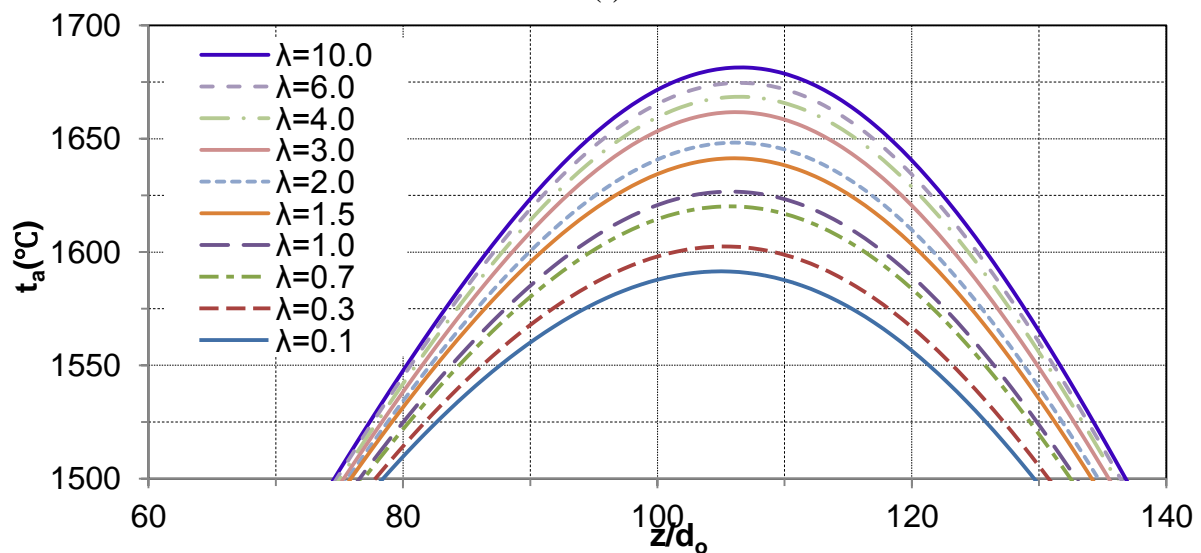
(ii)

Figure 5.36: (i) Influence of the excess air number of the combustion gas on axial temperature profiles along the flame (ii) exploded view of the maximum temperature part
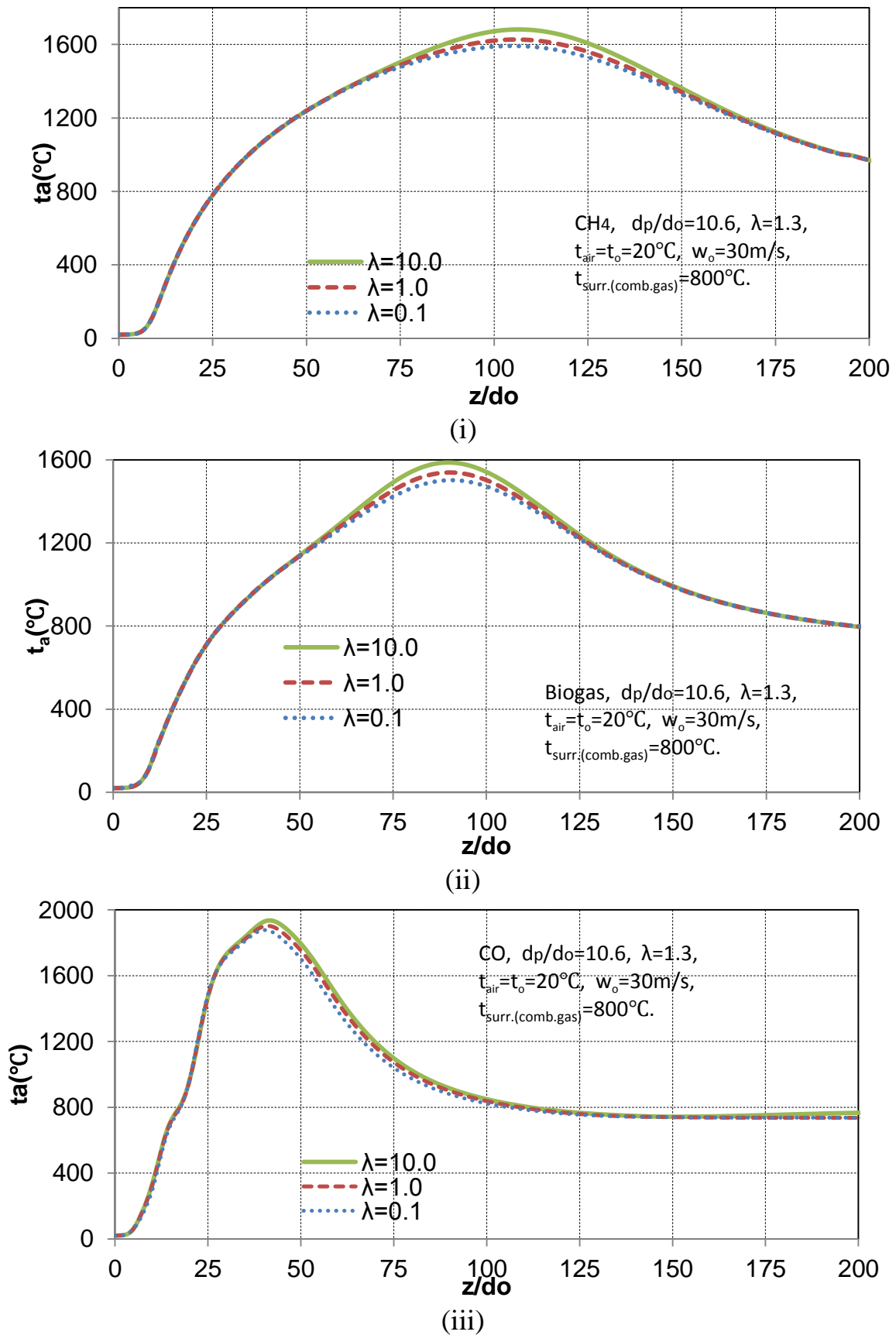
Figure 5.37: influence of excess air number of combustion gas on axial temperature profiles along the flame for different fuels(i) CH4(ii) Biogas and(iii) CO

5.5.6 The influence of the combustion gas temperature

The influence of surrounding air temperature is studied for different fuels (CH_4, Biogas, and CO) and are shown in section 5.4.3. The results were presented that the air temperature has a significant effect on the axial temperature profile and the flame length for any fuel, while it has a small effect on the velocity profile. The influence of the combustion gas temperature on the axial temperature profile and flame length for the annular ring burner is presented in this section. As shown in the figure 5.38, the combustion gas temperature has an obvious effect on the axial temperature profile. This behaviour can be explained by making proposition that the surrounding temperature increases the temperature of the mixture. As a consequence, it increases the disorder of the system and that leads to the increased available energy. Furthermore, it can be observed the axial temperature distribution is relatively less widespread than the surroundings as air (see Figure 5.27).

$CH4$, d_P/d_o=10.6, λ=1.3, $t_{air}=t_o$=20°C, w_o=30m/s

.... tsurr.(comb.gas)=600°C
- - - tsurr.(comb.gas)=800°C
——— tsurr.(comb.gas)=1000°C
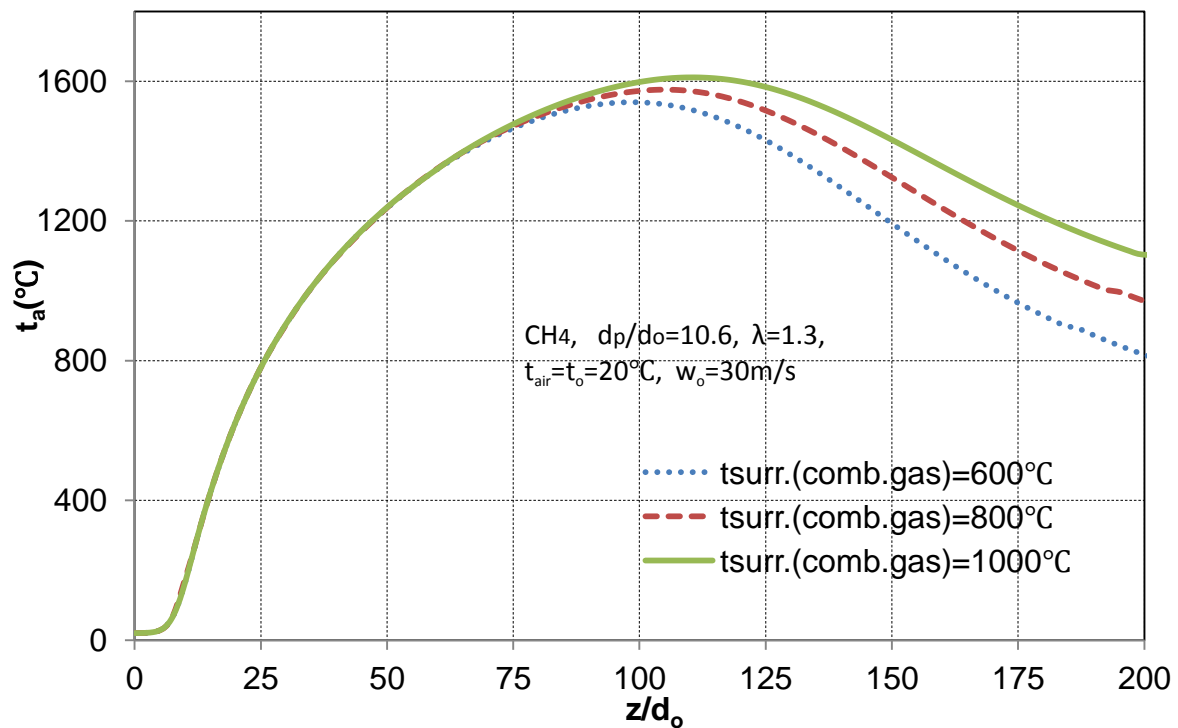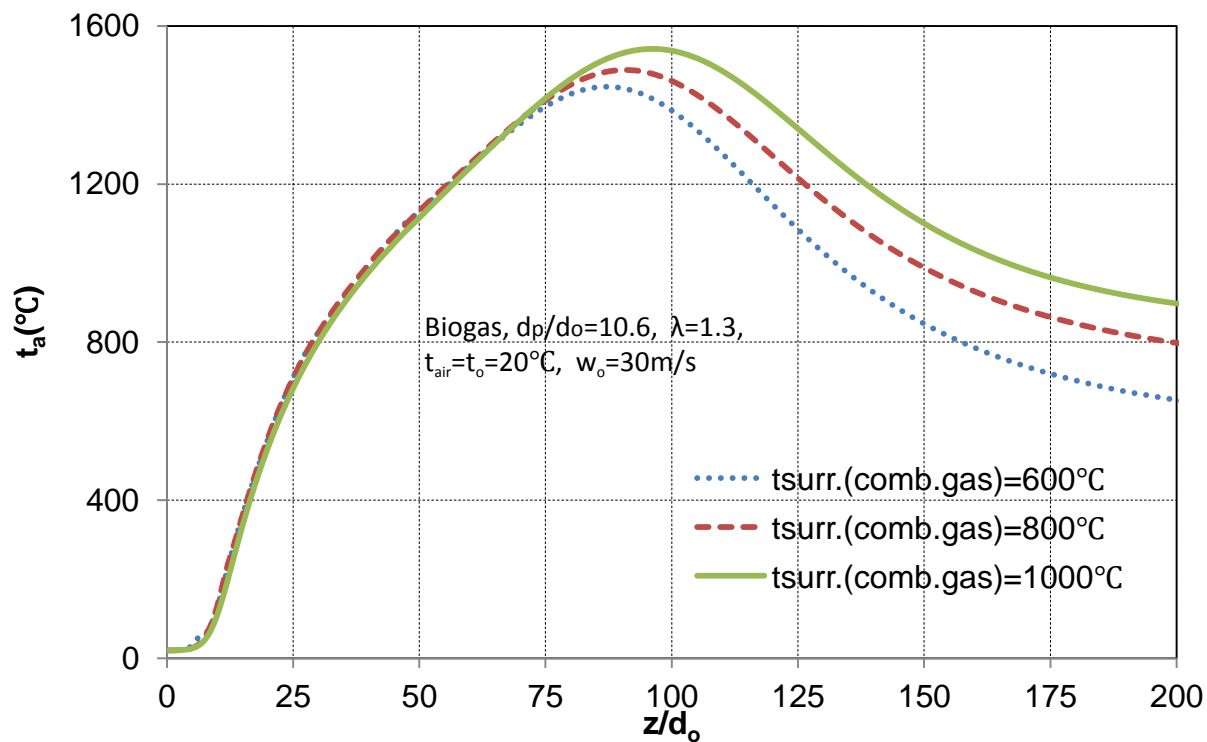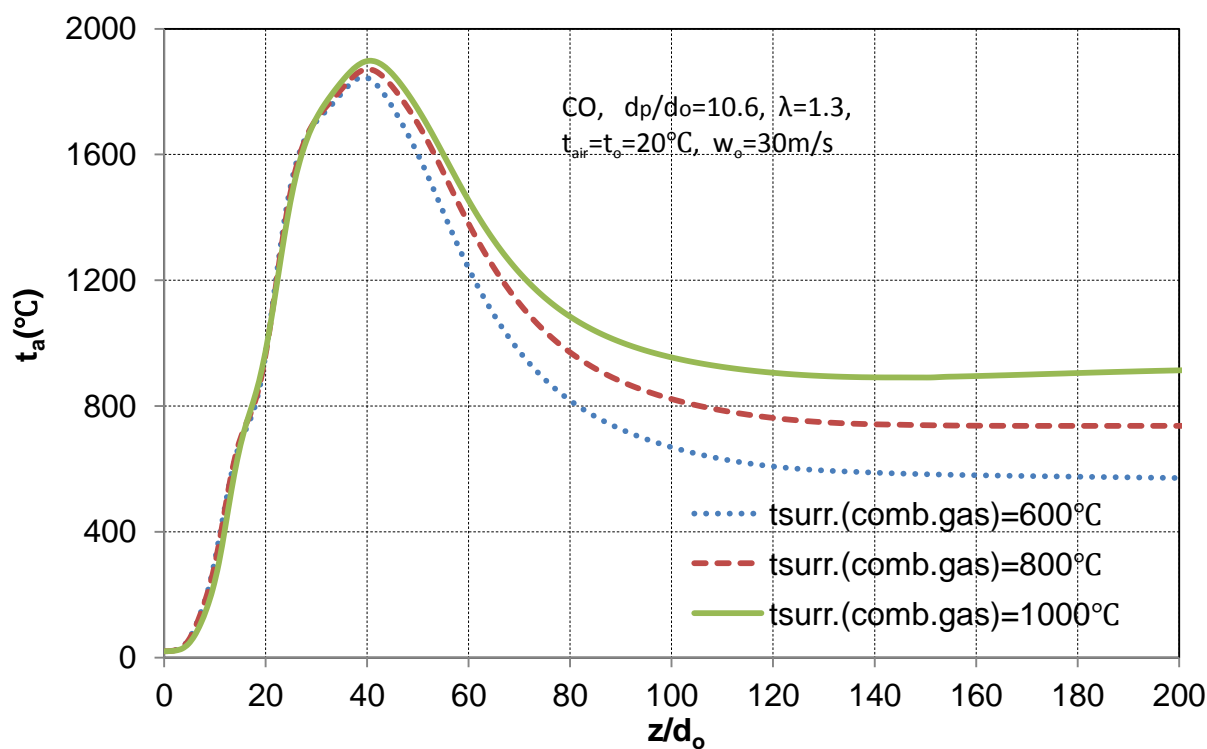
(i)

Figure 5.38: Influence of combustion gas temperature on axial temperature profiles along the flame: (i) CH4, (ii) Biogas, (iii) CO

5.5.7 The influence of fuel velocity

To study the influence of the fuel velocity on the flame temperature distribution and flame length, two different values of fuel velocity (30 m/s and 60 m/s) are used. As a comparison, two different dimensionless annular diameters and three gaseous fuels are studied. Due to the constant excess air number, the air inlet velocity will change with the increasing fuel velocity. In other words, when the fuel velocity is doubled, the air inlet velocity should be also doubled. The influence of the fuel velocity on the axial flame temperature profiles for three gaseous fuels (CH4, Biogas, and CO) with a two different dimensionless annular diameter (dp/do=5.1 and 15.9) is shown in Figure 5.39. The fuel velocity has a small effect on the axial temperature profile with a smaller dimensionless annular diameter for three fuels. While it has almost no effect on the temperature profile with the larger dimensionless annular diameter for three fuels.

(i)

(ii)

(iii)
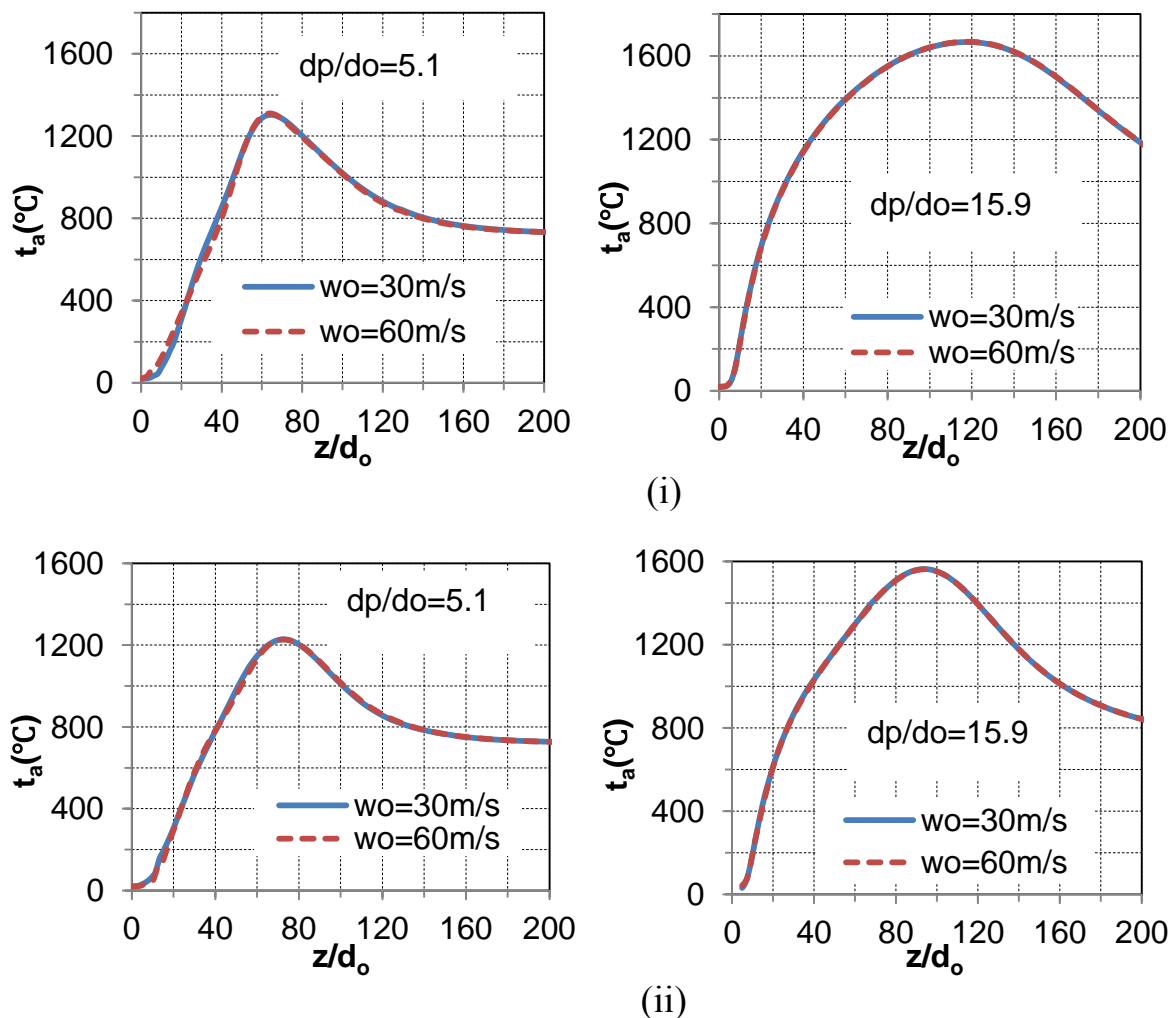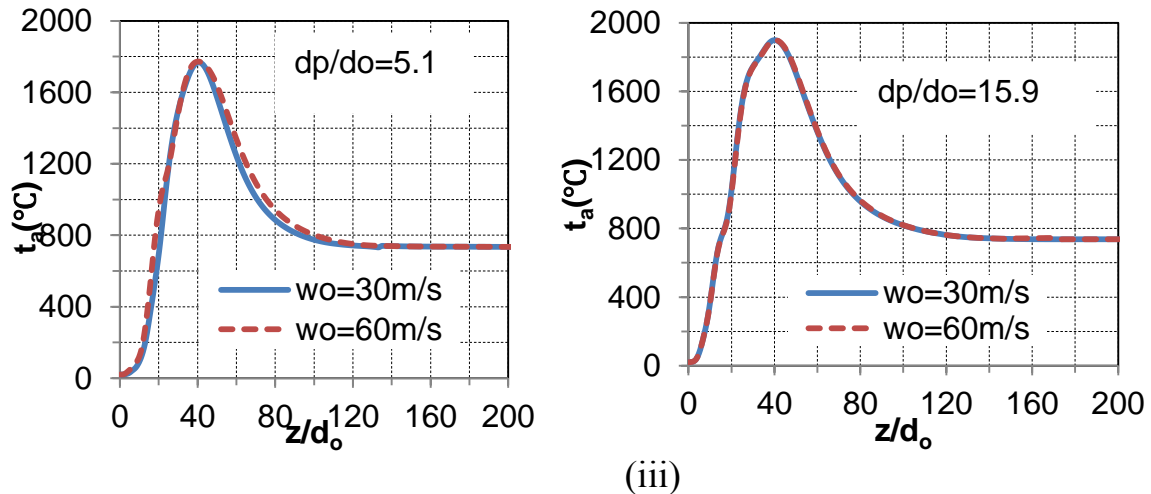
Figure 5.39: Influence of fuel velocity on the axial temperature profiles at $(d_p/d_o=5.1$ and $15.9)$, $t_{air}=t_o=20°C$, $t_{surr.(comp. gas)}=800°C$, $\lambda_{surr.comb.gas}= \lambda =1.3$ and different fuel velocity for different fuels (i)CH_4 (ii) Biogas and (iii)CO

5.6 Flame length behaviour of under various operating conditions

The final computed results of flame length in dimensionless form under different conditions for different fuels are summarized and presented in this section. The method of stoichiometric mixture fraction is used to define the flame length.

5.6.1 Effect of air inlet diameter

Figure 5.40 displays the dimensionless flame length as a function of the air inlet diameter when the surrounding is combustion gas. Here, the different values of annular diameter in dimensionless form are used, i.e. (3.7, 5.1, 7.4, 10.6, 15.9, and 31.1) for CH_4, Biogas and CO fuels. The flame length is directly proportional to the dimensionless annular diameter at CH_4 and Biogas fuels. The trend of flame length profile of Biogas fuel is similar to that for CH_4 fuel. Both of the CH_4 and Biogas flame length increases with the increase of the dimensionless annular diameter. This behaviour, is due to decrease in primary air velocity with increasing diameter. As a consequence, less oxidizer can penetrate in the fuel and the combustion process will complete at the longer distance. Therefore, the flame length of CH_4 and Biogas fuel increases with the increase in the air inlet diameter. Furthermore, the air inlet diameter has a small effect on the flame length of CO fuel.

Figure 5.41 displays the dimensionless flame length as a function of the dimensionless annular diameter when the surrounding is air and for CH_4 as a fuel. The different values of annular diameter are used, i.e. (3.7, 5.1, 7.4, 10.6, 15.9, 31.1, 35 and 40) in this study. From the figure, it can be observed the flame length is increasing at every size of the dimensionless annular diameter till d_p/d_o 31.1. Furthermore, the flame length does not increase after d_p/d_o 31.1, as flame starts behaving as free jet flame.

Regarding Figure 5.42 shows the influence of the ambient on the dimensionless flame length. The different surroundings (air and combustion gas) are used in this study. The temperature of the ambient is 800°C, the excess air number is 1.3 and the excess air number of combustion gas is 1.3. The temperature of the primary air and fuel is 20°C. From this figure, we can note that, the dimensionless flame is longer in the case when ambient is air. It could be attributed to the difference in peak temperatures for their case. Peak temperature in the case of the ambient air is relatively higher than the combustion gas. this behaviour can observe for all different dimensionless annular diameter (d_p/d_o).
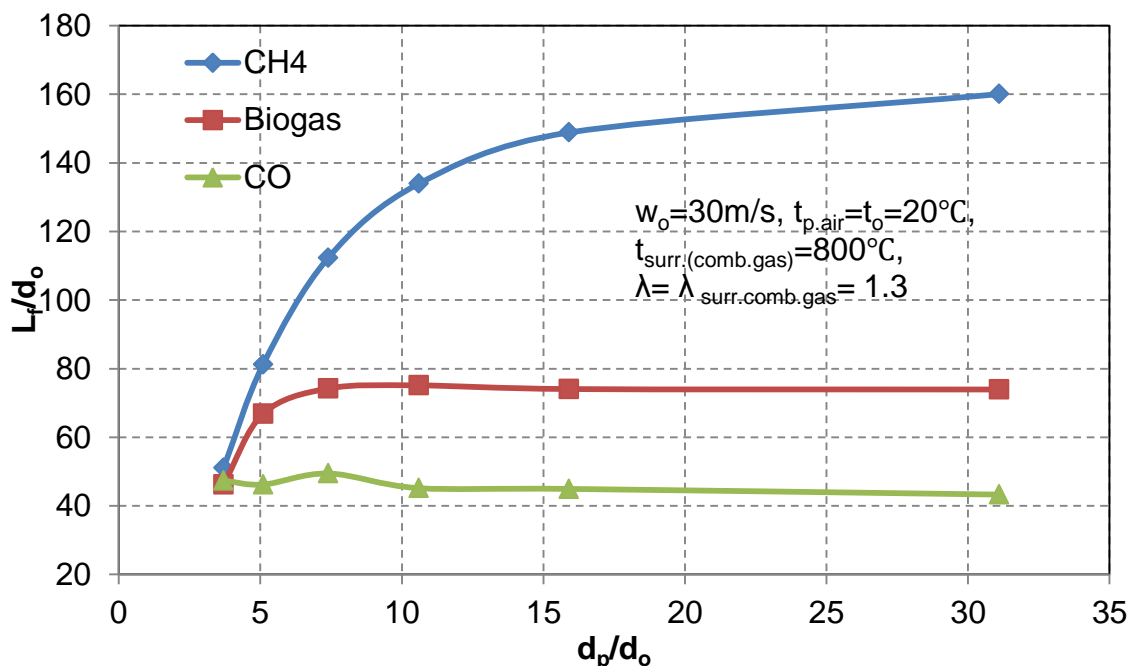

Figure 5.40: Influence of dimensionless annular diameter on flame length for different gaseous fuels (CH4, Biogas, and CO)
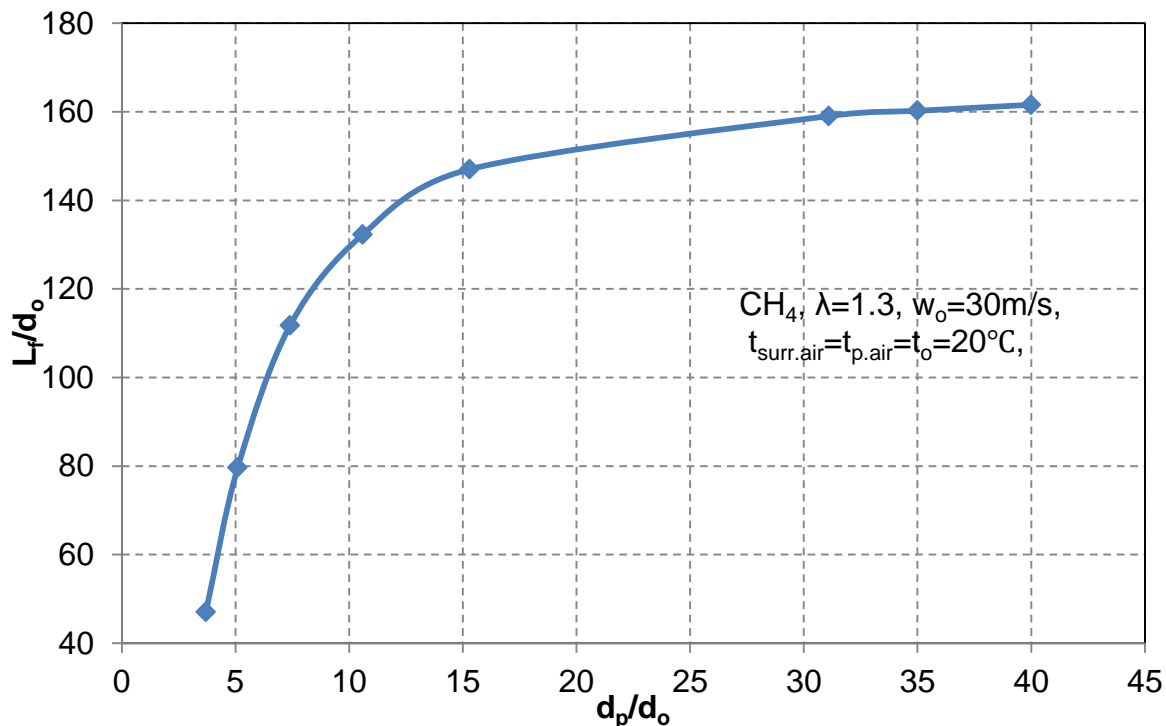
Figure 5.41: Dimensionless flame length as a function of different annulus diameter at the surroundings is air
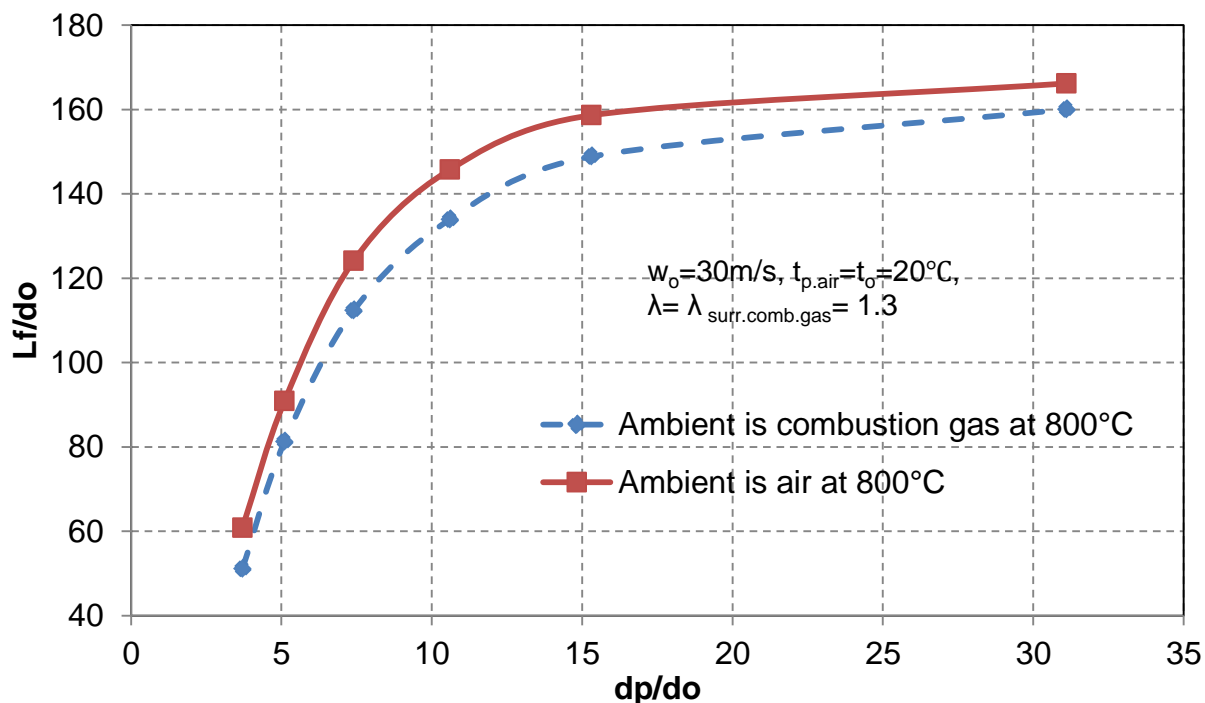

Figure 5.42: Dimensionless flame length as a function of dimensionless annular diameter at the surroundings is air and combustion gas

The flame length in dimensionless form also is calculated analytically. The method of stoichiometric mixture fraction is used to define the flame. Therefore, Eq. 5.25 can be written as:

$$\frac{L_f}{d_o} = \left\{ \left(2 * \frac{\frac{x_o}{x_{st.}} * \frac{\rho_f}{\rho_j}}{\left[\frac{\rho_f}{\rho_j} + \frac{\rho_f}{\rho_j} * \frac{\rho_f}{\rho_p} * \frac{\left(\lambda L * \frac{d_o}{d_p}\right)^2}{1 - \left(\frac{d_o}{d_p}\right)^2} \right]^{\frac{1}{2}}} \right) - 1 \right\} \Big/ 2 * \tan\frac{\alpha}{2} \qquad (5.27)$$

Here, the different values of annular diameter in dimensionless form are used, i.e. (3.7, 5.1, 7.4, 10.6, 15.9, and 31.1) for CH4, Biogas and CO fuels.

To solve equation 5.27, the density of the jet (ρ_j) should be calculated. In this study, it is calculated in two different approaches. Firstly, it is calculated from the numerical simulation by adopting the average in an axial direction along the length of the flame. The temperature of the combustion gas surroundings is 800°C. The temperatures of the air and fuel are 20°C. The components of the combustion gas are ~75% nitrogen and residual it is distributed between oxygen, water vapour and carbon dioxide. All other parameters in equation 5.27 are shown in table 5.2.

The analytical results are compared with the numerical results. Figure 5.43 describes the comparison between numerical and analytical results of flame length in dimensionless form at different dimensionless annular diameter. From this figure, it can be noted that the numerical results for different dp/do takes same behaviour with analytical results. The dimensionless flame length increases with increasing the dimensionless annular diameter. Also, it is evident that, the rate of increasing in dimensionless flame length drops after d_p/d_o=15.9 in both results. In general, the relative error is ranged between 0.8% and 62%.

Secondarily, the surroundings of the combustion chamber are considered as nitrogen. The temperature of the combustion gas (nitrogen) is alterable.

It is always related to the density of the jet (ρ_j) in which to achieve matching between the analytical and numerical results.

Figure 5.44 displays the conformity between the numerical and analytical results when the dimensionless flame length as a function of the dimensionless annular diameter for differents gaseous fuel (CH4, Biogas and CO fuels).

Table 5.4 shows the density of the jet (ρ_j) related to the dimensionless annular diameter and to the temperature of the jet. From this table can be noted that the

density increases with increasing the dimensionless annular diameter. Also, it increases with decreasing the temperature.
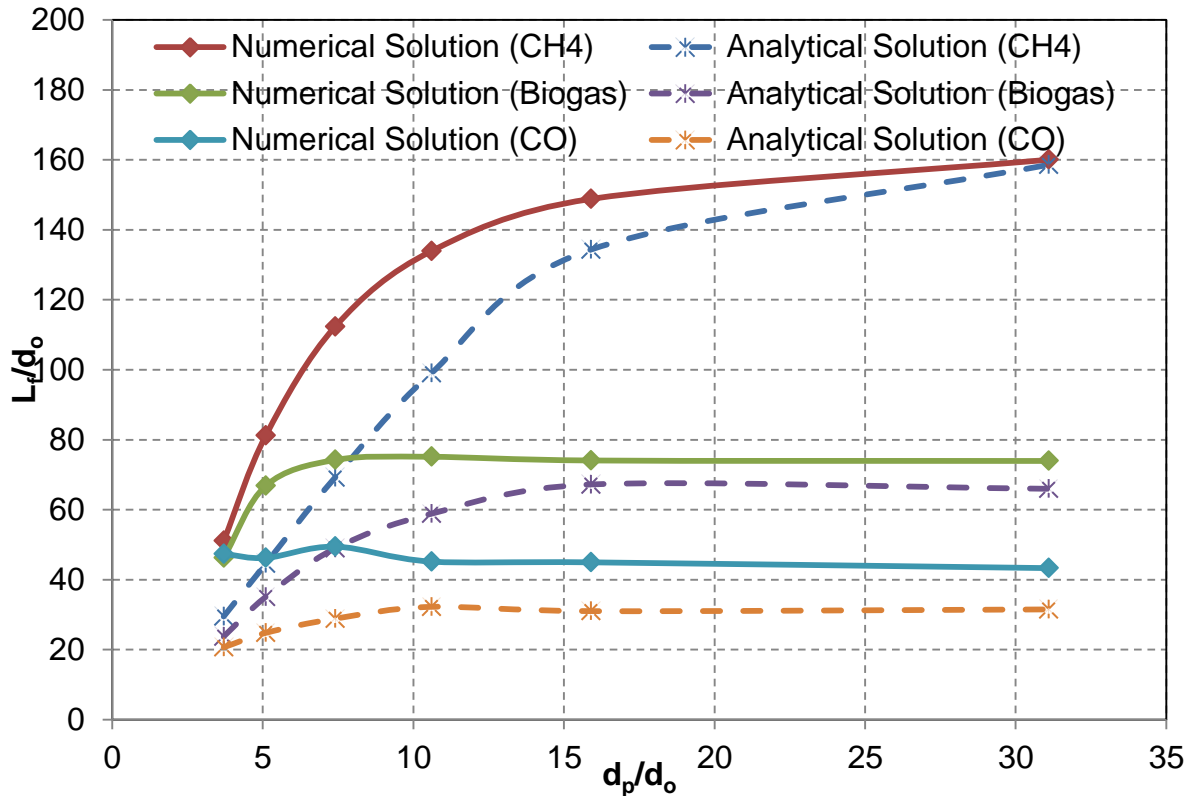

Figure 5.43: Comparison between the analytical and numerical results for the dimensionless flame length as a function of dimensionless annular diameter
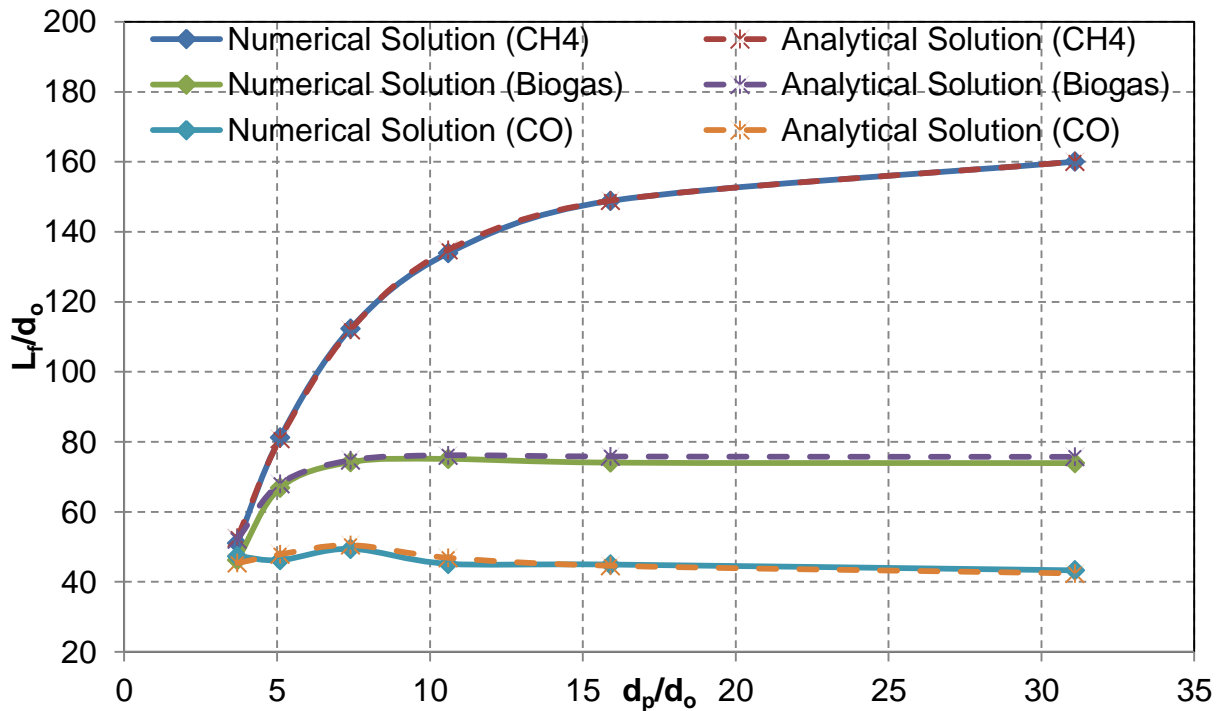

Figure 5.44: Comparison between the analytical and numerical results for the dimensionless flame length at the density of jet (ρ_j) as a function of dimensionless annular diameter

Table 5.4: Relationship between the density of the jet (ρ_j), the dimensionless annular diameter and the temperature of the jet for three gaseous fuels (CH4, Biogas and CO)

dp/do	CH$_4$		Biogas		CO	
	t(°C)	ρ(kg/m^3)	t(°C)	ρ(kg/m^3)	t(°C)	ρ(kg/m^3)
3.7	2570.75	0.12	2352	0.13	2352	0.13
5.1	3139.5	0.1	2352	0.13	2002	0.15
7.4	2977	0.105	1734.53	0.17	1859.8	0.16
10.6	2352	0.13	1278	0.22	1433.2	0.2
15.9	1622.8	0.18	990.1	0.27	1210.7	0.23
31.1	1039.5	0.26	827.8	0.31	1039.5	0.26

5.6.2 Effect of temperature of surrounding atmosphere

The effect the surrounding air temperature on flame length for different fuels (CH$_4$, Biogas, and CO) is shown in figure 5.45. The air temperature has a small effect on the flame length for CH$_4$ and Biogas, and it almost has no effect on the CO flame length. This is because the relative higher stoichiometric mixture fraction of the CO fuel. The flame length of fuel CH$_4$ and Biogas increase slightly with increasing air temperature. Furthermore, it can be observed the flame length is increased by∽ 12% and 5.3% for CH4 and Biogas respectively by increasing the surrounding temperature from 20 to 1000 °C.

Regarding Figure 5.46 show the effect of the surrounding gas temperature on flame length for different fuels (CH$_4$, Biogas, and CO). The similar trend for dimensionless flame length is observed as that in case when ambient is air (Figure 5.45). Moreover, the flame length is increased by∽ 3.2% for CH$_4$ by increasing the surrounding gas temperature from 800 to 1000 °C. While it is increased by 2% for same fuel and same temperature range in the case of air surrounding. As a consequence, there is no big difference between gas and air surrounding as far as the effect of their temperature on the flame is considered.
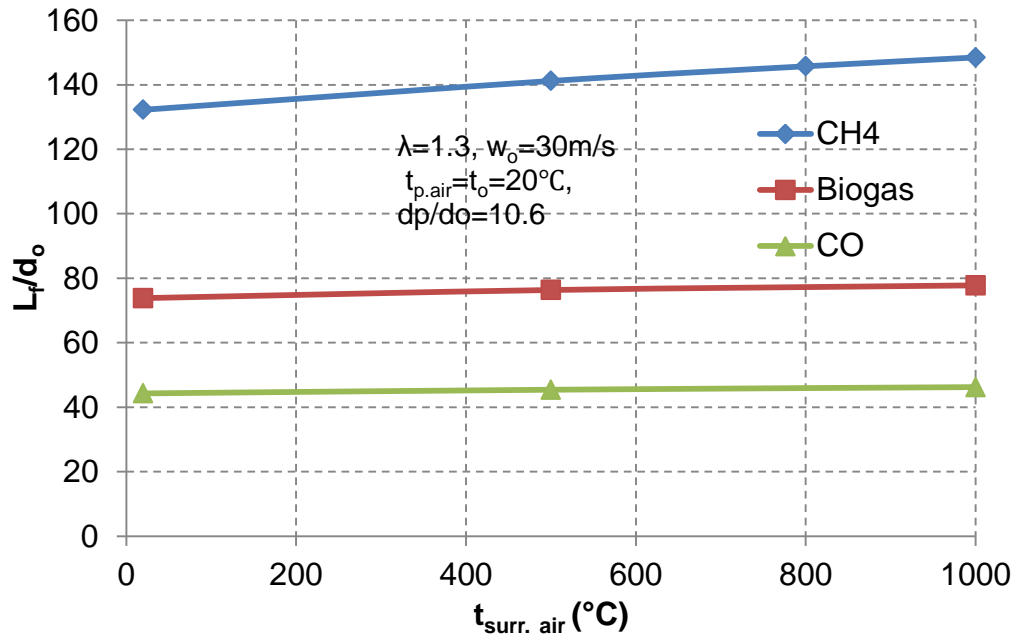
Figure 5.45: Influence of surrounding temperature on flame length for different fuels (CH4, Biogas, and CO) at the surrounding air
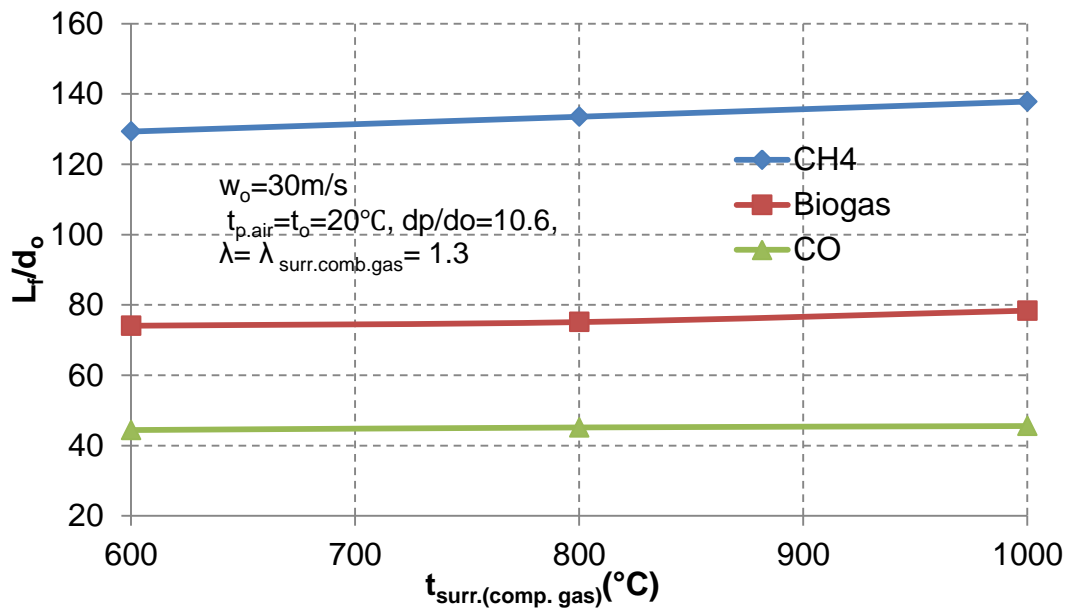

Figure 5.46: Influence of surrounding temperature on flame length for different fuels (CH4, Biogas, and CO) at the surrounding combustion gas

5.6.3 Effect of excess air number

Figure 5.47 demonstrates the influence of excess air number on dimensionless flame length with different gaseous fuels. The annular diameter (d_p/d_o=10.6) is considered. Excess air is changed from 1.05 to 2.0 and the excess air number of the combustion gas is taken as constant $\lambda_{surr.comb.gas}$= 1.3. Three different fuels (CH_4, Biogas, and CO) are used in this study. The excess air number has a small effect on the flame length for these three fuels. Moreover, the flame length of the Methane fuel has a slight decrease with the increase of the excess air number, while this trend is inverse with the Biogas fuel. As for Carbon monoxide fuel, the flame length is the shortest, and the influence of excess air number is minimal. The results show the flame length is decreased by ∼3.6% with the increasing of the excess air number for Methane fuel, while this value is increasing ∼7% for Biogas.

Figure 5.48 show the effect of an excess air number of the combustion gas on dimensionless flame length with different gaseous fuels. The excess air number of the primary air is λ=1.3 and the excess air number of combustion gas is changed from 0.1 to 10. Table 5.5 demonstrates the relationship between excess air number and O_2-concentration of the combustion gas of three fuels (CH_4, Biogas, and CO). As shown in the Figure, the excess air number of combustion gas has almost limited effect on the flame length for any fuel. Also, it can be noted a slight rise in flame length with increasing excess air number.

Table 5.5: Relationship between excess air number and O2-concentration of the combustion gas for three fuels (CH4, Biogas, and CO)

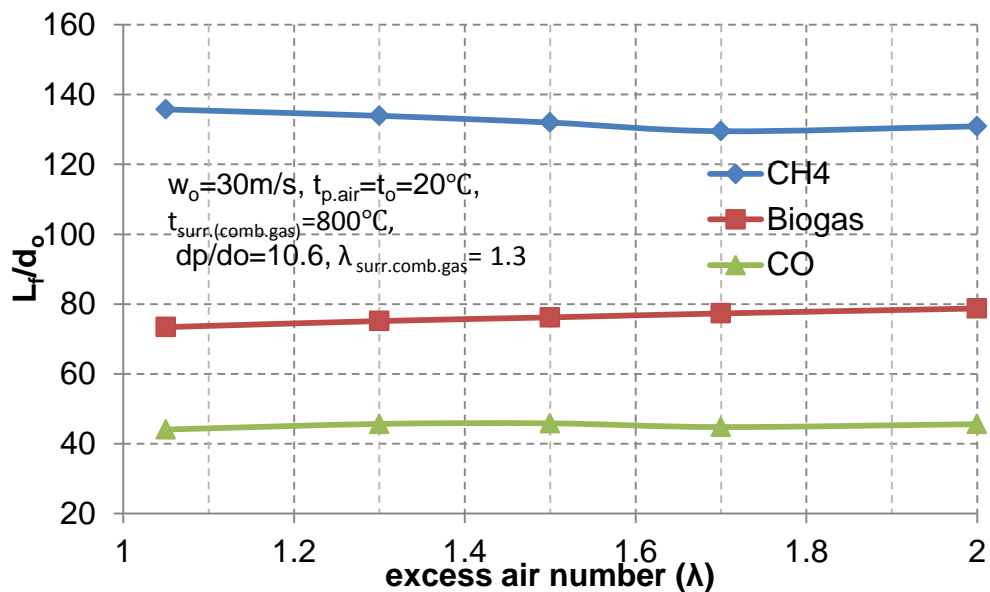| Fuel	Excess air number in the combustion gas ($\lambda_{surr.comb.gas}$)	O2-concentration in the combustion gas (%)
CH4	0.1	6.0
	1.0	11.0
	10	19.0
Biogas	0.1	6.0
	1.0	12.0
	10	20.0
CO	0.1	5.0
	1.0	11.0
	10	18.0

Figure 5.47: Influence of excess air number of primary air on dimensionless flame length for different gaseous fuels (CH4, Biogas, and CO)
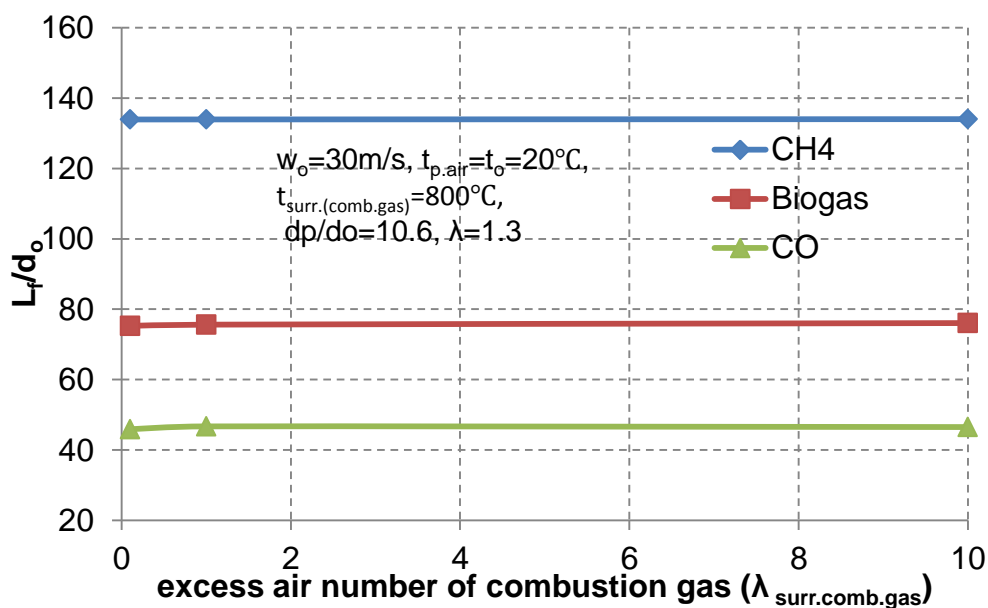

Figure 5.48: Influence of excess air number of combustion gas on flame length for different fuels (CH$_4$, Biogas, and CO)

6. 3-D modelling of roller kiln and burner design

Three different designs are proposed to study (i) air sucked directly (ii) air sucked by bore hole in the roof insulation (iii) air sucked by bore hole in the roof insulation with longer burner outlet. The results in this section include the influence of the cone length, the amount of air suction, and the behaviour of the streamline (without combustion) which scope of this research.

The second purpose is to find the temperature distribution at the outlet (with combustion) in two different cases, when the burner is installed against the direction of the main flow (Upstream), and the other when the burner is installed in the same direction as that of the main flow (Downstream).

The difference between   three different burner designs on the velocity distribution and on the direction of the streamline is demonstrated in figure 6.1 and 6.2.

Figure 6.1 illustrates the contours of velocity distribution inside roller kiln with different models. Figure 6.1(i) shows the first design burner installed with the orifice of the suction air exposed stream of the main flow, so that air is sucked directly from the surrounding. Figure 6.1 (ii) and (iii) show the air is sucked by bore hole in the roof insulation.

The outlet of the burner is supported with guide at angle 28.3^{o}, to control the direction of the stream and this is used for other models too. The velocity of the main flow is 2 m/s, and air is injected into the burner with velocity 12 m/s.

From this figure, it can be observed that, the velocity distribution is similar in all models. Furthermore, it can be seen that the streamline is exposure directly on the tiles in the first and second models, while in the third model (iii) the streamline is not in tangent to the product. Although the steam guide is used in all models.

The velocity distribution within the burner at different levels is shown in figure 6.2. Figure 6.2 a shows the position of the selected points along the burner. Figure 6.2b (i) shows that the velocity distribution completely changed and increased in the suction region (between 0.9 and 0.872m), and the same behaviour can be seen in the other designs as shown in figure 6.2b (i) and (ii). As observed the maximum velocity is about 90 m /s at cone outlet, and it is decreased to 20 m /s at the burner outlet. The value of air sucked is about 13, 15 and 12 m^{3}/h respectively. Furthermore, the cone length is studied and found that by doubling the cone length, the air sucked is increase about 40%.
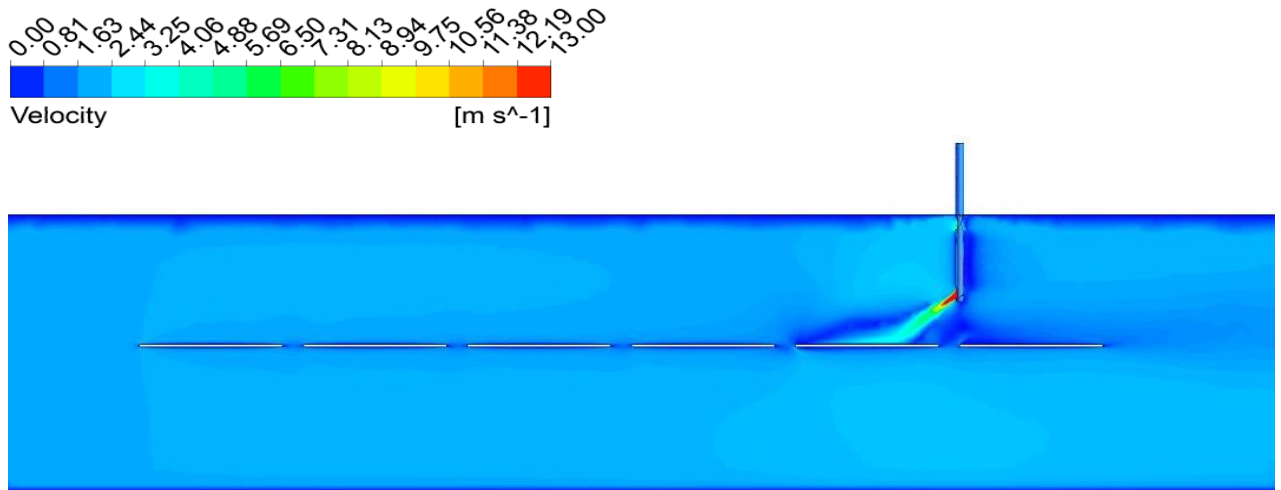
(i)   First model (air suction directly)

(ii) Second model (air suction by bore hole in the roof insulation)
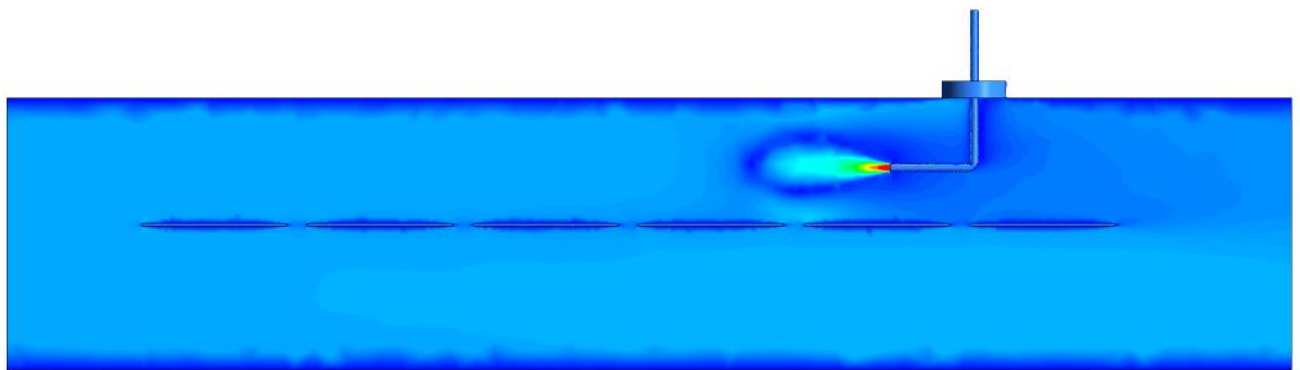
(iii) Third model (air suction by bore hole in the roof insulation with longer burner outlet)

Figure 6.1: Contours of velocity distribution at z=0.978m in longitudinal direction
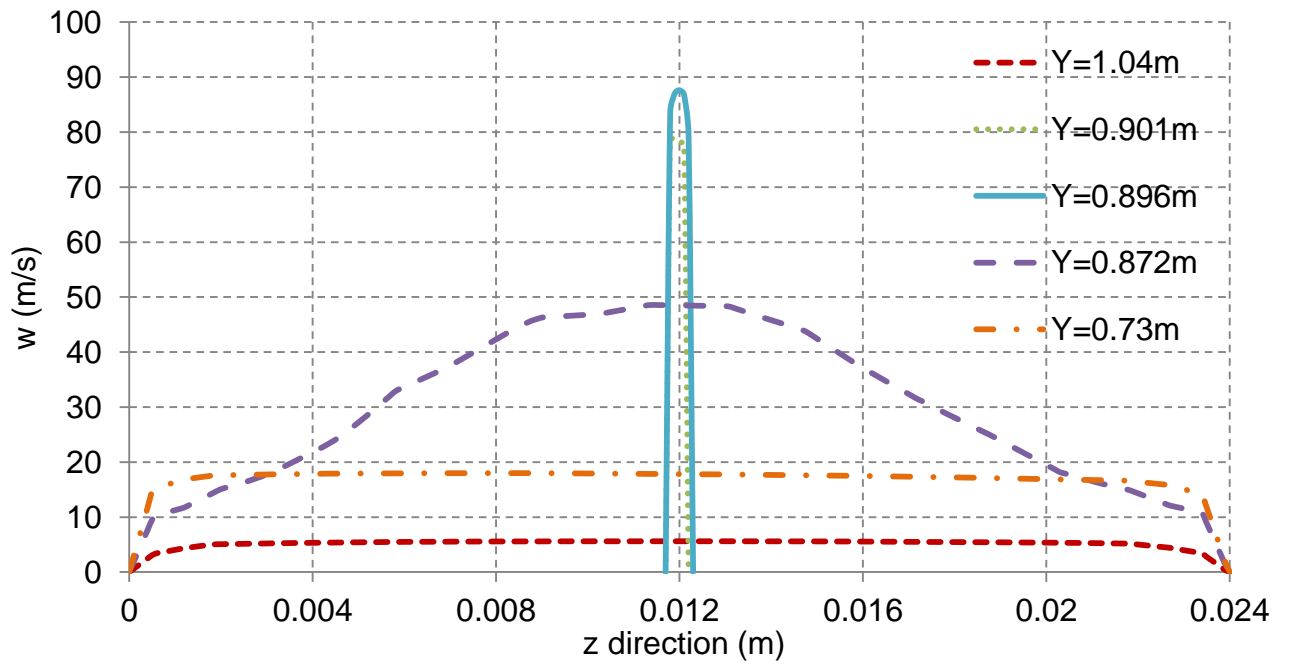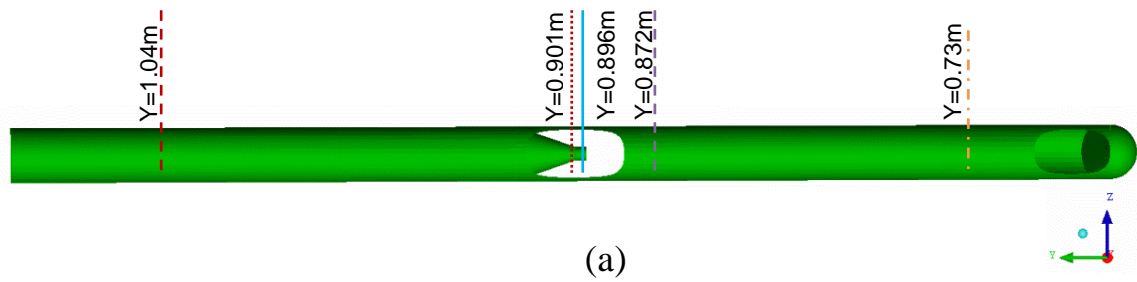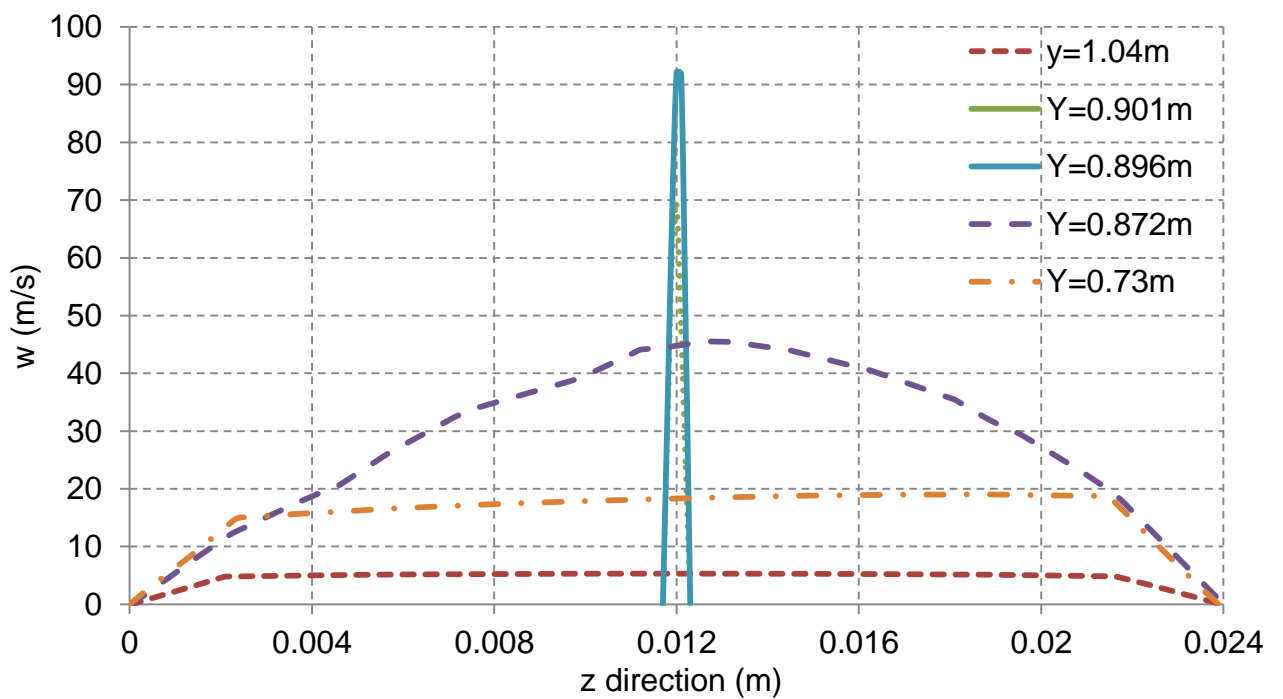
(a)

(i) First model (air suction directly)

(ii)   Second model (air suction by bore hole in the roof insulation)
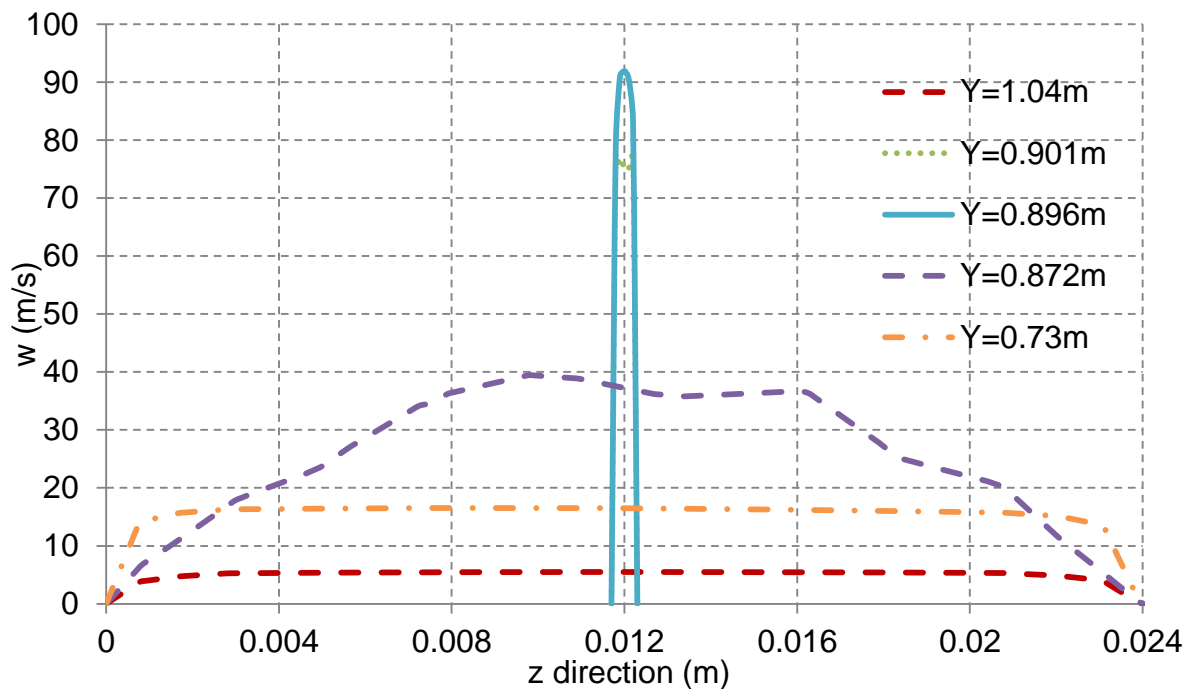
(iii)   Third model (air suction by bore hole in the roof insulation with longer burner outlet)

Figure 6.2: (a) burner (b) velocity distribution inside the burner system at different levels

The shape of the premixed flame in two cases (the burner fires in the same direction and against the direction the main flow) is presented in figure 6.3. Here the premixed combustion model (Zimont model) is used. The temperature of the main flow and the mixture is 1000°C and 600°C respectively, and the velocity is 2m/s and 12m/s respectively.

From figure 6.3a, it can be observed that, the buoyancy effect of the burner if fired in the same direction to the main flow (downstream flow). On the other hand, it can note that, the temperature distribution around the burner as shown in figure 6.3b (upstream flow) is better distributed.

Figure 6.4 shows the temperature distribution at the outlet of the kiln in two different cases, upstream and downstream of the main flow. The width of the temperature distribution has no big difference and always between 1000 and 1163 °C, but it can be noted that there is a very small increase in upstream case. Moreover, it can be observed that, the peak of temperature distribution in case of downstream has increased about 14% of that upstream case. This is due to the impact of the main flow on temperature distribution in the domain.

(a)

(b)
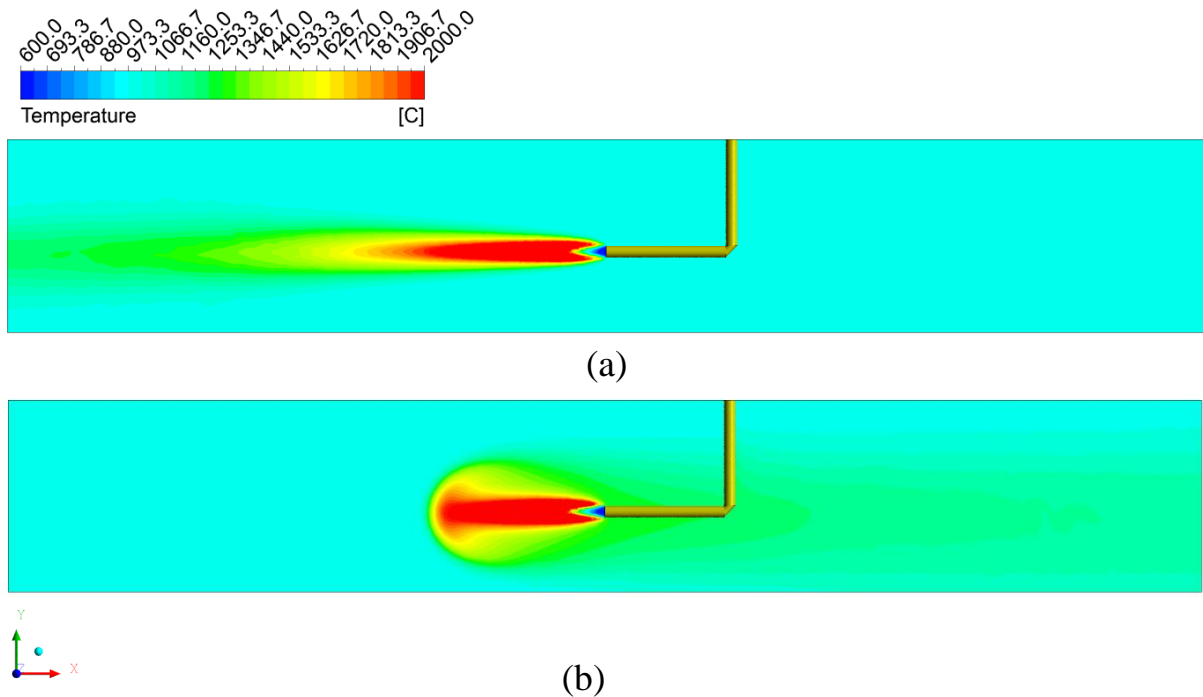
Figure 6.3: Influence of the burner direction on temperature contours (a) downstream flow (b) upstream flow

Figure 6.4: Temperature distribution at outlet of the kiln as a function of burner direction

7. Summary and conclusions

7.1 Summery

The CFD simulations are being used in a wide range such as analysis of the systems involving fluid flow, heat transfer and chemical reactions. In this study demonstrated that CFD can be used as an effective tool for developing the industrial kilns. 3D simulations using commercial CFD (ANSYS) for the preheating zone in a tunnel kiln are used to evaluate the quality of mixing.

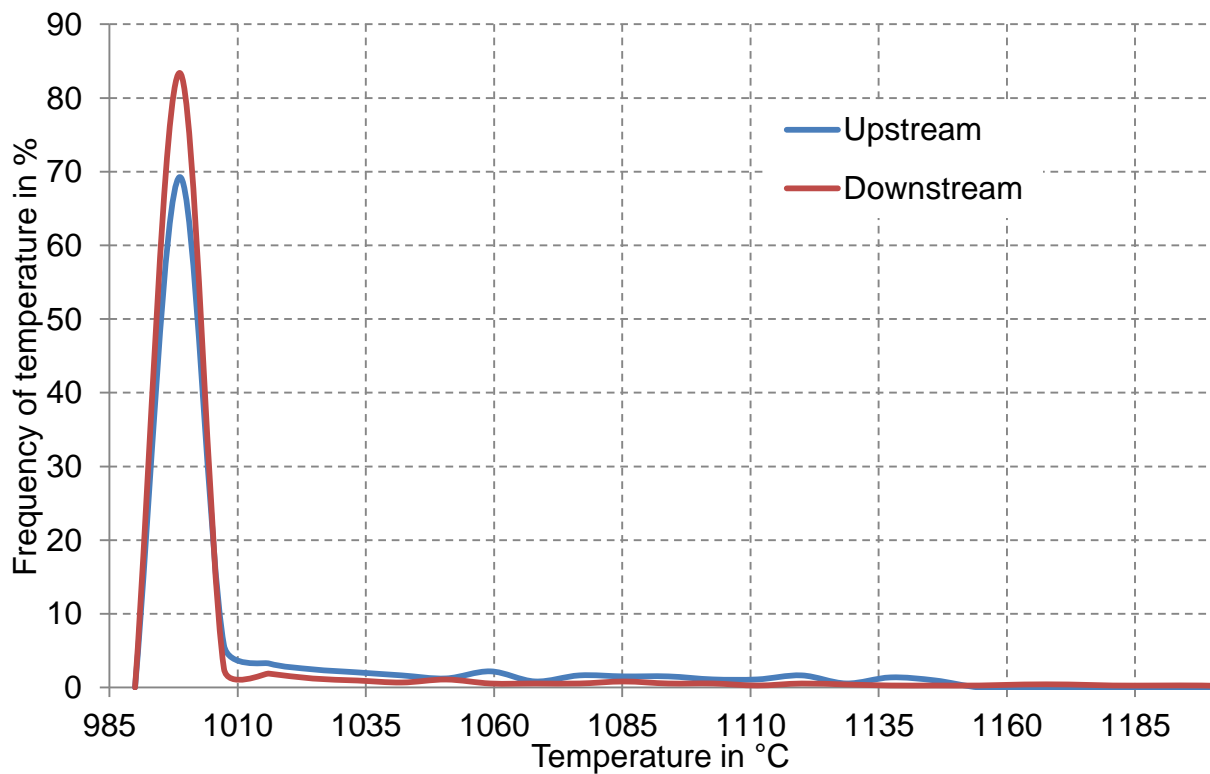Here, the influence of the geometrical parameters on temperature distribution in the preheating zone is studied, which include the injection nozzle position, cross section area of the ware zone, shape of side injection and kiln geometry.

Furthermore, the effect of the   operating parameters which involving temperature and velocity of side injection, mixing ratio, number of side injection, and velocity of the ware stream to the gas stream ratio are studied.

In ANSYS is allowed to evaluate the quality of the mixing in three different ways are contour plotting, plot frequency of temperature distributions and maximum temperature difference. Furthermore, the post-process is used to show the effect of the used parameters on the mixing.

Regarding firing zone, 2D simulations using ANSYS software for annular ring burners with different gaseous fuels are conducted and presented in order to study the flame behaviour. The effect of operating and geometrical parameters is also considered.

The mass fraction of gaseous fuels and the velocity of the mixture in dimensionless form is calculated analytically using equations derived from the laws of conservation of mass and momentum. Moreover, it is used to evaluate the numerical results. In this section, the simulation of the non premixed flame is divided into two parts, according to the atmosphere of the combustion chamber (air or combustion gas). At first, the flame characteristics of different gas fuels (CH_4, Biogas, and CO) with air surroundings are investigated and presented. The effects of the primary air velocity and secondary air temperature on the axial velocity, axial temperature and mixture fraction profiles are discussed and presented.

Whereas in the reality, the burner works under the conditions where the atmosphere is a combustion gas. The actual environment is that the chamber is full of combustion gas, in other words, the flame is surrounded by the combustion gas instead of the air. Therefore, the research of the non premixid flame with the air surroundings is used as a preliminary step for flame simulation with the combustion gas surroundings. The simulations predict the

influence of the air velocity, excess air number, O_2-concentration of combustion gas and the temperature of the combustion gas on flame behaviour and axial temperature profiles for three gas fuels (CH_4, Biogas, and CO).

Regarding roller kiln, at the end of the firing zone the atmosphere consists of hot air from the cooling zone, flowing as the main flow in contrary direction to the tiles through the whole kiln. Therefore, some burners fire against and some of them like the direction of the main flow. A 3D simulation for injector nozzle is used to evaluate the maximum velocity, quantity of air suction, streamlines and temperature distribution in roller kiln.

7.2 Conclusions

The main conclusions drawn from this study are as follows:

- One side injection is not suitable for the mixing in the kiln (cross section and longitudinal).
- Two air injections, located on the opposite wall, develop a whirl, which leads to mixing in the entire cross section.
- The quality of mixing can be increased by increasing the vertical distance between two opposite air injections (maximum H_R).
- Extremely high injection velocity is not recommended for the mixing, because of distance limitations between kiln cars.
- Using a large amount of side air injector leads to decrease the temperature of the mixture.
- The injection velocity and the injected mass flow rate can be combined in the impulse as a parameter.
- The homogeneity of the mixing does not depend only on velocity or on the mixing ratio of side injection, but always it is related to the impulse of side injection.
- By increasing the impulse flow rate up to 4 N, the cross sectional temperature difference decreases strongly. For higher impulse flow rates, the temperature difference decreases comparatively slower.
- Generally, the injection temperature does not affect the mixing quality. But, it only effects on the average temperature of the mixture.
- As the ware to gas relative velocity (w_r) decreases the mixing quality improves.
- By increasing the kiln geometrical ratio ($G_{k,R}$), the mixing is being better in the middle of the kiln cross section, but it is worst near the side walls.

Moreover, a long distance from the injection is needed to obtain the homogeneity of the temperature distribution.

- The rate of temperature difference ratio decreases with moving away from the side injection.

- The shape of the cross section area of the nozzle has no influence on the mixing quality.

- The peak of frequency of temperature distributions is close to the average temperature of the mixture as the cross sectional area of the ware increases.

- The geometry of products has a great influence on the mixing inside the kiln.

- Products inside the kiln makes the lower temperature difference.

- The flame behaviour (flame length) is directly proportional with the geometrical and operating parameters such as air inlet diameter and secondary air temperature.

- Shorter flame with smaller air inlet diameter (higher air velocity).

- The excess air number and the O2-concentration of combustion gas have a small effect on the flame temperature profiles.

- The fuel velocity has almost no effect on the flame behaviour.

- The temperature of the surroundings has an obvious effect on the flame temperature profiles and flame length.

- The peak of the temperature when the surroundings of the combustion chamber as air relatively higher than the peak of the temperature in the case of the surroundings of the combustion chamber as combustion gas.

- The flame length when the surroundings of the combustion chamber is air, is relatively longer than the flame length in the case when the surroundings of the combustion chamber is combustion gas.

- The maximum velocity is about 90 m/s at outlet of the cone in the case of roller kiln.

- The upstream model has a more temperature distribution in the cross-section area than the downstream model in a roller hearth kiln.

- Burner with longer outlet protects the product from direct exposure to the flame in case of the roller hearth kiln.

8. Recommendation for future work

According to what is mentioned above, the project concentrates on the modelling of a part of tunnel kiln. Whether it is in the preheating zone or in the firing zone of the tunnel kiln. Several results have been obtained for these two zones. The results are complementary to each other. i.e. it is possible to use the results from preheating zone (quality of mixing) to find the best position to install the annular ring burner on the side walls of the firing zone.

The effect of axial flow on flame behaviour, temperature and pressure distribution and energy consumption is also very important for the performance of tunnel kiln. Therefore 3D- CFD simulation of tunnel kiln (preheating, firing and cooling zone) are recommended for future investigations. These simulation shall also be carried out with considering ware.

Bibliography

[1] European Comission "Reference Document on Best Available Techniques in the Ceramic Manufacturing Industry" August, p. 161, 2007.

[2] Energy Conservation Center (ECC) "Energy Conservation on Ceramic Industry" United Nations Industrial Development Organization, Ministry of International Trade and Industry and Mineral Resources, Ministry of Power and Energy, Sri Lanka the Energy Conservation Center (ECC), Japan, 1994.

[3] Ceramic Industry, URL http://www.ceramicindustry.com.

[4] Civil blog, URL http://civilblog.org/.

[5] Superior Clay Corporation, URL http://superiorclay.com.

[6] Gladding, McBean, URL http://www.gladdingmcbean.com.

[7] J. Shular, "The Emission Factor Documentation for AP-42" Section 11.7 Ceramic Products Manufacturing for U.S, 1996.

[8] Wikipedia, Pottrey, URL http://en.m.wikipedia.org/wiki/Porcelain.

[9] Sun light, URL www.sunlight-ceramics.com.

[10] Karamo Technical Ceramics, URL http://www.keramo.com.

[11] N. Arizona University and the HBCU/MI Technology "Lecturees in Soil Science" URL http://www2.nau.edu/~doetqpp/courses/env320/index.htm.

[12] P. Meng "Solid-Solid Recuperation to Improve the Energy Efficiency of Tunnel Kilns" Ph.D. dissertation, Otto-von-Guericke-Universtät, Magdeburg, Germany, 2011.

[13] Takasago Industry Co. Ltd., URL www.takasagoinc.co.jp/eg/sk1/shuttle1.htm.

[14] J. B. da Silva, B. R. Fischer, G. R. Alves and B. M. Alves "A Remote Engineering Solution for Automating a Roller Hearth Kiln" JOE – Vol. 4, Issue 3, August 2008.

[15] S. Kaya, K. Küçükada, and E. Mançuhan, "Model-Based Optimization

of Heat Recovery in The Cooling Zone of a Tunnel Kiln," Appl. Therm. Eng., vol. 28, no. 5–6, pp. 633–641, 2008.

[16] R. Oba, T. S. Possamai, and V. D. P. Nicolau, "Numerical Simulation of Tunnel Kilns Applied To White Tile With Natural Gas" 21st Brazilian Congrress Of Mechanical Engineering,Natal, RN,Brazil, 2011.

[17] H. Refaey, "Mathmatical Model to Analyze the Heat Transfer in Tunnel Kiln for Burning of Ceramics" Ph.D. dissertation, Otto-von-Guericke-Universtät, Magdeburg, Germany, 2013.

[18] Edward Orton Jr. Ceramic Foundation, URL https://www.ortonceramic.com.

[19] M. F. Naccache, M. S. P. Gomes, and A. O. Nieckele, "Numerical Simulation of Flow and Heat Transfer Through a Tunnel Kiln" 81[th]International Congress of mechanical Engineering Ouro Preto, Nov. 2005.

[20] A. H. Tehzeeb, M. Bhuiyan, and N. Jayasuriya, "Evaluation of Brick Kiln Performances Using Computational Fluid Dynamics" Energy Environ. Eng. Vol. 1, no. 2, pp. 1–8, 2012.

[21] T. S. Possamai, R. Oba, and V. D. P. Nicolau, "Numerical Simulation of a Ceramic Kiln Used in Frits"20th International Congress of Mechanical Eng. Gramdo,RS, Brazil, Nov. 2009.

[22] F. Becker, L. Lorenz, and G. Walter, "Heat Exchange in a Fast Firing Kiln for Glost Firing of Porcelain" CFI Ceramic Forum International, Vol.83, no. 9, pp. e59-e65, Aug. 2006.

[23] T. Zhanxu, L. Haixia, M. Fanmao, and W. Fahui, "Numerical Simulation of Waste Heat Utilization in Coal Gangue Brick Tunnel Kiln" Conf. Energy Environ. Technol., pp. 222–224, 2009.

[24] R. Oba, T. S. Possamai, and V. P. Nicolau, "Thermal Analysis of a Tunnel Kiln Used to Produce Roof Tiles" Appl. Therm. Eng., vol. 63, no. 1, pp. 59–65, 2014.

[25] B. Yu, "Dynamic modeling of a tunnel kiln," Heat Transf. Eng., vol. 15, no. 2, pp. 39–52, 1994.

[26] V. D. P. Nicolau and A. P. Dadam "Numerical and Experimental Thermal Analysis of a Tunnel Kiln Used in Ceramic Production," J. Brazilian Soc. Mech. Sci. Eng., vol. 31, no. 4, pp. 297–304, 2009.

[27] E. Mancuhan, K. Kücükada and E. Alpman " Mathematical Modeling and Simulation of the Preheating Zone of a Tunnel Kiln," J. of Thermal Science and Technology, ISSN 1300-3615, 2011.

[28] O. B. Goltsova, V. S. Klekovkin, and V. a. Tenenev, "Development and approval of a mathematical model of a brick firing kiln," Glas. Ceram., vol. 65, no. 3–4, pp. 100–102, 2008.

[29] G. Halax, J. Toth and K. M. Hangos"Energy- Optimal Operation Conditions of a Tunnel Kiln" Comput. Chem. Eng., Vol. 12, no. 2/3, pp. 183-187, 1988.

[30] J. Durakovic, S. Delalic," Temperature Field Analysis of Tunnel Kiln for Brick Production" RMZ- Materials and Geoenvironment, Vol. 53, no. 3, pp. 403-408, 2006.

[31] Z. Chen, H. Zhang, and Z. Zhu, "An Integrated Intelligent System for Ceramic Kilns," Expert Syst. Appl., vol. 16, no. 1, pp. 55–61, 1999.

[32] E. Mançuhan, "Analysis and Optimization of Drying of Green Bricks in a Tunnel Dryer," Dry. Technol., vol. 27, no. 5, pp. 707–713, 2009.

[33] S. Kaya, E. Mançuhan, and K. Küçükada, "Modelling and Optimization of the Firing Zone of a Tunnel Kiln to Predict the Optimal Feed Locations and Mass Fluxes of the Fuel and Secondary Air," Appl. Energy, vol. 86, no. 3, pp. 325–332, 2009.

[34] S.H. Pulko, A.L. Hurst, H.R. Newten, "Simulation The Behaviour of Ceramics During Firing," Department of Electronics Engineering University of Hull Cottingham.

[35] M. G. Carvalho and M. Nogueira, "Improvement of Energy Efficiency in Glass-Melting Furnaces, Cement Kilns and Baking Ovens," Appl. Therm. Eng., vol. 17, no. 8–10, pp. 921–933, 1997.

[36] R. H. Essenhigh, "Studies in Furnace Analysis: Prediction of Tunnel Kiln Performance by Application of the Integral Energy Equation," Energy & Fuels, vol. 15, no. 3, pp. 552–558, 2001.

[37] A. Mezquita, J. Boix, E. Monfort, and G. Mallol, "Energy Saving in Ceramic Tile Kilns: Cooling gas heat recovery," Appl. Therm. Eng., vol. 65, no. 1–2, pp. 102–110, 2014.

[38] E. Mancuhan and K. Kucukada, "Optimization of Fuel and Air Use in a Tunnel Kiln to Produce Coal Admixed Bricks," Appl. Therm. Eng., vol. 26, no. 14–15, pp. 1556–1563, 2006.

[39] H. K. Versteeg and W. Malalalsekera, "Computational Fluid Dynamics,"Longman Scientific & Technical (Longman Grop Ltd 1995).

[40] B. Andersson, R. Andersson, L. Hakansson, M. Mortensen, and B. G. M. van Wachem, "Computational Fluid Dynamics for Engineers," Cambridge University, 2012.

[41] Y. Cengel, "Fluid mechanics: Fundamentals and Applications, Second Edition, McGraw Hill, New York 2010.

[42] E. Frguson, K. Gremillion, M. Ravenstahl and J. Cooper, "ANSYS Advantage," volume. VII, issue 3, 2013.

[43] J. Tu, G.Yeoh and C. Liu, "Comptational Fluid Dynamics Apractical Approach," Elsevier Ltd, Second Edition, 2013.

[44] ANSYS ICEM CFD 14 User Manual, Tutorial Manual, 2013.

[45] J. Chacon, J. M. Sala and J. M. Blanco, , ''Investigation on the Design and Optimization of a Low NOx-CO Emission Burner Both Experimentally and through Computational Fluid Dynamics (CFD) Simulations,'' Emergy & Fuels, Vol. 21, pp. 42-58, 2006.

[46] ANSYS Inc., 2009, ANSYS FlUENT 14.0 Theory Guide, Canonsburg, USA.

[47] E. Specht, Lecture Notes of Combustion engineering, University of Magdeburg, Germany, 2014.

[48] H. Struchtrup, ''Thermodynamics and Energy Conversion,'' Springer-Verlag, Berlin Heidelberg, 2014.

[49] W. Pabst & E. Gergorova ''Characterization of particles and particle systems'' PABST & GREGOROVÁ (ICT Prague), 2007.

[50] F. Becker, ''Becker Energy Consulting'' Elsterweg 6 90530 Wendelstein, Germany.

[51] H. F. Elattar, ''Flame simulation in rotary kilns using computational fluid dynamics'', Ph.D. dissertation, Magdeburg University, 2011.

[52] B. Cushman ''Environmental Fluid Mechanics'', John Wiley & Sons, Inc., 2014.

List of publications:

1. **Three Dimensional Analysis of thermal Stresses and Strains in Composite Exhaust Tube Model at Different Salt Concentration Ratios**
Raed Naeem[1], Azhar Sabah Ameed[2] and Adnan G.Tuaamah Al-Hasnawi[3]
[1]Petroleum Technology Department - University of Technology
[2]Electromechanical Engineering Department - University of Technology
[3]Center of Training and Factory- University of Technology, Baghdad, Iraq.
The Iraqi Journal for Mechanical and Material Engineering, Vol.14, No1, 2014.

Articles planned to publish:

2. **Combustion and Flow Mixing in the Gap between the Cars in Tunnel Kilns**
Adnan Al-Hasnawi[1]; Abdul Qayyum[2]; Eckehard Specht[3]
11th European Conference on Industrial Furnaces and boilers (INFUB-11)
Albufeira. Algarve. Portugal. 18-21April 2017 (accepted)

3a. **CFD Simulation of Flow Mixing in Tunnel Kilns by Air Side Injection**
Adnan G. Al-Hasnawi[1*], Hassanein A. Refaey[2], Tino Redeman[3], Echehard Specht[4]
[1, 3, 4] Institute of Fluid Dynamics and Thermodynamics, Otto von Guericke University, Universitätsplatz 2 D-39106 Magdeburg, Germany.
[1,] Training and Workshop Center, University of Technology, Tal Muhammad 10066, Baghdad, Iraq.
[2,] Mechanical Power Engineering Department, Shoubra Faculty of Engineering, Benha University, 108 Shoubra street, Cairo, Egypt.
Journal for Applied Thermal Engineering

3b. **Influence of Different Tunnel Kiln Geometries on Flow Mixing**
Adnan G. Al-Hasnawi[1*], Echehard Specht[3]
[1, 3], Institute of Fluid Dynamics and Thermodynamics, Otto von Guericke University, Universitätsplatz 2 D-39106 Magdeburg, Germany.
[1], Training and Workshop Center, University of Technology, Iraq, Baghdad
Journal of Kiln Tile

4. **Analytical and Numerical simulation for flames of annular ring burner with different gaseous fuels**
Adnan G. Al-Hasnawi[1], Abdul Qayyum[2], Echehard Specht[3]
[1, 2,3], Institute of Fluid Dynamics and Thermodynamics, Otto von Guericke University, Universitätsplatz 2 D-39106 Magdeburg, Germany.
[1], Training and Workshop Center, University of Technology, Tal Muhammad 10066, Baghdad, Iraq.
Gaswärme International

List of master thesis supervised

1. Y. Li ''CFD-Simulation of Flames for Annulus Ring Burner with gaseous Fuels,'' Master Thesis, Otto-von-Gurecke Univerität Magdeburg, 2015.

2. Y. Cao ''A Comparative Analysis of Different Position Burner in Tunnel Kiln by CFD,'' Master Thesis, Otto-von-Gurecke Univerität Magdeburg, 2016.

Curriculum Vitae

Personal Information

Name	: Adnan Ghareeb Tuaamah Al-Hasnawi
Date of Birth	: 01.07.1980
Place of Birth	: Baghdad, Iraq
Nationality	: Iraqi
E-mail	: adnan_tuaamah@yahoo.com
Social status	: Married, 1 child

Academic Qualification

2013-2016

Doctor of Engineering
Otto von Gurericke University of Magdeburg, Germany
Thesis Title: Mixing Behaviour of Side Injection of Air Jets and
Gaseous Fuel Jets into The Axial Flow of Tunnel Kilns

2006- 2009

Master of Science Thermal Engineering Technology
Technical College – Baghdad, Iraq
Thesis Title: Theoretical and Experimental Study of Active Carbon
Methanol Adsorption Units

1998-2003

Bachelor of Engineering in Mechanical Engineering / Air - Conditioning
and Refrigeration
University of Technology, Baghdad, Iraq

Work Experience

2003- 2013

Assistant Lecturer at Training and Workshop Center, University of
Technology, Baghdad, Iraq

2013-2016

Doctoral research in institute of Fluid Dynamics and Thermodynamics
(ISUT), Faculate of Process and System Engineering, Otto von Guericke
University of Magdeburg, Germany